FACULTEIT WETENSCHAPPEN

Department of Geology

A MICRO-CT INVESTIGATION INTO PORE-SCALE CO_2 SEQUESTRATION PROCESSES IN FRACTURED RESERVOIR ROCKS

Thesis submitted in fulfilment of the requirements
for the degree of Doctor of Science: Geology

Proefschrift voorgedragen tot het bekomen
van de graad van Doctor in de Wetenschappen: Geologie

Jeroen Van Stappen

Promotor:	Prof. dr. Veerle Cnudde
Examencommissie:	Dr. Tim De Kock
	Prof. dr. Stijn Dewaele
	Dr. Suzanne Hangx
	Prof. dr. Stephen Louwye
	Prof. dr. Snorre Olaussen
	Prof. dr. Jan Van den Bulcke

UNIVERSITEIT GENT

Academiejaar: 2017 - 2018

Dankwoord

In november 2013 begon ik aan mijn doctoraat. Vele beursaanvragen verder, enkele conferenties, veldwerk en enorm veel scanuren later, is het af. Ik ben enorm trots op mijn werk, maar natuurlijk had ik dit niet kunnen doen zonder de steun van de vele mensen rondom mij. Daarom had ik graag enkele personen bij naam bedankt.

Allereerst had ik graag mijn dank betuigd aan Veerle, mijn promotor. We weten allebei dat mijn doctoraat er één was van vallen en opstaan. Desondanks heb jij nooit je vertrouwen verloren in mij. Jouw raad en steun hebben ervoor gezorgd dat dit boekje er na vier jaar en een paar maanden eindelijk ligt. Bedankt om me te begeleiden en wegwijs te maken in de eerste stappen van mijn academische carrière. Ik loop niet zo heel ver weg en het wereldje is niet zo heel erg groot, dus je bent nog niet helemaal van me af.

Snorre and Kim, I would like to thank you for the nice times in Svalbard and the discussions we had about my work. I greatly appreciate the confidence you put in me for conducting this research.

Ook zonder Tim en Marijn zou deze thesis er niet gekomen zijn. Om één of andere reden zag jij wel potentieel in me, Tim, waardoor ik mijn master thesis bij Veerle kwam doen. Wat volgde is geschiedenis. Bedankt voor de leuke tijden, wijze raad en vele etentjes. Marijn, bedankt om me onder je hoede te nemen, de truken van de EMCT bij te brengen en ons openhartig gesprek op de terugtocht naar de Airbnb in Padua. Wesley en Tom, bedankt om me wegwijs te maken in de wondere wereld van conferenties, waar het maar logisch is om nog een bord nacho's te bestellen in

plaats van de stad te gaan bezichtigen. Jan en Hannelore, als groep-oudsten waren jullie voor mij vaak de bakens van rust waar ik terecht kon als het wat te druk werd in de andere bureaus. Aurélie, Delphine en Victor, bedankt voor de leuke tijden samen in en vaak ook net naast de S8, in wat vroeger nog gewoon de Barloo was.

Ondertussen zijn we vier jaar verder, is de Barloo de Eetoile geworden, SGIG is PProGRess geworden, en ikzelf ben de persoon geworden op het einde van zijn doctoraat. Onze groep is gegroeid, en ook wat voor mij de nieuwe doctoraatsstudenten zijn, ben ik dankbaar voor de leuke tijden samen. Maxim, bedankt om het laatste jaar met mij samen te hokken in de disco-bureau. Zonder jou zouden een groot deel van de figuren in deze thesis er anders hebben uitgezien. Redouane, thanks for your help in the SINTEF experiments. Without you, I would not have succeeded in these tests and I would definitely not have invested in Bitcoins. By the way: I still need to see the Eifel tower. Geraldine, bedankt voor je vrolijkheid en vitamientjes die je ten gepaste tijde kwam brengen. Ik wens je enorm veel plezier en succes in Ledeberg! Stefanie en Laurenz, ik hoop dat ik jullie in die beperkte tijd wat heb kunnen bijbrengen omtrent fluid flow, tubing en connectoren. Nu is het aan jullie! Timo, although we did not see each other that often, you were there on the most important moments. I wish you all the luck for your thesis.

Ik had in die vier jaar tijd het grote geluk en eer om niet alleen deel te mogen zijn van PProGRess, maar bij uitbreiding ook van het UGCT. Mijn dankbaarheid gaat uit naar alle huidige en vroegere leden van dit centrum die me met raad en daad hebben bijgestaan. Specifiek zou ik volgende personen willen bedanken: Matthieu, die na een korte geologische uitstap toch maar gewoon terug naar “de fysica” is gegaan. Bedankt om mijn voornaamste hulplijn te zijn bij theoretische en praktische problemen bij de scanners. Jan VdB, jou wil ik graag danken voor de fijne ervaringen op ICTMS 2015, jouw oprechte interesse in mijn onderzoek en natuurlijk de commentaren die je me gaf als jurylid. Manu en Thomas, jullie

hebben beiden mijn scan-skills naar boven gehaald. Amélie, bedankt om niet tegen Veerle te zeggen dat ik stiekem nog kwam scannen terwijl ik al enige tijd moest focussen op het schrijven. Ivan, although we have different approaches in tidying the bunkers, I am very happy you joined the team. Thanks for all coffee breaks we had together. Niet enkel PProGRess blijft groeien, maar ook de andere groepen van het UGCT. Ik ben heel benieuwd waar we (want ik blijf toch steeds een beetje teamlid natuurlijk) binnen vijf jaar zullen staan met het centrum. Nogmaals bedankt aan alle UGCT leden, en bij uitbreiding XRE-leden, voor de fijne tijden en samenwerking.

I would also like to thank Chris Spiers, Suzanne Hangx and the members of the HPT lab at Utrecht University for their help during the last year and a half of my PhD. Thanks to your help, we got the SINTEF cell working and I could better understand what exactly I was doing with it. I look forward to reinforce the team and learn even more from all of you during my stay abroad.

Om in de academische wereld te blijven wil ik graag nog de leden van de MinPet groep bedanken die de traditie van pizza Friday hebben verstevigd. In het bijzonder wil ik Elien bedanken voor haar steun tijdens het schrijven van de thesis. Het maakte het hele proces wat aangenamer, wetende dat ik niet alleen voor de nakende deadlines stond. Bedankt aan alle laboranten die me hielpen, Danielle voorop, maar natuurlijk ook Veerle, Ann-Eline en Jan. Ook wil ik de “mannen van het atelier” in de Proeftuinstraat bedanken voor hun bereidwilligheid telkens ik een samplehouder of flow cell nodig had. Bedankt voor het snelle werk. Ik bedank ook graag alle studenten die me toevertrouwden met de begeleiding van hun bachelorproef of masterthesis. Laura, Hilke, Meysam en Benjamin, ik hoop dat jullie evenveel van mij geleerd hebben als ik van jullie.

Aan alle onderzoekers van SEPOCOM, SECEMIN en ISHECO wil ik mijn dank betuigen voor de goede samenwerking. Ook al is self-healing van polymeren of beton niet meteen mijn core business,

toch heb ik er veel van opgestoken. Net als van de vele bezoekers die ik mocht begeleiden aan de scanners. An-Sofie, Stef, Lode, Michela, Aurélie, Filip, Amir en de vele andere bezoekers die de revue zijn gepasseerd: bedankt om mijn scancapaciteiten telkens weer op de proef te stellen.

De vrienden van Denderleeuw en omstreken wil ik bedanken voor de onspanning, de avonden in de Standaard of bij “den Bol”, en de vele spelletjes-avonden. Jonas, Kevin, Steven, Inneke, Lise, Freya, Lien, Thomas (x2), Lieselot, Jeroen: merci voor alle fijne momenten. Bedankt ook aan Ine, Arno, Tessy en Nore voor het leuke reisgezelschap. Jammer genoeg moest ik passen voor Parijs, maar dat halen we nog eens in. Bedankt ook aan de vrienden van de geologie van het eerste (en tweede) uur. Als ik me niet vergis ben ik de eerste van een hele reeks geologen van ons jaar die zijn doctoraat zal verdedigen. Het was me een waar genoegen vijf jaar (en meer) plezier met jullie te mogen maken. Wout, Nore, Tim, Jens, Chloë (en Manon), Embo (en Liesbeth), Stef, Maarten, Pille, Thijs, Jeroen J.,…: dat er nog veel feestjes mogen volgen. Thanks to all of my Erasmus friends who followed me from a distance during my PhD. May the Universe bring good luck and happiness to all of you. Thanks Moniek, Laurens and Severs; Steffen and Silke; Fanny, Anna, Eva, Thessa, Caitlin and everyone I forget. Bedankt ook aan de vrienden en vriendinnen van Lentekind. Voor zij die zich afvragen waarom ik nu in hemelsnaam vier jaar aan een stuk stenen heb water gegeven, gevochten met ijsberen en de wereld heb afgereisd: lees gerust verder, het staat allemaal beschreven op de volgende pagina’s.

Tot slot, maar zeker niet in het minst, wil ik mijn familie bedanken. Zij waren een bron van continue steun en liefde, waar ik niet zonder zou kunnen. Allereerst wil ik mijn Mama bedanken, Hilde Staels. Geen moeite is haar te veel voor het geluk van haar kinderen. Bedankt Mama, dat je er altijd voor me was en me altijd gesteund hebt. Bedankt ook aan mijn Oma, Leona Goubert, om de hele familie telkens weer samen te brengen rond een goed gevulde

tafel. Bedankt aan mijn broers, zus en schoonzussen, Dieter en Jolien, Fien, Tomas en Lucine: jullie kleine broer kan nu eindelijk aan het grote-mensen-leven beginnen. Bedankt ook aan mijn nonkels en tantes, neven en nichten voor de fijne familiemomenten, in een gîte in de Ardennen, of gewoon bij Oma aan tafel.

Veel leesplezier met de rest van mijn thesis!

Jeroen Van Stappen

Gent, 2017

English summary

Without doubt, anthropogenic climate change is one of the major challenges faced by our planet in the 21st century. The most important factor affecting the earth's climate is the emission of greenhouse gases. Since 1750, the atmospheric concentration of the most important greenhouse gases (CO_2, CH_4 and N_2O) has increased to unprecedented heights in the last 800,000 years. The main contributor to the average global temperature is CO_2. This is the most abundant greenhouse gas in the atmosphere. Recently, a binding climate agreement was decided on in Paris. In this agreement, the signatories agree to limit the global temperature raise to a maximum of 2°C above the pre-industrial level. To reach this goal, a series of actions have to made: the energy efficiency has to improve, energy saving measurements are to be promoted, the usage of high carbon fuels has to diminish, renewable energy needs to be promoted and geo-engineering approaches to decrease the emission of greenhouse gases need to be applied.

One of those geo-engineering approaches is Carbon Capture and Sequestration (CCS). In this approach, the idea is that CO_2 is captured at large point-sources of CO_2 emission, transported and permanently closed off from the atmosphere. The most important locations for CO_2 storage are governed by large saline rock formations which act as reservoirs. CCS is globally considered as a technique which is highly necessary to control the global emission of CO_2 in the future. This is why CCS was the subject of numerous scientific studies in the last decennia. Despite the global consensus

that CCS is one of the most promising techniques for CO_2 mitigation, the technique is currently only applied in a few large-scale projects.

The need for pilot projects, where the technique can be fully deployed and monitored, triggered a research and development project in 2007 on the feasibility of CCS in Longyearbyen, Spitsbergen. Spitsbergen is the largest island in the archipelago Svalbard in the northeastern part of the Barents Sea. Longyearbyen is the main settlement on the island group with approximately 2000 inhabitants. Energy and heating are locally supplied via a coal-combustion power plant. The coal is locally mined in the direct vicinity of the town. On a yearly basis, the coal-combustion power plant is responsible for an emission of nearly 60,000 tons of CO_2. The research and development project started with the identification of geological layers which could serve as reservoir for CO_2 storage. In 2009, these were found at a depth of approximately 800 meters below Longyearbyen. The geological units were characterized by a low to medium porosity and a very low permeability. However, the layers are affected by fractures, which make the reservoir a dual-porosity system. The fractures are considered to form the most important pathways for fluid conductivity and are known to range from a few micrometers in size to structures of several meters long.

In this dissertation, the influence of microscopic fractures on the fluid flow behavior in the reservoir is studied, as well as the influence of the fractures on pore-scale processes related to CO_2 sequestration at a depth of 800 meters. To investigate this, a series of experiments were conducted on small-scale rock cores taken from the reservoir sections. In these rock cores, natural or induced fractures were present. The experiments were monitored using high resolution X-ray computed tomography (micro-CT). All experiments were performed at the Center for X-ray Tomography at Ghent University (UGCT).

In the introduction of this dissertation, the socio-environmental context is given of this thesis. The necessity for CO_2 mitigation is discussed, as well as the most important geo-technical approaches to achieve this. Injecting CO_2 in the underground changes the geo-chemical properties of the formation fluids within the reservoir. This alteration can affect the reservoir properties. In the introduction, the pore-scale processes which are expected in a CO_2 sequestration process are discussed. Subsequently, the local project in Longyearbyen is discussed, as well as the manner in which the experiments presented in this thesis contribute to this project.

Subsequently, the most important rock properties, linked to fluid flow behavior in reservoir rocks are discussed, as well as the mechanical strength of geomaterials (Chapter 1). The most common techniques used to determine rock porosity, permeability and mechanical strength are explained. Because the reservoir sections in the Longyearbyen CO_2 project represent a dual-porosity system, the different manners in which fractures potentially influence these parameters are also discussed.

Next, an overview of the most important 2D and 3D imaging techniques which were used in this dissertation (Chapter 2). As the most important technique is micro-CT, this technique is discussed in-depth. The most important aspects of this non-destructive technique are discussed, with attention towards its use for the quantification of fractures in geomaterials. The chapter ends with an overview of the micro-CT scanners at UGCT, with as main focus the systems and add-on equipment used in this dissertation.

Chapter 3 provides the in-depth characterization of the reservoir sections of the Longyearbyen CO_2 project. In this chapter results are combined from standard characterization methods concerning the porosity, pore size distribution and the permeability of the reservoir sections, as well as results from micro-CT scans of core and outcrop samples from the reservoir sections. In these micro-CT

scans, the focus was put on the characterization of fractures and fracture apertures through the typical micro-CT analysis methods. This led to the first hard data on fracture apertures, obtained from decompacted core samples. Certain micro-CT scans had a spatial resolution that was high enough to visualize and segment the entire pore structure of the rock cores. Based on the segmentation of this pore structure, image based fluid flow modelling could be performed. This allows the prediction of the amount of CO_2 which can be retained by the pore network of the rocks, as well as the determination of fluid flow properties which are otherwise determined by elaborate laboratory tests.

In Chapter 4, experiments are discussed which focus on the influence of sample size on the mechanical strength of geomaterials. A series of tests were performed on standard sized rock cores, as prescribed by international standards, with a diameter of 45 mm and a length of approximately 90 – 100 mm. On the same rock types, a series of small-scale experiments were also conducted to determine the mechanical strength on centimeter-scaled rock plugs. The experiments were carried out on four limestone types that are commonly used as building material in Belgium, France and The Netherlands. On reservoir samples from the Longyearbyen CO_2 project, small-scale tensile strength measurements were carried out. These strengths were compared to measurements described in literature.

Chapter 5 discusses the influence of confining pressure on fractures in reservoir rocks of the Longyearbyen CO_2 project. Previous studies in which these fractures were investigated provided information obtained from decompacted core samples. In this chapter, small rock plugs (with a diameter of 5 mm and a length of 14 mm) are subjected to confining pressures similar to those in the actual reservoir at a depth of 800 meter. To do this, a small-scale in-situ triaxial device, provided by SINTEF, Norway, was used. Through micro-CT imaging, the fracture aperture of natural and induced fractures could be determined at different confining pressures. The

analysis was performed using a Matlab script, developed in the course of the PhD research. The script is included as Appendix A of this dissertation. On top of this, the influence of microscopic fractures on the fluid flow behavior through these rock plugs was quantified and linked to the measured fracture apertures.

In Chapter 6, a series of experiments is presented in which processes linked to CO_2 sequestration are imitated in rock cores of the Longyearbyen CO_2 project. Here, the focus is put on the influence of rock fractures on these processes. Experiments are conducted which mimic the drying behavior in the reservoir, close to the CO_2 injection well, as well as experiments in which an acidic solution is pumped through the rock cores. The acidic solution is similar to the acidic solution that forms when CO_2 dissolves in the formation fluids.

We end with the main conclusions of this dissertation (Chapter 7). In this chapter, a critical remark on micro-CT analysis and visualization of fractures is given. This is known to be a critical aspect in many research applications. Whether the application is the geotechnical study of polymer treated clays, the use of engineered materials with self-healing properties, or the weathering of (natural) building materials, fractures typically add complexity to the analysis. Often it is important to detect the initiation of fractures. Using micro-CT as a detection tool, this often leads to the downscaling of the sample size. Also in the experiments performed in this dissertation that was the case. The question then arises how representative such tests remain. In this research, we have shown that the reservoir rocks of the Longyearbyen CO_2 project in fact are very reliable on fractures for their fluid flow behavior. Even miniscule fractures can locally significantly increase the permeability of the reservoir. Injection of CO_2 causes a number of geo-chemical processes which can locally influence the fracture itself and the surrounding of the fracture. The experiments described in this dissertation add to the knowledge on the reservoir

sections of the Longyearbyen CO_2 project and, by extension, to the knowledge of pore-scale processes in dual-porosity reservoirs.

Nederlandse samenvatting

Antropogene klimaatsopwarming is zonder twijfel één van de belangrijkste uitdagingen voor onze planeet in de 21ste eeuw. De belangrijkste drijvende factor voor de opwarming van de aarde is de uitstoot van broeikasgassen. Sinds 1750 is de atmosferische concentratie van de drie belangrijkste broeikasgassen (CO_2, CH_4 en N_2O) gestegen tot ongeëvenaarde hoogtes in de laatste 800.000 jaar. Het belangrijkste broeikasgas in de atmosfeer is CO_2: het is het meest voorkomende van alle broeikasgassen en heeft de meeste invloed op de gemiddelde temperatuur op aarde. Recent is een bindend klimaatakkoord gesloten in Parijs. Hierin werd internationaal afgesproken om de globale temperatuurstijging te beperken tot maximaal 2°C boven het pre-industriële niveau. Om dit te bereiken dienen er een reeks maatregelen genomen te worden: de energie-efficiëntie moet verbeteren, besparing van energie dient bevorderd te worden, we moeten het gebruik van koolwaterstofbronnen verminderen, hernieuwbare energie inzetten en ten slotte kunnen we aan de hand van geo-technologische toepassingen de uitstoot van broeikasgassen naar de atmosfeer inperken.

Één van deze geo-technologische toepassingen is CO_2 sequestratie. Hierbij wordt CO_2 gecapteerd bij locaties zoals fossiele brandstofcentrales. Vervolgens wordt het vervoerd en permanent afgesloten van de atmosfeer. De belangrijkste locaties waarin CO_2 kan worden opgeslagen zijn ondergrondse geologische reservoirgesteenten. CO_2 sequestratie is een techniek die

wereldwijd wordt beschouwd als uiterst noodzakelijk om de CO_2 uitstoot in de nabije toekomst onder controle te kunnen houden. De laatste decennia is er dan ook veel onderzoek verricht naar de haalbaarheid van de techniek. Toch zijn er wereldwijd nog maar een aantal locaties waar het ook effectief op grote schaal wordt toegepast.

De nood aan test-sites, waar de techniek kan worden uitgetest op een kleine schaal, zorgde ervoor dat in 2007 een project startte om de haalbaarheid van CO_2 sequestratie in en rond Longyearbyen, Spitsbergen te onderzoeken. Spitsbergen is deel van de eilandengroep Svalbard in het noordoostelijke deel van de Barentszzee. Longyearbyen is de belangrijkste nederzetting op de eilandengroep met ongeveer 2000 inwoners. Hier wordt steenkool lokaal ontgonnen en omgezet tot elektriciteit voor de stad in een steenkoolverbrandingscentrale. Deze zorgt jaarlijks voor een lokale uitstoot van ongeveer 60.000 ton CO_2. Het project startte met de zoektocht naar gesteentelagen die bruikbaar zijn als reservoir voor CO_2 opslag. In 2009 werden gesteentelagen op een diepte van ongeveer 800 meter onder Longyearbyen geïdentificeerd als de beste mogelijke locatie voor CO_2 opslag. Deze gesteentelagen werden gekenmerkt door een lage tot gemiddelde porositeit, gelinkt met een zeer lage permeabiliteit. Al gauw werd ontdekt dat de belangrijkste bijdrage voor het vloeistoftransport in het reservoir geleverd werd door breuken in het gesteente. Het reservoir is dus een zogenaamd dubbel-poreus gesteente. De breuken in het reservoir variëren van enkele micrometers in grootte tot structuren van 1 tot 10 meter lang.

In deze dissertatie wordt de invloed van microscopische breuken op het vloeistoftransport in het reservoir onderzocht, alsook de invloed van de breuken op processen gelinkt met de sequestratie van CO_2 op een diepte van 800 meter. Hiervoor werden een reeks experimenten uitgevoerd op gesteentekernen van het reservoir waarin natuurlijke of geïnduceerde breuken voorkwamen. Deze experimenten werden in 3D opgevolgd via hoge resolutie X-stralen

computationele tomografie (CT), uitgevoerd aan het Centrum voor X-stralen tomografie van de UGent (UGCT).

In de introductie tot deze dissertatie wordt de socio-ecologische context geschetst van deze thesis. De nood voor het beperken van de CO_2 uitstoot wordt verduidelijkt, alsook de belangrijkste opties voor het verminderen van de netto uitstoot via geo-technologische oplossingen. Het injecteren van CO_2 in de ondergrond zorgt voor de verandering van de geo-chemische samenstelling van de vloeistoffen die in de gesteentelagen aanwezig zijn. Deze geo-chemische alteratie kan een effect hebben de reservoir eigenschappen van de gesteentelagen. In de introductie wordt verduidelijkt welke interacties kunnen verwacht worden op de porie-schaal van de gesteenten. Vervolgens wordt het lokale CO_2 sequestratie project in Longyearbyen verduidelijkt, alsook de manier waarop de gepresenteerde experimenten in deze thesis bijdragen tot dit project.

Hierna wordt dieper ingegaan op volgende gesteente-eigenschappen (hoofdstuk 1): de porositeit, de permeabiliteit en de mechanische sterkte van gesteentekernen. Aangezien de reservoirgesteenten in het lokale CO_2 sequestratie project van Longyearbyen zogeheten dubbel-poreuze gesteentelagen zijn, wordt ook dieper ingegaan op de manier waarop breuken een invloed hebben op deze parameters.

De belangrijkste 2D en 3D visualisatietechnieken, gebruikt in dit onderzoek worden besproken in hoofdstuk 2. Aangezien er in deze thesis voornamelijk gebruik werd gemaakt van X-stralen tomografie, ligt de focus hierop. De belangrijkste aspecten van deze niet-destructieve techniek worden toegelicht, met aandacht voor de specifieke analyse technieken voor het kwantificeren van breuken in geomaterialen. Voorts worden de X-stralen scanners van het UGCT expertise centrum besproken, waarbij de nadruk wordt gelegd op de specifieke systemen en add-on apparatuur gebruikt voor deze thesis.

De reservoirgesteenten van het sequestratie project in Spitsbergen werden via de gebruikelijke technieken gekarakteriseerd voor wat betreft hun porositeit, porositeitsverdeling en permeabiliteit. Resultaten van deze standaard karakterisatie zijn weergegeven in hoofdstuk 3. Hierbij worden ook de eerste resultaten gegeven van een X-stralen tomografie studie specifiek gericht op de breuken in deze gesteenten. Voor het eerst in het sequestratie project was het via X-stralen CT mogelijk om breuken te karakteriseren voor wat betreft hun (maximale) breukopening. Bepaalde CT scans waren gekenmerkt door een resolutie die hoog genoeg was om de volledige poriestructuur in de gesteentekernen te visualiseren. Op basis van de segmentatie van die poriestructuur kon vloeistoftransport in de reservoirgesteenten gesimuleerd worden. Deze simulaties kunnen gebruikt worden voor het voorspellen van de hoeveelheid CO_2 die lokaal kan weerhouden worden in de poriestructuur van het gesteente en voor het bepalen van vloeistoftransport parameters waarvoor anders uitgebreide en tijdrovende experimenten nodig zijn.

Vervolgens worden experimenten toegelicht die gericht zijn op het identificeren van de invloed van staalgrootte op de mechanische sterkte van gesteenten (hoofdstuk 4). Hiervoor werden een reeks testen uitgevoerd op gesteentekernen met een grootte voorgeschreven in de internationale standaarden. Deze gesteente stalen hebben typisch een diameter van 45 mm en een lengte van 90 – 100 mm. Er werd ook een reeks testen op zeer kleine gesteentekernen van hetzelfde materiaal uitgevoerd (diameter van ± 10 mm en lengte van 20 mm). Deze experimenten werden initieel uitgevoerd op vier verschillende goed gekarakteriseerde carbonaatgesteenten die in België, Frankrijk en Nederland gebruikt worden als bouwstenen. Ook werden er mechanische sterkte metingen op de reservoirgesteenten van Longyearbyen uitgevoerd en vergeleken met waarden gekend uit de literatuur.

Hoofdstuk 5 gaat dieper in op de invloed van omgevende druk op de breuken in de reservoirgesteenten van Longyearbyen. Voorheen

werden karakteristieke eigenschappen van breuken in dit reservoir bepaald op gedecomprimeerde gesteentekernen van de ondergrondse reservoir secties. In deze dissertatie werden kleine gesteentekernen (met een diameter van 5 mm en een lengte van 14 mm) met een in-situ triaxiale opstelling onderworpen aan omgevende drukken zoals deze voorkomen in het eigenlijke reservoir op een diepte van ongeveer 800 meter. Door 3D beeldvorming via hoge resolutie X-stralen tomografie kon de breukopening van natuurlijke en geïnduceerde breuken bepaald worden. Hiervoor werd gebruik gemaakt van een Matlab script dat ontwikkeld werd in de loop van dit doctoraatsonderzoek. Dit Matlab script is integraal weergegeven als Appendix A van deze dissertatie. Verder werd ook de precieze invloed van microscopische breuken op het vloeistoftransport doorheen de gesteentekernen gekwantificeerd en gelinkt aan de gemeten breukopening.

Tot slot geeft hoofdstuk 6 een reeks experimenten weer waarin processen gelinkt aan CO_2 sequestratie werden nagebootst in gesteentekernen van het Longyearbyen CO_2 project. Ook hier ligt de focus op de invloed van breuken op deze processen. Meer specifiek werden experimenten gericht op het uitdrogen van gesteenten door de injectie van CO_2 weergegeven, alsook experimenten waarin een zure oplossing doorheen gesteentekernen werd gepompt. Deze zure oplossing is gelijkaardig aan het zuur dat vormt wanneer CO_2 wordt opgelost in de formatie-vloeistoffen.

Afsluiten doen we met de voornaamste conclusies van dit onderzoek (hoofdstuk 7). Bovendien wordt een kritische analyse gegeven omtrent beeldvorming van breuken via X-stralen tomografie. Dit is namelijk gekend als een heikel punt in verschillende onderzoekdomeinen, gaande van geotechnische studies in verband met kleien, over applicaties met hoogtechnologisch ontwikkelde materialen met zelfhelende eigenschappen, tot verwering van (natuurlijke) bouwmaterialen. In

al deze toepassingen kunnen breuken zorgen voor extra complexiteit. Bovendien is het vaak belangrijk om de breukvorming zelf te kunnen visualiseren. Om aan de vereiste beeldkwaliteit en resolutie te komen met behulp van X-stralen tomografie, is vaak een verkleining van de staal-grootte vereist. Dit was ook het geval in het onderzoek beschreven in deze dissertatie. De vraag komt dan vaak naar boven hoe representatief zulke testen dan nog blijven. In dit onderzoek hebben we aangetoond dat de gesteenten van het Longyearbyen CO_2 project zeer afhankelijk zijn van breuken wat betreft hun vloeistoftransport. Zelfs minuscule breuken kunnen lokaal de permeabiliteit van het gesteente significant verhogen. Bovendien zorgt de injectie van CO_2 voor een reeks geo-chemische processen die, in de nabijheid van breuken, lokaal een invloed kunnen hebben op de breuk zelf. De uitgevoerde experimenten verhogen dan ook de kennis omtrent de reservoirgesteenten van het Longyearbyen CO_2 project en bij uitbreiding omtrent porie-schaal processen in dubbel-poreuze gesteenten.

List of abbreviations

AR5	Fifth Assessment report
ASTM	American Society for Testing and Materials
CCD	Charge Coupled Device
CCS	Carbon Capture and Storage
CH_4	Methane
CO_2	Carbon dioxide
CsCl	Cesium chloride
Da	Damköhler number
DH1-DH8	Drill Holes 1 to 8
ECBM	Enhanced Coal Bed Methane
EMCT	Environmental Micro-CT system
EOR	Enhanced Oil Recovery
FEP	Fluorinated ethylene propylene
Fm.	Formation
FWHM	Full-Width-Half-Maximum
GHG	Green House Gas
Gt	Giga tons
HECTOR	High Energy CT system Optimized for Research
ICP-OES	Inductively Coupled Plasma – Optical Emission Spectrometry
IPCC	Intergovernmental Panel on Climate Change
ISRM	International Society for Rock Mechanics
Kppm	1,000 parts per million
L:D	Length:Diameter ratio
MA	Missing Attenuation

mD	Milli-Darcy
(Micro-)CT	(High resolution) computed tomography
MIP	Mercury Intrusion Porosimetry
N_2O	Nitrous oxide
Pe	Péclet number
PEEK	Polyether ether ketone
PH	Peak Height
PMMA	Polymethyl methylacrylate
PProGRess	Pore-scale Processes in Geomaterials Research
PSF	(Gaussian) Point Spread Function
PTFE	Polytetrafluoroethylene
PVC	Polyvinyl chloride
RCPs	Representative Concentration Pathways
Re	Reynolds number
REV	Representative Elementary Volume
SDD	Source Detector Distance
SEM(-EDS)	Scanning Electron Microscopy (with energy dispersive X-ray spectroscopy)
SOD	Source Object Distance
sst	Sandstone
$UCS_{(c)}$	(corrected) Uniaxial Compressive Strength
UGCT	Centre for X-ray Tomography at Ghent University
UNIS	University Centre in Svalbard

Contents

0.

Introduction and dissertation outline

Anthropogenic climate change is one of the main challenges facing our planet in the 21st century. From 1880 to 2012, human interference in the global climate system has increased the annual mean air temperature by roughly 0.8°C (IPCC, 2013). These values are based on historical records for which multiple independently produced datasets exist (IPCC, 2013). One of the most important factors driving anthropogenic climate change is the emission of greenhouse gases (GHG). Based on ice core measurements, it could be concluded that since 1750, the atmospheric concentrations of the most important GHG, carbon dioxide (CO_2), methane (CH_4) and nitrous oxide (N_2O) have all increased to unprecedented levels in at least the last 800,000 years, due to human activities (IPCC, 2013). The main contributors to the recent anthropogenic emission of CO_2 are the industries related to fossil fuel combustion and cement production. CO_2 emissions from these industries are estimated to have released 375 Gt of carbon (= 1375 Gt of CO_2) between 1750 and 2011 (IPCC, 2013) (Figure 0.1). Adding up to that are the contributions from global deforestation and other land use changes, which have emitted 180 Gt of carbon in the atmosphere.

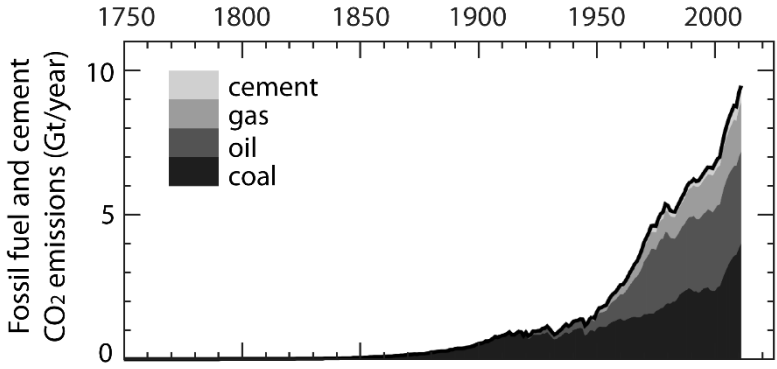

Figure 0.1. Estimated anthropogenic CO_2 emissions from the fossil fuel and cement industries (Gt/year) since 1750. Figure from (IPCC, 2013).

Globally, there is a dynamic exchange in the CO_2 concentrations between the atmosphere on the one hand and terrestrial and aquatic environments on the other hand. From the cumulative

anthropogenic CO_2 release, this dynamic exchange has naturally sequestered 155 Gt of carbon (= 568 Gt of CO_2) in the earth's oceans, and an estimated 160 Gt of carbon (= 587 Gt of CO_2) in the natural terrestrial ecosystems. This means that the remaining 240 Gt of carbon, or 880 Gt of CO_2 has accumulated in the atmosphere since 1750 (IPCC, 2013). It makes CO_2 the most abundant GHG in the atmosphere, and the most important one causing the increase in the average global temperature. Due to this accumulation, the atmospheric CO_2 concentration has increased from 270 ppm in 1750 to 391 ppm in 2011 (IPCC, 2013) and has even reached the threshold of 400 ppm in 2015 (Keenan et al., 2016).

In the Fifth Assessment report (AR5) of the Intergovernmental Panel on Climate Change (IPCC) a set of scenarios for the future global and regional climate change were presented (Figure 0.2): the Representative Concentration Pathways (RCPs) (IPCC, 2014, 2013). All scenarios assume a further increase of CO_2 emissions to the atmosphere during the course of the 21st century, leading up to higher atmospheric CO_2 concentrations in 2100 than the present day. The most favorable scenario is RCP2.6 with expected CO_2 concentrations reaching 430 - 480 ppm by the year 2100, while the least favorable scenario, RCP8.5, assumes a concentration of 936 ppm by the year 2100 (IPCC, 2013). These scenarios only focus on the change in anthropogenic emissions and thus not include changes in natural CO_2 emissions, for example through volcanic activity.

0.1. Necessity for CO_2 mitigation

Recently, a binding international climate agreement was achieved at the 2015 climate summit in Paris (UNFCCC, 2015). In this Paris agreement, the long-term goal was set to keep the increase of the global average temperature below 2°C above pre-industrial levels, with an aim to limit the increase to 1.5°C. This requires the reduction of CO_2 emissions and the emission of other GHG: either by preventing that they are released to the atmosphere (conventional mitigation), or by actively removing them from the

atmosphere (to achieve so-called negative emissions). Current climate policies are mainly focusing on conventional mitigation. Yet, it is known that this alone will not be sufficient to achieve the goals set out in the Paris agreement (Gasser et al., 2015; Sanderson et al., 2016) (Figure 0.2). In the second half of this century, a balance will be needed between emission sources and sinks, or negative emissions (UNFCCC, 2015).

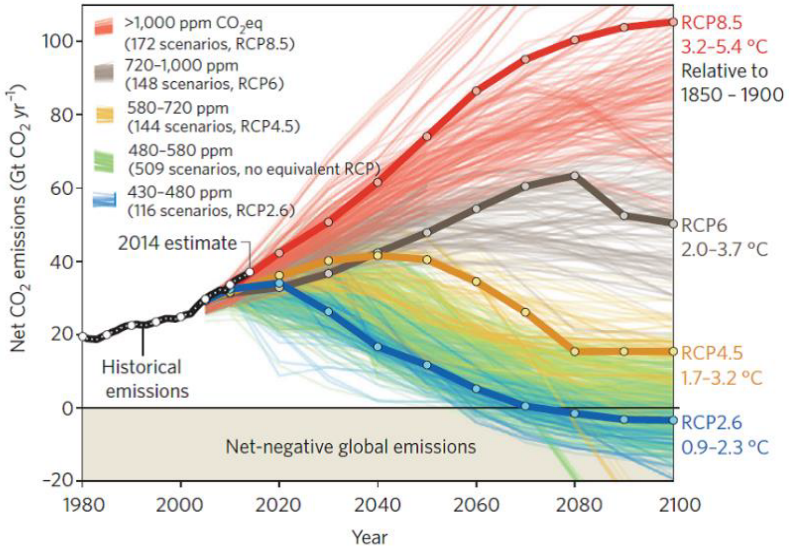

Figure 0.2: To achieve the goals set by the Paris climate agreement (UNFCCC, 2015), net-zero-emissions are necessary through a decarbonization of the global economy. Only the RCP2.6 scenario (blue), set up in the fifth IPCC assessment report (IPCC, 2014) is compatible with the targets of the Paris agreement (Fuss et al., 2014). This requires negative net global CO_2 emissions by the year 2070. Figure from (Fuss et al., 2014).

No single technological option on its own will provide all of the necessary emission reductions. It is rather a portfolio of mitigation measures which will be necessary (Metz et al., 2005): one should improve energy efficiency, promote energy conservation, decrease the usage of high carbon fuels, deploy renewable energy and apply geoengineering approaches (Leung et al., 2014). In the scope of this thesis, focus is put on one of these engineered options to further reduce anthropogenic atmospheric CO_2 release: Carbon Capture and Storage (CCS). In such a negative emissions scenario, CO_2 is

captured and concentrated at large point sources like fossil-fueled power plants after which it is transported and permanently closed off from the environment. Currently, most agree that CCS is necessary for a meaningful CO_2 reduction in the near future. The transition from a global fossil-fuel dependent energy system to one based on renewable and clean sources of energy is believed to be a gradual one up to 2100 (Abas et al., 2015). Although oil and natural gas-based energy reserves are at the decline, coal production and use is believed to still reach its peak around 2050, due to emerging economies (Abas et al., 2015). With this in mind, the Stern review on the economics of climate change states that: “CCS is essential to maintain the role of coal in providing secure and reliable energy for many economies” and “the forecast growth in emissions from coal, especially in China and India, means CCS technology has particular importance” (Stern, 2006). In their special report on carbon dioxide capture and storage, the IPCC reports on potential sources, capture and transport processes and eventual storage of CO_2. Storage options include ocean storage, mineral carbonation and geological storage (Metz et al., 2005).

0.1.1. Ocean storage

CO_2 could be deliberately injected into the ocean at great depth. Currently the oceans naturally take up about 2 Gt of carbon (= 7 Gt of CO_2) per year due to the increase in atmospheric CO_2 from anthropogenic emissions. It is believed that due to this natural exchange, the oceans will take up most CO_2 over the course of several centuries when anthropogenic CO_2 emissions would cease to exist. Because of their vast volume , there is no practical limit to the uptake of anthropogenic CO_2 by the oceans. Over the past 35 years, there have been numerous theoretical, laboratory and modelling studies towards intentional CO_2 storage in the ocean. However, so far it has not yet been deployed or thoroughly tested, except in some small-scale field experiments (Metz et al., 2005). It is believed that injection of a few Gt of CO_2 in the ocean would induce a local change in the ocean’s chemistry, while continuous

injection of a few hundreds of Gt of CO_2 would eventually produce a chemical change over the entire oceanic volume. This would potentially harm marine organisms with a potential impact on the bigger ecosystem in the oceans.

0.1.2. Mineral carbonation

In the process of mineral carbonation, CO_2 reacts chemically with calcium- and/or magnesium containing minerals to form stable carbonates (Olajire, 2013; Metz et al., 2005). As with ocean storage, this is a process which occurs in nature as well, however at a very slow reaction speed. There is a difference between in-situ and ex-situ carbonation: with in-situ carbonation, CO_2 is injected in porous rocks and the carbonation process occurs in the subsurface. For in-situ carbonation to be successful, it is paramount that a good injection site is chosen into metal-oxide bearing rocks (Oelkers et al., 2008). Mafic volcanic rocks are considered ideal for such processes. These rocks are rich in magnesium and iron with olivine, pyroxene, amphibole and biotite as most common rock-forming minerals. They often also contain calcium-rich varieties of plagioclase feldspar. Ex-situ carbonation is when the process takes place above the ground: natural minerals or industrial residues are carbonated in a processing plant. Despite experimental successes, and promising process ideas for the carbonation of rock material, currently very little of the concepts for carbonation of natural minerals has matured to the state of large-scale implementation (Olajire, 2013; Matter et al., 2014, 2009). Critical challenges are the improvement of the carbonation reaction kinetics, and the development of commercially acceptable processes. It is a relatively new research area in which substantial progress has been made and is expected to follow in the future.

0.1.3. Geological storage

The most viable option, however, for the storage of large quantities of CO_2 is considered to be geological storage (Leung et al., 2014). From the 1970s onwards, underground geological storage of CO_2

has been successfully explored both onshore and offshore and is currently applied as mitigation strategy in several pilot (Würdemann et al., 2010; Doughty et al., 2008) and commercial projects (Benson et al., 2005; Arts et al., 2008; Orr, 2009). In fact, the accumulation of CO_2 in the underground is a known natural phenomenon (Benson et al., 2005). Geological storage of CO_2 is possible in a broad range of geological settings, such as sedimentary basins (Doughty et al., 2008; Chadwick et al., 2005), deep volcanic rocks (Matter et al., 2009), salt caverns (Bachu and Dusseault, 2005), or abandoned mines (Piessens and Dusar, 2004). Figure 0.3 illustrates the reservoir possibilities for geological CO_2 storage (Benson et al., 2005).

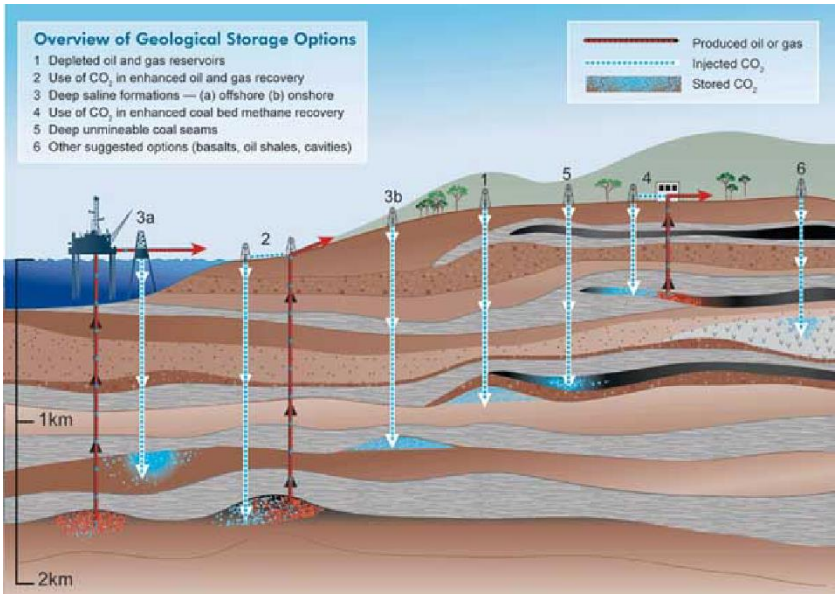

Figure 0.3: Overview of the options for geological storage of CO2 as stated in the IPCC special report on CCS (Benson et al., 2005).

The most important requirements for CCS through geological storage include appropriate porosity and permeability of the reservoir, its volumetric extent, a stable geological environment and the presence of a cap rock sealing the reservoir (Solomon et al., 2008). The most promising settings are: 1) (nearly) depleted oil and

gas reservoirs; 2) unmineable coal beds and 3) saline aquifers. In the case of (nearly) depleted reservoirs, infrastructures and techniques necessary for CCS are mostly available, reducing costs which might affect the potential for CCS. Injection of CO_2 in such cases increases the reservoir pressure, which provides the force to extract residual oil and gases. As such, CCS is used as an Enhanced Oil Recovery (EOR) technique. After primary production, when the active reservoir is depleted, up to 40% of the residual oil can be extracted through the injection of CO_2 (Blunt et al., 1993). One of the best known CCS-EOR projects is in the Weyburn field in central Canada. This was one of the first pilot scale projects, where ideas and theories related to CCS could be tested for future application to larger projects (Whittaker et al., 2011).

Similarly to CCS in enhanced oil and gas reservoirs, CO_2 injection in unmined coal beds may aid in the recovery of methane trapped in the porous structure of the coal. This process is called CO_2 enhanced coal bed methane (ECBM) extraction. It is successfully carried out in several ECBM sites around the world, primarily in the USA and Canada (Leung et al., 2014). However, CCS in coal beds is highly dependent on the permeability of the layers. In coal this is mainly dependent on the fracture networks and their related permeability. These networks are particularly sensitive to changes in stress and pressure.

Saline formations are deep sedimentary rocks filled with brines, containing dissolved salts. They are widespread worldwide and contain large quantities of water, unsuitable for human use or consumption (Benson et al., 2005). Of all three candidates for geological storage of CO_2, deep saline formations are considered to hold the highest potential capacity for geological storage (Table 0.1). Appropriate formations are considered to be at such a depth that injected CO_2 becomes supercritical (typically depths of >1000 m). Then, CO_2 has a liquid-like density (approximately 500 – 800 kg/m^3) which is beneficial for efficient use of the available underground storage space.

Table 0.1: Storage capacity for different geological settings. Table adapted from (Metz et al., 2005).

Reservoir type	Lower estimate of storage capacity (Gt CO_2)	Upper estimate of storage capacity (Gt CO_2)
Oil and gas fields	675	900
Unmineable coal	3-15	200
Saline formations	1,000	Uncertain, possibly 10,000

Two well-known CCS projects are currently running in Norway: the Sleipner project in the North Sea (Arts et al., 2008; Michael et al., 2010), which was the first commercial-scale project dedicated to CO_2 storage (in 1996); and the CCS project in the Snøhvit field in the Barents Sea (Maldal and Tappel, 2004), since 2008. In these projects, an extra incentive for storing CO_2, apart from the environmental cause, is the high CO_2 emission tax imposed by the Norwegian government.

0.2. Processes related to CO_2 injection

0.2.1. Physical and chemical properties

The physical state of CO_2 varies with temperature and pressure as shown in Figure 0.4. With increasing depth, the temperature and pressure of the reservoir rises to a point that gaseous CO_2 is naturally converted to liquid CO_2 and, when reaching the critical point, to supercritical CO_2. This is the point when the liquid and gas phase cannot exist as separate phases and CO_2 develops supercritical properties. Supercritical CO_2 exhibits characteristics of both gaseous and liquid CO_2. It effuses through solids like a gas and dissolves material like a liquid. At this point, small changes in pressure or temperature result in large density changes (Metz et al., 2005). The temperature and pressure conditions for each sedimentary basin vary. However, on average, based on typical geothermal and hydrostatic gradients, the minimum depth for CO_2 to be in a supercritical state is considered to be 800 m (van der Meer, 1993).

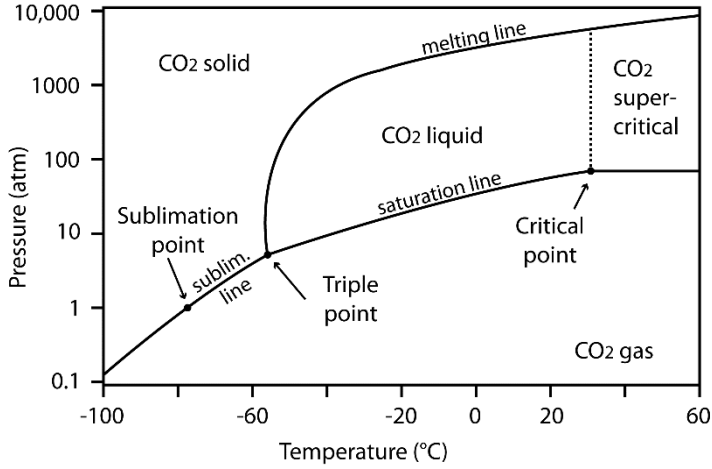

Figure 0.4. Phase diagram for CO_2. The triple point is at -56.6 °C and 5.11 atm, the critical point at 31.1°C and 72.8 atm. Figure modified from (Metz et al., 2005).

CO_2 in an aqueous solution will form carbonic acid. At ambient conditions (25 °C and 1 atm), the solubility of CO_2 in water is 1.45 g/L. The solubility decreases with increasing temperature and salinity of the formation water and increases with increasing pressure (Metz et al., 2005). Dissolving gaseous CO_2 in water involves a number of chemical reactions which can be represented as follows (Metz et al., 2005):

$$CO_{2\,(g)} \leftrightarrow CO_{2\,(aq)} \quad (0.1)$$

$$CO_{2\,(aq)} + H_2O \leftrightarrow H_2CO_3 \quad (0.2)$$

$$H_2CO_3 \leftrightarrow {H^+}_{(aq)} + {HCO_3}^-_{(aq)} \quad (0.3)$$

$${HCO_3}^-_{(aq)} \leftrightarrow {H^+}_{(aq)} + {CO_3}^{2-}_{(aq)} \quad (0.4)$$

Addition of CO_2 to formation water will lead to an increase in the amount of dissolved CO_2. This reacts with water to form carbonic acid, which dissociates to form bicarbonate ions and carbonate ions. Depending on the amount of CO_2 which can be dissolved in the formation water, the pH of the system will decrease based on the carbonic acid/bicarbonate/carbonate equilibria. The brine then becomes corrosive to all materials in contact with it (well materials, rocks, pipelines, etc.) (Gaus et al., 2008). This corrosive reaction can

have an important impact on CO_2 storage operations and might even determine the success or failure of CCS projects (Gaus et al., 2008).

0.2.2. Pore-scale interactions at depth

Once injected, the fraction of CO_2 which is retained by the storage formation depends on both physical and geochemical trapping mechanisms (Bachu, 2008; Benson et al., 2005). Physical trapping is typically provided by an impermeable cap rock layer above the storage formation and can be complemented by capillary forces, retaining CO_2 in the pore space of the rock. Often, the storage formation remains open on one or more sides, and other processes are necessary to assure long-term entrapment. These are geochemical processes occurring due to the interaction of the injected CO_2 with the in-situ formation water and the host rock material (Benson et al., 2005). These processes typically occur over a time scale of hundreds to thousands of years after the injection. They include sinking of CO_2-loaden water down into the formation, and chemical reactions between the dissolved CO_2 and rock minerals. The latter converts part of the injected CO_2 to solid carbonate minerals over ten thousands to millions of years (Gaus et al., 2008). Formation of calcium, magnesium and iron carbonates are expected to be the primary reactions occurring (Izgec et al., 2008). Of course, this strongly depends on the ionic composition of the formation water, and the mineralogical composition of the host rock.

Dependent on the distance from the injection well, different pore-scale processes occur in the storage unit (Gaus et al., 2008). Figure 0.5 illustrates this in a schematic way. As mentioned in section 0.2.1, injected CO_2 will dissolve into the formation water and change its chemical composition (Figure 0.5 zone 2). The pH of the brine decreases and typically reaches a value between 4.0 – 5.0 (Gaus et al., 2008). The dissolution of rock matrix can affect the reservoir quality positively. However, when the dissolved minerals

precipitate again, reservoir quality can be affected in a negative way. If CO_2 injection is only sustained for a short period of time, only this zone will form. In long-term injection projects, the acidification phase is typically followed by a desiccation phase when the formation water can no longer take up CO_2 (Gaus et al., 2008). Around the injection well, a CO_2 bubble will form, pushing the formation water away from it. In this zone (Figure 0.5 zone 5) the storage unit is fully desiccated due to the dissolution of residual water in the CO_2-rich dry phase. Zone 2 and zone 5 constitute the end members concerning gas and liquid saturation. In zone 5 the gas saturation is equal to 1, while in zone 2 the liquid saturation is 1. Between these zones, two other zones can be distinguished: one with very low formation water saturations (Figure 0.5 zone 4), and one where the gas and liquid phases are in chemical equilibrium (Figure 0.5 zone 3).

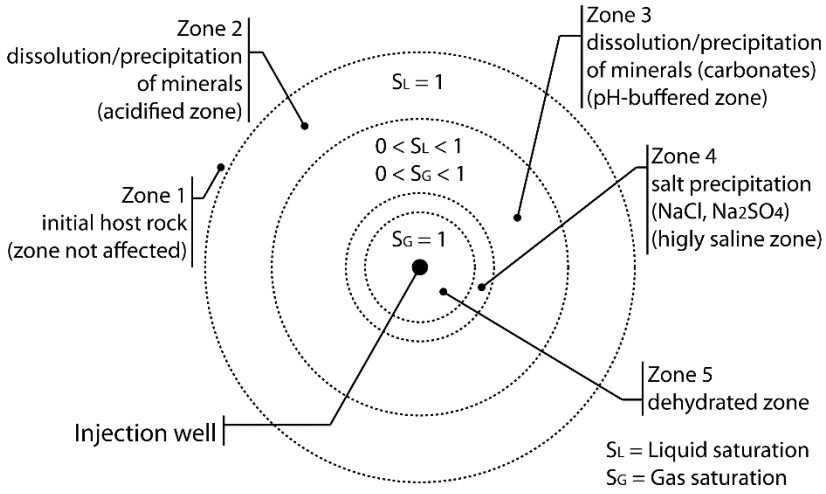

Figure 0.5. Pore-scale processes related to the injection of CO_2 in the subsurface. Different zones can be differentiated. Figure modified from (Gaus et al., 2008).

In zone 4, the formation water trapped in the micro-pores of the system evaporate through a continuous flow of CO_2. In this zone, dissolved salts typically precipitate (Gaus et al., 2008; Rosenbauer et al., 2005), which can influence the injectivity of the storage unit.

In zone 3, the most important processes include the dissolution of minerals due to the acidification of the formation water. However, depending on the reservoir conditions, secondary minerals can also precipitate from the formation water. Depending on the balance between dissolution and precipitation, the porosity of the storage unit changes locally.

0.3. Global status of CCS

CCS projects deployed during the last decades have shown the potential of the technique. They have provided important lessons which need to encourage future CCS development (Page, 2016). In the AR5, the IPCC highlighted that the cost, without deployment of CCS, to achieve the projected 430 - 480 ppm CO_2 by 2100, as set out in the most favorable scenario RCP2.6, could be 138 % higher than in scenarios including CCS (IPCC, 2013). To achieve this, CCS should account for an annual storage of 4 Gt of CO_2, which is 100 times the amount expected to be in operation by the end of 2017 (International Energy Agency, 2016). Although research and development have more than doubled the capacity of the operational CCS projects, the progress is expected to slow considerably in the next five years (Page, 2016). From 2010 to the end of 2017, the number of operational large-scale CCS projects has increased from fewer than 10 to just above 20. However, the momentum is slowing down due to decreasing governmental funding, a sharp reduction in the carbon price in Europe and policy uncertainties in some countries (Page, 2016).

0.4. CCS on Spitsbergen

0.4.1. Svalbard treaty

Svalbard is an archipelago located along the northwestern margins of the Barents Sea. It comprises all islands between latitudes from 74° to 81° North and longitudes from 10° to 35° East. These islands represent the uplifted and exposed northwestern corner of the Eurasian continental plate. Of the nine main islands, Spitsbergen is the largest, and Longyearbyen, located on Spitsbergen is the largest

settlement with approximately 2000 inhabitants. Figure 0.6 illustrates the location of Svalbard, Spitsbergen and Longyearbyen.

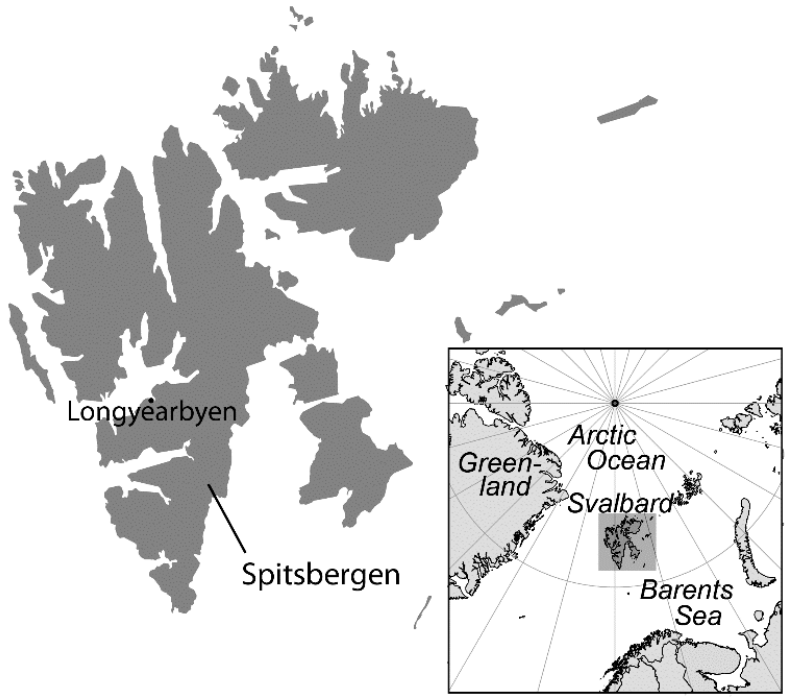

Figure 0.6. The location of Svalbard, and its main island Spitsbergen, as part of the northeastern margin of the Barents Sea. Longyearbyen, the main settlement on Spitsbergen is located in the fjord Adventdalen.

In 1920, after the first World War, 14 countries signed the so-called Svalbard Treaty to regulate the demilitarization of the archipelago. The treaty recognizes the sovereignty of Norway over the island group, but gives all signatories equal access rights to the archipelago, as well as equal rights to engage in commercial activities. Currently 45 countries rectify the treaty, however, only Norway and Russia make use of their right to engage in commercial activities on the archipelago. The main commercial sectors include coal mining, fisheries and tourism.

0.4.2. Coal as energy source on Spitsbergen

Industrial coal mining on Spitsbergen developed during the early 20th century. In 1906, private mining operations started in Longyearbyen. Since then, the amount of extracted coal increased gradually (Hisdal, 1998). At the moment, an annual production of approximately 90.000 tons is obtained from Gruve 7, the only producing mine in Adventdalen. The coal, mined in Longyearbyen and its surroundings, is obtained from coal seams from the Paleogene period (66 Ma – 23 Ma). At the end of the Cretaceous, Svalbard was situated close to the northern part of Greenland, at a latitude of approximately 60° North. During the Paleocene and early Eocene (66 Ma – 41 Ma), the North Atlantic Ocean started to open. As a response to the North Atlantic Ocean Paleocene-Eocene breakup, a fold-and-thrust belt formed in the western parts of Spitsbergen. This caused associated tectonic subsidence to the east of it, so that the Central Spitsbergen basin was formed (Lüthje et al., 2010; Blythe and Kleinspehn, 1998). In this basin, deposits from the mountains, prone to erosion, accumulated. These sediments are now preserved as Paleogene sandstones and shales in the Van Mijenfjorden Group (Marshall et al., 2015). The low-lying flatlands surrounding the basin, were occupied with forests, bogs and rivers, and were periodically flooded. This flooding buried decayed organic material below large quantities of sediments from the highlands, which later formed the coals seams that are now being, or were mined in and around Longyearbyen. Figure 0.7 shows the stratigraphic units of the Van Mijenfjorden Group in the Spitsbergen Central Basin from Southwest to Northeast.

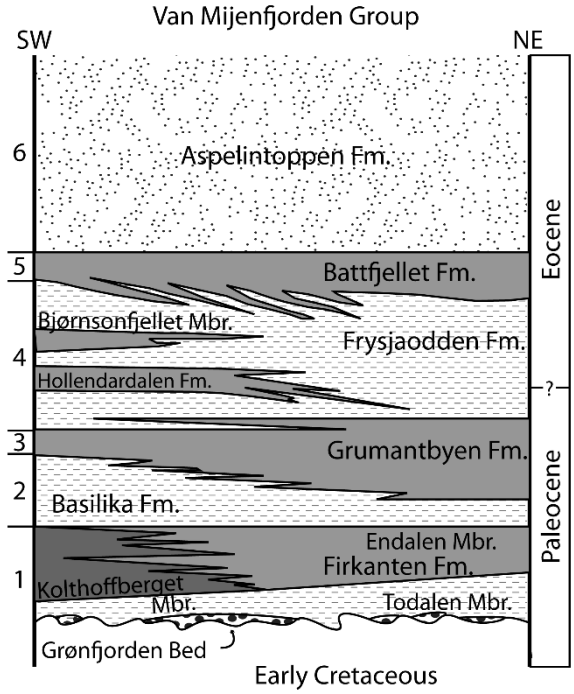

Figure 0.7: Stratigraphic units of the Van Mijenfjorden Group in the Central Basin in Spitsbergen. Central Basin units 1, 3 and 6 contain coal seams. Figure modified from (Harland et al., 1997).

In Adventdalen, the fjord in which Longyearbyen is located, there are six historic and one active coal mine (Figure 0.8). They target the coal bearing Formations within the Mijenfjorden Group. There are three rock Formations that are known to contain coal seams. Two of these contain only thin seams, up to 30 cm thick, while the third, the Paleocene Firkanten Formation (Figure 0.7), forms the main source of coal in Svalbard (Harland et al., 1997). In this Formation, 5 distinctive coal seams are present. At Gruve 7, the active coal mine, the Longyear seam is targeted, with a thickness between 1 and 2 meters.

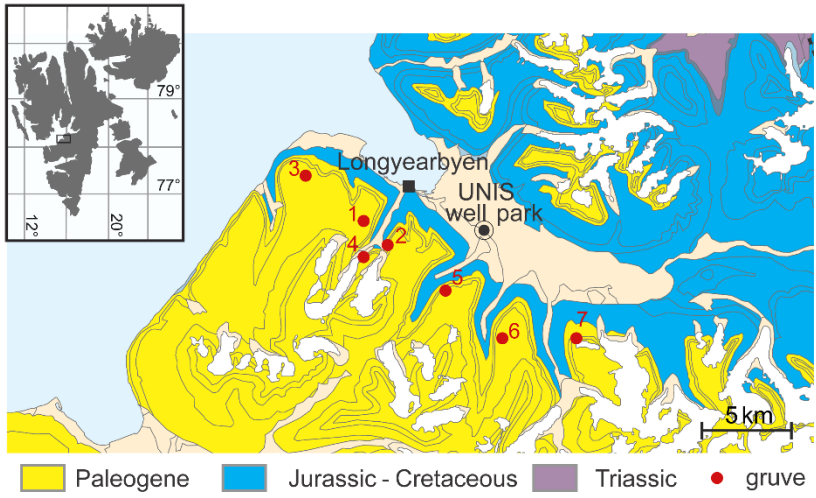

Figure 0.8: Location of the historic (1-6) and the active coal mine (7) providing energy and heating for Longyearbyen.

Most of the extracted coal is exported for use in the metallurgic industry. Approximately 25.000 tons per year, however, is used in the local coal-combustion power plant to generate electricity and community heating for Longyearbyen and its 2000 inhabitants. This is responsible for a local annual CO_2 emission of ca 60,000 tons (Senger et al., 2015).

In a global perspective, coal-fired power plants provide over 42% of the global electricity supply, while accounting for 28% of the global CO_2 emissions, and more than 40% of CO_2 emissions specifically from fossil-fuel combustion (US Energy Information Administration, 2016; Coal industry advisory board, 2010).

0.4.3. Longyearbyen CO_2 project

The dependency of Longyearbyen on the coal-combustion power plant is often regarded as a disgrace for climate researchers and environmental groups in the high Arctic (Sand et al., 2014). The small community, their independence from imported energy sources, and the global need for CO_2 injection test sites, triggered research on the feasibility of a CCS project on the archipelago of Svalbard, Norway, led by the University Centre in Svalbard (UNIS).

Since 2007, research has been going on with the aim to develop the full CCS value chain in Spitsbergen as a global show case, taking care of the CO_2 from the source to the solution. The university-driven research and development project for local CCS initially aimed at identifying suitable saline aquifers near Longyearbyen where CO_2 could be stored. For this, eight slimhole wells (DH1 – DH8) were drilled and fully cored at two sites near Longyearbyen, with six wells located within a 100 m radius at the UNIS CO_2 well park, approximately 5 km south-east of Longyearbyen (Figure 0.8). In combination with seismic acquisition, wireline logging and reservoir studies including water injection tests, suitable sections were found in November 2009 with proven storage capability (Sand et al., 2014; Braathen et al., 2012). The focus was put on a sequence of Upper Triassic to Middle Jurassic sandstones, interbedded with shales and the overlying cap-rock succession. The best potential storage units were identified in one of the slimhole wells (DH4) at a depth between 672 m to 970 m. It comprises the Kapp Toscana Group, consisting of the Late Triassic De Geerdalen Formation, and the overlying condensed Late Triassic to Middle Jurassic Wilhelmøya Subgroup. These geological units are described in more detail in Chapter 3. Their location in the stratigraphic sequence in Spitsbergen is shown in Figure 0.9.

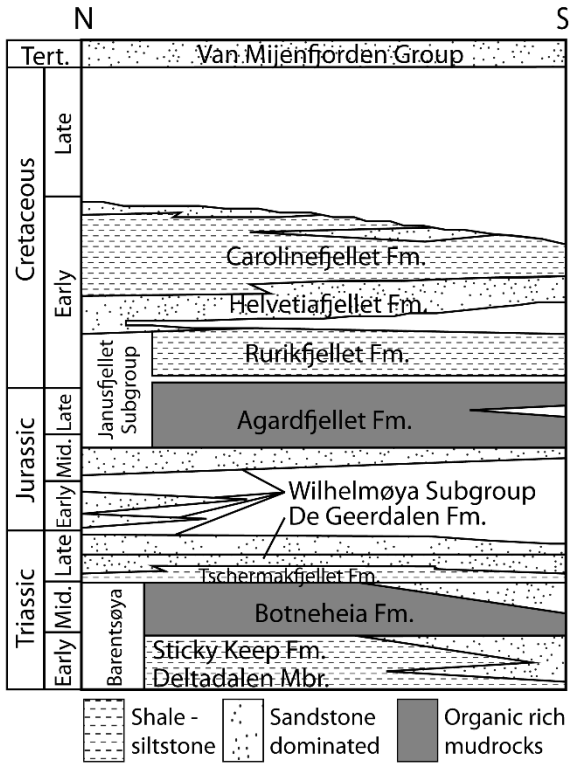

Figure 0.9: Stratigraphic overview of the Mesozoic to Cenozoic units in Spitsbergen. Figure modified from (Harland et al., 1997).

The geological map of Longyearbyen and its surroundings is shown in Figure 0.10.A. This is combined with a geological cross-section Figure 0.10.B from the Southwest towards the Northeast. The Kapp Toscana Group is part of the Central Spitsbergen Basin. This implies that these layers are located within a large synclinal structure, which can be seen on the geological cross-section in Figure 0.10.B. The De Geerdalen Formation and the Wilhelmøya Subgroup are found in outcrop approximately 14 to 20 km to the northwest of Longyearbyen, in the valleys to the East of Deltaneset and across the southern shores of Isfjorden (Figure 0.10.A).

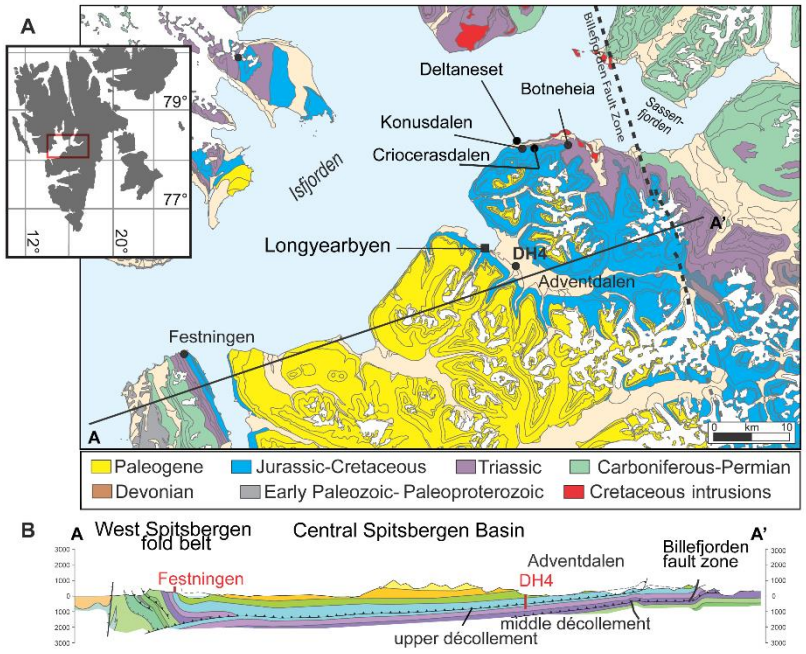

Figure 0.10: A. Geological setting of Longyearbyen and its surroundings. The location of DH4 is indicated in Adventdalen, and along the southern shore of Isfjorden, the Upper Triassic and Lower Jurassic reservoir sections of the De Geerdalen Formation and the Wilhelmøya Subgroup respectively crop out. B. Geological cross-section from the West Spitsbergen fold belt to the Billefjorden Fault zone, indicating the synclinal structure of the geological strata.

The cap rock to these reservoirs is given by organic-rich shales and marine mudstones from the Agardhfjellet Formation and the Rurikfjellet Formation respectively, which are deposited right above the Wilhelmøya Subgroup (Figure 0.9). Near the surface, all units are seemingly sealed by permafrost. The sealing efficiency of the permafrost may eventually be reduced by the global climate warming. However, the planned volume of CO_2 to be injected is small enough that the lateral expansion over a distance of 13 – 20 km to the outcrop zone is projected to take thousands of years (Braathen et al., 2012).

0.4.4. Fractured reservoirs

The reservoir sections are considered to be unconventional: they are known to have a general low to moderate porosity and a very low related permeability (Mørk, 2013; Senger et al., 2015). Porosity in the Wilhelmøya Subgroup ranges from 6 to 20 %, whereas the upper parts of the De Geerdalen Formation are characterized by porosities from 9 to 16 %. The lower parts in this Formation are only sparsely sampled, with porosity values from 2 to 16 % (Senger et al., 2015). The permeability for the sandstones in the Wilhelmøya Subgroup are within the range of 0.01 to 1 mD, while the De Geerdalen sections are typically less than 0.1 mD (Braathen et al., 2012). Because of successful water injection tests, it has been suggested that fracture permeability significantly affects fluid flow within these rocks, thereby impacting both injectivity and storage capacity. This includes both fracture-related secondary porosity within the rocks, and enhanced connectivity within the matrix due to micro-fractures. Fracture occurrences are known in the targeted reservoir units via so-called vertical scanlines in the slimhole wells: the upper zone exhibits an average frequency of 3.1 fractures per meter; the middle zone has an average fracture frequency of 3.4 fractures per meter, with a highest measured peak of 28 fractures per meter; and the lower zone is less fractured with 1.7 fractures per meter. The fracture frequency was calculated from visual counts in the extracted drill cores. Not only the frequency of occurrence is important when dealing with fractures, but also their aperture distribution. The fracture aperture is the perpendicular width of an open fracture. It controls the fluid flow and transport properties through the fracture (Sahimi, 2011). It is therefore that the fractures within the targeted sections were thoroughly characterized in both outcrops and drill cores (Ogata et al., 2014; Van Stappen et al., 2014). Besides fracture occurrence and aperture distribution, other important fracture parameters, such as their orientation, spacing, length and connectivity were determined from drill cores or in the field (Ogata et al., 2014). The targeted reservoir sections contain different fracture sets based on their

length, orientation and connectivity to other fractures. Therefore, the reservoir sections can be considered to be dual- or even triple-porosity systems. Information on the fractures' apertures, a key factor for fluid transport, comes mainly from indirect permeability measurements, or direct measurements from high-resolution X-ray computed tomography imaging (micro-CT) of decompacted drill core samples (Van Stappen et al., 2014). The exact influence of the burial depth of the reservoir on the 3D morphology of (micro-) fractures within it is unclear. Also, the influence of such fractures on the fluid flow through the system, as well as on the pore-scale processes related to the injection of CO_2 in the system, are unknown. In this work, we try to get an understanding of these processes and their effect on the reservoir properties, based on a series of lab-scaled tests performed on rock samples from the actual reservoir sections. The main technique that was used in order to investigate this, was micro-CT imaging. In the following section, an outline is provided of the structure of this dissertation, identifying the questions that are left to resolve.

0.5. Dissertation outline

In Chapter 1, the most important rock properties are described, related to fluid flow behavior in geomaterials and reservoir engineering. This includes rock porosity and permeability, as well as the mechanical strength of rock cores. In this chapter, the common methods are discussed for the quantification of these parameters. Since the reservoir sections of the Longyearbyen CO_2 project are so-called dual- or even triple-porosity reservoirs, in which fractures are the main contributors to the fluid flow within them, the influence of fractures on the permeability in a reservoir is discussed.

Chapter 2 discusses 2D imaging techniques and X-ray micro-CT. These techniques are invaluable for micro-structural studies of geomaterials and pore-scale processes occurring in them. The main focus of this chapter is put on high resolution X-ray computed tomography as a 3D imaging technique, since this is the main

method used in this work. The fundamentals of micro-CT with its limitations towards the achievable resolution are discussed in sections 2.2.1 to 2.2.3. In section 2.2.4, traditional data processing and image analysis is discussed, with a short discussion on the techniques used specifically for the analysis and quantification of fractures in micro-CT images. Section 2.2.5 discusses the technique of differential imaging, which is used throughout this work in order to visualize and quantify chemical and structural changes in rock samples subjected to different fluid flow conditions. Section 2.2.6 discusses different volume and image limitations linked to the technique of micro-CT. In this section, special attention is given to specific problems related to the imaging and representativeness of fractures in rock samples. In section 2.3, the micro-CT possibilities at the Center for X-ray Computed Tomography at Ghent University (UGCT) are discussed. In this section, only those micro-CT systems and pieces of add-on equipment are discusses which were used in this work.

In Chapter 3, the in-depth characterization of the Longyearbyen CO_2 project reservoir sections of the De Geerdalen Formation and the Wilhelmøya Subgroup is discussed. This characterization is based on standard porosity and permeability measurements, as discussed in Chapter 1, as well as on the analysis of micro-CT images obtained from decompacted core samples and outcrop material. The standard analysis methods on micro-CT images, discussed in Chapter 2, allowed a quantification of fracture apertures in the decompacted core samples and the outcrop material. High resolution micro-CT imaging allowed the segmentation of the pore space from several high permeable sections of the reservoir. This segmentation was used in order to perform image-based fluid flow modelling using commercial software packages and an in-house developed multi-scale pore network model.

Chapter 4 focuses on the mechanical strength of geomaterials. This parameter is normally determined through destructive tests on decimeter long rock cores. In this chapter we investigate the effect

of downscaling the sample size on the Uniaxial Compressive Strength (UCS) of geomaterials. A small-scale commercial compressive device, which was adjusted to fit on the micro-CT systems at UGCT, was used to determine the UCS of small-scale rock plugs from different limestone types which are commonly used as building material. These reference experiments showed the reliability of these small-scale measurements compared to standard sized UCS experiments. Unfortunately, for the reservoir sections of the Longyearbyen CO_2 project, the compressive device was too limited in force, so that only tensile strength could be determined based on small-scale Brazilian tests on rock plugs.

In Chapter 5, the influence of rock fractures on the fluid flow behavior at the reservoir conditions of the Longyearbyen CO_2 project is discussed. Small scale rock plugs, with a diameter of 5 mm and a length of 14 mm, could be subjected to confining pressures similar to the conditions at a depth of 800 meters below Longyearbyen. To achieve this, a small-scale in-situ triaxial device was used, which fits on one of the micro-CT systems at UGCT. This allowed the visualization of the closure of natural and induced rock fractures with a spatial resolution of approximately 11 µm. Through the characterization of the dip in X-ray attenuation, caused by fracture in the rock plugs, it was possible to determine local fracture apertures up to $1/10^{th}$ of the image resolution. The Matlab script which was developed to achieve this, is included in this dissertation as Appendix A. The experiments with the small-scale in-situ triaxial device further allowed the quantification of the permeability through the tested rock plugs at different confining conditions. Using this information, it was possible to determine the fracture permeability for natural and induced fractures in the tested plugs. Natural fractures have the ability to increase the local permeability of the reservoir to a factor of 5 times the permeability of an unfractured plug.

Chapter 6 discusses pore-scale processes in the Longyearbyen CO_2 reservoir rocks, linked to CO_2 sequestration. Micro-CT imaging

allowed the visualization of pore-scale drying processes (section 6.1) and dissolution behavior in fractured rock plugs (section 6.2). Pore-scale drying processes (linked to zone 4 and 5 in Figure 0.5) were first investigated in a monomineralic limestone with a bimodal porosity which acted as a reservoir analogue. This sample was fully saturated with a brine, after which CO_2 was injected to trigger drying of the rock plug and precipitation of salt within the sample. Micro-CT imaging allowed the localization of salt precipitation with respect to the complex pore structure. Subsequently, drying experiments were conducted on fractured rock plugs from the Longyearbyen CO_2 project. The drying behavior in these plugs could be explained linked to observed behavior within the reservoir analogue. In section 6.2. fractured rock plugs were subjected to the flow of an acidic solution through them in order to investigate the changes in the pore structure due to geochemical interactions between the rock's matrix and an acidic brine (linked to zone 2 and 3 in Figure 0.5). Such an acidic brine is formed due to the dissolution of CO_2 in the formation water. Experiments were conducted with rock plugs in which ideal fractures were induced, as well as rough fractures. Micro-CT imaging was complemented with elemental analysis of the outflowing fluids from the fractured rock plugs, in order to understand the geochemical reactions taking place.

In Chapter 7, the general conclusions are summarized of this dissertation. Also, a critical remark on the micro-CT imaging of fractures in general is provided, as well as experimental recommendations and a future outlook.

1.

Rock (fractures) and fluid flow properties

This chapter describes the most important rock properties, related to fluid flow behavior in geomaterials. Since the reservoir sections of the Longyearbyen CO_2 project are dual-porosity reservoirs, this chapter starts with a brief statement on the importance of individual fracture parameters on the fluid flow behavior. However, the characterization of these parameters is discussed in more detail in chapter 2. What follows is a discussion on the effective porosity and permeability of geological reservoirs, as well as how to determine these parameters. The fluid flow behavior can further be described by different dimensionless numbers which are also clarified within this chapter. To end, a section on rock mechanical testing is included. This is linked to the wellbore stability during drilling operations and the injection phase.

1.1. Fracture definition

Rock fractures exist on a wide range of scales, from the micrometer-scale and smaller to hundreds of kilometers in size. They are defined as the planes along which stress has caused partial loss of cohesion in rocks and are typically labelled in certain categories, depending on the particular division of earth sciences in which they are studied. For example, in geomorphological studies, the distinction is made on a descriptive basis, between *Mode I (opening), Mode II (shearing)* and *Mode III (tearing)* fractures. Each of these modes can occur separately, or in a combination with other modes. In the same field, the distinction is made between a rock joint (a crack formed by mode I movement, without lateral displacement along the fracture) and a rock fault (a crack along which the rock laterally displaces on both sides) (Adler et al., 2013).

In this work, rock fractures are considered from a hydrogeological perspective: fractures are a concentration of void space between a set of (rough) fracture walls, facilitating storage and movement of fluids through them. When fractures occur in an otherwise low permeable rock matrix, the reservoir can be described as a multiple-porosity reservoir. Typically, fluid flow then effectively takes place in one porosity system (the fractures), while most of the fluid is stored in the other (primary matrix porosity). In hydrogeology, the distinction is made between a single fracture, a fracture network, or a fractured porous medium (Sahimi, 2011; Adler et al., 2013). Dual-porosity reservoirs are per definition fractured porous media, in which individual fractures may be discretely present, or in which fractures form an interconnected network within the rock matrix. When individual fractures form a network, they will influence fluid flow properties to a greater extent as when fractures are discretely present in the porous medium (Long et al., 1996). Natural fractures and their networks vary enormously in their geometry, topology and in the structure of the internal surfaces of the fractures. One of the most important parameters for fluid flow and transport processes through fractures

is the fracture aperture. Because fractures have rough surfaces, there is no unique aperture (as used to define a hydraulic aperture), but rather a distribution of the apertures. Next to the aperture distribution, also the length of a single fracture determines its effect in a fractured porous medium, as well as the orientation of the fracture in the reservoir. These parameters are typically characterized by 2D and 3D imaging techniques (chapter 2). In this chapter, the focus is on reservoir properties and the techniques traditionally used to characterize them, while in chapter 3 imaging techniques will be thoroughly discussed, with an emphasis on fracture characterization.

1.2. Effective porosity

Rock porosity is one of the two parameters to define the quality of a storage unit. The other, permeability, will be discussed in section 1.3. Particularly the storage capacity is characterized by the porosity of the system, and the size of the reservoir. Rock porosity is defined as the non-solid or pore-volume fraction of the rock. In reservoir studies, it is important to know the effective, or open porosity of the system. This refers to the fraction of the total rock volume in which fluid flow is effectively taking place. It includes so-called dead-end pores, which are pores that are only connected to the pore network with one connection, and interconnected pores (Rahmouni et al., 2014). This is schematically illustrated in Figure 1.1. In this schematic drawing, micro-porosity is illustrated within a cemented part of the illustration. The definition of micro-porosity strongly depends on the research context in which it is used. In the "Oilfield Glossary" composed by Schlumberger Limited, micro-porosity is defined as: "the part of the pore space that has a characteristic dimension less than 1 µm. Water in micropores is not expected to flow on production". Often, however, the term micro-porosity refers to the pores which are below the resolution of the imaging technique. This is also how the term is used in this work: micro-pores are those pores which could not be resolved in a high-

resolution micro-CT scan (typically with a resolution higher than 5 µm).

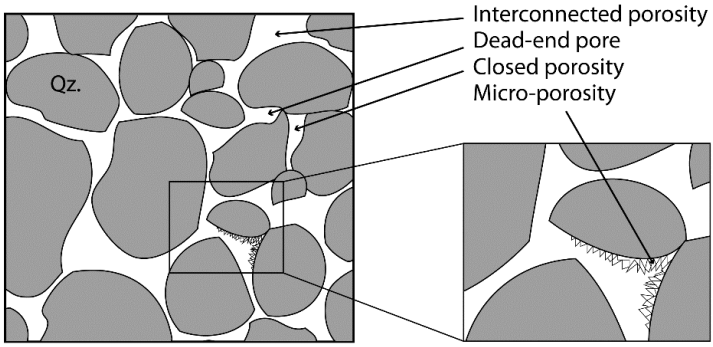

Figure 1.1. Schematic illustration of different types of pores in a sandstone. Effective porosity includes interconnected pores and dead-end pores, but does not include closed porosity.

In core samples, the open porosity is defined as the void fraction of the rock volume connected to the outside of the core. In this work, open porosity was determined using the European standard for natural stone test methods EN 1936 (UNE-EN 1936, 2006). After drying to constant mass, the open porosity is determined by vacuum assisted water absorption and submerged weighing of the rock samples. This non-destructive test allows the samples to be used for further experiments afterwards, as opposed to the determination of total porosity (including closed pores), which requires the rock sample to be pulverized. The open porosity is expressed by the ratio of the volume of open pores and the apparent volume of the sample by the equation (UNE-EN 1936, 2006):

$$\phi = \frac{m_s - m_d}{m_s - m_h} * 100 \qquad (1.1)$$

with ϕ the open porosity (%), m_s the mass of the water-saturated sample (kg), m_d the mass of the dry sample (kg) and m_h the mass of the sample immersed in water (kg). Although this method is commonly used, complete saturation of the open pore structure is rarely obtained. To get a more accurate measurement for the

effective porosity, Boyle's Law method, or helium porosimetry, can be used. In such an experiment, helium is used to saturate the sample. This inert gas will not easily be adsorbed onto mineral surfaces and enters the micro-porosity of the system very rapidly. There are two methods to conduct this measurement: either the sample is confined within a rubber sleeve and helium is forced through it, or, the sample is placed within a steel chamber of a known volume, which is brought to an equilibrium with a second chamber filled with helium. It must be noted that the first method is not very well suited for fractured rocks, or samples with large cavities. In this case, there is a possibility of closing off the fracture, or collapse of individual pores due to the confining pressure applied to the rubber sleeve.

Not only the quantification of open porosity is of significant importance, but also the pore size distribution, which affects the quality of storage units. This is typically determined through other techniques, such as Mercury Intrusion Porosimetry (MIP, section 1.2.1), 2D visualization methods (section 3.1) and 3D imaging techniques like micro-CT (section 3.2).

1.2.1. Mercury Intrusion Porosimetry (MIP)

MIP is a destructive test, based on the premise that a non-wetting liquid (contact angle greater than 90°) only intrudes pores under pressure. A small sample, up to several millimeters in diameter, is placed in a chamber, which is flooded with mercury. During the experiment, the pressure on the mercury is slowly increased. Doing so, mercury is forced through progressively smaller pores. The pore size distribution is determined from the volume of mercury intruded at each pressure increment. MIP is the standard method for the characterization of pore size distributions in porous media from the micron scale (> 1 µm) to the nano-scale (1 µm to ± 10 nm) (Josh et al., 2012). It should be noted, however, that MIP detects the pore throat sizes instead of the real diameter of the pore. Therefore some assumptions need to be made. First, all pores are

assumed to be cylindrically shaped and fully accessible for mercury penetration from the surface. This means that only the open porosity can be quantified. Secondly, constant values for the surface tension and for the contact angle of intruded mercury are assumed to calculate the pore size. Taking this into account, the pore radius can be determined via the relationship between the actual pressure P (Pa) and the cylinder pore radius R (nm), expressed by the Washburn equation (Washburn, 1921):

$$P = \frac{2\,\sigma\cos\theta}{R} \qquad (1.2)$$

with σ the surface tension of mercury (480 x 10^{-3} N/m) and θ the contact angle (141.3°). MIP is especially useful for determining porosity distributions in samples with a low porosity and low permeabilities (Olson and Grigg, 2008). During this work, MIP was used on cylindrical subsamples from the Longyearbyen CO_2 project drill cores (section 3.2.2). Experiments were carried out at the Magnel laboratory for concrete research at Ghent University on a Thermo Scientific (Pascal 140 series and Pascal 440 series) apparatus with a maximum test pressure of 400 MPa.

1.3. Permeability

1.3.1. Darcy's law

Permeability is a measure of the ability of a rock (or any other porous medium) to allow fluids to pass through it. It is heavily related to the pore structure of the material, particularly to the connectivity of individual pores within a pore network. The SI unit for permeability is m², however, the *darcy (D)* or *millidarcy (mD)* is more commonly used in reservoir engineering (1 m² = 1.01 x 10^{12} D). This unit is named after the French engineer Henry Darcy, who was the first to describe the flow of water through sand filters for potable water supply (Darcy, 1856). The Darcy law relates rock permeability k (m²) to the ratio of the volumetric flow rate Q (m³/s) to the pressure difference ΔP (Pa) between the inlet and the outlet of the sample:

$$k = -\frac{\mu L Q}{A \Delta P} \tag{1.3}$$

with μ the percolating fluid's dynamic viscosity (Pa s), L the length of the sample in the direction of the flow (m) and A the cross-sectional area of the sample (m^2). The quality of a reservoir rock can be classified according to their permeability as follows (Eysa et al., 2016): fair if $1 < k < 10$ mD; good if $10 < k < 100$ mD; very good if $100 < k < 1000$ mD; and excellent if $k > 1000$ mD.

The concept of Darcian permeability is only valid when two important conditions are met: 1. the permeating fluid should be Newtonian (i.e. the fluid stresses are proportional to the fluid strains) and 2. the inertial forces should be small when compared to viscous forces. This second condition states that the permeating fluid has a laminar flow in the pore system as opposed to a turbulent flow. The difference between these two states is illustrated in Figure 1.2.

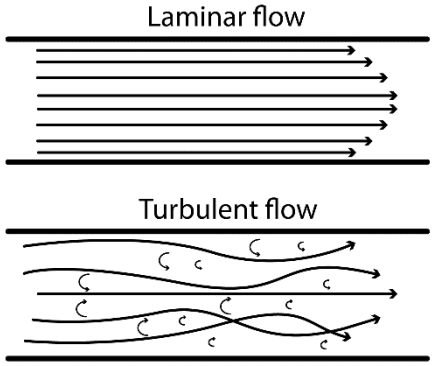

Figure 1.2. The difference between laminar and turbulent flow, illustrated in a simplified tubular pore system.

For normal reservoirs, these conditions are typically met. However, transport processes in fractures can be different than those in rock pores. To determine whether the second condition is met, the dimensionless Reynolds number *Re* can be determined as follows (Zimmerman et al., 2004; Adler et al., 2013):

$$Re = \frac{\rho \, \bar{\upsilon} \, D}{\mu} \tag{1.4}$$

with ρ the density of the liquid (kg/m³), $\bar{\upsilon}$ the average velocity (m/s), D the characteristic scale of the flow system (m) and μ the dynamic viscosity of the fluid (Pa s). In the case of fluid flow through fractures, D typically is the mean fracture aperture, or hydraulic aperture. Only when the Reynolds number is significantly lower than 1, the inertial forces can be considered negligible to the viscous forces, so that the flow in the system can be considered to be laminar and the permeability can be described by Darcy's law.

1.3.2. Fracture permeability

Since the second half of the 20th century, research has been carried out in order to understand the link between fracture morphology and permeability (Witherspoon et al., 1980; Sahimi, 2011). Empirical data analysis, based on experimental work with both natural and induced fractures provided a relationship between the effective fracture permeability k_f and its mean aperture w (Barton et al., 1985; Sahimi, 2011; Witherspoon et al., 1980; Kranzz et al., 1979):

$$k_f = \frac{w^3}{12 \, R} \tag{1.5}$$

with R a constant between 1.0 and 1.65, accounting for the effect of surface roughness. In the early works, fractures were typically represented as channels between two parallel plates (Snow, 1968). It is obvious that if one takes into account the roughness of the internal surfaces of fractures, the prediction of fluid flow and transport processes through fractures becomes more and more complex (Brown, 1995). Despite this simplification, the parallel plate model allows a descriptive method for fluid flow representation in rock fractures. Assuming very low flow rates, causing laminar flow through a parallel fracture, equation 1.5 can be simplified to (Farokhpoor et al., 2011):

$$k_f = \frac{w^2}{12} \tag{1.6}$$

In this equation, *w* represents the hydraulic aperture of the rock fracture (m). In a dual-porosity system, fluid flow is not fully governed by the fractures alone. The total volumetric flow rate is the sum of the fracture flow and the rock matrix flow rate, so that the overall permeability k_{av} can be described as (Farokhpoor et al., 2011):

$$k_{av} = \frac{k_f wL + k_m(A - wL)}{A} \tag{1.7}$$

with k_f the fracture permeability (m²), k_m the matrix permeability (m²), *w* the hydraulic aperture (m), *L* the rock plug or core's length through which fluid flow takes places and *A* the cross-sectional area of the rock plug or core (m²).

1.3.3. Permeability measurements

In the field, and in laboratory, permeability can be measured with a portable air permeameter, the TinyPerm-II (New England Research, Inc.). To determine the permeability across a rock's surface, the nozzle of the permeameter is pressed onto it and a vacuum is created within this nozzle. The atmospheric pressure is recovered through the flow of air from within the rock towards the nozzle. The TinyPerm-II is calibrated so that the time it takes for the atmospheric pressure to fully recover can be linked to the rock's permeability. This portable air permeameter is reliable for permeability measurements between approximately 10 mD and 10 D. In this research, the TinyPerm-II was used on the field, to determine relatively high permeable sections in outcrop, which could then be sampled. This device is known to be prone to operational errors, such as poor sealing around the nozzle, and temperature variance (Magnabosco et al., 2014). The TinyPerm-II should not be used on (partly) wet surfaces, which can limit the use of it on the field. More accurate measurements can be obtained

with steady-state gas permeability measurements. In such a setup, the sample is confined in a sleeve and gas is forced through the sample at various pressures. At these pressures, permeability can then be determined with the Darcy equation 1.3. As with the helium porosimetry measurements, the applied confining pressure might partly close rock fractures, or induce pore collapse. However, only with this kind of setup, the permeability of low permeable rock cores can be determined. It allows the determination of permeability within the range of 0.001 mD and 25 D. Although the absolute permeability of a porous rock is a constant value, unchanged by the type of fluid used to calculate it, gases at relatively low pressures tend to give a calculated permeability greater than the true permeability of the rock. This is due to the Klinkenberg effect, or gas slippage effect (Klinkenberg, 1941). When gases occupy pores in a rock, they have a finite velocity in the direction of the flow at the pore walls. This is in contrast to liquid laminar flow in which the layer of molecules in contact with the solid material remains stationary. As gas molecules do not flow in layers, the calculated gas permeability is greater than the true absolute permeability of the rock. The Klinkenberg effect depends on the chemical composition of the gas and the mean pressure to the system (Tanikawa and Shimamoto, 2006). In this research, a couple of steady-state gas permeability measurements were carried out by PanTerra Geoconsultants B.V. (The Netherlands), as well as in-situ permeability measurements in fluid flow cells with H_2O and a CsCl-brine substituting the formation water of the storage unit (Chapter 5).

1.3.4. Dimensionless numbers for (reactive) flow

In order to fully understand pore-scale processes related to (reactive) fluid flow through geomaterials, several dimensionless numbers are defined. For dissolution and precipitation processes, the relevant dimensionless parameters are the Péclet (Pe) and Damköhler (Da) numbers (Békri et al., 1995; Bhat et al., 1999). The Péclet number relates the rate of advection of a physical quantity

to the rate of diffusion of the same quantity, driven by an appropriate gradient. The Damköhler number relates the timescale of a given chemical reaction to the transport phenomena rate in the system. A large Damköhler number (Da >> 1) thus corresponds to a very fast chemical reaction rate in comparison to the other processes (Izgec et al., 2008). The Péclet and Damköhler numbers can be determined as follows:

$$Pe = \frac{advective\ transport}{diffusive\ transport} = \frac{vd}{D} \tag{1.8}$$

$$Da = \frac{reaction\ rate}{mass\ transport\ rate} = \frac{(1 - \phi)\alpha L k}{v} \tag{1.9}$$

with v the characteristic fluid flow velocity (m/s), D the solute diffusivity (m²/s), d and L characteristic dimensions (m), ϕ the porosity, α the surface area of the reacting mineral(s) (m²) and k a first-order rate constant (m^{-2}) (Izgec et al., 2008). Depending on the relation between the Péclet and Damköhler numbers, reactive fluid flow transport will behave in a certain manner. Figure 1.3 illustrates this for the dissolution of minerals due to the flow of an acidic fluid through geomaterials (Egermann et al., 2005).

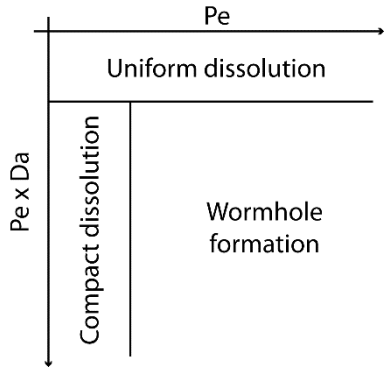

Figure 1.3. Dissolution regime as function of the Péclet and Damköhler numbers. Figure modified from (Egermann et al., 2005).

A very low Da number typically result in a uniform or homogeneous dissolution in the pore space of the rock. In such conditions, the

reaction rate is low compared to the fluid transport rate. The fluid thus has the time to spread out into the geomaterial before reaction can take place. At low Pe numbers and medium to high Da numbers, compact dissolution takes place at the injection surfaces. When both the Pe number and the Da number increases, wormholes start to form. These are preferential fluid flow paths along which reaction takes place, locally increasing the porosity and permeability of the system.

1.4. Mechanical testing

Knowledge of the rock mechanical properties is essential for geomechanical evaluations in reservoir engineering (Mehrabi Mazidi et al., 2012). In geotechnical and geomechanical studies, the stress level at which a rock fails is called the strength of the rock. This is one of the most important geomechanical parameters to be defined in geo-engineering projects. Reliable quantitative data on the strength of reservoir material at specific depths can only be derived from standardized laboratory tests on core samples (Asadi et al., 2016). However, rock coring is very expensive. Moreover, cores are generally very sensitive to stress unloading (Rabbani et al., 2012). Still, it is considered that direct measurements on rock cores are critical in reservoir studies. A material's strength depends on the rock fabric and is influenced by the composition, shape and size of the sample (Siegesmund and Dürrast, 2011).

1.4.1. Uniaxial Compressive Strength (UCS)

In Uniaxial, or Unconfined, Compressive Strength (UCS) tests, a rock is put in between a pair of pistons to be compressed by axial loads. The UCS of the rock is reported as the last amount of axial stress before the rock fails. During the experiment, the tested rock sample typically experiences several different phases. To illustrate this, a typical stress-strain curve is shown in Figure 1.4.

A primary phase includes the closure of pre-existing microscopic fractures (zone A in Figure 1.4). This is followed by nearly linear elastic behavior (zone B in Figure 1.4), after which new micro-cracks

start to form and align (during zone C in Figure 1.4), until the peak stress, or the UCS, is reached and the sample fails (Siegesmund and Dürrast, 2011). Zone D (Figure 1.4) represents the post-deformation region.

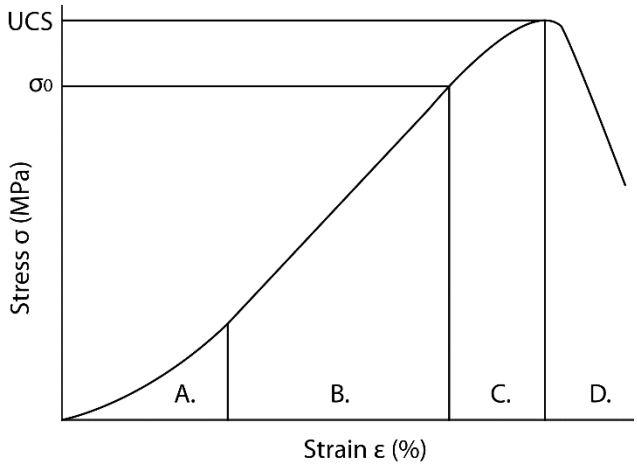

Figure 1.4. A typical stress-strain curve with the UCS as the last axial stress before the rock fails, and σ_0 the last stress before permanent deformation occurs. In zone A, consolidation of the sample is observed in which pre-existing micro-cracks are closed; in zone B, the sample shows nearly linear elastic behavior. In zone C, micro-crack formation takes places which leads to the failure of the sample at the UCS. Zone D is the post-deformation part of the curve, depending on the behavior of the material. Figure modified from (Jaege et al., 2007).

To determine the UCS of a rock, several standards were defined worldwide (ASTM C170/C170M-16, 2016; UNE-EN 1926, 2007; ISRM, 2007). Typically, cylindrical, cubic or prismatic samples are tested in a compression machine. Most critical in the execution of the experiment is the quality of the end-faces, which must be co-planar with an accuracy of 0.1 %. According to the European standard (UNE-EN 1926, 2007), either cubic samples with an edge length of 70 ± 5 mm or 50 ± 5 mm, or right circular cylinders with a diameter and height equal to 70 ± 5 mm or 50 ± 5 mm and thus a length:diameter ratio (L:D) of 1:1 must be used. In practice, the material available for laboratory tests is often limited in volume. Moreover, in geotechnical studies, the L:D ratio needs to be larger

or equal to 2:1 in order to represent the "true" UCS value (Siegesmund and Dürrast, 2011). When determining a UCS on samples with a lower L:D ratio, deviating values are obtained. In this work, both standard sized samples were tested, as small rock plugs. The standard sized experiments were carried out on an MFL 6000 kN closed-loop compressive testing machine at the Magnel laboratory for concrete research at Ghent University. This device allows the compression of samples at a constant stress rate of 1 ± 0.5 MPa/s. Small-scale UCS measurements were carried out with a commercial small-scale UCS device. More details on this device are given in section 3.3.2.1. Since the available reservoir material is limited, the UCS experiments were carried out on limestones, used as building material in Belgium and France. This was done in order to test the validity of small-scale UCS measurements on rock plugs instead of actual cores.

1.4.2. Tensile strength

Besides the UCS of geomaterials, the tensile strength can also be determined. This determines the capacity of the rocks to withstand tensional stresses. It can be used to predict the formation of a horizontal fracture in a vertical borehole (Bohloli et al., 2014). For this to happen, the injection pressure needs to exceed the sum of the vertical stress, σ_v, and the tensile strength, σ_t (Bohloli et al., 2014):

$$P_f = \sigma_v + \sigma_t \tag{1.10}$$

In order to determine the tensile strength of rock cores, they can be subjected to the so-called Brazilian test (Li and Wong, 2013). In this test, a disc, or core shaped specimen of the rock is loaded by two opposing loading jaws at the disc's periphery. The diameter of the disc/core must be larger than, or equal to 54 mm, and the disc/core must have an L:D ratio larger than 2.0 (ISRM, 2007; Li and Wong, 2013). The tensile strength of the material is determined by the peak stress, observed upon failure of the rock core and is determined as follows (ISRM, 2007):

$$\sigma_t = 0.636 \frac{P}{D * L} \qquad (1.11)$$

with *P* the applied load at failure (N), *D* the diameter of the sample (mm) and *L* the length of the plug, measured at its center (mm). The Brazilian tensile strength typically relates to the true tensile strength in a 2:1 ratio (Siegesmund and Dürrast, 2011).

1.4.3. Triaxial tests

UCS tests do not completely represent the actual conditions in the subsurface. Triaxial testing, however, provides realistic simulations of in situ rock properties. By subjecting core-scaled specimens to axial and confining pressures, while also controlling the temperature condition, triaxial testing allows to predict how rock masses respond to changes in load, stress, displacement, failure and other conditions. Conventional triaxial tests involve subjecting a cylindrical rock core to a certain confining pressure and a controlled increase in axial stresses. Figure 1.5 provides an illustration of a core-scale triaxial device which can be used to perform conventional triaxial tests in cylindrical rock samples with a diameter of 5-7 mm and an L:D ratio of 2:1 (Hangx et al. 2010).

It comprises a main pressure vessel with the sample in it, within a fluorinated ethylene propylene (FEP) heat shrink jacket and an ethylene propylene diene monomer (EPDM) rubber sleeve, a linked auxiliary pressure vessel, and a load transmitting piston assembly, driven by a motor (Figure 1.5). The piston assembly is advanced in order to load the sample, while simultaneously displacing confining fluid from the main pressure vessel to the auxiliary vessel. As such, the system volume is kept nominally constant (Hangx et al., 2010). The device allows to measure sample volume changes while keeping the confining pressure constant and increasing the axial load. The strain on the sample is measured both in vertical and horizontal direction: for the vertical strain, the displacement of the piston assembly is measured in the auxiliary pressure vessel below the main pressure vessel; and for the horizontal strain, the volume

of outflowing confining liquids, necessary to keep the confining pressure constant, is measured. This volume is equal to the horizontal expansion of the sample.

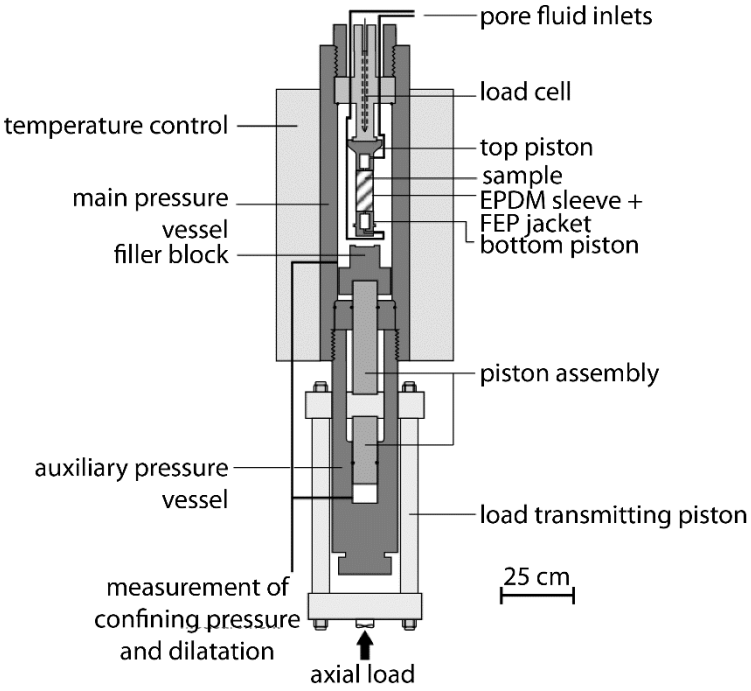

Figure 1.5. The Heard apparatus of the experimental rock deformation group at Utrecht University, The Netherlands. Figure modified from (Hangx et al., 2010).

In this work, no core-scale (diameter of approximately 3 to 5 cm and a length of 6 to 10 cm) triaxial tests on the reservoir sections of the Longyearbyen CO_2 project are reported. However, a simplified small-scale triaxial device, with similar components as in the Heard apparatus allowed bringing rock plugs with a diameter of 5 mm and a length of 14 mm to reservoir conditions. This device is discussed in more detail in section 2.3.2.2.

2.

2D imaging and X-ray micro-CT

2D and 3D imaging techniques are invaluable for microstructural studies of geomaterials and pore-scale processes occurring in them. In order to understand the complexity of the pore system, fractures and physical and chemical interactions between the geomaterials and pore fluids, one is obliged to visualize the geomaterials and the processes in high spatial, and often temporal resolution. In this chapter, the most widely used 2D imaging techniques are discussed. However, the focus of the chapter is on high resolution X-ray computed tomography as a 3D imaging technique, because this was the main method used in this work. A specific emphasis is put on the complexity of fracture characterization in both 2D and 3D imaging methods. Particularly the determination of the fracture aperture distribution is discussed, which is one of the most important parameters linked to fluid flow and transport processes.

2.1. 2D imaging

Traditionally, geological materials and fractures within them are analyzed through optical microscopy or Scanning Electron Microscopy (SEM) (Hakami and Larsson, 1996). These techniques provide information in 2D and require the sample to be prepared in a destructive manner, leaving it useless for further analysis. Fracture apertures specifically can also be determined through profilometric measurement. These three techniques are shortly described in the following sections.

2.1.1. Optical microscopy

The most widespread and standardized method for the visualization of geological materials is thin section analysis, using an optical microscope. This technique is fast, cheap and widely accessible. It provides two dimensional (2D) mineralogical and structural information on small slabs of rock, typically with a thickness of 30 µm. High-end light microscopes are typically limited in resolution to about 0.23 µm (Gustafsson, 2000). In this research, a Zeiss Axioscope petrographic microscope was used for the petrographic study of storage unit materials. Some thin sections were impregnated with a fluorescent dye (Epodye, Struers) in order to more easily reveal the pore structure of the rocks. However, most of the thin sections in this research were used to provide a mineralogical description of the different storage units.

2.1.2. Scanning Electron Microscopy (SEM)

2D imaging at higher resolution can be obtained with Scanning Electron Microscopy (SEM). In this technique, a high-energy electron beam scans the surface of the sample. The electrons penetrate the sample to a depth of a few microns and interact with the atoms at the surface. This produces signals containing information on the topology and chemical composition at the surface. These signals include secondary electrons, backscattered electrons and characteristic X-rays. SEM machines with an energy-dispersive X-ray spectroscopy detector (EDS or EDX) are able to

provide chemical information. The excited photons are collected in function of their energy and the spectrum of the energy-dependent photon intensity is analyzed to measure the chemical composition of the sample. For topological imaging, or for porosity analysis, the secondary electrons and backscattered electrons are measured. Specifically for topological measurements, the use of secondary electrons is recommended, since these typically are generated in the first 50-500 Å of the sample. Geological samples normally need a preliminary treatment for SEM analysis. The samples require a conductive coating to prevent electric charging under electron bombardment. In an environmental, or low-vacuum SEM, this coating can be avoided. In this work, samples were coated with carbon and the JEOL JSM-5310LV microscope (Dept. of Geology, Ghent University) was used. A carbon coating was chosen instead of gold coating, since this does not interfere with chemical EDS measurements. The used SEM system is equipped with such an EDS detector and thus allows both structural and chemical characterization of geological samples at their surface.

2.1.3. Profilometry

The roughness of two opposing fracture surfaces can be determined through tactile or laser profilometry. The difference in both techniques is that the surface is mapped with a small needle-like protrusion and with a laser respectively. Currently, profilometry allows to detect micron-scale surface elevations on grids with a spatial resolution of approximately 10 µm (Ameli et al., 2013). This technique is particularly interesting to determine surface roughness itself (Poon et al., 1992). However, to determine the actual aperture distribution of a single fracture, the fracture needs to be opened up. To preserve the open space of a fracture, resin is therefore usually injected into it, before the fracture is opened. Still, relating surface elevations to actual fracture aperture distributions remains very challenging (Schmittbuhl et al., 2008).

2.2. Micro-CT

The most important technique in this research is high resolution X-ray computed tomography, or micro-CT. Because of its importance, this technique will be discussed more thoroughly as the other techniques, focusing on its particular aspects which are relevant to this research. Micro-CT is a non-destructive method to obtain a three-dimensional (3D) digital representation of an object with a micrometer-scale resolution. As such, it allows the visualization of the internal structures of materials, which provides additional information on both the internal and external 3D composition and structure of the object. Of course, micro-CT does not provide direct chemical information of the different minerals, however, with prior knowledge and when the technique is combined with thin section analysis, or SEM measurements, one can often identify the different minerals in the micro-CT images. The technique is based on the penetration of X-rays, electromagnetic radiation with a wavelength between 0.01 and 10 nm, through the material of interest. Based on the source of the X-rays, micro-CT can be subdivided in lab-based micro-CT and synchrotron-based micro-CT (section 2.2.2). Because X-rays can penetrate matter, they are used in medical applications and for (airport) security. Radiographs, which are 2D projections of an object after X-ray penetration, provide valuable information in these cases. However, simple radiographic imaging lacks depth information, which is necessary for true 3D interpretation of digital images. This is where CT comes into play. (Micro-)CT combines the information from a series of radiographs, taken at a range of angles from 0° to 360° around the object, and transforms it into a 3D representation of the object (Hounsfield, 1973). The mathematical transformation of a series of radiographs through an object into a stack of (micro-) CT images is done in the reconstruction phase. CT was first designed for medical purposes. However, it was quickly adopted in many other scientific fields. Because CT was originally meant to scan patients, with a limitation of the resolution to several hundreds of micrometers, and a limited energy at which could be scanned, the systems were

not appropriate for other materials. Therefore, the research field of micro-CT emerged, adapting the systems to allow scanning other materials at a higher resolution (du Plessis et al., 2016). One of the adaptations was done in the setup: in medical CT scanners, the object of interest is positioned between a rotating X-ray source and detector. The most common micro-CT setup, however, is one where the rotation is provided by the sample stage in between the X-ray source and detector. Other adaptations of the traditional CT systems towards micro-CT systems included changes in the operational X-ray voltages and thus a higher penetrating power, as well as improved image quality for dense objects (du Plessis et al., 2016). In the last three decades, micro-CT grew to a commonly used technique in geosciences specifically (Cnudde and Boone, 2013; Andrew et al., 2014), and material sciences in a broader perspective (Maire and Withers, 2014).

2.2.1. Physical principle

Micro-CT is based on the attenuation of X-rays when they pass through material: the X-ray beam interacts with the material and a part of the X-rays will be absorbed by the material, or scattered. X-rays interact with matter in different ways. For micro-CT the most relevant interactions are photoelectric absorption, Compton Scattering and Rayleigh scattering (Seibert and Boone, 2005). The Lambert-Beer equation (equation 2.1) describes the attenuation of monochromatic radiation with an incident intensity I_0 to the transmitted intensity I when it passes through a homogeneous material with a thickness T:

$$I = I_0 e^{-\mu T} \tag{2.1}$$

with μ the material's specific linear attenuation coefficient. Most geological materials, however, are not homogenous and consist of multiple components. In such cases, the more generic form of Beer's law must be applied (equation 2.2). In this equation, the integral is taken over the X-ray path s with $\mu(s)$ the local linear attenuation coefficient:

$$I = I_0 e^{-\int_T \mu(s) ds} \quad (2.2)$$

The attenuation coefficient basically describes the fraction of an X-ray beam that is absorbed or scattered per unit thickness of the absorber. It depends on the density of the material, its chemical composition and the energy of the used radiation. As stated before, these equations are valid for monochromatic X-ray beams. Lab-based micro-CT systems, however, are equipped with sources which produce polychromatic beams. This influences the measurement of the attenuation coefficient and causes imaging artefacts (section 2.2.6.3).

2.2.2. A lab-based micro-CT setup

The typical lab-based micro-CT setup is shown in Figure 2.1. In lab-based systems, X-rays are generated by an X-ray tube. In this tube, electrons are emitted from a heated filament, which acts as a cathode, and are accelerated under high vacuum towards an anodic target. This target is often composed of tungsten or molybdenum and is typically cooled from the backside, since most of the electrons' energy is converted to heat when the electrons hit the target. A portion of the electrons is converted to polychromatic X-ray radiation (Vlassenbroeck, 2009). The radiation depends on the chemical composition of the target and the accelerating voltage of the electrons. To reduce the spot size, where the electrons impact the target, an electrostatic focusing cup, or control grid, can be used to focus the emitted electron beam from the filament. An electromagnetic focusing mechanism can also be added to further lower the spot size of the X-ray source (Vlassenbroeck, 2009). A lower spot size is beneficial to achieve a better resolution, however, it affect the X-ray flux and thereby the operation time for a micro-CT scan.

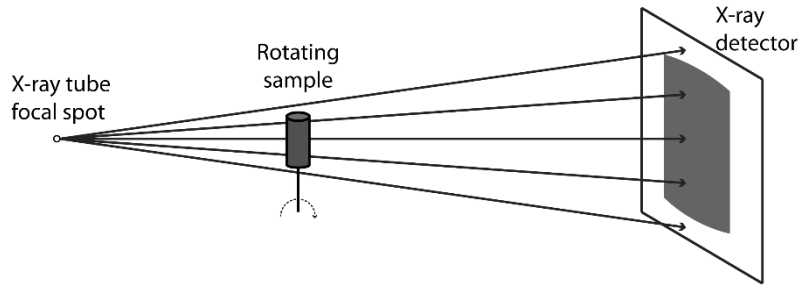

Figure 2.1. A lab-based micro-CT setup with the X-ray tube focal spot, producing conical X-rays, a rotating sample and the X-ray detector. Figure modified from (Cnudde and Boone, 2013).

The X-rays leave the X-ray source and form a cone-shaped beam (Figure 2.1). After passing through the object of interest, they hit the X-ray detector. In this detector, the X-rays interact with a scintillating material, where the deposited energy is converted into visible light. This light is guided to a charge coupled device (CCD) sensor, where the light is converted to an electric signal. The signal contains combined information on the incident X-ray flux and its spectrum. As such, radiographies are obtained. Lab-based systems come in all sizes, allowing the investigation of geomaterials from the core scale (up to 15 – 20 cm in diameter) to the plug scale, where a sample can be as small as 1 mm or less.

2.2.3. Achievable resolution

As stated before, high resolution imaging in lab-based micro-CT is typically achieved through geometrical magnification of the sample. By placing the sample closer to the X-ray source, and thus decreasing the Source Object Distance (SOD), while maintaining the Source Detector Distance (SDD), a higher magnification is obtained. The main limiting factor for the achievable resolution is the focal spot size of the X-ray source, under the condition that the obtained voxel (3D pixel) size is smaller than the spot size (Ketcham and Carlson, 2001). Recent work has led to the development of X-ray tubes with a spot size down to 100 nm (Nachtrab et al., 2015). In

most cases, the limitation of the spot size can be neglected, since the reconstructed voxel size of the micro-CT images is larger than the focal spot size of the X-ray source. This leads to the fact that the terms voxel size and resolution are often used as synonyms in micro-CT applications. The resolution *R* then mostly depends on the ratio between SDD and SOD through following equation:

$$R = \frac{d}{M} + \left(1 - \frac{1}{M}\right)s \qquad M = \frac{SDD}{SOD} \tag{2.3}$$

with *d* the detector pixel size, *s* the focal spot size and *M* the magnification. To achieve the highest magnification *M*, the object thus has to be placed as close as possible to the source (small SOD). However, to completely visualize the object, it needs to rotate within the cone-beam during the micro-CT acquisition (Figure 2.2). This implies that the size of the object limits the SOD, and thus the magnification and achievable resolution. High resolutions can thus only be obtained for small samples.

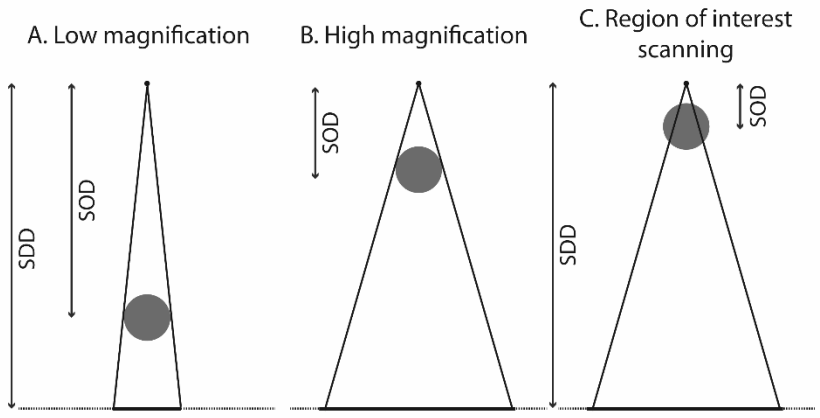

Figure 2.2. Illustration of the differences in sample magnification with a large SOD (A) and a small SOD (B). When the sample is placed so that only a region of it is covered by the X-ray beam from source to detector, only this inner region is visualized (C: region of interest scanning).

In the systems used in this work, a general rule of thumb is that the resolution of the micro-CT images is about one thousand times smaller than the diameter of the sample. For a sample with a

diameter of 1 mm a resolution of 1 µm can be achieved, if the spot size of the X-ray tube is small enough.

If a sample has a (quasi-) homogeneous composition, it is possible to perform a scan where only a region of the sample is covered by the X-ray beam from source to detector. This does not necessarily needs to be the center of the sample, however, the sample still needs to be able to fully rotate in front of the source. When performing such a region of interest scan (Figure 2.2.C), only that part of the sample is visualized which is covered by the X-ray beam. It allows imaging the inside of larger samples with a better resolution than in a normal scan (Maire and Withers, 2014). However, when the sample is too heterogeneous, or the sample is encased within a high attenuating container, region of interest scanning will induce extra image artefacts and the scan will be of poor quality. This can partly be solved by acquiring more images during the micro-CT scan, or by increasing the frame rate of a single projection. Typically, a region of interest scan in which approximately 1/3rd of the original cylindrical rock plug or core is imaged with an increased resolution can be conducted.

2.2.4. Data processing and analysis

2.2.4.1. Image reconstruction

Once a series of radiographies is acquired, over an angular range from 0° to 360°, the projections need to be converted to a 3D volume via so called tomographic reconstruction algorithms. The projections, taken from different angles are combined to reconstruct the attenuation values of single voxels through the technique of filtered backprojection, the most common approach for micro-CT reconstruction (Michael, 2001). This is the analytical approach to reconstruct the micro-CT images. There are also iterative reconstruction techniques, however, since they were not used in this research, only the analytical approach is discussed. In simple backprojection, the images are formed by smearing each

projection back through the image, in the direction it was originally acquired. The final image is then the sum of all the backprojected views. This technique results in a blurry image of the actual object. This blurring is corrected for in “filtered backprojection”. The process of filtered backprojection is illustrated in Figure 2.3.

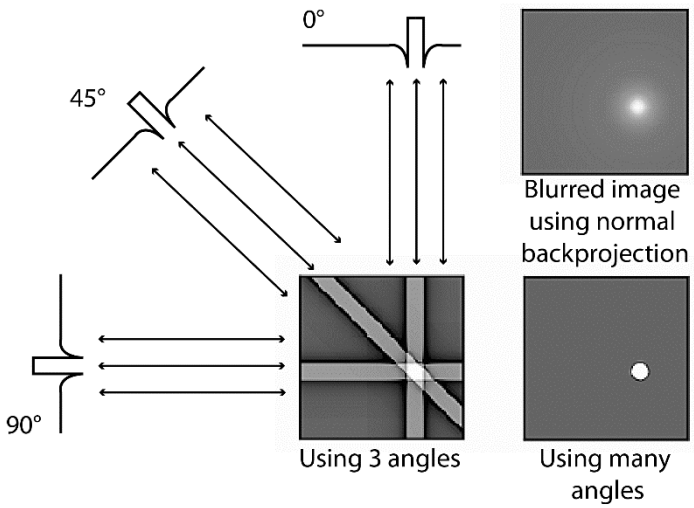

Figure 2.3. Schematic representation of the filtered backprojection technique to reconstruct the image of a white dot. Using normal backprojection, the reconstructed image would be a blurred version of the “correct” image, while filtered backprojection removes this blurring. Figure modified from (Michael, 2001).

The image produced by filtered backprojection is theoretically identical to the “correct” image if an infinite number of views and an infinite number of points per views are obtained (Michael, 2001).

In the reconstruction phase, the 2D projections are first normalized to correct for acquisition-specific effects in the data. Every micro-CT scan is therefore accompanied by a number of open beam, or flat field images, and dark images, or offset images. Flat field images are radiographies taken when there is no sample in between the X-ray source and detector, while dark images are taken while the X-ray tube is switched off. The dark images are subtracted from each of the projections of the scan, to correct for detector features,

while the flat field images are necessary to correct for the X-ray beam inhomogeneity. Very dark or bright pixels in the radiographies can be corrected with a spot filter (Vlassenbroeck et al., 2007). A last preprocessing filter which can be applied is a ring filter. It tracks non-linearities from the detector pixel by pixels and removes them. If they would not be removed, ring artefacts could be present in the reconstructed images (Section 2.2.6.3). When the necessary corrections are applied, sinograms are constructed, which is the 2D array of data containing the projections. In combination with the normalized images, the micro-CT images can then be reconstructed.

In this research, two reconstruction packages were used: Octopus reconstruction (Masschaele et al., 2007; Vlassenbroeck et al., 2007) and the Acquila software suite. Both of these software packages are currently further developed by XRE NV, a spin-off company of the Centre for X-ray Tomography at Ghent University (UGCT, yet originally developed at UGCT.

2.2.4.2. Image analysis and visualization

For quantitative analysis of the acquired 3D datasets, dedicated software is used. In this research, commercial software packages were used as well as in-house developed software and open source programs. The most important software suites used in this work are: Avizo, distributed by FEI (www.fei.com); VGStudioMax (www.volumegraphics.com); Matlab (www.mathworks.com); the in-house developed software of UGCT, Octopus Analysis, formerly known as Morpho+ (Brabant et al., 2011) and currently further deployed by the spin-off company XRE NV; and the open-source image analysis package Fiji (Schindelin et al., 2012). Standard micro-CT analysis workflows are thoroughly documented (Ketcham and Carlson, 2001; Brabant et al., 2011; Cnudde and Boone, 2013; Bultreys et al., 2016a). Therefore only the basic principles will be explained in short. It should be noted that quantitative 3D analysis often is not straightforward and is inherently prone to several systematic errors due to e.g. noise and discretization effects. It is

heavily reliable on user input, which means the results have to be interpreted with care. Researchers need to be aware of the limitations during acquisition and analysis of the obtained data (Cnudde and Boone, 2013). Figure 2.4 illustrates the different steps in the standard micro-CT analysis workflow, starting from an image of stacked glass beads (Figure 2.4.A).

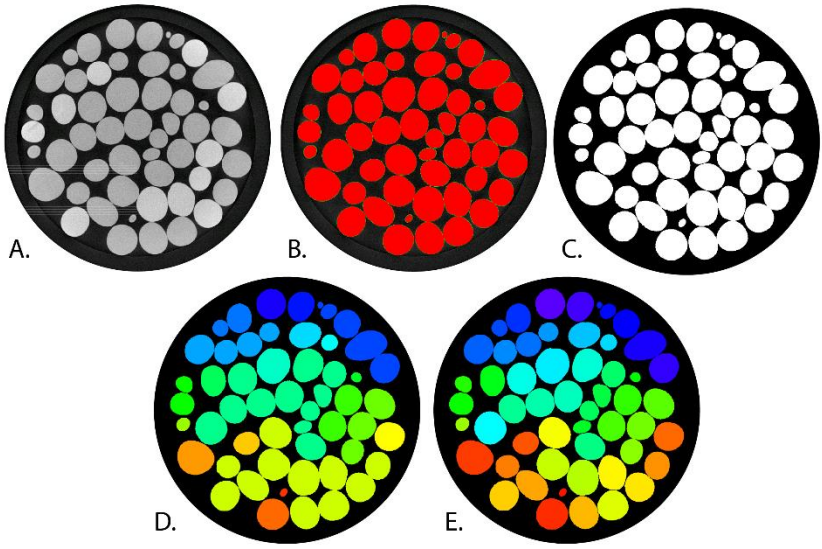

Figure 2.4. An illustration of the different steps in the micro-CT analysis workflow, illustrated with a scan of a glass bead pack: A. represents the unaltered micro-CT image; B. is the thresholding step, in which the glass beads get segmented from the pore structure; C. is the binarized image, resulting from the thresholding; D. shows labels assigned to different glass beads. Where glass beads physically touch each other, two or more glass beads are labelled as one object; E. the labels after the watershed segmentation algorithm has separated individual glass beads.

Each of the above mentioned software packages allows primary *filtering* steps that can be applied to the micro-CT data. This might be necessary to further reduce noise or artefacts in the images which can remain after the pre-processing steps. Image noise and sharpness is often a recurring issue which can be solved with such a filtering step (Wildenschild and Sheppard, 2013).

As stated before, micro-CT images are grey value images in which the grey value depends on the local attenuation of X-rays. This is

linked to chemical composition and density of the material. Minerals with a heavier elemental composition (e.g. pyrite: FeS_2) will appear brighter than minerals such as quartz (SiO_2) or calcite ($CaCO_3$). In geomaterials, the phase of interest is often the pore space of the rock. This is clearly distinguishable from the rock matrix, given that the resolution of the images resolves the pores.

Different phases in the micro-CT images can be separated from each other in a binarization step, which is often referred to as *thresholding* or *segmentation* (Figure 2.4.B). In this analysis step, the grey value voxels are partitioned in binary phases. As with the filtering, there are several methods to threshold an image. Many automated threshold techniques exist, however, this step is very often performed manually. This implies a strong user-dependency, which is one of the major drawbacks of image-based analysis methods. Automated methods are vital to reduce the user-dependency. However, because of the diversity of applications and possible artefacts, this remains a very challenging task. After thresholding, the binary image (Figure 2.4.C) can typically be further improved to reduce noise, using different binary operations.

The different segmented objects in the binary image are then *labelled* (Figure 2.4.D). In this step, individual objects are defined from the binary image. In the illustration (Figure 2.4.D), glass beads that physically touch each other are labelled as one object. It is thus necessary to separate these individual objects from each other, which is done in the next step: a *watershed separation* algorithm (Vincent and Soille, 1991; Landis and Keane, 2010) allows to separate objects at their narrowest points.

Once this step is done, the micro-CT data is converted to a stack of images in which individual objects (grains, pores, mineral phases) are labelled (Figure 2.4.E). From then, different volume parameters can be determined for individual objects, such as their volume, orientation, maximum inscribed sphere, elongation, etc.

Fracture analysis and visualization

When dealing with more complex structures, additional tools, which are not readily built-in into most analysis software packages, might be necessary. Specifically for very thin fractures in geomaterials, with an aperture close to the resolution of the scan, image segmentation is not straightforward. First of all, geomaterials are often not homogeneous and consist of different minerals which attenuate X-rays differently. This implies that fractures are found with different minerals and thus different grey values on either side of the fracture. Specialized semi-automated scripts exist, to be used in Fiji and Matlab, specifically for fracture segmentation (Voorn et al., 2013; Deng et al., 2016; Huo et al., 2016). However, these scripts perform best to separate fractures in nearly homogeneous materials. When the composition of the fractured geomaterials is too heterogeneous, these scripts tend to fail. Quantitative information on the fractures (on their aperture, orientation and length) can then only be determined based on the individual slices through the 3D volume.

In this research, a combination of tools in Fiji and Matlab were used to retrieve such information, as well as own developed scripts in Matlab, partly based on Ketcham et al. (2010), to measure the orientation and aperture distributions of micro-fractures. These Matlab scripts are given in Appendix A. For local fracture aperture measurements, they rely on grey value profiles, which are taken perpendicular to the fracture. The fracture results in an attenuation dip in the grey value profile, which can be fitted by a Gaussian point spread function (PSF) (Ketcham et al., 2010; Mazumder et al., 2006; Vandersteen et al., 2003). The PSF fitting process was based on the following equation:

$$CT_i = g - a * \exp(-((x-b)/c)^2) + d * \sin(2\,pi\,x\,/e + f) \quad (2.4)$$

in which CT_i is the CT value of voxel I, g represents the average material grey value, the factor $a*exp(-((x-b)/c)^2)$ is used to

represent the dip in attenuation caused by the fracture and the factor *d*sin(2 pi x/e + f)* is used to fit the natural variation in material or matrix grey value.

To determine the local fracture aperture from this PSF, either the full-width-half-maximum of the attenuation dip can be determined (FWHM-method), or the missing attenuation (MA-method), or the peak height of the attenuation dip (PH-method) (Ketcham et al., 2010). The difference between these approaches is shown in Figure 2.5.A.

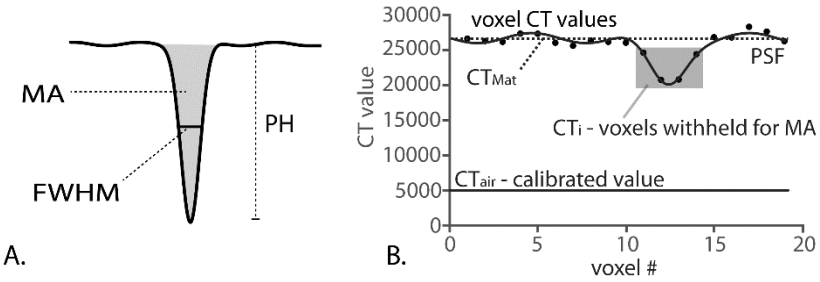

Figure 2.5.A. An illustration of the principle of full-width-half-maximum (FWHM), missing attenuation (MA) and peak height (PH) determination on the dip of a point spread function (PSF) to quantify the local fracture aperture; B. A PSF fit to a traverse across a narrow fracture. The CT values of the voxels surrounding the attenuation dip are used to determine CT_{Mat}, while the CT value for air is a known calibrated value. The voxels making up the attenuation dip are used to determine CT_i, with which an MA value can be determined.

The FWHM-method is best suited for well-pronounced fractures (Ketcham et al., 2010). When the fracture aperture is close to the resolution of the micro-CT images, the MA-method or the PH-method is better suited to provide a measure of the aperture. These methods require a calibration of the CT-values for air in the particular scan. In this work, the MA-method was used for the characterization of thin fractures. The general equation describing the MA-method is (Ketcham et al., 2010):

$$d_{foi} = d_{vox} \left(\sum \frac{CT_{Mat} - CT_i}{CT_{Mat} - CT_{air}} \right) + C \qquad (2.5)$$

With d_{foi} the dimension of the feature of interest (in this case, the fracture aperture), d_{vox} the resolution of the micro-CT image, CT_{Mat} the average surrounding CT values for the material, CT_i the CT value of a voxel *i* part of the fracture, CT_{air} the calibration of the CT value for air, and *C* a constant which is ideally zero (Ketcham et al., 2010). The summation has to take into account all voxels part of the attenuation dip in the PSF. Figure 2.5.B illustrates the MA determination on a PSF, with an indication of all calibration values used in equation 2.5.

2.2.5. Differential imaging

In order to monitor chemical and textural changes in reservoir samples (for example due to injection of an acidic brine, or an increase in confining pressure), sequential micro-CT scans can be obtained in the course of an experiment. By subtracting the images of the first micro-CT scan from the images of the following scans, a differential image can be obtained. This image shows the changes in the material (Boone et al., 2014). The technique also enhances the visualization of sub-resolution features in micro-CT images.

In fluid flow experiments, an X-ray contrasting agent can be injected in rocks in order to enhance the visualization of pores and fractures which are otherwise difficult to image. When a contrasting agent was necessary in this work, a cesium chloride brine (CsCl) was used. The needed concentration of such a brine depends on the rock's mineralogy. A CsCl-brine is often chosen as substitute for reservoirs' formation water (Kwak et al., 2005). Even at relatively high concentrations, the CsCl-brine is known to have a similar dynamic viscosity as H_2O. By generating a differential image between a micro-CT scan of the material in a dry state and the micro-CT scan of the material saturated with the CsCl-brine, the pore structure becomes isolated from the material. The obtained differential images only show the signal of the added fluid. This makes it possible to unambiguously analyze the pore and fracture structure of the rock. Especially for fracture segmentation, differential imaging is a very useful technique.

2.2.6. Volume and image limitations

2.2.6.1. Partial volume effect

Micro-CT images are 3D digital images, consisting of a stack of voxels, i.e. 3D pixels, with a certain grey value representing the local attenuation of the X-ray beam. This means it gives a rasterized representation of the reality. All features within the scanned object that are smaller than the voxel size of the image will thus not be identified as separate feature in the micro-CT images. Every feature, however, that fits completely or partially inside a voxel will contribute proportionally to the grey value of that voxel. This phenomenon is called the partial volume effect. This has the practical consequence that sharp edges within the micro-CT images are smeared out over multiple voxels, a phenomenon also known as the spillover effect. The smaller the object of interest and thus the closer it is to the actual voxel size, the harder it will be to identify it as such. The partial volume effect is illustrated in Figure 2.6. Both of these micro-CT images are from a conglomerate of the Longyearbyen CO_2 project. The image on the left (Figure 2.6.A) illustrates a section of a micro-CT scan with a voxel size of 12 µm. This was the highest resolution possible for a scan in which the sample was fully covered by the conical X-ray beam (Figure 2.2.B). The image on the right (Figure 2.6.B) is the result of a region of interest scan and illustrates approximately the same slice through the material. In this scan, a voxel size of 3.7 µm was obtained, more than 3 times better than the original scan on the left. It is clear that the image with the highest voxel size, and thus the lesser resolution (Figure 2.6.A), is more blurry. The grain boundaries are less pronounced and little to no structures are visible in the large void in the top part of the inset. When the voxel size decreases, and thus the resolution increases (Figure 2.6.B), the edges are much sharper, and even very small pores become distinguishable, which were not visible in the micro-CT scan with a voxel size of 12 µm.

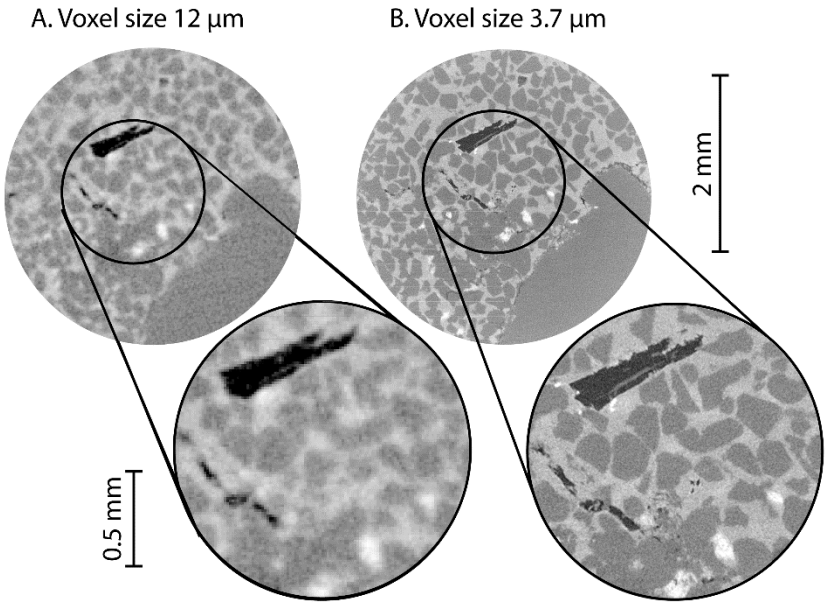

Figure 2.6. Illustration of the partial volume effect on micro-CT scans from a conglomerate sample of the Longyearbyen CO_2 project reservoir, both taken at HECTOR (Section 2.3.1). The scan to the left (A) illustrates a section from a micro-CT scan with a voxel size of 12 µm, while the images on the right (B) are from the same micro-CT slice obtained with a region of interest scan to obtain a voxel size of 3.7 µm.

Even if some features fall below the resolution of the image, they can still be observed. Sometimes, enough information is preserved to be able to quantify the orientation of sub-resolution objects. However, a quantification of their precise width below the resolution is harder to obtain. Especially in homogeneous materials, the variation in grey value due to the partial volume effect can enable users to estimate to some extent features below the resolution of the scan: for instance the micro-porosity in a homogeneous material. This can only be done on the condition that there are also areas with 100% porosity and entirely solid areas in the image to provide for a calibration of grey values. It is important to understand this limitation when retrieving quantitative information from micro-CT images. Quantification of features is strongly dependent on the number of voxels representing that feature.

2.2.6.2. Representative elementary volume

As stated before, spatial resolution of micro-CT images is linked to the analyzed volume of an object. High resolution images can only be acquired from a limited volume and requires either sub-sampling of the material, or region of interest scanning. Either way, the analyzed volume decreases with increasing resolution, especially when taking into account that often only a central sub-volume of the original 3D image is used for quantitative analysis in order to exclude side effects. The sub-volumes are not necessarily representative for the entire volume of the original sample (Costanza-Robinson et al., 2011). The sample size at which the observed area of a material is representative for the entire material, so that reliable conclusions can be made for a certain parameter, is called the representative elementary volume (REV). Figure 2.7 illustrates how an REV can be determined: one measures a certain parameter (for example, porosity) at different volumes of the digital image stack and plots this. When the volume is below the REV (zone A in Figure 2.7), so-called microscopic effects influence the local measurement of that parameter. Below the REV, the measurements depend on the volume and location of that volume in the global 3D volume. At the smallest sample size for example (in the case of micro-CT images this is one individual voxel), the porosity is either 100% or 0%. The variation of the measured parameter will decrease when the volume increases, up to the REV. Once the REV is reached (zone B in Figure 2.7), the measurements will stay the same, independent from the location where the volume is defined. It must be noted that zone B in Figure 2.7 represents an idealized situation. In fact, the measurements are often still characterized by small measurement errors. When the volume of measurement is further increased, the measurements stay localized around one particular value, until the volume is large enough to capture macroscopic heterogeneity in the 3D images (zone C in Figure 2.7).

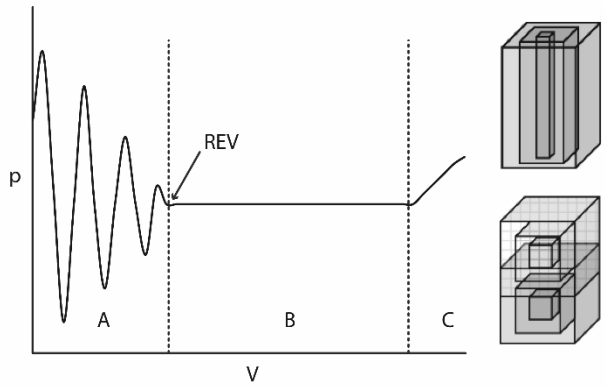

Figure 2.7. Concept of Representative Elementary Volume (REV): zone A is the domain of microscopic effects; zone B is the domain of the porous medium and zone C is the domain of the macroscale heterogeneity. V represents a volume in which parameter p is measured. The images to the right show strategies for measuring different volumes in the micro-CT images. Figure modified from (Costanza-Robinson et al., 2011).

The REV will be influenced by the fact that small details cannot be captured at larger samples. Therefore, one needs to weigh the importance of either reaching an REV in the micro-CT images, or being able to capture small details by scanning a smaller sample. A commonly used scanning technique to cope with these volume requirements for measurements is downscaling: first a scan is made of the material at a low to medium resolution, after which, through digital dissection, areas of interest are chosen. There, subsamples can be taken which can be scanned at a higher resolution. As such, an overview scan, in which certain details are missed, can be combined with a higher resolution micro-CT scan, taken for quantification. Figure 2.8 illustrates this principle with a drill core sample of the Longyearbyen CO_2 project.

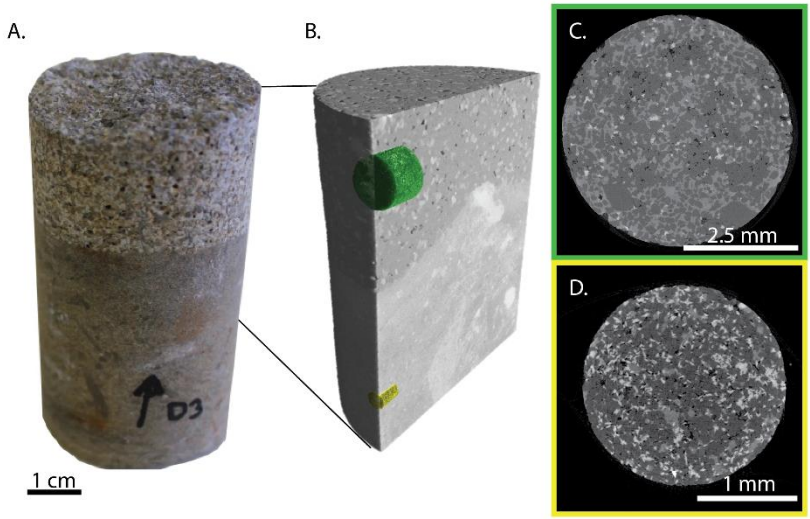

Figure 2.8. Principle of subsampling illustrated with a sandstone core of the Longyearbyen CO_2 Lab. The drill core (A.) is characterized by a sharp change in lithology. Digital dissection of the core, at a low resolution of approximately 50 µm (B.) allows the definition of sub-sample areas, where higher resolution scans (at a resolution of 4 µm and 2.8 µm for C. and D. respectively) allow for a porosity measurement. Figure from (Mulrooney et al. in prep.).

Most rock fractures are considered as self-similar structures. This means that the fracture morphology repeats itself at different length scales. Fractures thus possess scale-invariant properties (Sahimi, 2011; Miao et al., 2015). This implies that extending the concept of REV to fractured rocks is problematic since there is no characteristic size limit to fractures (Barton and La Pointe, 2012). When fracture morphology is determined, it is thus important to keep in mind the length scale of observation. The concept of extrapolating fracture characteristics (particularly morphological parameters) to the scale(s) of interest is possible, but not linearly like in the REV framework (Marrett et al., 1999).

2.2.6.3. Other image artefacts

Besides the limitations linked to image resolution and REV, micro-CT imaging is prone to several types of image artefacts. Most of these artefacts can be reduced by applying measures during the

acquisition (such as adding a hardware filter), during reconstruction (spot and ring filter), or as image processing step (filter options and binary operations). Below, some of the most common artefacts in lab-based micro-CT are discussed. These are the artefacts which were most important in this research.

Lab-based X-ray sources produce a polychromatic X-ray beam. Because the attenuation coefficient is energy-dependent, this gives rise to artefacts. When the X-ray beam passes through material, low-energy photons are more easily attenuated compared to high-energy photons. This leads to the increase of the average energy of the X-ray beam that reaches the detector, although the overall intensity decreases. This phenomenon is called *beam hardening.* At the edges of a sample, this effect results in relatively higher measured attenuation coefficients than in the center of the sample (Ketcham and Carlson, 2001). After reconstruction, this appears as a brighter outside rim of the sample, even if the sample is homogeneous. This effect is also known as the cupping effect in grey value images. Figure 2.9 A and B illustrates the effect of beam hardening on acquired images. One can correct for this effect by using a metal filter during the acquisition of the scan. This ensures that low energy X-rays are filtered out prior to passing through the material. In the reconstruction phase, one can also apply beam hardening correction algorithms.

Ring artefacts (Figure 2.9A) usually occur due to defects in the detector. They represent local faulty high or low intensities in projection images. Ring artefacts can be reduced with flat-field images and by software corrections during the reconstruction phase (Ketcham and Carlson, 2001).

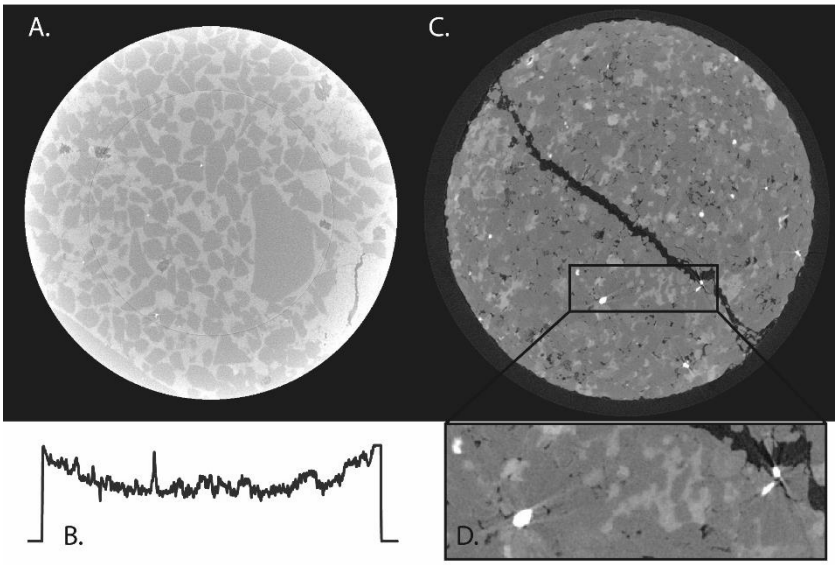

Figure 2.9. Illustration of some of the most common image artefacts in micro-CT: A. micro-CT image of a conglomerate section of the Longyearbyen CO_2 reservoir with severe beam hardening, and a less pronounced ring; B. grey value profile of the middle section of the micro-CT image in A.; C. sandstone section of the Longyearbyen CO_2 reservoir with metal artefacts around a dense mineral, probably a zircon; D. is an inset of C. to illustrate the metal artefacts more clearly.

Metal artefacts (Figure 2.9 C and D) are present when dense phases are present in a sample. In geomaterials these dense phases often are iron-bearing minerals, such as pyrite, or other dense minerals, such as zircons. Around these dense phases, dark streaks occur. Only photons with the highest energy can pass through these materials, leading to very low attenuation and thus dark streaks. Metal artefacts can be reduced by applying computationally demanding iterative reconstruction algorithms.

Other possible artefacts are related to the typical setup of lab-based micro-CT systems. Due to the cone beam for example, an object is typically under sampled at the top and bottom of the images, leading to the so called *cone beam artefact*. Some parts of the object, on the top and bottom, are not in the beam path for every projection angle. This artefact typically blurs out horizontal features in these regions and can be countered by using helical CT

scanning. In such a setup, the sample moves vertically during the image acquisition.

Motion artefacts are caused by the movement of the sample during the acquisition of the images. Due to movement, the object is typically blurred in the reconstructed images. These artefacts become more important at higher resolution and when imaging dynamic processes (Bultreys et al., 2016b). In the latter case, they can be reduced by 4D filtering algorithms.

2.3. Micro-CT at UGCT

All micro-CT scans in this research were performed at the UGCT, an interdisciplinary research center, founded in 2006 by Prof. Dr. Luc Van Hoorebeke (Department of Physics and Astronomy, Ghent University) and Prof. Dr. Patric Jacobs (Department of Geology, Ghent University). The UGCT performs research on the technological development and applications of X-ray micro- and nano-tomography. Currently, the UGCT is an interfaculty collaboration between the Radiation Physics group (Dept. of Physics and Astronomy), led by Prof. Dr. Luc Van Hoorebeke and Prof. Dr. Matthieu Boone, the laboratory for Wood Technology (Woodlab, Dept. of Forest and Water management), led by Prof. Dr. Joris Van Acker and Prof. Dr. Jan Van den Bulcke, and the PProGress group (Dept. of Geology), led by Prof. Dr. Veerle Cnudde. The center has developed several modular micro-CT setups. Currently, five systems are available: HECTOR, EMCT, MEDUSA, Nanowood and HERACLES. Each of these systems are capable of performing high-quality imaging of a large range of sample sizes and types. Hardware and software are developed in-house, often in collaboration with the spin-off company XRE NV. This allows the full control of every step in the acquisition, reconstruction and analysis process of micro-CT imaging.

2.3.1. Micro-CT systems used in this research

HECTOR, or the High Energy micro-CT system Optimized for Research, currently is the most used micro-CT system at the UGCT. It is equipped with an X-RAY WorX directional X-ray source, which can operate at a maximum voltage of 240 keV and a maximum power of 280 W (Masschaele et al., 2013). The resolution limit of the system, linked to the best spot size of the source, is approximately 3 to 4 µm. HECTOR (Figure 2.10) is equipped with a large PerkinElmer flat panel detector with a 2048 by 2048 pixel resolution and a pixel size of 200 by 200 µm. Additionally, it is equipped with a piezo micro-positioning sample stage for small samples, which can also be removed to enable the manipulation of heavy samples up to 80 kg. The system is very flexible and was originally designed to specifically image large and heavy samples (e.g. stone and concrete cores of more than 10 cm in diameter), hence the large power and voltage range and the large detector. To ensure stability, the entire system is fixed on a large granite back plate.

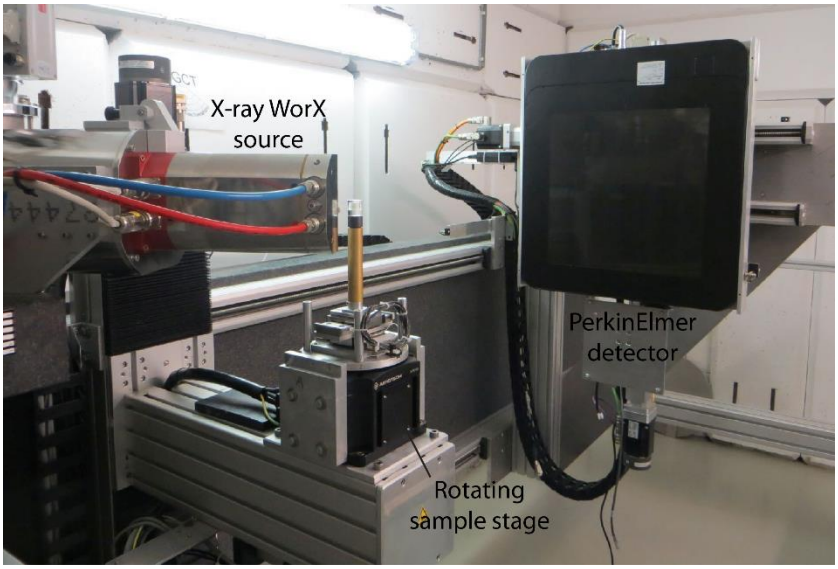

Figure 2.10. HECTOR, with a high-energy directional X-ray source, a strong rotation motor and a large PerkinElmer detector.

EMCT is the Environmental Micro-CT system at the UGCT. This unique system is quite different from traditional micro-CT setups (Dierick et al., 2014). It is specifically designed for in-situ imaging of materials. Therefore, it is often used in combination with different types of add-on equipment in order to condition the sample. In this setup the X-ray source and detector rotate around the sample, while the sample remains stationary. This is because conditioning of samples, for example to certain temperatures, relative humidity or pressures, often requires numerous wires and tubing to run to and from a condition cell. Designing such cells for a rotating sample stage is very complex. The EMCT is also often used for dynamic scanning. The possibility to continuously rotate around the sample and simultaneously acquire images allows the 4D monitoring of changes in the system (Bultreys et al. 2015a; Bultreys et al. 2016b). Geometrical magnification is still possible due to a gantry system, with a maximum resolution of 5 µm. The X-ray source is a Hamamatsu L9181 directional tube which can go up to 130 keV and 35 W. The detector is a Xineos-1313 high speed CMOS flat-panel detector with a resolution of 1300 x 1300 pixels and a pixel size of 100 x 100 µm. Both the source and detector are chosen deliberately to fit the needs of a rotational source-detector setup for fast imaging. The detector has a frame rate of up to 30 frames per second at full resolution (= 20 ms per radiography), which makes it ideal for fast dynamic imaging. Images of the EMCT are provided in section 2.3.2.1 and 2.3.2.2).

2.3.2. Add-on equipment

The PProGress (Pore-scale Processes in Geomaterials RESearch) group has strongly invested in the development of both in-house and commercially available add-on equipment. These modules allow the imaging of objects under certain external conditions such as temperature and pressure. In this research, add-on modules were used to follow small-scale uniaxial compression of samples and fluid flow through geomaterials under different confining conditions. Apart from the equipment discussed in the following

sections, other modules have been developed or acquired by the UGCT, such as a freezing stage, or a relative humidity chamber. However, since these are not in the scope of this work, they are not further discussed.

2.3.2.1. CT5000-TEC by Deben Ltd.

The CT5000-TEC system by Deben Ltd., UK, is a commercially available small-scale uniaxial compressive and tensile stage. This device allows for in-situ uniaxial compressive or tensile loading of small-scale samples with a maximum load up to 5 kN. It was specifically adjusted to fit on both HECTOR and the EMCT. Figure 2.11.A illustrates the system on the EMCT. The upper and lower piston, in between which the sample is placed, can be temperature controlled from -20°C to +160°C.

The glassy carbon only attenuates X-rays slightly. Depending on the expected strength of the material, the device can be fitted with one of four exchangeable load cells with maximum loads of 500 N, 1000 N, 2000 N and 5000 N. Each of these load cells operates with a known accuracy of 1% of their maximum load. In this work, the device was used to perform small-scale UCS tests. Therefore, the tensile setup, optimized for so-called dog-bone samples, will not be discussed. In a compressive test, the setup is such that the two pistons, or jaws, go from a fully open position to a closed one. The upper jaw remains stationary, while the lower jaw moves up at a certain speed (adjustable between 0.1 mm/min and 1 mm/min). The compression is limited to 10 mm, starting from fully opened jaws.

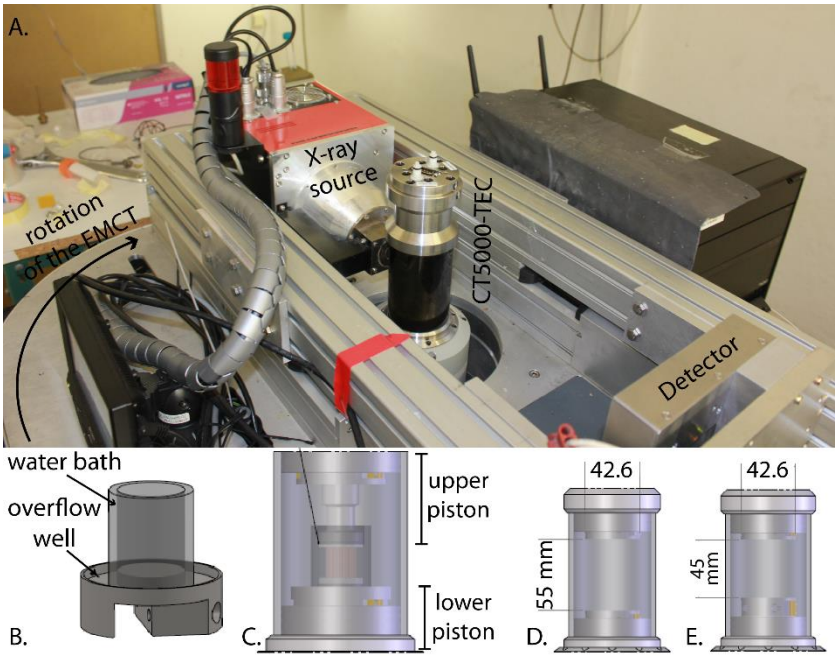

Figure 2.11. The CT5000-TEC system, produced by Deben Ltd., UK, on the EMCT: A. picture of the setup, with the indication of the X-ray source and detector, the CT5000-TEC device and the rotation of the EMCT around it; B. the water bath, set up on the lower piston in C.; D. and E. two flat surfaces on the upper and lower piston, in fully opened position (D) and fully closed position (E).

Two setups are possible for compressive testing of materials. A first one requires the use of a water bath (Figure 2.11B and Figure 2.11C). This restricts the height of the sample to a maximum of 21 mm and the diameter of it to 22 mm. The water bath allows samples to be tested while partially or fully (water-) saturated. The water bath is made from glassy carbon, allowing X-rays to pass through it. When no liquid is added to the water bath, it still provides an extra safety barrier for debris from failing rocks. This is necessary, since the driving mechanism of the lower piston is located below the sample stage and could be harmed from rock debris falling between the gears of the system.

A second setup allows larger samples to be tested. In this setup, two simple flat surfaces are placed on the top and bottom jaw of the system (Figure 2.11D and Figure 2.11E). Samples with a

diameter of maximum 40 mm and a height of maximum 55 mm can be uniaxially compressed. The CT5000-TEC system is controlled by the MicroTest software. It allows up to 10 measurements per second to be saved. The software detects both the force (N) applied to the sample and the absolute compression (mm). This allows the user to construct stress-strain curves based on the specific sample dimensions.

2.3.2.2. Fluid flow cells: from simple to sophisticated

Different fluid flow cells were used for the investigation of the fluid flow properties and processes in the reservoir units. They range from relatively simple designs to highly sophisticated ones. Typically, the flow cells with a more simple design are more easily adaptable to fit the needs of an individual experiment. More complex fluid flow cells are more time-consuming and expensive to produce. Therefore, their design is more robust and typically fixed for use with a certain sample size. Figure 2.12A illustrates the most simple flow cell design: a sample is fixated within a Fluorinated ethylene propylene (FEP) heat shrink that is glued within a polyvinyl chloride (PVC) cell.

The FEP heat shrink was first treated with an etching fluid in order to generate an increased adhesion, both of the FEP heat shrink to the sample, as of the heat shrink to the glue used to fixate it in the PVC cell. This type of flow cell was used for long-lasting experiments on chemical alteration of fractured reservoir rocks due to an acidic brine (Chapter 6). The samples had a diameter of 10 mm, and a length of 20 mm or more. For each sample, an individual flow cell was constructed.

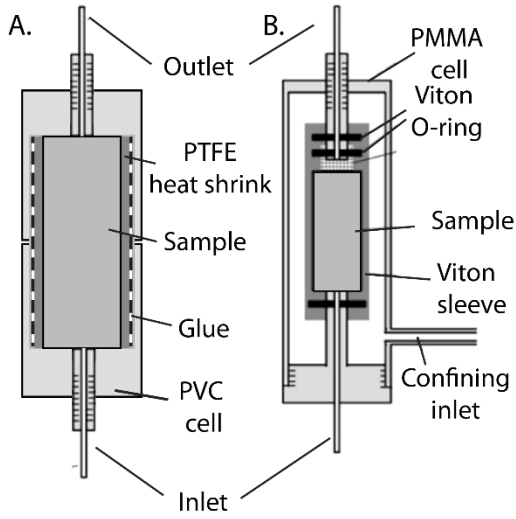

Figure 2.12. Two types of fluid flow cells: A. a simple fluid flow cell, in which a sample is encapsulated in a FEP heat shrink and glued in a PVC cell; B. a PPMA cell, in which the sample is surrounded by a viton sleeve and confined with a pressurized liquid. Figure B modified from (Bultreys et al. 2016b).

A slightly more sophisticated fluid flow cell is illustrated in Figure 2.12B. In this design, the sample is fixed within a viton sleeve, which is a type of synthetic rubber commonly used in petroleum related research. The polymethyl methacrylate (PMMA) cell is transparent, which is necessary for placing the sample inside it. A confining pressure can be applied to the sample within the viton sleeve to ensure fluid flow to take place through the sample and not along the sides of it. This confining pressure is applied with a manual balloon catheter pump, adjusted to fit on the flow cell. At UGCT, four such identical flow cells are available, designed to hold cylindrical rock samples with a diameter of 6 mm and a height between 15 and 20 mm (Bultreys et al. 2016b).

The SINTEF cell, illustrated in Figure 2.13, is a small-scale in-situ triaxial device, provided to UGCT by SINTEF, Norway. The cell is constructed for small rock plugs, with a diameter of 5 mm and a length of 14 mm. With the device, these plugs can be brought to actual reservoir pressures and temperatures. The SINTEF cell itself is tested for pressures up to 40 MPa in all directions (axial pressure,

confining pressure and pore pressure). However, the actual maximum operational pressure might be limited by other components in the fluid flow setup (tubing, connectors, pumps).

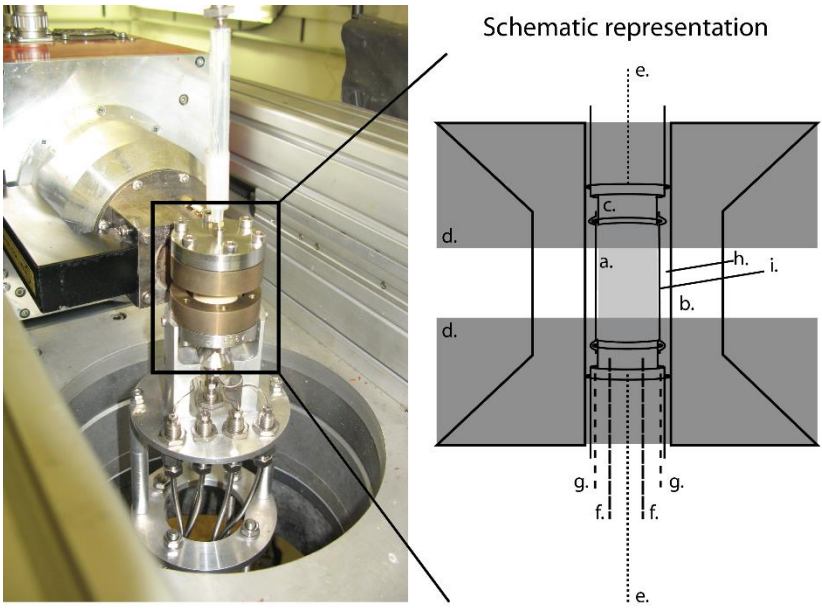

Figure 2.13. The SINTEF cell mounted on the EMCT, with a schematic representation of the cell: a. the sample, a rock plug of 5 mm in diameter and 14 mm long; b. a PEEK hourglass-shaped holder; c. the upper, stationary piston; d. metal rings holding the cell together; e. fluid flow line through the sample, in- and outflow; f. fluid flow lines providing the axial pressure to the lower piston; g. fluid flow lines providing the confining pressure to the confining chamber h. around the sample; i. a viton sleeve.

Within the SINTEF cell, the sample is placed within a viton sleeve which fits over small protrusions on the top and lower piston. Around the sample and the pistons, a polyether ether ketone (PEEK) hourglass-shaped holder is placed. The PEEK holder is kept in place by two metal rings, which are screwed to a top and bottom metal plate. The PEEK holder, in combination with O-rings on both pistons, creates a small space between the viton sleeve and the PEEK holder. This is where the confining fluids (degassed H_2O) are brought to. The axial pressure is given by a small fluid chamber underneath the lower piston. This piston is able to move axially, depending on the applied pressure, and the strength of the sample

above it. The upper piston remains stationary. Calibration tests have shown that the pressure necessary to overcome the lower piston's frictional force is around 5 MPa.

2.3.2.3. Fluid control

Pumps are necessary to enable the inflow of fluids in rock plugs. There are different types of fluid pumps, depending on their application and the function they fulfill in a fluid flow setup. In this section, the different types of pumps used in this work are discussed.

Open source syringe pumps (Wijnen et al., 2014) were constructed for long-term experiments on the effect of acid brines on fractured reservoir rocks (Chapter 6). These syringe pumps were constructed with 3D printed parts, and readily available stepper motors. Syringe pumps like this are also commercially available. However, the cost of open source syringe pumps is in the order of 5% or less than one would pay for a commercial system with similar performance (Wijnen et al., 2014). These pumps need to be calibrated before use and are limited in the volume they deliver to the volume of a single syringe. The syringe pumps are used with polytetrafluoroethylene (PTFE) tubing with an outer diameter of 1/16 inch, or approximately 1.6 mm. Both the type of syringe which is used, and the tubing to deliver the fluids limit the achievable pressure.

A more continuous flow is obtained with the commercial microprocessor-controlled milliGAT® pump by GlobalFIA, USA. Within the pump casing, a rotor is fitted with four pistons. Each of them delivers 25 µL of fluid. Using micro-stepping of the stepper-controlled motor, constant flow rates between 0.004 µL/s and 167 µL/s can be achieved. The inside of the pump can withstand pressure up to 0.69 MPa. This means that the flow line between the pump and the rock sample in a fluid flow setup needs to be limited by a pressure relief valve of 0.69 MPa. For moderate and high permeability samples, this causes no practical problems. However, this pressure limit imposes flow rate limitations in less-permeable

systems. This causes typical experiments with low-permeable rocks to take up quite some time. Nonetheless, the milliGAT® pump was used to control fluid flow through reservoir samples of the Longyearbyen CO_2 Lab, both encased in the PMMA cell and the SINTEF cell.

In order to control the axial and confining pressure in the SINTEF cell, two ReaXus 6010R reciprocating pumps by Teledyne Isco, USA, were used. These pumps are specifically designed to supply a fluid flow under constant pressure. It has an accurate flow rate control up to 10 mL/min and a pressure capability up to 41.4 MPa. This pressure range exceeds the pressures at which the SINTEF cell was tested. The ReaXus 6010R pumps are not to be used with PTFE tubing. Instead, special PEEK tubing was used to handle the high pressures in the fluid flow lines. Currently, at the UGCT, high-pressure experiments with the ReaXus 6010R pumps are limited to a pressure of approximately 31 MPa, linked to the particular tubing which is available. With an in-house developed LabVIEW code, the ReaXus 6010R pumps can be controlled from an external computer, and pressure and flow measurements can be easily obtained.

3.
Reservoir characterization

This chapter discusses the in-depth characterization of the Longyearbyen CO_2 project reservoir sections of the De Geerdalen Formation and the Wilhelmøya Subgroup. To start, a broad overview is given of the geology of Svalbard, after which the targeted reservoir sections are discussed. They were characterized with standard porosity and permeability measurements, as well as with high-resolution X-ray micro-CT. Based on the segmentation of the pore structure of certain core samples, fluid flow simulations were carried out to determine the storage capacity and permeability behavior of the reservoir sections. This chapter is primarily based on Van Stappen et al. (2014), which was published in the *Norwegian Journal of Geology*. Some general sections are based on Mulrooney et al., which is in preparation for the *Norwegian Journal of Geology* and co-authored by the PhD candidate. Results of the multi-scale pore network modelling, discussed in section 3.3.2, are published in Bultreys et al. (2016c), co-authored by the PhD candidate, in the *Journal of Geophysical Research. Solid Earth*.

*Van Stappen et al. (2014): Van Stappen J. was the main author for this publication, who performed the experiments and the analysis and prepared the manuscript. De Kock T. and Boone M.A. were involved in the discussion. Olaussen S. and Cnudde V. were the promotors of the work.

*Mulrooney et al. (in prep): Van Stappen J. was co-author of this publication and provided the section on micro-CT imaging of reservoir sections.

*Bultreys et al. (2016c): Van Stappen J. was co-author of this publication and performed the micro-CT imaging of the Longyearbyen CO_2 project core.

3.1. Geology of Svalbard.

The Svalbard archipelago consists of nine main islands, of which Spitsbergen is the largest. The geological units on Spitsbergen therefore represent most of Svalbard's geological history (Harland et al., 1997). They can be subdivided in five fundamental groups (Steel and Worsley, 1984; Bergh et al., 1997): (1) Pre-Cambrian to Silurian basement; (2) localized Devonian to Carboniferous rift basin fills, dominated by sandstones, shales, carbonates and evaporites; (3) Permian stable marine platform deposits, constituted of carbonates and evaporites; (4) Mesozoic shelf to fluvial deposited sandstones and shales; and (5) Cenozoic foreland basin infills, linked to fold-thrust development, combined with uplift and rifting in the west. Figure 3.1 provides an overview of this broad subdivision of the geological units on Svalbard.

For the local CCS research, the Mesozoic strata are the most important geological units, since they provide the potential reservoir and cap rock sequence. The Cenozoic development of a fold-and-thrust belt in the West of Svalbard caused associated tectonic subsidence in Central Spitsbergen. Here, the Central Spitsbergen Basin was formed, leading to deep burial of Mesozoic rocks and a syn-tectonic sedimentation up to 3 km thick (Helland-Hansen, 2010). Due to this subsidence, the Mesozoic strata are now part of a large synclinal structure, bound above and below by a pair of sub-horizontal detachment zones. The subsidence led to an extensional fault system developing together with the fold-and-thrust belt in the West of Svalbard (Ogata et al., 2014; Roy et al., 2014). The most recent tectonic deformation phase took place in the Pliocene and Pleistocene: Svalbard and the Barents Sea shelf region were subject to uplift, erosion and glacial bound-rebound (Henriksen et al., 2011). It is estimated that a net uplift of the Central Spitsbergen Basin of approximately 3.5 km has occurred (Throndsen, 1982). Before this transtensional tectonic phase, the deposits of the Wilhelmøya Subgroup may have been exposed to temperatures up to 180°C, leading to extensive chemical

compaction which reduced initial porosity and permeability of the rocks (Mørk et al., 1989; Marshall et al., 2015). The Upper Paleozoic to Cenozoic development of Svalbard strongly correlates with that of the Barents Sea shelf area. Here, several oil and gas fields have been discovered, indicating proper reservoir quality (Braathen et al., 2012).

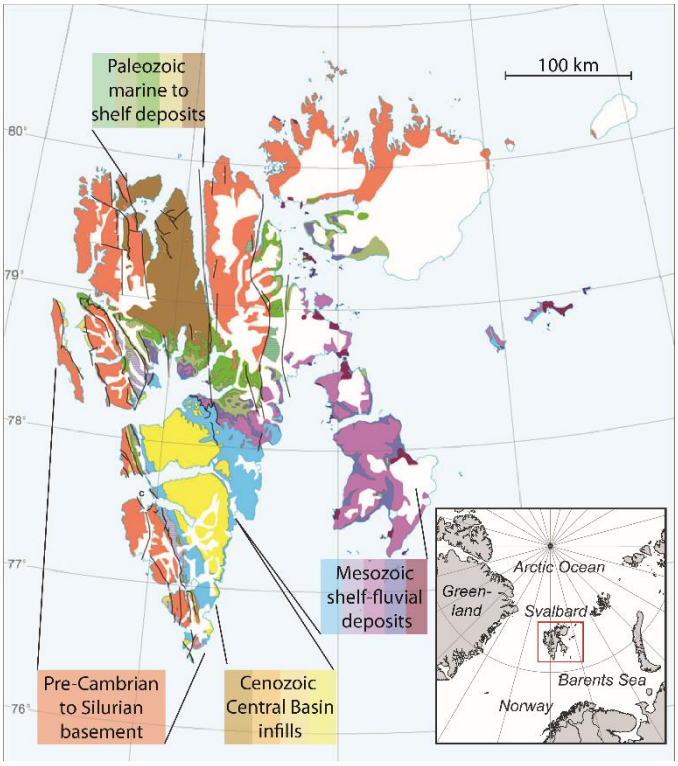

Figure 3.1. Geological map of Svalbard with the indication of the main geological units: the Pre-Cambrian to Silurian basement, the Paleozoic marine and shelf deposits, the Mesozoic shelf to fluvial deposits and the Cenozoic infill of the Central Tertiary basin. Figure modified from (Dallmann, 1999).

3.2. Targeted reservoir sections for CO_2 sequestration

The targeted reservoir units comprise the Late Triassic De Geerdalen Formation and the overlying Late Triassic to Middle Jurassic Wilhelmøya Subgroup. Together they form the Kapp Toscana Group. In the slimhole wells, drilled in the near vicinity of

Longyearbyen, these sections are found at a depth between 672 m to 970 m. The thermal gradient below Longyearbyen is estimated to be between 33°C/km and 40°C/km (Braathen et al., 2012; Senger et al., 2017). In combination with an average ground temperature of 5°C and an estimated permafrost thickness of approximately 160 m, this implies a temperature of about 30°C at a depth of 800 m below Longyearbyen. The reservoir is known to have a significant underpressure: the reservoir pressure is approximately 30% of the hydrostatic pressure, indicating a good sealing cap rock (Braathen et al., 2012; Miri et al., 2014). However, this underpressure affects the physical state of CO_2 injected in the system. While normal pressure conditions (100% of the hydrostatic pressure) would allow gaseous CO_2 to shrink and convert into a liquid condensate at a depth of approximately 800 m, the underpressure of the reservoir implies that the CO_2 remains as a gaseous phase at this depth (Braathen et al., 2012). Mixing of CO_2 with hydrocarbons (which are also naturally present in the targeted reservoir) would, however, change fluid-phase properties, such as density, viscosity and the critical point of the system (Miri et al., 2014).

The rocks of the Kapp Toscana Group crop out in the valleys and shorelines east from Deltaneset (Figure 0.10 shows the geographical and geological map of the location and Figure 3.2 illustrates the different outcrops with pictures). In this work, both drill core samples and outcrop material were studied. Two of the slimhole wells penetrate the De Geerdalen Formation, while 4 wells completely cover the Wilhelmøya Subgroup (Braathen et al., 2012). Drill core samples were obtained from wells DH2 and DH4, where both the De Geerdalen Formation and the entire Wilhelmøya Subgroup are represented. Outcrop samples from the Wilhelmøya Subgroup were taken in Konusdalen and Criocerascalen (Figure 3.2.A and Figure 3.2.B). In these valleys, Paleogene extensional fault systems are exposed (Figure 3.2.A). The De Geerdalen Formation rocks were sampled along the southern shore of Isfjorden (Figure 3.2.C), between Deltaneset and Botneheia (Figure 0.10) approximately 15 km north-east of Longyearbyen.

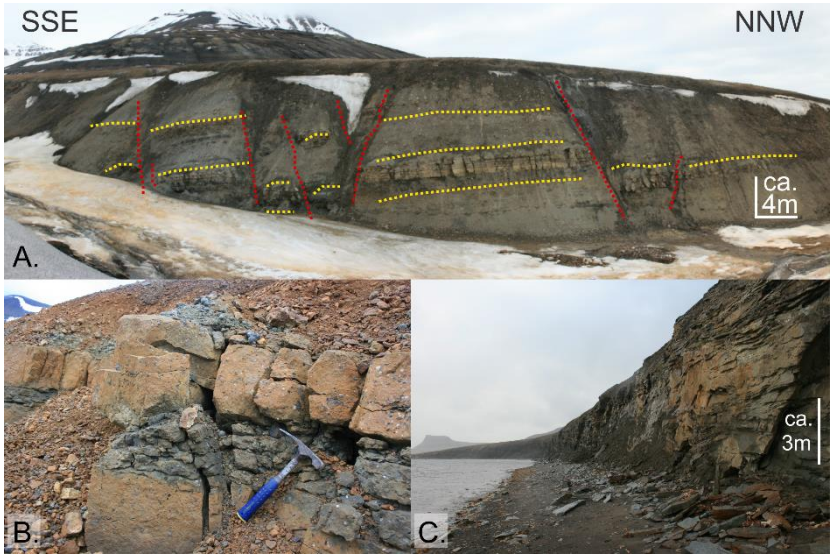

Figure 3.2. Outcropping sections of the Kapp Toscana Group. The reservoir units of the De Geerdalen Formation and the Wilhelmøya Subgroup crop out along the shore between Deltaneset and Botneheia; in Konusdalen and in Criocerasdalen. A. An overview of the outcrop of the Wilhelmøya Subgroup in Konusdalen, with an indication of the different rock layers (in yellow) and the Paleogene extensional fault systems (in red); B. The Brentskardhaugen Bed crops out in Criocerasdalen; C. A view along the shore between Deltaneset and Botneheia, where the De Geerdalen Formation crops out.

From the De Geerdalen Formation and the Wilhelmøya Subgroup, only the sandstone sections are targeted as storage unit (Braathen et al. 2012; Rismyhr et al. in prep.). The aquifer in the Kapp Toscana Group can be subdivided in three compartmentalized zones: an upper zone, comprised of the entire Wilhelmøya Subgroup; a middle zone, formed by the uppermost De Geerdalen Formation; and a lower zone, formed by the lower parts of the De Geerdalen Formation (Senger et al., 2015). Storage resource estimates consider that approximately 65.4% of the injected CO_2 would be stored in the upper De Geerdalen Formation, while for the upper and lower zone, this is 15.2% and 16.9% respectively (Senger et al., 2015). It is believed that a total of 2.5% of the storage potential is contained in the natural fracture network throughout the entire aquifer. The fractures thus provide limited storage potential as

opposed to the rocks' porosity, however, they are considered to be crucial for fluid conductance in the system. They are thus particularly important for the permeability in the reservoir. In the drill cores, the fractures have therefore been mapped and classified: as open fractures, allowing fluid flow through them; as healed fractures (closed by the enveloping stress); or as sealed fractures (filled with secondary minerals) (Braathen et al., 2012). Most of the fractures are regarded as either open or healed fractures, while only few are considered to be sealed fractures (Ogata et al., 2013, 2012). Their role might even increase when considering a reservoir pressure increase due to the injection of CO_2.

3.2.1. The De Geerdalen Formation

The De Geerdalen Formation is a succession of shallow-marine sandstone units, alternating with shales and hard calcareous siltstones. The sandstones are considered to be both texturally and compositionally immature. Two types of sandstones occur: (1) massive, medium-grained and structure-less sandstones which coarsen upwards and (2) upward-fining sandstones with sharp lower contacts in which ripple structures and cross-bedding alternate with parallel bedding. These two types of sandstones correspond to different geological settings, ranging from shallow shelf to deltaic environments (Rød et al., 2014). At Botneheia (Figure 3.2.C.), where this Formation crops out, sandstone units up to 20 m thick are observed. Outcrop samples were obtained from sections along the southern shore of Isfjorden (Figure 3.3.A.). Here, fairly homogeneous sandstone banks crop out, with pyritic and sideritic nodules and clay lenses in distinct layers. Thin section analysis of the obtained samples show that the sandstone section consists of sub-millimetric quartz grains within a calcite- and iron-rich chlorite matrix. This was confirmed through SEM-EDS analysis in order to quantify the distribution of the calcitic matrix as opposed to the quartz grains (Figure 3.3.B. and Figure 3.3.C.). To a

lesser extent, also plagioclase, glauconite, zircons and pyrite grains are present.

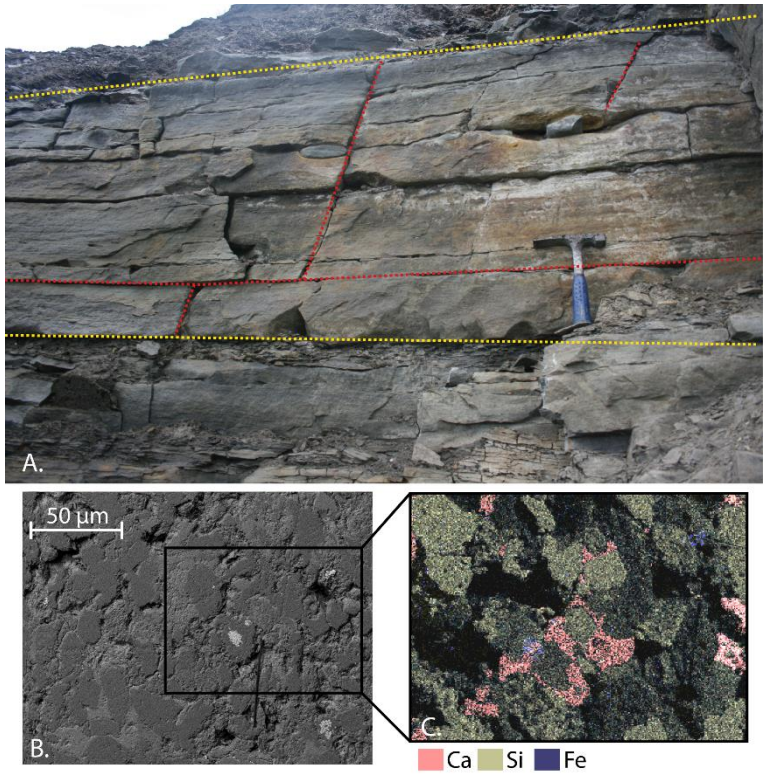

Figure 3.3. A. A closer look to one of the sandstone banks outcropping along the shore of Isfjorden, between Deltaneset and Botneheia. In the outcrop, fractures parallel to bedding are distinguishable, as well as fractures cutting through the bedding. B. SEM image of a sample obtained from these sandstone banks, with the inset C. showing the chemical information obtained from the EDS signal. Besides calcium, silicon and iron, also aluminum, potassium and small amounts of sulfur and titanium were detected.

In the drill cores, the upper part of the De Geerdalen Formation (which can be correlated to the section sampled in outcrop) is represented by bioturbated fine sandstones with horizontal to wavy bedding and widespread pyrite nodules. Similar to the outcrop, the De Geerdalen Formation consists of large, meter-thick sandstone sections, alternated by siltstones in which decimeter-scale sandstone banks are found. The upper sandstone sections of the De Geerdalen Formation are typically coarsening-upwards

sequences, ending in carbonate beds of a few decimeters tick. In one of the drill cores (DH2), residual oil was found in the uppermost sandstone bed of the De Geerdalen Formation.

The sandstone section which was sampled in outcrop has an average open porosity between 9 and 13%. This was determined through the vacuum assisted water saturation technique as recommended in the European Standard for natural stone test methods (UNE-EN 1936, 2006). This section correlates with rocks at a depth between 770 m and 800 m in DH4. In this drill core, similar porosities were measured (Farokhpoor et al., 2010). Standard permeability measurements showed that this section is rather tight, with permeabilities smaller than 0.1 mD.

3.2.2. The Wilhelmøya Subgroup

The Wilhelmøya Subgroup is one of the most investigated units in Svalbard. Recently, the focus of the Longyearbyen CO_2 Lab on the Subgroup has led to the proposition of a new sequence stratigraphic division of it (Rismyhr et al. in prep.). In central Spitsbergen, the Subgroup is highly condensed and shows significant lateral variations (Rismyhr et al. in prep.). In the drill cores, and in outcrop at Konusdalen, the Wilhelmøya Subgroup is represented by the Knorringfjellet Formation. This Formation was deposited in shallow marine environments and is enclosed within two distinct marker horizons: the Slottet Bed at the base and the Brentskardhaugen Bed at the top. The Slottet Bed is a fine- to medium-grained quartzose with phosphatic nodules at the base. The upper part of it is represented by a siderite-cemented sandstone with glauconite (Mørk, 2013). The Brentskardhaugen Bed is composed of conglomerates and calcareous sandstones (Mørk, 2013). In it are polymict pebbles consisting of chert and siderite, phosphate nodules and fossils included in lithic pebbles. This unit is up to 2 m thick and can be identified in the drill cores as a sequence of decimeter-scale clast-supported conglomerates, interbedded with matrix-supported conglomerates. The matrix of the conglomerates is grey to yellowish in color. However, in

outcrop, they weather to a distinctive yellow, orange and rusty red color indicating the presence of iron-bearing minerals. Figure 3.4.A. shows a simplified sedimentological log of the Wilhelmøya Subgroup as found in outcrop at Konusdalen. Next to it, thin section (Figure 3.4.B) and SEM images (Figure 3.4.C-E) are shown to indicate the maturity of the sandstone and conglomerate sections. In Figure 3.4.E a small fracture is present in the pore structure of the SEM image. Originally this fracture was filled with clay minerals. However, these have probably been polished out during the preparation of the thin section.

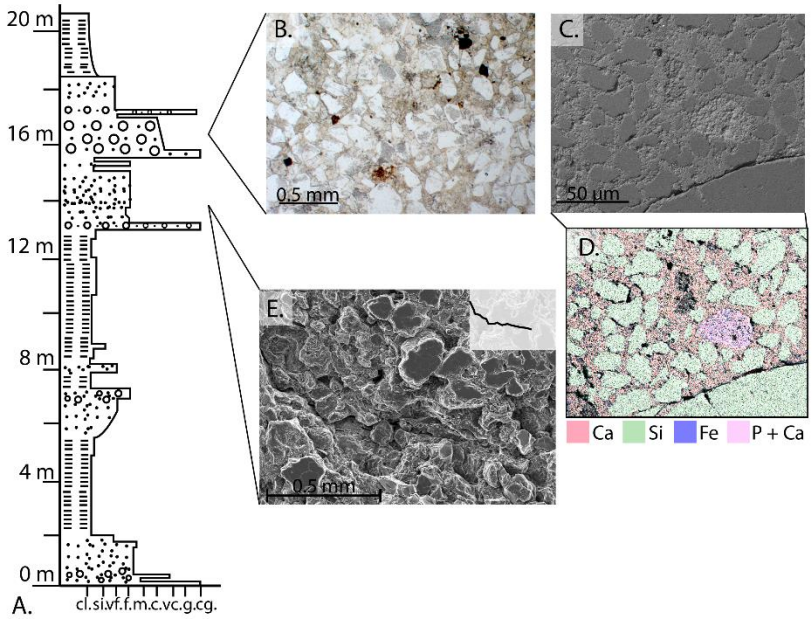

Figure 3.4. A. Simplified sedimentological log of the Wilhelmøya Subgroup as found in outcrop at Konusdalen, based on (Van Stappen et al., 2014) and (Rismyhr et al. in prep.); B. Thin section of the conglomerate matrix of the Brentskardhaugen Bed, mainly composed of sub-rounded quartz grains within a calcitic matrix; C. SEM image of a similar section of the Brentskardhaugen Bed, imaged at higher resolution, with D. representing the chemical composition of this section; E. SEM section of a fine-grained sandstone section within the Wilhelmøya Subgroup with a very narrow fracture from the top left to the middle right.

In Figure 3.5, detailed sedimentological logs of the Wilhelmøya Subgroup are given from the outcrop in Konusdalen and the drill cores DH4 and DH2, as published in Van Stappen et al. (2014).

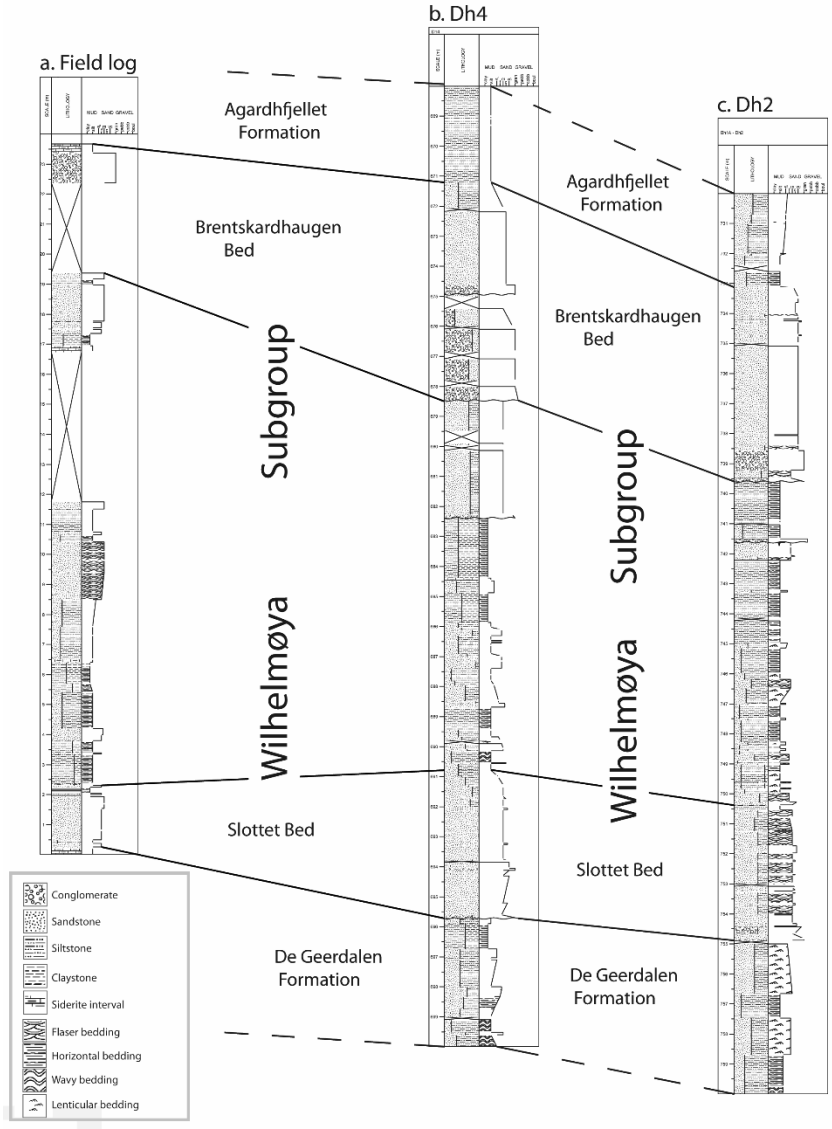

Figure 3.5. Sedimentological logs of the Wilhelmøya Subgroup in outcrop at Konusdalen and within the slimhole cores DH2 and DH4. In DH2, the section from 730 m to 760 m depth is represented, while in DH4, the section from 688 m to 700 m is represented.

The Subgroup can be broadly subdivided in 5 different facies associations, linked to the depositional environments (Rismyhr et al. in prep.). These associations can be recognized in both Figure 3.4.A. and Figure 3.5. However, for clarity, they will be discussed based on Figure 3.4.A.

A first association is the transgressive facies. This is present in the Slottet and Brentskardhaugen Bed (Figure 3.4.A. between 0 – 0.5 m and 16 – 17.5 m). This facies is characterized by conglomerates, immediately overlying erosional surfaces. They have accumulated in open marine environments, as lags formed by strong erosion of the substrate in shallow-water conditions during an overall transgression (Rismyhr et al. in prep.).

A second association is linked to shelf deposits which are highly condensed. This is found as decimeter-scaled deposits of glauconitic muddy sandstones, or microsparitic limestones. In Konusdalen, this occurs as a 30 cm thick sandstone bank right above the Brentskardhaugen Bed (Figure 3.4.A. between 17.5 – 18.5 m). The deposits are cemented with siderite and/or phosphate and limestones can be partly dolomitized. Also chamositic (Fe^{2+} end member of the chlorite group) and sideritic ooids can occur. These deposits are characterized by very low porosities (< 4 %).

A prodelta and distal delta front facies is characterized by interbedded mudstones, siltstones and fine-grained sandstones. These sedimentary layers can have lenticular, wavy and/or flaser lamination going to ripple-structures. This facies is characterized by gradual coarsening upwards (Figure 3.4.A. between 5.5 – 7 m).

One last facies, characterized by sandstone layers, is the shoreface facies. It is characterized by quartz arenites with a quartz or calcite cement. The sandstones can be very fine to medium-grained and are characterized by parallel laminations or (low-angle) cross-stratification. They can also be heavily bioturbated and contain ichnofossils (Figure 3.4.A. between 0.5 – 1 m and 13 – 15.5 m).

The large mudstone and siltstone sections, in which some thin-bedded sandstone layers can occur, are related to an offshore facies. It contains structureless clay- to siltstones with some siderite concretions concentrated in discrete horizons. The small sandstone layers are heavily bioturbated and are characterized by sharp erosional boundaries (Figure 3.4.A. between 1 – 5.5 m and 7 – 13 m). These rock associations are also present in the different drill cores (DH2, DH4, DH5 and DH7), but vary laterally in thickness. Some facies types completely thin out laterally, while others are more clearly represented.

The porosity of the sampled sandstone sections of the Wilhelmøya Subgroup range from as low as 2 % to 17 %. This is the case for both outcrop samples and drill core samples. Permeability of these sections typically does not exceed 1 mD (Van Stappen et al., 2014; Farokhpoor et al., 2011). Table 3.1. summarizes some measurements concerning porosity (determined by water absorption under vacuum) and permeability (determined as steady-state gas permeability by Penterra Geoconsultants B.V., The Netherlands), carried out on drill core samples of DH2 and DH4 (Van Stappen et al., 2014). These measurements are in line with the general porosity and permeability trends within the reservoir (Braathen et al., 2012).

The measurements in Table 3.1. indicate that there can be quite some difference in porosity, depending on the method (H_2O-saturation as opposed to He-porosimetry). This is most obvious in one of the claystone samples, but also occurs in sandstone and conglomerate samples. It indicates the presences of pores which are intruded by He, but not by H_2O. In order to get a better understanding of pore size distribution, MIP measurements were carried out. The MIP measurements could only be carried out on rock plugs with a diameter in the order of 1 cm or smaller, while the cores are typically several centimeters long and approximately 4.5 cm in diameter. Therefore, it is very important to know from which section of the rock a plug is taken.

Table 3.1. Porosity and permeability values of different drill core samples obtained from DH2 and DH4. He-porosimetry and permeability measurements were only conducted for a number of samples. Table extended from (Van Stappen et al., 2014).

Drill core	From (m)	To (m)	lithology	H_2O-ϕ (%)	He-ϕ (%)	Per. (mD)
DH4	-671.92	-672.00	Claystone	1.2	/	/
DH4	-674.48	-674.56	Cemented sandstone	7.1	10.9	0.14
DH4	-677.12	-677.20	Conglomerate	13.0	15.3	0.77
DH4	-677.47	-677.53	Sandstone	16.2	/	/
DH4	-680.94	-681.00	Sandstone	7.5	/	0.07
DH4	-687.10	-687.12	Sandstone	13.9	/	/
DH4	-689.64	-689.70	Siltstone	1.8	/	/
DH4	-691.00	-691.08	Claystone	3.9	7.1	0.03
DH4	-693.96	-694.00	Sandstone	10.7	/	0.54
DH4	-695.22	-695.28	Sandstone	12.6	12.6	0.11
DH4	-736.73	-736.81	Sandstone	1.8	/	/
DH2	-741.67	-741.72	Cemented sandstone	1.1	/	/
DH2	-752.30	-752.38	Sandstone	4.7	/	/
DH2	-671.92	-672.00	Sandstone	1.2	/	/

Figure 3.6 represents the results of MIP measurements on four drill core samples. In these samples, small plugs were sampled in those areas where the highest porosity was expected based on micro-CT images. This slightly biases the actual pore size distribution to larger pores. However, even in these areas nanometer scaled pores are present in all samples. The four samples represent a claystone (at a depth of 736.8 m in DH4), a bioturbated sandstone (at a depth of 671.95 m in DH2), a sandstone with interbedded clay layers (at a depth of 687.11 in DH4) and the conglomerate matrix of the Brentskardhaugen Bed (at a depth of 677.15 m in DH4).

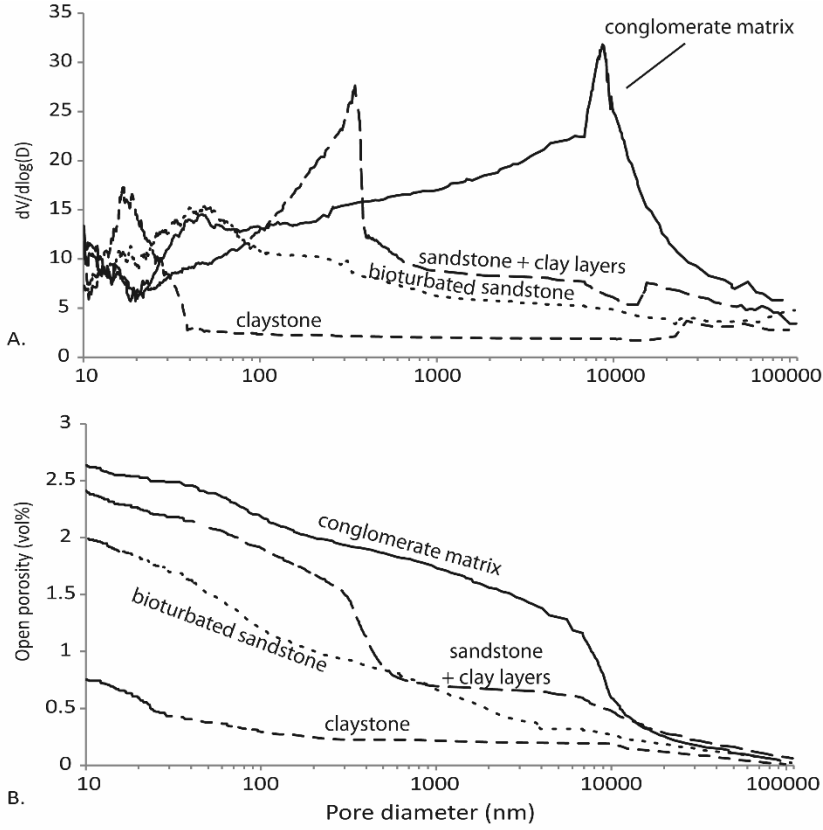

Figure 3.6. MIP data of four drill core samples: a claystone (depth of 736.8 m in DH4), a bioturbated sandstone (depth of 671.95 m in DH2), a sandstone with clayey interbedding (depth of 687.11 m in DH4) and a part of the conglomerate matrix from the Brentskardhaugen Bed (depth of 677.15 m in DH4). A. The pore throat size distribution expressed as the increase in pore volume in relation to the normal logarithm of the diameter; B. The cumulative curve showing the porosity of the sample related to the pore diameter.

Approximately 65% of the total pore volume penetrated by mercury is found in pores with a diameter smaller than 100 nm in the claystone plug. Also in the bioturbated sandstone sample, the main peak is found below 100 nm. However, in this sample, the pore throat distribution is more spread out to higher values as well. This is due to the mix between sand and clay grains within the sample. A similar observation can be made in the sandstone sample which is interbedded with clay layers. In the conglomerate matrix,

the peak of the pore throat distribution is found at a pore throat diameter of approximately 8 µm. However, the average pore diameter in this sample is far below 1 µm. Table 3.2. summarizes the pore characteristics of these samples.

Table 3.2. Overview of the results of MIP measurements on core samples from DH4 and DH2.

Lithology	Average pore throat diameter (nm)	Mean pore throat diameter (nm)	Pore volume smaller than 100 nm (%)	Pore volume smaller than 500 nm (%)	Pore volume smaller than 1 µm (%)
Claystone	26.1	35.1	0.55	0.62	0.63
Bioturbated sandstone	58.2	184.0	0.84	1.20	1.38
Sandstone with interbedded clay	69.6	363.2	0.59	1.63	1.81
Conglomerate matrix	102.6	4198.0	0.52	0.84	0.96

3.3. Micro-CT imaging and modelling.

3.3.1. Fracture characterization.

Micro-CT imaging allowed the identification of the internal structures in decompacted drill core samples and outcrop material from the Longyearbyen CO_2 project reservoir sections. Micro-CT scans were specifically carried out in order to get an initial understanding of the 3D fracture orientation in the samples and the fracture aperture distribution in decompacted reservoir sections. In the outcrops, fracture characterization was possible in 6 samples from within the sandstone sections at Konusdalen, which are part of the Wilhelmøya Subgroup (samples T1 to T5 and sample S3 indicated in Appendix B). Additionally, fractures could be characterized in 5 drill core samples from DH2 and DH4 (sample D2 for DH2 and C1, C3, C4 and C8 for DH4 indicated in Appendix B respectively).

Observations relating fracture occurrence to competence contrasts in sandstone and clay layers (Ogata et al., 2014, 2013) were confirmed at the pore scale level. A comparison between fractures present in field samples and in the drill cores further confirms the model of Ogata et al. (2012), which relates the decompaction, because of unroofing, to rejuvenation of pre-existing fractures. Micro-CT analysis showed a clear difference in fracture length between the outcrop fractures and those in the drill cores. However, the fractures found within these samples, display geometry prone to fracture propagation under the stress of freeze-thaw cycles (Tharp, 1987). Hence, frost wedging can also be considered as a mechanism to explain these differences. Their orientation is predominantly horizontal, although the observed fractures are sometimes interconnected through vertical fractures.

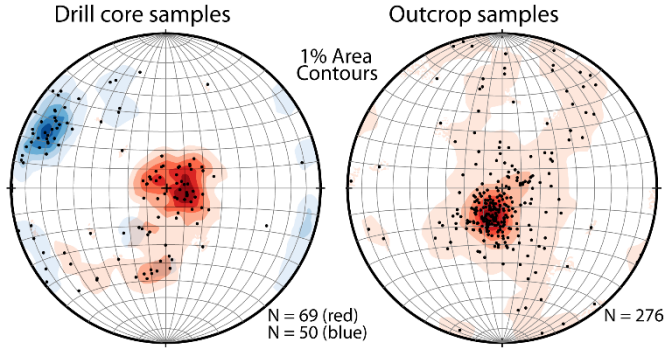

Figure 3.7. The orientation of fractures in drill core samples from DH2 and DH4 and outcrop samples respectively. The poles to the planes of the fractures are plotted so that points in the middle of the stereoplot represent horizontal fractures and points at the sides represent vertical fractures.

Figure 3.7. shows two geological stereoplots indicating fracture orientations obtained from micro-CT images. These orientations correspond to fracture orientations as observed directly in outcrop (Ogata et al., 2014). It must be noted however, that the drill core samples themselves were not oriented. The stereographic projections thus only provide information on the dip of the observed fractures in the micro-CT images, not on the strike of them.

In order to determine fracture apertures in this initial micro-CT study, the fractures were segmented from the overall rock matrix with a fracture filtering tool for micro-CT images (Voorn et al., 2013). Subsequently, the digitally segmented fractures are subdivided in different fracture segments based on a watershed separation algorithm. Each fracture segment was virtually packed with spheres with their central point in the middle of the fracture. The size of these is then increased until they reach the fracture walls (Brabant et al., 2011). The diameter of the sphere at this point is considered as the maximum opening of that individual fracture segment. Because of this approach, the accuracy of the fracture aperture measurements is limited to integral multiples of the image resolution. However, it still gives a certain indication of the aperture distribution within the rocks. This technique was used to quantify fractures in relatively low resolution micro-CT scans (40 – 55 µm). Figure 3.8. summarizes these measurements.

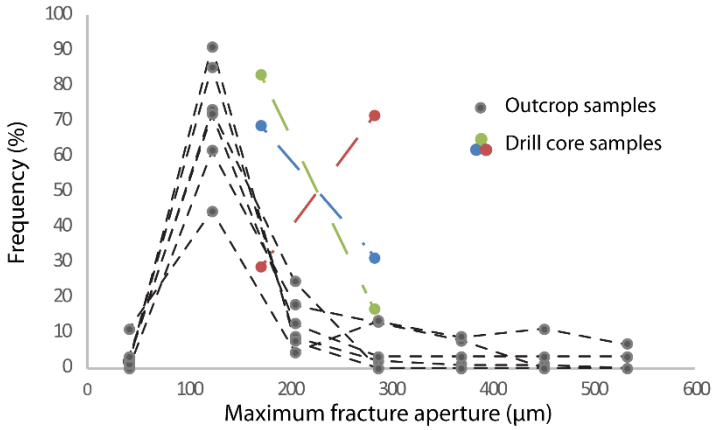

Figure 3.8. Fracture aperture determination of decompacted rock cores in low-resolution micro-CT scans. Apertures were characterized with the maximum inscribed sphere or maximum opening method.

Fracture apertures were found to be similar in outcrop and core samples, with most apertures ranging between 120 and 280 µm. There is a small discrepancy between the absolute values of the measured fracture apertures for field and drill core samples.

However this is immediately linked to way the maximum aperture is calculated (Brabant et al., 2011). In this study only the largest fractures were detected due to the limited resolution of the micro-CT scans of full cores.

3.3.2. High resolution micro-CT and modelling.

High resolution images, in which most of the rock plug's porosity is discernable, allow for pore scale modelling of fluid flow through the pore network. In reservoir studies this can provide additional and highly valued information on the physical properties of the reservoir. This is especially so in studies where rock samples from the subsurface reservoir sections are only sparsely available. In many oil and gas wells, water wells and wells for mineral exploration, only drill cuttings, i.e. small pieces of rock, are available from the actual reservoir or rock layers of interest. Performing multiple lab-based measurements, or fluid flow simulations on these limited rock samples from a reservoir can provide rock physical information which can be applied in an upscaled reservoir model (Dvorkin and Nur, 2009; Andrä et al., 2013).

Typically, fluid flow modelling is carried out with commercial software packages. In this work, the former software package E-core by Lithicon, Norway, was used for fluid flow modelling. Starting from the 3D images, the user typically labels the porosity, after which a skeleton of the pore structure is constructed. In this skeleton, pore throats are represented by cylindrical connections between the pore bodies, which are represented by spheres. As such, a so-called ball-and-stick model is obtained from the pore network.

Two drill core samples from DH4 were subsampled and scanned at a resolution of 2.8 µm. These subsamples had a diameter of 6 mm. They should thus not be taken as representative for the entire drill core samples with a diameter of approximately 4.5 cm, let alone for the entire sandstone section which they are part off. The drill core samples from which these subsamples were taken, were labeled as

C6 and C7 from slimhole well DH4. They are found at a depth of 680.97 m and 677.17 m respectively. The subsamples were subjected to MIP measurements after the high resolution imaging. The results of these measurements are reported in Figure 3.6 and Table 3.2 (the sandstone sample with interbedded clay and the conglomerate matrix respectively).

Although these subsamples do not represent the entire drill core samples, the high resolution images and their analysis allowed the simulation of CO_2 drainage within the pore network, followed by the imbibition of water. The fluid flow simulation of one of these samples is visualized in Figure 3.9. It represents part of the sandstone sample interbedded with clay material which was also subjected to MIP measurements (Figure 3.6). This sandstone has a dominant pore size peak between 100 and 500 nm, which can be associated with secondary porosity in illite clays.

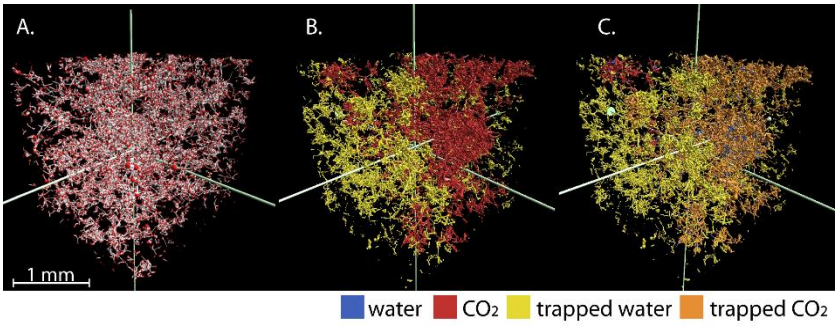

Figure 3.9. A. Pore network, extracted from a micro-CT scan of a sandstone sample from DH4 (at a depth of 680.96 m). This pore network is virtually filled with water, after which a non-wetting phase can be injected; B. The end state of the non-wetting phase drainage, with the distribution of trapped water and CO_2; C. The end state after water flooding. Approximately 50% of the pore network is filled with trapped CO_2.

These kind of simulations allow a virtual measurement of the plug's permeability and capacity to retain a non-wetting phase after waterflooding. In the represented sample, a permeability of 0.43 mD was obtained, while a reference permeability of 0.07 mD was expected. This discrepancy can be explained by the fact that fluid flow simulation was only carried out on part of the micro-CT scan

for computational reasons. The micro-CT scan only represents the plug which was taken as a subsample from the larger core on which the experimental permeability was determined. The plug can thus represent a more porous and permeable part of the larger core. At the end of the waterflooding simulation, approximately 50% of the pore network remained filled with trapped CO_2. This is in line with predictions in literature on similar sandstone sections of the Longyearbyen CO_2 project reservoir (Senger et al., 2015).

In order to get a more accurate representation of the fluid flow properties of the sample, simulations were also carried out with a multiscale pore network model described in Bultreys et al. (2015b). Results of these simulations are published in Bultreys et al. (2016c). As shown in Figure 3.10., this pore network model takes into account unresolved micro-porosity from the micro-CT images and distinguishes it from the macro-pores which are resolved in the images.

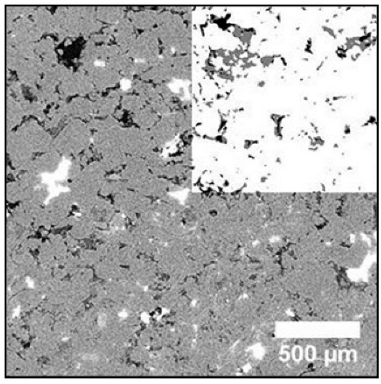

Figure 3.10. Micro-CT data set of the sandstone sample investigated with a multiscale pore-network model by (Bultreys et al., 2015b)*. In the top right corner, the micro-CT slice is overlain with the segmented data set. Solid voxels are displayed in white, microporous voxels in grey and pore voxels in black. Figure from (Bultreys et al., 2016c).*

The macro-pores form a network, similar to the ball-and-stick model described above. However, this representation is obtained through the so-called maximum balls method, developed at Imperial College, London (Dong and Blunt, 2009). It calculates the largest inscribed spheres centered on each pore voxel in the image

that just touches the boundary of the pore space. As such, the macro-scale pore network model is constructed by finding constrictions and dilations in the pore space and classifying them as pore throats and bodies.

The micro-porous zones in the image are assigned certain up-scaled properties for multi-phase fluid flow, such as conductivity and breakthrough pressure for non-wetting fluids, as well as a cut-off length in order to obtain realistic results. Other than in the fluid flow simulations depicted in Figure 3.9., this multi-scale pore network modelling allows the determination of relative permeabilities during multi-phase flow (= permeability depending on the degree of water saturation). Specifically in this sample, clusters of connected macro-pores are small. The flow behavior of this sample is thus strongly dominated by serial coupling of micro-links from the unresolved porosity (Bultreys et al., 2016c). During drainage, the water relative permeability drops down very quickly. This renders both the wetting fluid and the non-wetting fluid immobile over a large range of water saturations. This is similar behavior as observed in experiments (Farokhpoor et al., 2010, 2012), indicating that the pore network model is capable of simulating realistic behavior in very tight samples. The trapping efficiency for non-wetting fluids, based on these multi-scale pore network simulations are similar to trapping estimates from the fluid flow simulation depicted in Figure 3.9. (between 45% and 65%) (Bultreys et al., 2016c).

3.4. Conclusion

The sandstone sections of the De Geerdalen Formation and the Wilhelmøya Subgroup were analyzed with a combination of traditional techniques and high-resolution micro-CT imaging and image-based modelling. It was shown that the tight sandstones, targeted for CO_2 sequestration, are characterized by complex pore structures, ranging from the nanometer scale up to several tens of micrometers for the more permeable sections. None of the techniques allows the complete detection of the entire range of

pore sizes. For reservoir characterization, it is thus of the utmost importance to understand the limitations of the techniques that are used.

Using micro-CT, it was possible to obtain hard data on fracture apertures in decompacted core samples from the Longyearbyen CO_2 project reservoir sections. Fracture apertures in both the outcrop sections and in the core samples of the Wilhelmøya Subgroup range between approximately 40 and 500 µm. The majority of the observed fractures is characterized by apertures between 100 and 300 µm. However, the detection of fractures within these centimeter scaled rock cores is strongly linked to the spatial resolution of the micro-CT images. Through downsampling, the resolution of the images can be increased to a few micrometers. When approximating the fracture aperture through the technique of digitally segmenting the fracture and determining the size of the maximum sphere within them, fractures can be quantified with an aperture of at least three times the resolution of the scan. When the aperture is smaller than this, the segmentation of the fracture typically becomes too difficult and no distinction can be made between the fracture and noise which is inherently present in the images. Micro-CT analysis of the fractures further showed a difference between outcrop fractures and drill core fractures, concerning their propagation length. This can be linked to a model theory linking fracture propagation to decompaction because of unroofing, as well as to crack propagation due to frost wedging. The orientation of the fractures within the cores showed predominant horizontal fractures at boundaries between different lithologies.

In rock samples in which the pore structure is almost completely resolved by the resolution of the micro-CT scan, image-based fluid flow modelling can help in the understanding of non-wetting phase trapping in the pore network. These models are constantly being improved to include more information, such as unresolved micro-pores, in order to refine their ability to accurately predict fluid flow properties. The success of such models is strongly linked to the

ability of resolving all pore throats which connect the larger pore bodies. In the reservoir sections of the Longyearbyen CO_2 project, this limits the use of such models to only the most permeable sections. The added value of such models to the reservoir characterization lies within their ability to provide information based on only small subsections of the reservoirs. This is especially important in projects in which reservoir material is not readily available. In most oil and gas research, mineral exploration and even in ground water studies, actual reservoir material to conduct experiments on, is only sparsely available. Often, only rock cuttings from reservoir drilling are present. These sections of the reservoir are too small, and irregularly shaped to perform fluid flow experiments on. In such a case, high-resolution micro-CT imaging and fluid flow modelling can provide information on the geophysical properties of the reservoir. For upscaling to the field scale, however, tens to hundreds of fluid flow simulations would have to be run to determine one single geophysical parameter for upscaling (for example to determine the permeability or non-wetting phase trapping potential of a sandstone section of a few meters thick) (Dvorkin and Nur, 2009).

4.

Rock mechanical strength

from the core- to the plug-scale

This chapter investigates the influence of sample size on the determination of rock mechanical strength properties. A series of Uniaxial Compressive Strength measurements on four different limestone types was conducted, both on small-scale plugs with a diameter of approximately 10 mm and on standard sized cores with a diameter of 45 – 50 mm. Micro-CT imaging was used in order to explain the failure mode observed in the different rock types. On samples from the Longyearbyen CO_2 project reservoir sections the tensile strength was determined via small-scale Brazilian tests. The results of these measurements were compared to the tensile strength of similar sections reported in literature.

4.1. Introduction

The uniaxial compressive strength (UCS) of a rock material is considered to be the most accurate parameter to determine the rock's mechanical strength. It depends not only on the rock's chemical and mineralogical composition, but also strongly on its porosity, the rock's fabric, and the size and shape of the tested material (Siegesmund & Dürrast 2011). In reservoir applications, the mechanical strength of the reservoir rocks is an important parameter to understand the stability of the reservoir during the drilling and injection phases of a CCS project. The UCS is also used as one of the most important parameters to quantify the quality of natural building materials. Because of its importance in different geological fields, several international standards were developed to determine a rock's UCS. They require the tested material to have certain shapes and minimum dimensions. In reservoir engineering, the volume of obtained drill core samples is often limited. This makes these samples very valuable. Depending on the conducted drilling operations, drill core samples might not meet these minimum dimensions. Table 4.1 summarizes the requirements for three of the most commonly used standards: the European standard for natural stones (UNE-EN 1926 2007), the standard developed by the American Society for Testing and Materials (ASTM) (ASTM C170/C170M-16 2016) and the International Society for Rock Mechanics (ISRM) standard (Bieniawski & Bernede 1979).

Table 4.1. Different standards developed for rocks' mechanical strength testing and their requirements towards samples' shape and dimensions.

International Standard	**Shape of the sample**	**Minimum dimensions**	**L:D ratio**
UNE-EN 1926	Cylindrical or cubic	D = 50 mm or 70 mm	1.0
ASTM C170	Cylindrical	D > 47 mm or 10 x largest grain	2.0 - 2.5
ISRM	Cylindrical	D > 54 mm or 10 x largest grain	2.5 - 3.0

The European standard clearly stands out: it allows the tested samples to be either cylindrical or cubic. It specifies that "Test specimens shall be cubes with (70 ± 5) mm or (50 ± 5) mm edges or right circular cylinders whose diameter and height are equal to (70 ± 5) mm or (50 ± 5) mm" (UNE-EN 1926 2007). This implies the use of an L:D ratio of 1:1, which differs from the ASTM C170 and the ISRM specifications. However, it is known that the shape of the tested material affects the outcome of the UCS measurements (Siegesmund & Dürrast 2011). This is linked to the localization of a high stress and strain region below the load platens due to friction, as illustrated in Figure 4.1 (Thuro et al. 2001). The strain region in the middle of the sample shows the true brittle behavior of the rock sample. The localization of regions of high stresses along the compressive platens can thus be considered as end effect, distorting the measurements.

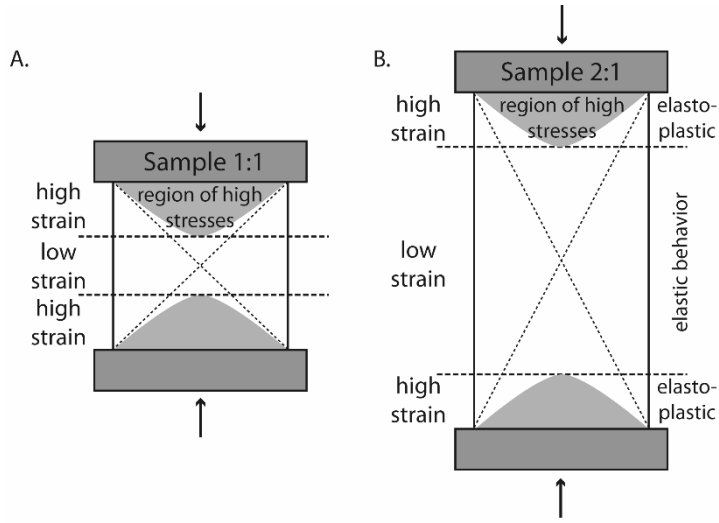

Figure 4.1. Conceptual explanation for the shape effect affecting UCS measurements. A. Stress and strain localization in a sample with L:D ratio of 1:1; B. Stress and strain localization in a sample with L:D ratio of 2:1. Figure modified from (Thuro et al. 2001).

In geotechnical studies, an L:D ratio of at least 2:1 is considered to represent the true UCS of a material. All standards, however, require the samples to have similar minimum dimensions. They also

specify that the diameter, or edge length of the sample, must be at least 10 times larger than the largest grain. In the Longyearbyen CO_2 project reservoir sections, the sandstones are fine- to medium grained. This would mean that sandstone plugs with a diameter of 5 – 7 mm would suffice to comply with the requirement that the tested sample needs to be at least 10 times larger than the largest grain. Of course, this does not include the conglomerate sections, in which clasts are present of several millimeters in diameter.

Previously, experimental investigations have been carried out to scale different sized UCS measurements (Hoek & Brown 1980; Hudson & Harrison 2000; Al-rkaby & Alafandi 2015). Most of these studies focus on samples with dimensions higher than those stated in the governing international standards (> 50 mm). In this chapter, the link of the UCS measured on small scale plugs (± 10 mm in diameter) to the true UCS, measured on standard core samples, is investigated. All tested samples differed in size, but had the same L:D ratio of 2:1. As such, it is investigated whether these measurements on small scale plugs could substitute UCS measurements on standard core samples. The standard core samples had a length and diameter of 89-91 mm and 45-45.6 mm respectively, which deviates slightly from the recommended dimensions in the different international standards. This is due to the specific drill bits which were used. For the small-scale plugs, the length amounted to 17-19 mm, with a diameter of 8-9 mm. Standard core-sized measurements were carried out on an MFL 6000 kN closed-loop compressive testing machine at the Magnel laboratory for concrete research at Ghent University. Plug-sized UCS measurements were carried out in the CT5000-TEC device, developed by Deben, UK. Figure 4.2 shows this device as mounted on the sample stage of HECTOR (Section 2.3.1) (Masschaele et al. 2013). During the experiments, the CT5000-TEC system was controlled with the Deben Microtest software. Because compression with a constant stress rate was not possible, a constant strain rate of 0.1 mm/min was used during the UCS measurements of the small-scale plugs.

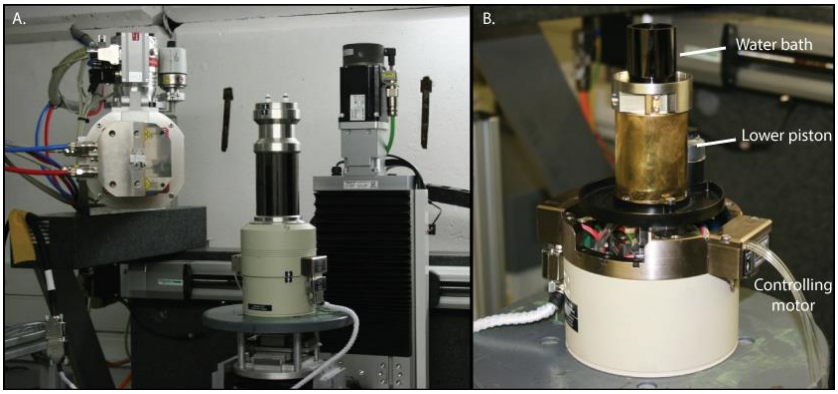

Figure 4.2. The Deben CT5000-TEC device, as mounted on the HECTOR sample stage (A), and a detail of the lower part of the compression cell (B), with a water bath on top, which provides an extra safety barrier in case a rock sample fails very rapidly and individual grains are blasted away.

For eight of the forty investigated plugs, micro-CT scans were taken prior to and after reaching the peak stress during a UCS measurement. Table 4.2 summarizes the scanning parameters for the micro-CT scans carried out during these experiments. As micro-CT scanning allows the visualization of the rocks' microstructure and failure pattern, this will provide vital information to understand the micro-dynamic processes in the rocks under different stress-strain conditions. Additionally, it helps in the identification of discontinuities in the rock fabric along which the sample breaks. This direct observation links the UCS to the mode of failure of the rock.

Table 4.2. Scanning parameters of the experiments conducted with the CT5000-TEC device.

Micro-CT system	Source acc. Voltage (keV)	Output power (W)	# projections	Scan time (min)	Resolution (µm)
HECTOR	140	22	1400	23.3	21.0-23.5

4.2. Theory

Hoek and Brown (1980) stated that a rock's UCS decreases progressively with an increase of its sample diameter. They proposed a formula to convert UCS results, measured on specimens

with different diameters to those which would be obtained on a 50 mm diameter sample:

$$UCS_{50} = \frac{UCS_m}{(50/d)^{0.18}} \qquad (4.1)$$

with UCS_{50} the UCS value of an analogue 50 mm diameter sample, UCS_m the UCS value which was measured on a specimen with d as diameter (mm). Equation 4.1 is based on UCS measurements on crystalline materials, while only one limestone was tested by Hoek & Brown (1980). Since then, a series of empirical relations were proposed to relate the UCS with other physical properties of sedimentary rocks. These have been compiled and discussed by Chang et al. (2006). For limestones, they reported three formulas which relate the UCS to the rocks' porosity:

$$UCS = 276 * (1 - 3ø)^2 \qquad (4.2)$$
$$UCS = 143{,}8\ exp(-6{,}95ø) \qquad (4.3)$$
$$UCS = 135{,}9\ exp(-4{,}85ø) \qquad (4.4)$$

with *UCS* the uniaxial compressive strength of the rock, and ø the sample's total porosity. Equation 4.2 defines an upper bound of the UCS for a given porosity ø and is considered to be only favorable for limestones with moderate porosities (10 % > ø > 20%). Equation 4.3 and 4.4 on the other hand give an estimate of the average rock strength for a given porosity. According to Chang et al. (2006) these equations tend to fit the data quite well for limestones with a low to moderate porosity (< 20 %) and a relatively high UCS (> 30 MPa and > 10 MPa for equation 4.3 and 4.4 respectively).

The European standard postulates the use of an L:D ratio of 1:1 (UNE-EN 1926 2007). However, most other standards suggest the use of a minimum L:D ratio of 2:1. For deviating shapes, the following shape correction equation is proposed by the ASTM (ASTM C170/C170M-16 2016):

$$UCS_{eq} = \frac{UCS_m}{0.778 + 0.222(l/d)^{-1}} \qquad (4.5)$$

with UCS_{eq} the UCS of an equivalent rock with an L:D ratio of 1:1 and UCS_m the UCS value of a rock with a certain *l/d* ratio deviating from 1:1.

In this work, all UCS measurements were converted using equation 4.5 in order to compare the obtained UCS values from small-scale plugs and standard sized rock cores. They are thus corrected for differences in shape, but not for size differences, as it is the intention to check whether UCS measurements on small rock plugs can substitute for standard sized UCS measurements. This results in corrected UCS values representing the mechanical strength for equivalent rock samples with an L:D ratio of 1:1. These values will be referred to as corrected UCS values, or UCS_c.

4.3. Materials

Prior to the testing of reservoir samples of the Longyearbyen CO_2 project, a first study was conducted on four different French building stones: Savonnières, Massangis, Rocheville and Saint-Maximin limestones. The reason of selecting those limestones was because they are all mineralogically rather pure, but they differ from each other structurally in their pore size distribution. This way, different rock types could be tested, characterized by a broad range in porosity. Figure 4.3 shows thin section images of the investigated limestones in which the different pore types are identified and illustrated.

Savonnières limestone (Figure 4.3.A) is a monomineralic oolithic grainstone (Dunham 1962) (Late Jurassic, Tithonian), extracted in Savonnières-en-Perthois, France, from the stratigraphical unit 'Oolithe Vacuolaire'. The pore structure in the rock consists of vacuolar ooids, connected by intra-oolithic micro-porosity to the inter-granular micro- and macro-pores. The stone is further characterized by local layers of (dissolved) shell fragments, which adds to the complexity of the rock's microstructure (Derluyn et al. 2014; Roels et al. 2001). The porosity of Savonnières limestone is known to range from 22 to 41 %. The samples in this study have an

open porosity, determined through the vacuum assisted water absorption method (UNE-EN 1936 2006), between 29 and 35 %.

Massangis limestone (Figure 4.3.B) is an oolithic packstone to grainstone (Dunham 1962) of the 'Oolithe Blanche Formation' (Middle Jurassic, Bathonian), extracted in Massangis, France. Similar to the Savonnières limestone, it consists almost entirely of $CaCO_3$ (up to 98 %). Besides the ooids, which can be up to approximately 1 mm large, bioclasts are presents in the form of crinoids, bryozoans, gastropods and brachiopods. Massangis limestone is typically characterized by a low porosity (13 to 14 %), which is partly inter-granular due to the dissolution of microsparite (micro-pores), and partly moldic, related to dedolomitisation (macro-pores) (Makhloufi et al. 2013). The samples in this study have an open porosity ranging from 13.5 % to 15.6 %.

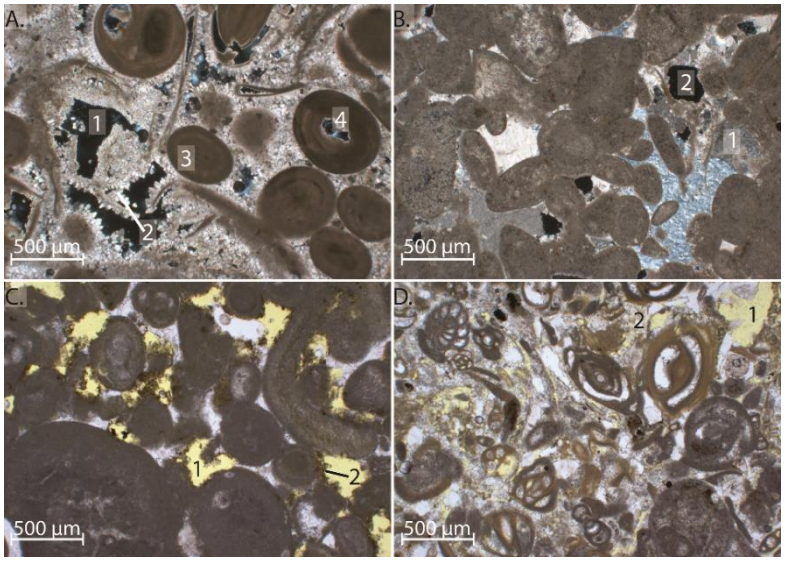

Figure 4.3. Thin section images of the investigated limestones: A. Savonnières limestone, with intergranular macro- (1) and micro-pores (2) and intragranular micro- (3) and macro-pores (dissolved interior of the ooids) (4); B. Massangis limestone with intergranular micro-pores (1), due to dissolution of micro-sparite, and moldic macro-pores (2) due to dedolimitization; C. Rocheville limestone with intergranular macro- (1) and micro-pores (2); D. Saint-Maximin limestone with intergranular macro- (1) and micro-pores (2) and several partly dissolved bioclasts.

Rocheville limestone (Figure 4.3.C) (Middle Jurassic, Bathonian) is an ooilithic packstone to wackestone (Dunham 1962), extracted in Villaines-en-Duesmois, France. The bioclasts which are present are rather large and partly micritized. Their origin is diverse (gastropods, lamellibranches, algae, foraminifera, crinoids,…). Rocheville limestone has a typical porosity ranging from 20 to 25 %, which is intergranular and dominantly related to dedolomitisation. The samples investigated in this work are characterized by open porosities between 17.5 % and 26.9 %.

Saint-Maximin limestone (Figure 4.3.D) is a miliolid limestone from the Calcaire Grossier (Eocene, Lutetian) in the North of the Paris Basin (Fronteau et al. 2010). In this study, the 'Roche Franche Construction' variety was used, which is characterized by a pore structure dominated by the dissolution of bioclasts. It has a typical porosity ranging from 25 to 35 %. The samples reported in this work have an open porosity between 23.5 % and 26.1 %.

4.4. Results

4.4.1. UCS

Figure 4.4 represents the UCS_c measurements both on standard core-sized samples (filled dots, inclined squares, triangles and normal squares) and small-scale plugs (same geometrical shapes, but hollow). For the range of porosities represented by the tested samples (from ± 13 % to 35 %), equations 4.2, 4.3 and 4.4, which relate the UCS_c of limestones to their porosity, are plotted as well. It must be noted that these equations use the total porosity of a rock sample, while the porosities determined on the samples studied in this work are open porosities, based on the water saturation method under vacuum. However, in the studied rock types, the total porosity and open porosity are known to be almost identical. They contain little to no closed pores. Therefore, it is still possible to perform a qualitative evaluation of the proposed equations, based on the studied rock samples.

Figure 4.4 shows that both equation 4.3 and 4.4 follow the natural distribution of the experimental UCS_c values. Equation 4.3 provides an upper limit for most of the measurements, while equation 4.4 tends to fit both standard size and small-scale plug measurements. Fitting equation 4.4 to the experimental data in Matlab allows the designation of an R^2 value to the fit. This describes how well the actual measurements are replicated by the model equation. R^2 values range between 0 and 1, with an R^2 value of 1 equal to a perfect fit. For the standard sized samples, the equation fits the data with an R^2 value of 0.84. For the small-scale plugs, the R^2-value of the fit is 0.81. Especially Savonnières samples fit the equation very well, while Massangis and Saint-Maximin samples have a larger spread in their UCS_c.

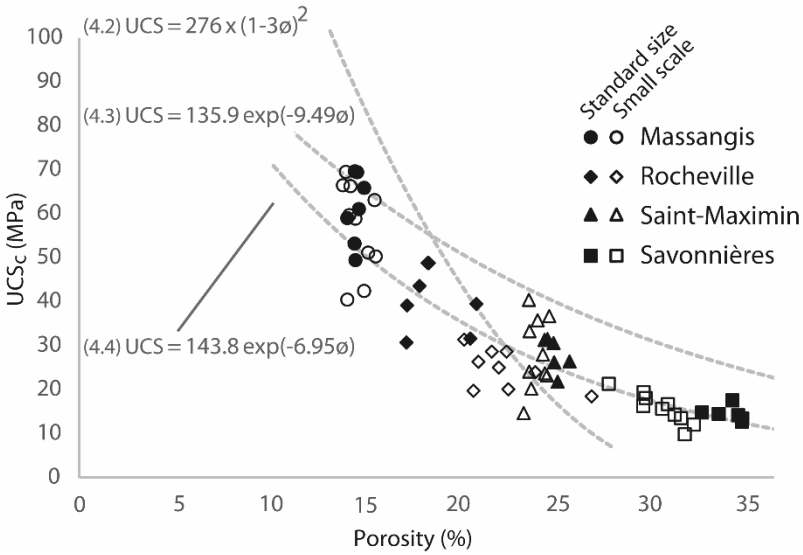

Figure 4.4. UCS_c (MPa) of limestones as a function of their porosity (%). The UCS_c measurements of the Massangis, Rocheville, Saint-Maximin and Savonnières limestones are represented by circles, tilted squares, triangles and squares respectively. These measurements were carried out on cylindrical samples with a diameter of approximately 450 mm (filled symbols) and 8-9 mm (hollow symbols) for standard core-sized samples and small-scale plugs respectively. All samples had an L:D ratio of roughly 2:1. Literature trend lines (4.2, 4.3 and 4.4) are represented by dotted lines.

Despite this spread, the core- and plug-sized samples thus give very similar results, which can be approached by equations described in literature (Chang et al. 2006). This seems to contradict observations by Hoek & Brown (1980) on which equation 4.1 was based, which states that with decreasing sample size the rock's strength increases progressively. However, this equation was based on UCS measurements, mostly conducted on crystalline rocks. Since then many researchers have studied the so-called size effect of UCS measurements on sedimentary rocks. Most studies confirmed the decrease of strength when the tested sample's diameter increased above 50 mm (Al-rkaby & Alafandi 2015; Hawkins 1998; Bieniawski & Bernede 1979). There are several theories explaining this size effect, which often include local zones of weakness along which fractures are induced.

With an increase in bulk volume, the probability that areas of weakness are present within the sample increases so that the strength decreases (Paterson & Wong 2005). Hawkins (1998), however, discussed one of the few studies which includes sedimentary samples with a diameter smaller than 50 mm. In this study a decrease of strength with decreasing sample diameter below 50 mm was observed. For these small-scale plug experiments, as reported in this study as well, the size effect of the measurements is thus not as straightforward. To understand the failure of the material, one has to identify the potential structures of weakness in the sample. Typically, these are pre-existing micro-cracks, or alignments of weak minerals. Along these structures, micro-cracks develop, which align right before the failure of the sample (Lockner 1993; Eberhardt et al. 1999). To understand how such areas of weakness affect the failure of the tested plugs, micro-CT scans were taken before and after failure. Dynamic imaging on EMCT, with a temporal resolution of 12 seconds/scan and a spatial resolution of 35 µm, has shown to be insufficient to visualize the formation of micro-cracks prior to the rocks' failure. Besides this, the failure of the rock plugs is an event which occurs in a fraction of a second. Therefore, it was chosen to only show the results of the

micro-CT images taken before and after the failure. This ensured higher quality images, with a higher spatial resolution.

4.4.2. Micro-CT observations

Szwedzicki and Shamu (1999) investigated the effect of discontinuities on the strength and failure of rock samples. Prior to subjecting a rock sample to a UCS test, they detected microscopic flaws, such as micro-cracks or the presence of bedding planes, at the surface of rock samples with a fluorescent dye and optical microscopy. As such, the failure of the sample could be linked to pre-existing discontinuities in the rock sample. Four different failure modes were detected: simple shear, multiple shear, multiple fracture and vertical splitting. Figure 4.5 illustrates these different types of failure with a schematic representation of them.

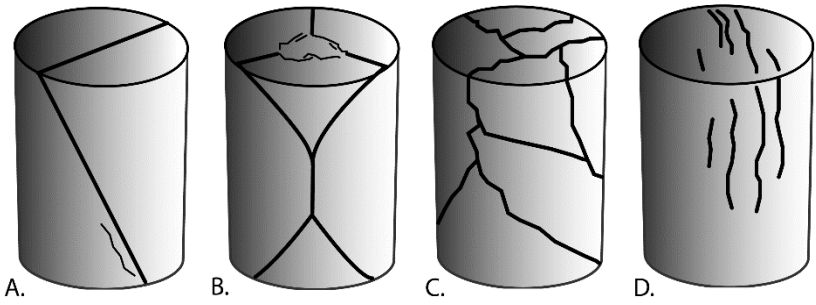

Figure 4.5. Failure modes in UCS tests: A. simple shear; B. multiple shear; C. multiple fracture and D. vertical splitting. Figure modified from (Szwedzicki & Shamu 1999).

Simple shear is the failure of a sample along one or more planes (parallel to each other) at an oblique angle to the direction of maximum compression. Multiple shear is the failure along two or more planes oblique to the direction of maximum compression, but not parallel to each other (Szwedzicki & Shamu 1999). When a rock sample disintegrates along many planes in random directions, the failure occurs in the multiple fracture mode. When the fractures propagate parallel to the direction of maximum compression, failure of the sample occurs through vertical splitting. It was observed that the location, orientation and size of areas of weakness influence the failure mode of a sample (Szwedzicki &

Shamu 1999). When such an area of weakness is located at the end sections of a sample, the sample will fail in simple shear or multiple shear mode, while samples with discontinuities in the middle of them tend to fail via multiple fracturing. Shear is linked to an oblique orientation of the discontinuities to the direction of the main load, while vertical splitting is linked to discontinuities parallel to the loading direction. The larger the zones of weakness in comparison with the sample, the higher the chance that the fracture will propagate through them.

Of each rock type, two samples were selected for micro-CT imaging. It allowed the observation of the failure mode of the different rock types. Figure 4.6 illustrates the observations on a Savonnières plug, with an initial open porosity of 29.7 %. It shows a vertical slice through the sample prior to failure (Figure 4.6.A) and after failure (Figure 4.6.B). The resolution of the micro-CT images (23.4 µm) was too limited to resolve the connections between individual macro-pores in the micro-CT scan taken prior to failure of the plug. After failure, a fracture is formed, which connects these individual macro-pores. It was possible to threshold the complete fracture, together with the original pores cut through by the fracture (Figure 4.6.C). A digital object separation step, based on the watershed separation algorithm, allowed the separation of the fracture in different smaller subsections. Of each of these subsections, the orientation within the micro-CT scan could be determined. These orientations were plotted in a stereographical projection in Figure 4.6.C as a heat map of the poles to the fracture planes. This data was filtered for the most oblique fracture segments, showing the presence of three separate fracture sets in this particular plug.

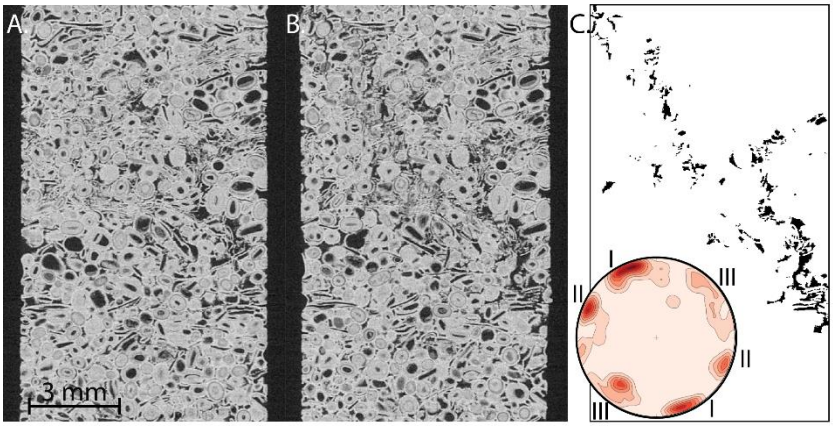

Figure 4.6. A. Savonnières sample prior to failure; B. same sample after failure, with a fracture from top left to middle right; C. pores affected by the fracture (in black) and the orientation of the fracture as poles to the fracture planes, depicted in a stereoplot.

In both investigated Savonnières plugs, the fracture formation was linked to the presence of local layers of dissolved shell fragments in between the ooids. These act as weak structures and allow the fracture to propagate along them. In both plugs, these layers were only present in the upper half of the fracture. According to Szwedzicki & Shamu (1999), the samples would thus fail in simple or multiple shear mode, which was confirmed through the micro-CT observations. However, the fracture did not form from top to bottom of the plug, but ended in the lowest shell layer.

Similar observations were made in the other limestones. Table 4.3 summarizes the observation in the micro-CT investigated samples. As mentioned, in the Savonnières plugs, the weak zones are formed by layers of dissolved shell. Also in the Saint-Maximin plugs, fractures propagate along weak structures, made by the dissolution of bioclasts, or the presence of an elongated weak bioclasts. Depending on the orientation of these structures, the sample fails in a different failure mode.

Table 4.3. Micro-CT visualization allowed the determination of the limestone plugs' failure mode, which could be linked to the presence of weak areas within the plugs.

Lithology	#	Open porosity (%)	UCS_c (MPa)	Failure mode	Weak zone constituents
Savonnières	A	30.9	16.6	Single shear	(Dissolved) shell layers
	B	29.7	16.3	Multiple shear	(Dissolved) shell layers
Rocheville	A	20.7	19.7	Single shear	*Oblique (botryoidal) calcite grains, acting as strong structures
	B	26.9	18.4	Vertical splitting	*Vertical (botryoidal) calcite grains acting as strong structures
St-Maximin	A	24.0	35.7	Single shear	Dissolved bioclasts
	B	23.4	14.6	Vertical splitting	Vertically elongated (dissolved) bioclasts
Massangis	A	13.9	66.4	Multiple shear	Botryoidal grains acting as strong structures
	B	14.2	59.6	Multiple shear	Botryoidal grains acting as strong structures

*Fractures tend to cut around these grains, which can be up to 4mm long

In Rocheville and Massangis samples, fracture propagation is rather influenced by strong structures than by weak structures. In these plugs, the fracture propagates around large, elongated calcite grains. Some of these grains are related to fossils (bivalve shell fragments), while others represent botryoidal grains. On the micro-CT images, these concretions of calcite do not seem to contain micro-pores, as opposed to the ooids within the matrix in which they are embedded. This makes that this matrix behaves as weak zone and the fractures tend to form around the larger grains. This is most obvious in the Rocheville limestone in which the large concretions are more abundantly present than in the Massangis plugs. However, also here, these grains are clearly elongated and measure up to 3.5 mm in length. It must be noted that these

structures might affect the UCS_c measurements of the plugs. As stated by all standards in Table 4.1, the strength must be measured on samples with a diameter which is at least 10 times the largest grain within the sample. This might explain the rather large spread in UCS_c measurements on the Rocheville and particularly Massangis plugs as shown in Figure 4.4. In Saint-Maximin limestone, the weak structures are micro-porous, or dissolved bioclasts. Also these are rather large, up to several millimeters. This might explain the large spread in UCS_c values of Saint-Maximin limestone samples, especially in the small-scale plugs.

4.5. Strength of Svalbard reservoir samples

The measurements on limestone plugs have shown that it is possible to obtain meaningful UCS_c data on rock samples with a diameter smaller than required by the governing international standards. The storage units under investigation in the Longyearbyen CO_2 project, however, are sandstones which are known to have a very high strength (Bohloli et al. 2014). The limited amount of UCS measurements performed on standard sized cores range from 75 MPa up to 142 MPa for the Wilhelmøya Subgroup and the De Geerdalen Formation sandstone sections. Because the CT5000-TEC system is limited to a maximum load of 5000 N (stress = load/area), these high-strength materials could only reach their peak stress when plugs with a diameter of 4.5 mm or much lower would be tested. However, this is considered to be undesirable, especially in the sections in which grains can be up to 0.5 mm long, or bigger. One could use a uniaxial compressive system which is capable of applying higher loads. However, such systems are often not constructed to be used on small-scale rock plugs.

The CT5000-TEC system could however be used to subject reservoir samples to Brazilian tests, measuring the uniaxial tensile strength of a rock plug in an indirect manner. In such a test the cylindrical rock plug is subjected to loading across its diameter. This induces tensile stresses inside the rock plug so that the sample fails in

tension. The tensile strength σ_t of a tested plug can then be determined as stated in equation 1.11 (Section 1.4.2. Tensile strength), by relating the applied load at failure to the dimensions of the tested plug.

In reservoir engineering, the tensile strength of rock samples can be used to determine the pressure at which a rock will fracture at depth (Bohloli et al. 2014). Just like UCS measurements, the Brazilian test typically requires the tested samples to have certain minimum dimensions (D > 50 mm and L:D ratio of 2.0 or higher). The tensile strength of standard size cores lies between 2.4 and 8.8 MPa for sandstones from the Wilhelmøya Subgroup and between 9.8 and 11.6 MPa for the De Geerdalen sandstone sections (Bohloli et al. 2014). It should be noted that the orientation of the core affects the results of the Brazilian test: the horizontal tensile strength can be up to 1.8 times lower than the vertical tensile strength (Bohloli et al. 2014; Ogata et al. 2012). However, this is mostly related to sub horizontal layering in the tested material. In this work, tensile strengths were obtained in samples in which vertical fractures had to be induced for fluid flow experiments. The limited amount of measurements on samples from the Brentskardhaugen Bed and the sampled De Geerdalen Formation sections are summarized in Table 4.4.

The obtained values are slightly higher than the expected values, based on standard core tests described in literature (Ogata et al. 2012; Bohloli et al. 2014). Although it is difficult to draw conclusions from a very limited amount of experiments, both in this work and reported in literature, a size effect for tensile strength is known to inflict higher strengths in smaller scale experiments (Rocco et al. 1999).

Table 4.4. Summary of Brazilian tests on Brentskardhaugen conglomerates (both iron-rich and iron-poor) and sandstone samples from the De Geerdalen Formation.

Lithology	Open porosity (%)	Diameter (mm)	Length (mm)	σ_t (MPa)
Brentskardhaugen (Fe+) conglomerate	4.4	9.9	22.1	7.9
Brentskardhaugen (Fe+) conglomerate	4.0	10.0	17.9	15.8
Brentskardhaugen (Fe-) conglomerate	8.0	9.9	22.2	12.7
Brentskardhaugen (Fe-) conglomerate	8.0	9.9	22.0	12.3
De Geerdalen Fm. sandstone	10.1	9.9	20.4	10.5
De Geerdalen Fm. sandstone	10.1	9.9	21.8	9.3

In the experiments, the tensile strength seems to decrease with increasing porosity. One of the Brentskardhaugen conglomerates, however, seems to contradict this. However, in these samples, it was attempted to obtain plugs particularly from the conglomerate matrix. This was possible in both iron-poor samples, and in one of the iron-rich samples (σ_t of 15.8 MPa). However, in the first sample reported in Table 4.4 several clasts were still present with a size of several mm long. This might have had a negative effect on the tensile strength measurement. For a quantitative description of the validity of these small-scale plug measurements, a larger study would be necessary in which a large amount of standard sized reservoir samples is compared to small-scale plug measurements.

4.6. Conclusion

The CT5000-TEC device has shown to produce reliable UCS measurements on small-scale plugs. This is highly valuable in studies in which sample material is sparse, expensive and/or difficult to obtain. The combination of the actual strength measurements with micro-CT imaging prior to and after rock mechanical testing further allows a qualitative check through the

identification of failure patterns. The limestone types which were tested in this work are commonly used as building material and in cultural heritage. In such studies sampling of long cores with a large diameter can be problematic. It is not favorable to drill such large samples from buildings or monuments. Small-scale plug measurements can then offer a solution. For reservoir studies, it is known that obtaining drill core samples is a time-consuming and expensive task. Drill core samples are therefore both sparse and very valuable. In the specific case of the Longyearbyen CO_2 lab, the maximum load of the CT5000-TEC was too limited in order to perform UCS tests on the reservoir samples. However, it was possible to determine the tensile strength of parts of the reservoir section through small-scale Brazilian tests. The results of these tensile strength tests are found within the range of expected strengths reported in literature. However, a larger study would be necessary in order to determine the validity of small-scale plug measurements for tensile strength determination. It should include more experiments, both on standard sized samples and small-scale plugs of different lithologies. It should also be noted that the experiments described in this chapter were conducted in agreement with the international standards. Hence, the strength measurements were conducted after the samples had been dried to constant temperature. In reservoir engineering, geological formations at depths are typically fully saturated with the formation brine. This is known to lower the strength of the material. If small-scale tests would be performed to understand the behavior at depth, one should thus deviate from the conditions set out by the governing international standards.

5.
Rock fractures at depth

This chapter discusses the influence of rock fractures on the fluid flow behavior at reservoir conditions. A series of experimental fluid flow measurements were conducted on small rock plugs with a natural fracture, an induced fracture and without fracture. Using a small-scale in-situ triaxial device, these plugs are brought to reservoir pressures. The whole setup was specifically designed to allow for micro-CT imaging during the course of the experiments. As such, the evolution of the fracture's aperture distribution could be followed at different confining pressures. Based on the segmentation of the fracture from the micro-CT images, fluid flow simulations were carried out to determine the fluid flow behavior inside the fracture specifically. This chapter is based on a manuscript (Van Stappen et al.)* which is currently in preparation for re-submission to *Environmental Science and Technology*.

*Van Stappen et al. (in prep.): Van Stappen J. is the main author for this publication, who performed the experiments and the analysis and prepared the manuscript. Meftah R. and Blykers B. provided practical assistance in the experiments. All co-authors were involved in the discussion.

5.1. Abstract

Using the in-situ triaxial device of SINTEF, Norway, rock plugs with a diameter of 5 mm and a height of 14 mm can be brought to reservoir pressures (confining pressure > 8 MPa and pore pressure of approximately 3.5 MPa) and temperatures while controlling fluid flow through the rock plug itself (Figure 5.1). In the described experiments, no external temperature control was applied because the controlled ambient temperature in the scanner room is similar to the actual reservoir temperature of approximately 30°C at 800 m depth (Braathen et al., 2012) (section 3.2).

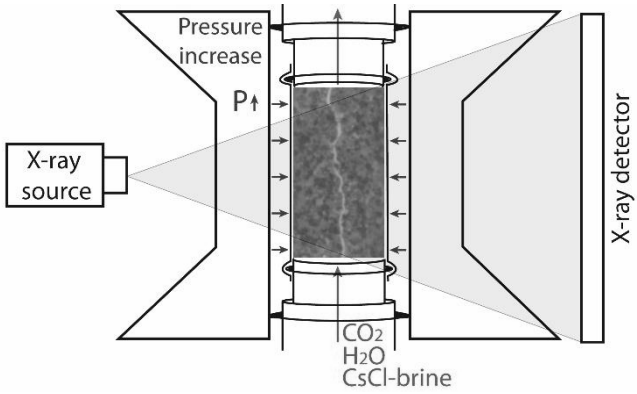

Figure 5.1. Conceptual drawing of the in-situ triaxial device, combined with X-ray CT imaging.

Experiments were conducted with rock plugs from the De Geerdalen Formation in order to understand the influence of fracture closure on the fluid flow behavior inside the pore system (= fracture + matrix porosity) in rock plugs subjected to increasing confining pressures. Micro-CT images were obtained with a spatial resolution of 11 µm, allowing the quantification of the aperture distribution in micrometer-sized fractures. Simultaneously, permeability measurements were conducted, which were complemented with permeability simulations based on the fracture segmentation from the obtained micro-CT images. As such, the relationship between fracture permeability and the imposed confining pressure could be determined and directly linked to the

measured fracture apertures. It was shown that in fractured plugs, the permeability of the fracture decreases exponentially with increasing confining pressure. The tested rock plugs also showed a strong dependency on the fractures for their permeability: even micrometer scaled fractures were shown to increase the permeability in these rock plugs to approximately 5 times the permeability of a non-fractured plug at depth.

5.2. Experimental setup

The setup of the triaxial device on EMCT, with the controlling fluid flow lines, is schematically represented in Figure 5.2. In order to control the confining and axial pressure on the sample, as well as fluid flow through it, an intricate fluid flow setup was built. It allows a controlled fluid flow through the tested rock plug, while the pressure difference between inflow and outflow is monitored. Using Darcy's law (section 1.3.1) the permeability of the sample can then be determined at different confining and axial pressure conditions. The setup consists of a fluid feed line from an open fluid container (a) to the milliGAT® constant flow pump (c). In between, a bubble trap is placed to ensure single phase flow during the experiment. Behind the milliGAT® pump, the fluid flow line starts with a pressure relief valve (d) limiting the pressure to 0.69 MPa, which is the upper pressure for the milliGAT® pump. The flow line passes a fluid switch (f), which allows the user to change between CO_2 injection (g) and the flow of the liquids from the open liquid container (a). The flow line then passes an Arduino controlled pressure sensor (h), after which it goes to the bottom part of the sample in the triaxial cell (i) and exits on top in an open fluid drain (e). The sample itself is contained in a viton sleeve, which fits over the two pistons below and above the sample. In combination with an hourglass-shaped PEEK part (i), the confining chamber is formed. A small chamber below the lower piston delivers the axial pressure on the sample. Two ReaXus 6010R constant pressure pumps (j), from Teledyne Isco, deliver the pressurized liquids to these chambers. H_2O was degassed in a vacuum chamber for 12 hours

prior to the use in the ReaXus pumps. This was done in order to avoid out-gassing of the pressurized liquids during the experiment, as well as possible cavitation due to the formation of vapor bubbles.

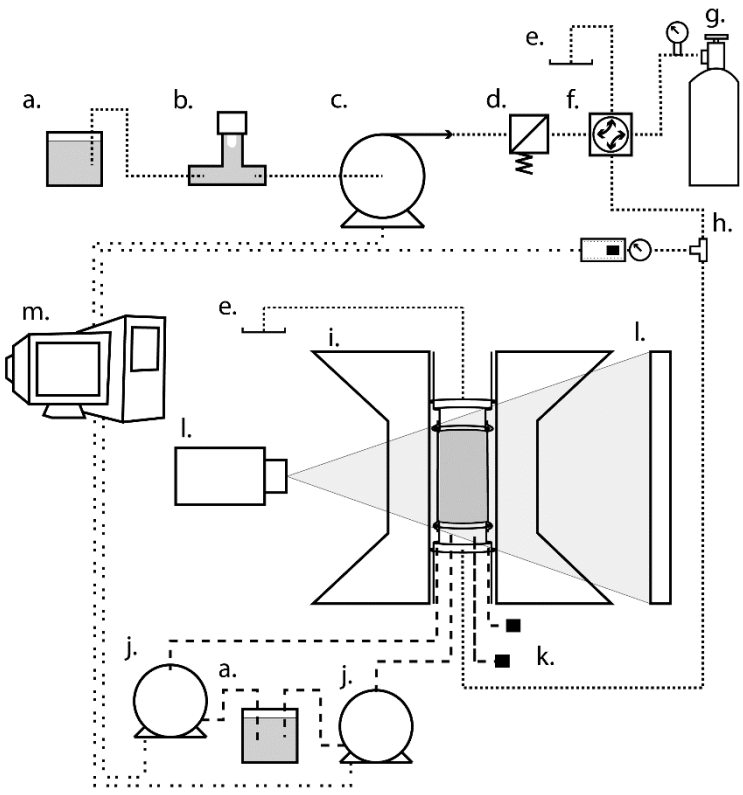

Figure 5.2. Schematic representation of the experimental setup with: a. open fluid container; b. bubble trap; c. milliGAT® pump, delivering fluids at a constant flow rate to the sample; d. pressure relief valve with an upper limit of 0.7 MPa; e. fluid drain; f. fluid switch; g. pressure controlled CO_2 gas; h. Arduino controlled pressure sensor; i. sample, within an FEP and viton™ sleeve, in between an upper and lower piston and surrounded by the confining fluids contained within a PEEK vessel; j. two constant pressure ReaXus 6010R pumps; k. closed end of the confining and axial fluid chambers; l. X-ray source and detector of the EMCT; m. controlling work station.

5.3. Experimental approach

Three rock plugs (with a diameter of 5 mm and a length of 14 mm) from the De Geerdalen Formation were brought to confining pressure conditions up to 15 MPa. The axial pressure was kept at approximately 5 MPa, which is the pressure necessary to overcome

the friction of the lower piston delivering axial load on the sample. The sandstone section out of which the three plugs were drilled comes from the outcrop along the southern shore of Isfjorden, discussed in Chapter 3. This section can be linked to the sandstone section found at a depth between 770 and 800 meters below Longyearbyen in DH4. Here, an average open porosity of 11 % and permeability of 0.5 mD was measured in previous studies (Farokhpoor et al., 2014). The samples from the outcrop material consists of sub-rounded quartz grains within a carbonate-cemented matrix. To a lesser extent, also clay minerals, plagioclase and pyrite are present. One of the three rock plugs contained a natural micro-fracture. The plug was prepared in such a way that the fracture was orientated parallel to the drilling direction. This plug will be referred to as *nf*-plug for "natural fracture". It has an open porosity of 11.9%. Like the other porosities reported here, this was determined using the vacuum-assisted water saturation method (UNE-EN 1936, 2006). The two other plugs did not contain any fractures visible to the naked eye, or with help of a high-resolution micro-CT scan (resolution of 5 µm). One of these plugs was tested as such, in order to determine the matrix permeability of the samples at different confining pressures. This plug will be further referred to as *int*-plug for "intact". It had an open porosity of 12.2%. The third plug was subjected to a small-scale Brazilian test with the CT5000-TEC device (Li and Wong, 2013). As such, a fracture parallel to the long axis of the plug was induced. Prior to the Brazilian test, the plug had an open porosity of 12.8%. This sample will further be referred to as *if*-plug for "induced fracture".

The aim of the experiments was the determination of matrix (via the int-plug) and (induced) fracture permeability (via the if- and nf-plug) at different confining pressures. The micro-CT scans further allow the characterization of local fracture apertures and fluid flow simulations based on the fracture segmentation. Table 5.1 summarizes the scanning parameters for the micro-CT scans conducted in these experiments.

Table 5.1. Scanning parameters of the experiments conducted with the SINTEF triaxial device.

Micro-CT system	Source acc. Voltage (keV)	Output power (W)	# projections per scan	Scan time (min)	Resolution (µm)
EMCT	90	8	1440	15	11.3 -11.6

On the int-plug, the permeability was measured in function of the applied confining pressure, using confining pressures of 1 MPa, 2 MPa, 4 MPa and 5 MPa. At higher confining pressure, it was impossible to experimentally measure the permeability due to the injection pressure limit (0.69 MPa) and flow rate limitation (min 0.004 µL/s) in the setup. The permeability at the different confining pressures was determined by adjusting the flow rate of H_2O through the plug so that a constant pressure drop across the plug was established (0.5 MPa). With the Darcy equation (equation 1.3), the permeability could then be determined.

The experimental approach for the if-plug and the nf-plug is a bit more complex. Figure 5.3. A and B schematically represents the approach for the if-plug and the nf-plug respectively. The if-plug was subjected to a stepwise increase in confining pressure up to 13.3 MPa. At different confining pressures (1.3 MPa, 2 MPa, 4 MPa, 6 MPa, 8.2 MPa, 10 MPa and 13.3 MPa), the permeability was determined twice, once with H_2O and a second time with a cesium chloride (CsCl) solution of 450 kppm. This brine is chosen as a substitute for the formation water in the reservoir (Kwak et al., 2005), and acts as contrast agent for micro-CT scans. In spite of its salinity, the brine is known to have a similar dynamic viscosity as H_2O (Kwak et al., 2005). A maximum flow rate of 0.2 µL/s was used in order to ensure a pressure drop across the plug of approximately 0.5 MPa. At each of the investigated confining pressures, a micro-CT scan was taken in which the if-plug was fully saturated with the CsCl-brine, and one in which the induced fracture was drained with the injection of CO_2 (g). In this step, care was taken that only the fracture inside the rock was drained, and not the rock matrix: the drainage process was monitored with real-time radiographic

imaging. At the moment that the fracture was fully drained, the injection of CO_2 was stopped and a new micro-CT scan was started. This allows differential images to be constructed so that the fracture could be easily segmented from these images.

CO_2 was used to drain the fracture, which could lead to the dissolution of CO_2 within the pore fluids present in the rock matrix, a local decrease in pH and subsequent dissolution of carbonates in the rock plug. However, it is believed that the duration of exposure to the CO_2 gas is too limited for these reactions to take place (± 20 min). After the micro-CT was taken with the drained fracture, the rock plug was fully water-saturated again and the plug was flushed with H_2O to remove any dissolved CO_2 in the pore solution.

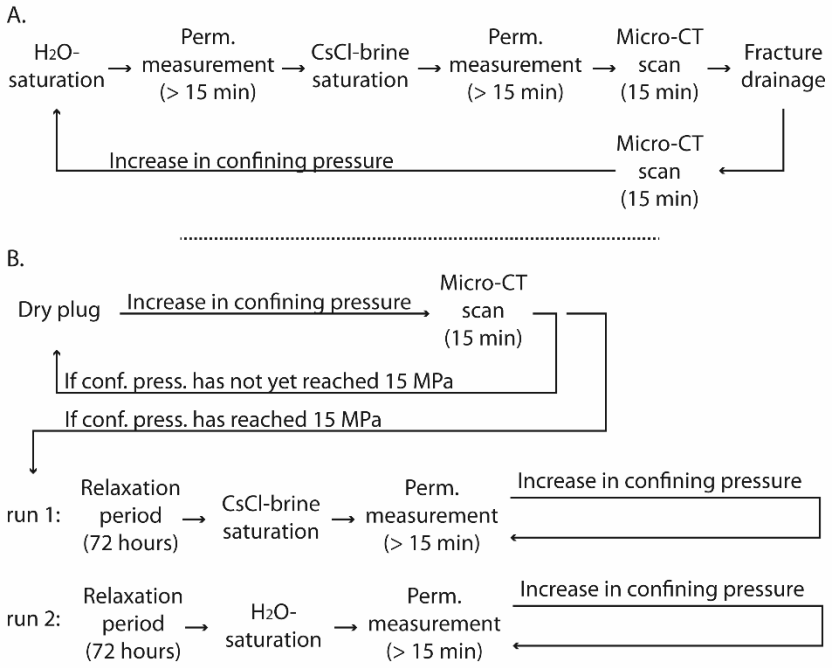

Figure 5.3. Experimental approach for the if-plug (A.) and the nf-plug (B.). Because of the low permeability in the nf-plug, the permeability determination was done separately from the micro-CT imaging. It was performed in two consecutive runs, with a relaxation period of 72h between both runs.

Lastly, the focus was put on the nf-plug. Because of the low inherent permeability of the plug, a different experimental strategy was used: first, the sample was subjected to four different confining conditions (2.9 MPa, 5 MPa, 10 MPa and 15 MPa) during which micro-CT scans were obtained without pore fluids in the plug. After these scans, the confinement around the sample was brought back to atmospheric conditions, after which a relaxation period of 72 hours was imposed. The triaxial experiment was subsequently retaken, now with a complete saturation of the pore space with the CsCl-brine; followed by a third time, saturated with H_2O. The experimental determination of the permeability change in function of the confining pressure was thus determined twice: once with the CsCl-brine, and a second time with H_2O. This approach was chosen because the low initial permeability renders the change of pore fluid during the experiment impractical with regards to the injection pressure limit of 0.69 MPa.

5.4. Micro-CT images

Figure 5.4 illustrates the obtained micro-CT data of the if-plug at a confining pressure of 2 MPa. The images in which the sample is filled with a CsCl-brine are registered with those in which the fracture was drained by CO_2 in order to construct the differential image. This registration was carried out with the Dataviewer software (Bruker Corp. Kontich, Belgium).

Differential imaging allows for the segmentation and quantification of the fracture and its aperture distribution. In the differential images, the roughness of the fracture is more easily visible, as well as the full closure of the fracture at certain locations. Of course, this has to be understood with respect to the resolution of the images, which is limited to 11 µm. This method remained successful for the if-plug at higher confining pressures.

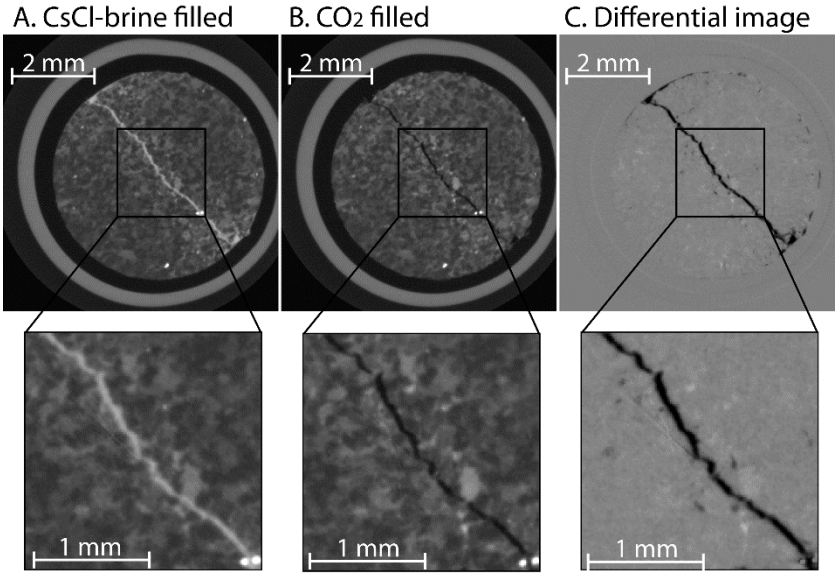

Figure 5.4. Micro-CT images of the if-plug at a confining pressure of 2 MPa. The registration of the CsCl-brine filled state (A.) and the drained state (B.) allows differential images (C.) to be constructed. The insets show the results more clearly for the three cases.

Because of the experimental approach used with the nf-plug, differential images between the drained state of the sample and a CsCl-brine filled state do not fully represent the entire initial fracture. This was because the fracture remained partially closed after the sample was brought to a confining pressure of 15 MPa in a drained state and subsequently brought back to atmospheric conditions. Therefore, in the second nf-plug experiment, with the CsCl-brine, the fracture did not have the same aperture distribution anymore. Aperture measurements therefore remain limited to areas in which the fracture was well-pronounced in the first set of scans (in the drained state). The results of these scans are shown in Figure 5.5. For visualization purposes, the insets were adjusted for their sharpness and contrast. It shows that the fracture's apertures are very close to the resolution of the images and therefore nearly indistinguishable in the rock's matrix.

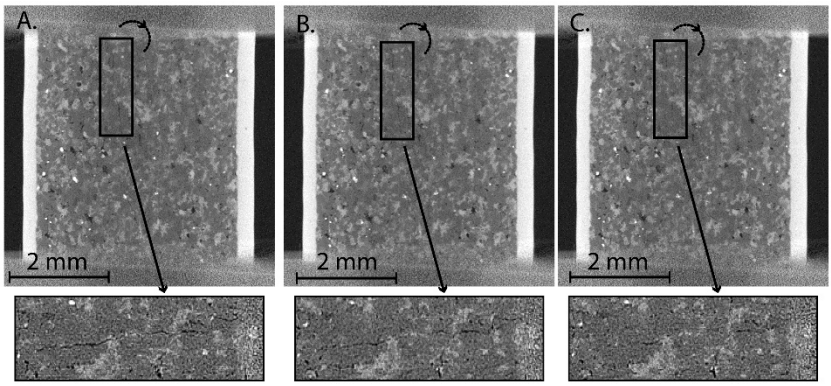

Figure 5.5. Vertical cross-sections through the micro-CT data of the nf-plug: A. at a confining pressure of 2.9 MPa; B. at a confining pressure of 5.0 MPa; C. at a confining pressure of 10.0 MPa. The gradual closure of the fracture is emphasized in the insets, in which the image is adjusted to enhance sharpness and contrast. This allows to more easily identify the fracture.

5.5. Permeability changes

The permeability of the int-plug shows an exponential decrease with increasing confinement (Figure 5.6.A). This is in slight contradiction with previous measurements of similar, unfractured rock cores (Farokhpoor et al., 2011). In (Farokhpoor et al., 2011), the unfractured rock cores showed a linear decrease of permeability with increasing confinement. It is possible that the int-plug has microscopic fractures which are closed upon increasing confining pressure. At a confining pressure of 5 MPa, the tested rock plug exhibits a permeability decrease of up to 64% compared to the situation with a confinement of 1 MPa (0.43×10^{-17} m² versus 1.2×10^{-17} m²). However, it must be noted that the amount of data is limited and no measurements were possible at confining pressures higher than 5 MPa.

The behavior of the fractured rock plugs is similar to that of the int-plug. For both the if-plug and the nf-plug, the permeability also decreases exponentially with confinement. For the if-plug (Figure 5.6.B), permeability measurements with the CsCl-brine and H_2O give very similar results. Differential images between the CsCl-brine

filled state and the state in which the fracture was drained with CO_2 were used as a basis for fracture segmentation.

The segmented fracture was then used for fluid flow simulations with the Avizo extension XLab-Simulation. This software package solves the Stokes equations (Blunt et al., 2013) and calculates the absolute permeability tensor through the Darcy equation. No-slip boundary conditions were used, and permeability was only determined parallel to the fracture, which is equal to the experimental determination.

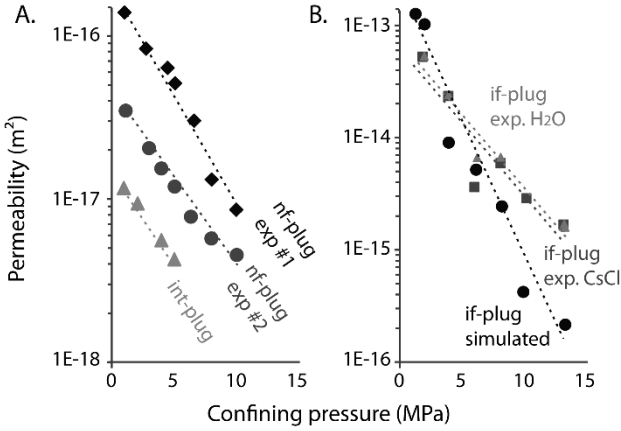

Figure 5.6. Permeability measurements and simulations based on micro-CT images, in function of the applied confining pressure. A. Permeability of the int-plug (triangles) and the nf-plug (squares and circles), in which the permeability was determined in two consecutive runs, once with the CsCl-brine, and once with H_2O; B. Experimental permeability of the if-plug, in which the permeability was determined both with a CsCl-brine and H_2O, and the simulated permeability, based on the segmentation of the fracture from the micro-CT images.

A small subsection of the micro-CT images was used for these simulations, composed of 260 x 260 x 400 voxels. This implies that not the entire fracture was included in the simulations. However, this was the largest subsection in which the fracture could be segmented. The subsection was taken in the middle of the rock plug to avoid edge effects from the Brazilian test. Results of these simulations represent the fracture permeability in this particular subsection (Figure 5.6.B). The results resemble the experimental

values, which are total permeabilities, quite well, especially at higher confining pressures. The permeabilities obtained in both the experimental investigation and the fluid flow simulations are quite high compared to the matrix permeability, measured in the int-plug. In the if-plug, the matrix permeability can therefore be neglected in the experimental permeability measurements. The total permeability which was determined experimentally can thus be considered to represent the fracture permeability in this plug.

The fluid flow simulations further allow visualizing the local fluid velocities inside the fracture (Figure 5.7). These results indicate the stepwise closure of the fracture, thereby cutting off potential fluid flow paths. At the lowest considered confinement (1.3 MPa) the simulations suggest quasi uniform fluid flow through the fracture.

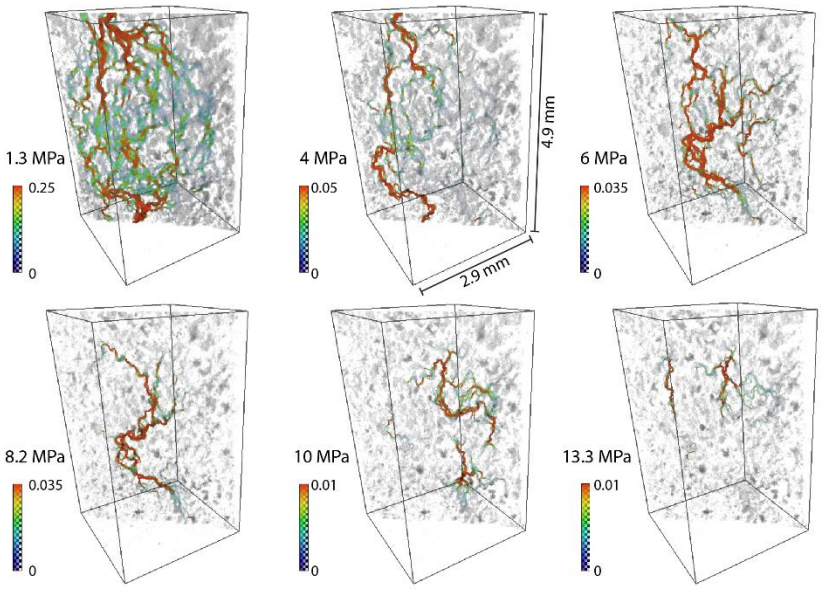

Figure 5.7. Visualization of fluid flow simulations in the if-plug, with increasing confining pressures. The simulations were carried out for identical regions within the rock plug, simulating a flow parallel to the fracture by solving the Stokes equations. It is important to note the decrease in local fluid velocity (in µm/s) with increasing pressure, as well as the channelization of the flow due to fracture closure.

The highest local velocities are found at the inflow and outflow boundaries of the retained sub-volume. This might be due to local

maxima in the fracture aperture at the boundaries of the retained volume, causing preferential in- and outflow at a certain location in the fracture. The fluid can then virtually spread out in the fracture, causing lower local fluid velocities in the central part of the fracture. After this, the fluids are redirected to the preferential outflow point where the local fluid velocity is increased to a maximum.

Like in previous studies (Kling et al., 2016; Huo and Benson, 2015), the increase in confining pressure causes partial closure of the fracture, so that preferential flow channels governing the principal fluid flow are formed. The connectivity within the fracture, as well as local permeabilities are generally decreased. This is due to smaller apertures linked to loading and an increase in the percentage of contact areas at the locations where the fracture fully closes.

Permeability measurements on the nf-plug (Figure 5.6.A) were carried out after the plug was brought to a confining pressure of 15 MPa and was left to rest at atmospheric conditions for 72 hours. After this period, the plug's permeability was measured with CsCl-brine at confining pressures of 1 MPa, 2.8 MPa, 4.5 MPa, 5.1 MPa, 6.6 MPa, 8 MPa and 10 MPa. At the lowest confinement, the nf-plug exhibited a measured permeability approximately 20 times higher than the int-plug. With increasing confining pressure, the permeability decreased exponentially. Compared to the if-plug, the nf-plug is up to 1000 times less permeable. Based on the micro-CT scans, it was noticed that the rock fracture remained partially closed after the initial increase in confining pressure. This affected the permeability experiment, which was run for a second time after the initial measurements with a CsCl-brine. In this second run, lower permeabilities were observed due to the partial closure of the fracture after the plug was subjected to the initial increase in confinement (Figure 5.6.A).

5.5.1. Hydraulic aperture quantification

Through a combination of equations 1.6 and 1.7 (section 1.3.2), a hydraulic aperture can be determined for the fractures in the if-plug and the nf-plug, based on the permeability measurements discussed in the previous section. The hydraulic aperture represents the average opening of a single fracture with parallel fracture walls through which fluid flow takes place (Snow, 1968; Witherspoon et al., 1980). In these equations, experimentally determined permeabilities can be taken as the total permeability k_{av}, the permeability determined on the int-plug represents the matrix permeability k_m, and the simulated permeabilities can be considered to be fracture permeabilities k_f. The results are summarized in Table 5.2.

Table 5.2. Hydraulic fracture aperture, based on the Hagen-Poiseuille law, both for experimental permeability determinations and permeability simulations.

Conf. P (MPa)	**Total perm. k_{av} (m²)**	**Matrix perm. k_m (m²)**	**Hydraulic aperture w (µm)**	**Simulated fracture perm. k_f (m²)**	**Hydraulic aperture w based on simulation (µm)**
If-plug					
2.0	5.3E-14	9.4E-18	9.6	1.0E-13	1.1
4.0	2.4E-14	5.6E-18	7.4	9.0E-15	0.3
6.2	5.1E-15	3.2E-18	4.4	5.2E-15	0.2
8.2	6.3E-15	1.9E-18	4.7	2.4E-15	0.2
10.2	2.9E-15	1.1E-18	3.6	4.2E-16	0.1
13.3	1.7E-15	0.5E-18	3.0	2.2E-16	0.1
Nf-plug					
1.1	1.1E-16	1.2E-17	1.2	-	-
2.9	5.2E-17	7.4E-18	0.9	-	-
4.3	4.0E-17	5.2E-18	0.8	-	-
5.1	3.2E-17	4.2E-18	0.8	-	-
6.5	1.9E-17	3.0E-18	0.6	-	-
8.0	9.4E-18	2.0E-18	0.5	-	-

The obtained hydraulic fracture apertures are found in the order of 10 µm and smaller for the if-plug, and only up to 1.2 µm for the nf-plug. These values are within the range expected from previous

studies (Farokhpoor et al., 2011). There is a discrepancy between the hydraulic aperture based on the experiments and the hydraulic aperture based on the fluid flow simulations carried out on the micro-CT images of the if-plug. However, one has to take into account the difference in analyzed volume. In the experiments, fluid flow takes place along the entire pore space across the plug with a diameter of 5 mm and a height of 14 mm. Fluid flow simulations were done on segmented fractures in a sub-volume of 4 mm and a height of approximately 5 mm.

Using a hydraulic aperture 10 times higher than the highest determined hydraulic aperture, and the highest fluid flow speed used in the experiments, maximum Reynolds numbers can be determined with equation 1.4. The choice to use a hydraulic aperture 10 times the highest determined hydraulic aperture is arbitrary. It ensures that the fluid flow conditions are exaggerated to check whether the Re numbers are still representative for a laminar flow (Re << 1). For the if-plug and nf-plug respectively, Re's of 8.5×10^{-3} and 3.4×10^{-5} were obtained. This shows that even with these exaggerated conditions, the fluid flow is still in the laminar flow regime for fractures (Mourzenko et al., 1995). Therefore, the results of the simulations are valid, since the XLab-Simulation extension in Avizo requires laminar flow conditions. Also, the assumptions in equations 1.6 and 1.7, which were used to determine the hydraulic aperture of the fractures, are met and the determined hydraulic aperture can thus be regarded as correct.

5.6. Local fracture aperture characterization

5.6.1. Local fracture apertures in the if-plug

To determine local fracture apertures quantitatively, image registration was applied in the case of the if-plug, to construct differential images between the brine-filled state and the state in which the fracture was drained with CO_2 (Boone et al., 2014; Ketcham and Iturrino, 2005). Grey value profiles were subsequently taken perpendicular to the fracture orientation. The fracture

results in a dip in the grey value profile, which can be fitted by a Gaussian point spread function (PSF) (Ketcham et al., 2010; Mazumder et al., 2006; Vandersteen et al., 2003). The PSF fitting process was based on equation 2.4. The entire Matlab code used to fit a series of grey value profiles with this PSF is given in Appendix A.

In the case of well pronounced fractures, as in the if-plug, the full-width-half-maximum (FWHM) of the dip of the PSF is an appropriate method to determine the local aperture (Ketcham et al., 2010; Van Geet and Swennen, 2001). For each scan of the if-plug, a total of 1200 grey value profiles were analyzed. Each fit was visually evaluated for its accuracy and discarded when considered insufficient (Figure 5.8). The grey value profiles were made in such a way that it was attempted to measure perpendicular to the fracture. Practically, this was done by measuring profiles perpendicular to the line connecting the two end points of the fracture in the micro-CT images. The induced fracture, as well as the natural fracture, is quite planar, allowing this approach. However, small angular discrepancies are known to be present, which result in slightly overestimated apertures. Still, it is considered that the measured data is able to represent the fracture closure with increased confining pressure.

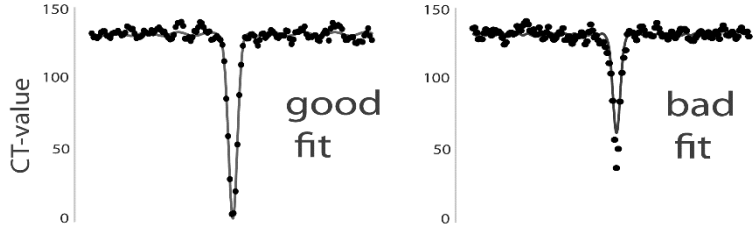

Figure 5.8. An illustration of a good fit of the Point Spread Function to the actual CT data along a grey value profile, and a bad fit which was discarded.

At a confining pressure of 1 MPa, 765 out of the 1200 PSF fits were considered to be in agreement with the spread of the CT data (Figure 5.8). This was determined through a visual check for every individual fit. At a confining pressure of 10 MPa, this only amounted

to 451 out of the 1200 PSF fits. This trend could be seen at the other confining pressures as well: the PSF fitting Matlab script (included as appendix A) is more successful for well-established fractures (at low confining pressure) as opposed to thin fractures (at higher confining pressure). Averaging these measurements might give a biased picture of the actual fracture aperture distribution in the rock plug. Nonetheless, the measured apertures, summarized in Figure 5.10, show the logical closure of the fracture with increasing confining pressure. Also, the minimum, maximum and median fracture width show a decrease with increasing confining pressure (Figure 5.10), except for the anomalous behavior at confining pressures of 8.2 MPa and 13.3 MPa. To complement this, Figure 5.9 gives a visual representation of the FWHM determined in the micro-CT scans taken at confining pressures of 1 MPa and 10 MPa.

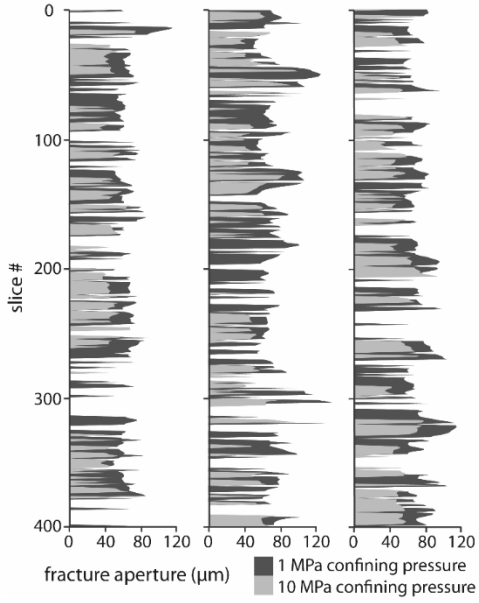

Figure 5.9. Fracture aperture distribution as determined by FWHM-measurements in the if-plug. The aperture is determined in micro-CT scans taken with a confining pressure of 1 MPa (dark grey) and 10 MPa (light grey) in three locations per slice and for 400 slices per scan. Blank areas are where the PSF did not match the CT data appropriately and the fit was discarded.

In Figure 5.9, blank areas shows the micro-CT slices where the PSF did not match the CT data appropriately and the PSF fit was discarded. In the micro-CT slices where a FWHM could be determined both for a confining pressure of 1 MPa and 10 MPa, the fracture closure could be quantitatively determined. The incremental fracture closure at a given confining pressure is visible in Figure 5.10. It is important to note that the change in average and median aperture with increasing confining pressure must be considered as a minimum average change, because local fracture closure, with regard to the micro-CT image resolution, is not detected as such by the PSF fit, although this was observed in the micro-CT images.

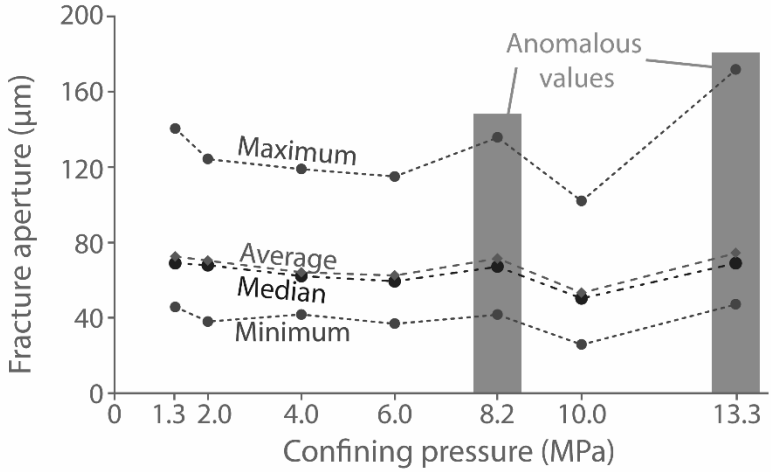

Figure 5.10. The minimum, median, average and maximum fracture aperture, measured at different confining pressures, measured with the FWHM method. The values at confining pressures of 8.2 MPa and 13.3 MPa show anomalous behavior.

The values in Figure 5.10 show anomalous behavior at confining pressures of 8.2 MPa and 13.3 MPa. This can be explained by the differential images at these confining pressures: they were obtained by subtracting the brine-filled images from the images in which the fracture was drained as illustrated in Figure 5.4. However, at the confining pressures of 8.2 MPa and 13.3 MPa, enhanced drying of the rock matrix around the fracture was

observed. This is shown by an increase in the brine concentration parallel to the fracture, a feature which was not observed at the other confining pressures (Figure 5.11).

It is believed that this enhanced drying from the rock matrix neighboring the fracture influences the FWHM characterization of the apertures. At confining pressures where this advanced drying was not observed (1.3 MPa, 2.0 MPa, 4.0 MPa, 6.0 MPa, 10.0 MPa), a logical progression of fractures apertures is observed (Figure 5.10). This, in combination with identical grey values for the rock matrix in these micro-CT images, makes the FWHM values at these confining pressures trustworthy for a correct local aperture determination.

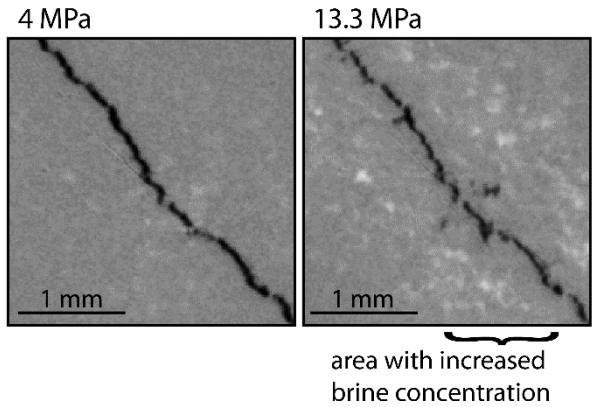

Figure 5.11. Illustration of the difference between the differential image at a confining pressure of 4 MPa (representative for confining pressures of 1.3 MPa, 2.0 MPa, 6.0 MPa and 10.0 MPa) and that at a confining pressure of 13.3 MPa (representative for confining pressure of 8.0 MPa as well). At 13.3 MPa, a zone with increased brine concentration is observed, which is related to enhanced drying starting from the fracture. This might affect the FWHM determinations of the fracture aperture.

5.6.2. Local fracture apertures in the nf-plug

The natural fracture in the nf-plug is less pronounced than in the if-plug. When such features need to be characterized, it is more appropriate to approach the fracture apertures with the Missing Attenuation method (MA) (Ketcham et al., 2010; Van Geet and Swennen, 2001). The matrix heterogeneity of the rock however,

complicates this quantification: the rock is mainly composed of quartz grains, with a calcite matrix. These materials attenuate the X-rays differently, so that they are represented by distinguishable grey values in the micro-CT images. Because the fracture tends to follow grain boundaries, the fracture is often surrounded by the lighter grey calcite on one side, and the darker quartz on the other side. The MA determination of the fracture aperture is very susceptible to such a gradient across the fracture (Ketcham et al., 2010). Therefore, MA measurements were restricted to small subsections along the fracture, where it was surrounded by quartz grains at both sides. It is considered this does not influence the local measurements, since the aperture distribution is independent from the minerals surrounding the fractures. The grey value profiles along the fracture, which are the basis for the MA measurements, were kept short, in the order of 40 voxels per measurement. This allows the determination of a local value for the average material CT value CT_{Mat} (equation 2.5). The MA-method allows for an aperture characterization at the edge of the resolution and below that. To illustrate this on the nf-plug, grey value profiles were made at confining pressures of 2.9 MPa, 5.0 MPa and 10.0 MPa, across the lower section of the fracture shown in the vertical slices illustrated in Figure 5.5. The results of this MA determination are listed in Table 5.3. The micro-CT scans at the different confining pressures were registered to each other. This allowed to perform the MA measurements on identical positions across the fracture in the different scans.

Only those measurements where a MA could be determined in at least two of the confining pressures are included. The results show that the MA method is capable of providing approximations of fractures' apertures smaller than the resolution of the images (11 µm). Ketcham et al. (2010) have shown that these measurements can be considered reliable down to one-tenth of a voxel width. In this case, it corresponds to measurements as small as 1.1 µm.

Table 5.3. Fracture aperture based on the MA-method in the nf-plug. The micro-CT scans at the different confining conditions were registered to one another. In an identical micro-CT slice for each of the confining conditions, one fracture was chosen in which MA measurements were conducted.

Aperture at conf. pressure of 2.9 MPa (µm)	Aperture at conf. pressure of 5.0 MPa (µm)	Aperture at conf. pressure of 10.0 MPa (µm)
14.8	8.2	4.3
7.3	5.4	5.0
9.8	4.8	-
6.6	3.9	-
3.6	4.3	4.7
8.9	3.6	-
5.9	3.6	-
4.3	-	7.4
-	15.3	4.5
11.0	10.8	8.6
13.9	9.7	-
22.2	8.1	-
16.6	16.6	-

Much like the FWHM measurements in the if-plug, the MA measurements show a logical decrease of the fracture width with increasing confining pressure for most of the grey value profiles which were measured. It is therefore believed that the MA measurements provide reliable approximations of the actual fracture width. However, in some grey value profiles, the fracture aperture, as measured with the MA-method, seemed to increase, or remained stable with increasing confining pressure. Some of these deviating values are found within the experimental error, which is considered to be approximately $1/10^{th}$ of the image resolution, while for other measurements the reason for the increase in fracture aperture is unclear.

5.7. Conclusion

Experiments with the in-situ triaxial device provided by SINTEF, Norway, allowed the study of small-scale rock plugs of the De

Geerdalen Formation at reservoir pressures. These experiments were performed on the EMCT system at the UGCT, which allowed direct imaging of the closure of both natural and induced fractures with a resolution of approximately 11 µm. During the experiments, the effect of the confining pressure on the fluid flow through the rock plug was used to determine the fracture permeability at each of the investigated confining pressures. Whether the fracture was natural, or induced, an increase of confining pressure had a similar effect on the permeability through the system: with increasing confinement, the permeability showed an exponential decrease. However, the permeability of the naturally fractured rock plug still was still up to 20 times higher than that of an unfractured rock plug from the same sandstone section. This elevated permeability can be attributed to a fracture with a calculated hydraulic aperture smaller than 1 µm. Local fracture apertures measurements, based on grey value profiles measured on the micro-CT images, show that some sections in this fracture are locally characterized by an aperture up to 10 times higher than the calculated fracture aperture. In the rock plug with the induced tensile fracture similar observations can be made.

The if-plug was subjected to a Brazilian test in order to induce an open fracture in it, with apertures several times larger than those found within the nf-plug. Tensile fractures typically are open structures. If the fracture was induced by subjecting the rock plug to a true triaxial test, a different type of fracture would have formed, i.e. a sheared fracture. In this case, the fracture would be partially filled with fault gouge material, which is unconsolidated material with a very small grain size, partly blocking the fluid flow path in the fracture. Given the low inherent permeability of the int-plug, this type of fracture would still increase the fluid conductivity of the plug. However, it would not do this to the same extent of the tensile fracture investigated in the if-plug.

This type of experiments provide valuable information on the importance of fractures for the permeability of the investigated

reservoir sections in the Longyearbyen CO_2 project. However, in order to fully understand this local system, experiments are to be conducted with altering injection pressures. This will affect the effective pressure of the system and will provide direct experimental evidence of the dependability of the system on fluid flow through fractures. Currently however, such experiments are not yet possible with the discussed fluid flow setup. Although the in-situ triaxial device can handle experiments with high pore pressures, an extra constant pressure ReaXus 6010R pump, or equivalent, would be necessary to control the flow through the sample. Also, a back-pressure regulator would be necessary in the fluid flow setup.

Despite these limitations, the experiments have already shown that, even at low injection pressures, the rock plugs remain dependent on fracture permeability as opposed to matrix permeability. On top of this, it was possible to quantify fracture closure at depth in naturally and induced fractured rock plugs. These experiments put the fracture aperture measurements described in chapter 3 into a broader context. In that chapter, fracture apertures in decompacted cores were observed with apertures between 40 and 500 µm. The experiments with the in-situ triaxial device described in this chapter have shown that the fracture aperture of these rock cores would be smaller at the depth of the reservoir. The permeability measurements have shown that the hydraulic aperture decreases with a factor of 2 to 3 when subjecting the plugs to a confining pressure similar to that at a depth of 800 meters.

6.
Pore-scale processes

This chapter discusses physical and geochemical processes related to CO_2 injection in the Longyearbyen CO_2 project reservoir sections. Close to the injection well, dehydration processes typically result in the precipitation of salts from the formation brine. In this chapter, pore-scale drying processes were investigated within fractured rock plugs of the De Geerdalen Formation and a reservoir analogue with a bimodal porosity. Micro-CT imaging with the EMCT system allowed the visualization of these processes with resolutions of approximately 11 µm. Although this does not resolve the micro-pores within the tested rock plugs, it suffices for the visualization of the redistribution of the brine within the plug during the injection of CO_2 and the precipitation of salt crystals in the reservoir analogue. Further away from the injection well, CO_2 dissolves into the formation brine and forms an acidic solution. Through geochemical reactions with the rock matrix, this can locally influence the porosity and permeability of the system. In this chapter, the influence of such an acidic solution on fractured rock plugs from the Longyearbyen CO_2 project reservoirs is investigated with simplified fluid flow setups. Micro-CT scans were carried out on HECTOR and the EMCT system at UGCT and allowed the visualization of dissolution patterns along fractures induced in centimeter scaled rock plugs.

6.1. Pore-scale drying processes

6.1.1. Theory

In the direct vicinity of a CO_2 injection well, the reservoir will dehydrate due to the injection of CO_2. This zone will be fully gas saturated and will grow upon continued injection of CO_2 (Gaus et al. 2008). In front of this fully gas saturated zone, a highly saline zone will form in which salts, from the formation brine, will precipitate (zone 4 and 5 in Figure 0.5). Ott et al. (2014) studied formation drying and salt precipitation due to gas injection using small-scale core flood experiments and micro-CT imaging. Similar to other studies (Nachshon et al. 2011; Lehmann & Or 2009), they found that the microscopic heterogeneity in rock texture plays a fundamental role in the exact location of salt precipitation. Depending on the location of salt precipitation, fluid flow properties can be affected significantly. Ott et al. (2014) suggested a clear distinction between the drying behavior in monomodal and bimodal porous media. Figure 6.1 illustrates this difference schematically. In a monomodal porous medium, the brine between the grains will evaporate and retract, after which salt will precipitate in between grains, where no CO_2 advection is taking place. This is clearly different in a bimodal porous medium. Considering some grains contain micro-pores, the brine still retracts in between the grains due to evaporation. However, evaporation also takes place along the boundary of the micro-porous grains. The retracted brine in between the grains will refill the partly drained micro-porous grain due to capillary forces. Therefore, the pore space in between the grains will fully desaturate after which evaporation can only take place on the boundaries of the micro-porous grains. This causes the salt to precipitate along these boundaries, reducing the cross sectional areas along which CO_2 advection is taking place, which reduces the overall permeability through the system.

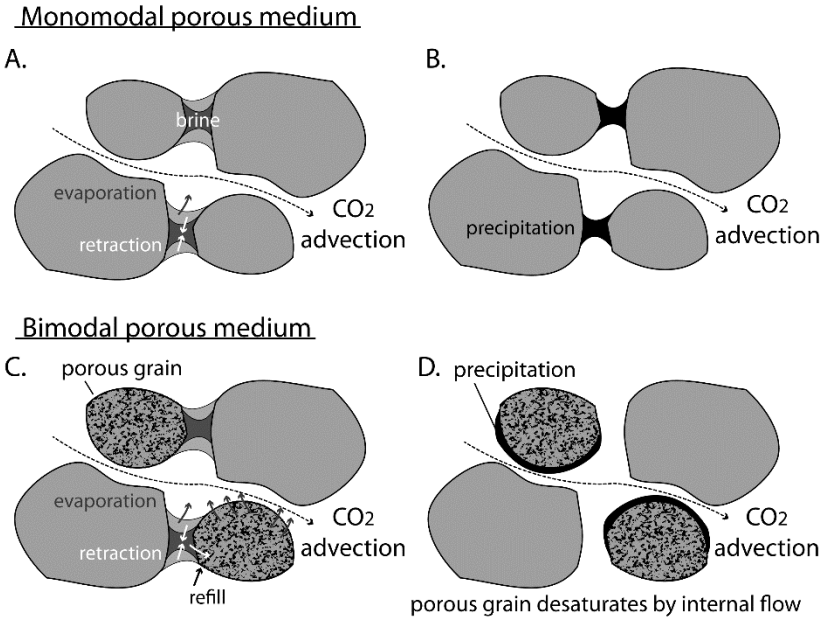

Figure 6.1. Microscopic model of solute transport and salt precipitation for monomodal (A & B) and bimodal (C & D) porous media. In the monomodal case, brine retracts between the grains (A) and salt precipitates in that location (B). In bimodal porous media, the brine retracts between the grains, but refills within the micro-pores of the porous grains (C). This porous grain desaturates by internal flow, causing salt precipitation on the grain itself (D). This reduces the cross sectional area between the grains, lowering permeability. Figure modified from (Ott et al. 2014).

6.1.2. Drying in a reservoir analogue

Because of the mineralogical and textural complexity of the samples from the Longyearbyen CO_2 project reservoir, drying experiments were first conducted on a monomineralic limestone with a bimodal pore network: the Savonnières limestone. The pore structure of this oolithic grainstone consists of vacuolar ooids, in which the intragranular macro-pores are connected by intragranular micro-porosity to the intergranular micro- and macro-pores (Derluyn et al. 2014). To illustrate this complex pore system, Figure 6.2 shows a thin section of the Savonnières limestone. The limestone is further characterized by local layers of (dissolved) shell fragments, which add to the complexity of the rock's microstructure (Roels et al. 2001; Derluyn et al. 2014).

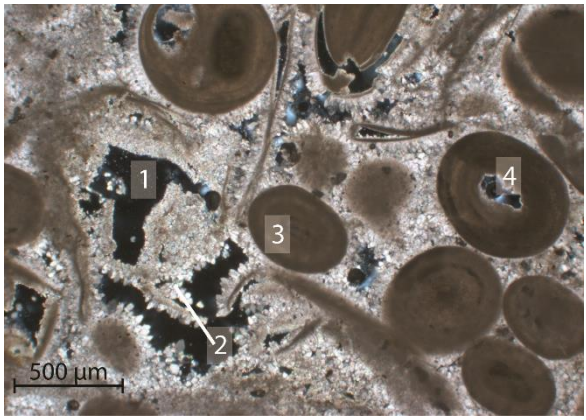

Figure 6.2. Thin section of Savonnières limestone showing intergranular macro-pores (1), intergranular micro-pores (2), intragranular micro-pores (3) and intragranular macro-pores (4).

Small plugs of this geomaterial were sampled, with a length of 12 mm and a diameter of 6 mm. They were inserted in one of the PMMA flow cells (section 2.3.2.2) and were subjected to confining pressures of approximately 1 MPa. Subsequently, the pore space of the plug was fully saturated with H_2O, after which it was replaced by a 200 kppm CsCl-brine. The fluids were pumped through the plug with a maximum flow rate of 0.2 µL/s. Continuous micro-CT imaging with the EMCT during the uptake of the brine allowed the determination of fluid flow paths as in Bultreys et al. (2016b). Advective fluid flow was shown to take place in the intergranular pores, which were filled first with CsCl-brine. The brine concentration in the intragranular pores in the dissolved ooids initially remained low and only equilibrates with the brine inside the intergranular pores after a certain amount of time of continuously pumping the brine through the plug. The brine only enters the intragranular pores through diffusion through the micro-porous ooids. Once the plug was fully saturated with CsCl-brine, CO_2 was injected into the sample at a constant pressure of 0.1 MPa. The injection of CO_2 from the bottom of the sample triggered drying within the pores. This was monitored through micro-CT imaging with a temporal resolution of 6 minutes/scan and a spatial

resolution of 11.3 µm. This spatial resolution is enough to differentiate macro-pores in the plugs, but does not resolve micro-pores. The drying process was registered during a total of 36 hours, with a time interval of 1 to 1.5 hours in between each micro-CT scan. Results of these scans are depicted in Figure 6.3.

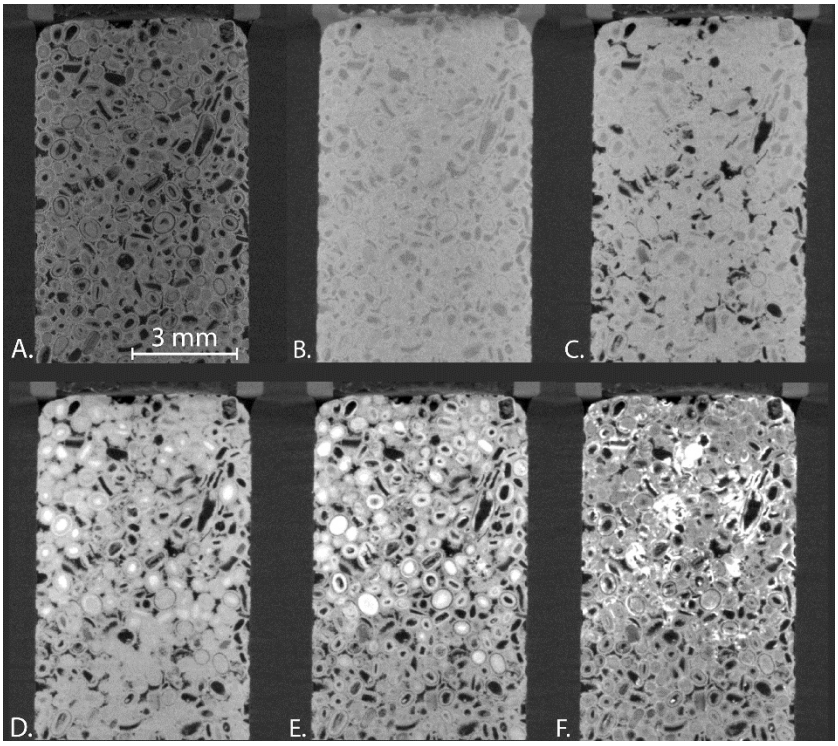

Figure 6.3. A. The initial, dry state of the Savonnières plug; B. The plug, saturated with a CsCl-brine. The ooids still have a lower CsCl-concentration as the advective fluid flow path, which has a similar grey value as the rock's material; C. Drying of the intergranular porosity, the state after 3 hours and 20 minutes of CO_2 injection; D. Increase of brine concentration in intragranular ooid pores, the state after 17 hours and 20 minutes of CO_2 injection; E. Further increase of intragranular brine concentration, after 25 hours of CO_2 injection; F. Precipitation of CsCl crystals, after 32 hours and 40 minutes of CO_2 injection.

It must be noted that this experiment illustrates the different zones related to the initial injection of CO_2 into a reservoir, schematically depicted in Figure 0.5. In this experiment, a fully saturated plug (Figure 6.3.B) represents the initial host rock (zone 1 in Figure 0.5).

At the end of the experiment (Figure 6.3.F) salt has precipitated in the top 2/3rd of the rock plug. In the bottom 1/3rd, little to no salt precipitation occurred. Here, we see the transition from a fully dehydrated zone (zone 5 in Figure 0.5) to a highly saline zone, characterized by the precipitation of salt from the brine (zone 4 in Figure 0.5).

The drying behavior follows the model proposed by Ott et al. (2014). The injected CO_2 drains the advective pathway through the plug, consisting of the intergranular micro- and macro-pores (from Figure 6.3.B to Figure 6.3.C). Subsequently, the CsCl-concentration in the brine increases in the pores which are only accessible through diffusion (intragranular pores). This is visible due to the increase in grey value within the ooids (from Figure 6.3.C to Figure 6.3.E). Due to the continued advection of CO_2 along the main fluid pathway in the plug, the brine evaporates and retracts within the micro-pores of the ooids, reaching the intragranular macro-pores. Evaporation continues along the advective pathway, eventually retracting the fluids out of the microporous ooids and causing precipitation of CsCl crystals along the advective pathway (Figure 6.3.F).

Because of the high solubility of CsCl in water, the plug could be saturated again with the CsCl-brine after the experiment. To do this, the plug was first flushed with H_2O, in order to dissolve the precipitated CsCl crystals in the continuous flow. Subsequently, the water was replaced with the 200 kppm CsCl-brine and the drying experiment could be conducted once more on the same plug. The location of salt precipitation in the second drying sequence was nearly identical as in the first one. The second drying sequence differed from the first by the amount of CsCl precipitation. This might be due to a difference in initial brine saturation, or might be linked to a small difference in CO_2 injection pressure. The process is considered to be fully reversible due to the solubility of CsCl in water. Up to 1910 g/L of the salt can be dissolved. This implies that the precipitated CsCl-crystals dissolve rapidly in water when

flushing fresh water through the sample at the end of the experiment.

6.1.3. Drying within the De Geerdalen Formation

The De Geerdalen reservoir units are known to have a complex pore system. Not only do they contain calcite and clay minerals, which contain micro-pores, but also the fractures within the reservoir system will affect drying processes. In order to investigate the effect of fractures within these rocks on such processes, drying experiments were conducted in the if-plug described in Chapter 5. At each of the confining pressures (1.3 MPa, 2.0 MPa, 4.0 MPa, 6.0 MPa, 8.2 MPa, 10.0 MPa and 13.3 MPa) in which fracture aperture distributions were investigated, the plug was filled with the CsCl-brine. CO_2 was subsequently injected, which was monitored through continuous micro-CT imaging with a temporal resolution of 40 seconds per scan. The drying, however, was only monitored the first 20 minutes after injection of CO_2 within the plug. This was enough to fully drain the fracture. However, the drying was not continued in order to not affect the CsCl concentration in the brine within the matrix adjacent to the fracture, as this would affect local fracture aperture measurements (section 5.6). The aim of these experiments was to visualize whether the rough fracture would be locally obstructed by precipitation in local fracture aperture minima. This is best inspected in differential images between the fully saturated micro-CT image and the scan in which the fracture is drained. Figure 6.4 illustrates these images in identical vertical cross-sections through the micro-CT data at different confining conditions. Fracture closure due to precipitation of CsCl crystals would generate bright spots within the fracture itself. However, these were not observed, even at higher confining pressures. The fracture was thus, at that moment, fully drained.

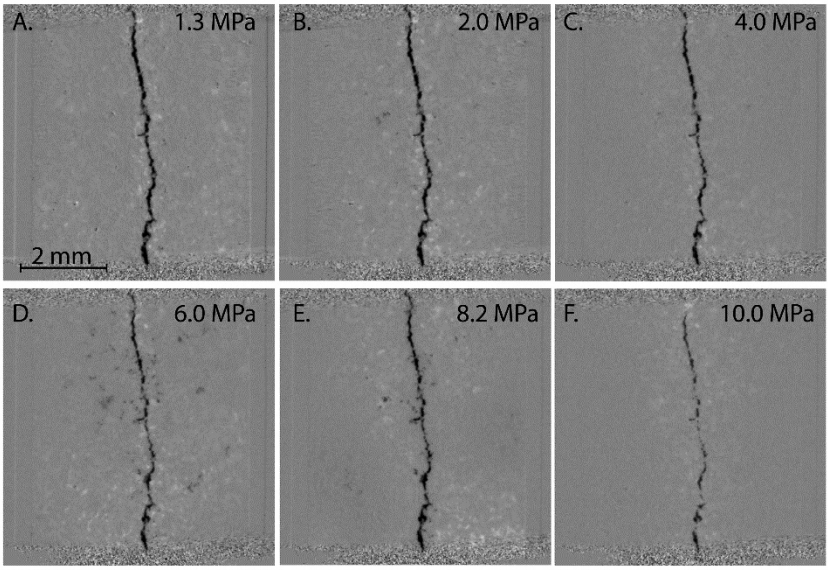

Figure 6.4. Differential images of the drained induced fracture at different confining pressures. Dark voxels represent the decrease in concentration or drainage of CsCl-brine from a certain location. Bright voxels infer an increase in brine-concentration. A. at a confining pressure of 1.3 MPa; B. at a confining pressure of 2.0 MPa; C. at a confining pressure of 4.0 MPa; D. at a confining pressure of 6.0 MPa; E. at a confining pressure of 8.2 MPa; and F. at a confining pressure of 10.0 MPa. On the top and bottom parts of the images, interference is seen from the metal rings of the in-situ triaxial device. This leads to metal artefacts.

When the drying process continues for a longer time period, the redistribution of the brine concentration becomes apparent. This was the case in the drying experiment carried out at a confining pressure of 13.3 MPa (Figure 6.5). Symmetrical to the fracture, a V-shaped area was formed in the rock's matrix in which an increased CsCl concentration was observed in the differential images. Under this zone an area with reduced CsCl concentration was formed. The rock's matrix acts as the micro-porous part of a bimodal distributed pore system. In this system, the fracture acts as the macro-porous zone, even at high confining pressures. It provides the advective pathway for the CO_2 to flow through along which the brine can evaporate. In the experiments, the fracture extended from the bottom of the plug all the way to the top of the plug. It is believed that if the fracture ended in a crack tip, the brine might have

concentrated along the tip in which CsCl then could have precipitated. Considering the model of Ott et al. (2014), fracture drainage would then lead to precipitation along the fracture walls, decreasing the fracture permeability.

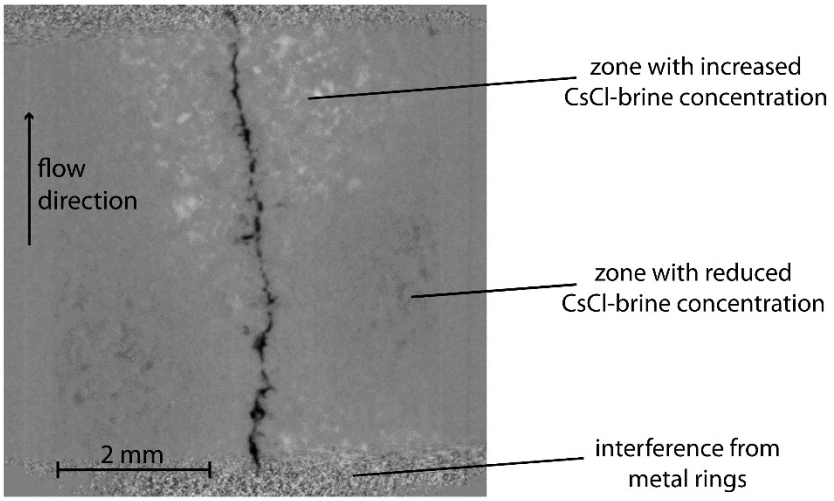

Figure 6.5. Prolonged drying in the plug at a confining pressure of 13.3 MPa caused a V-shaped area, symmetrical to the fracture, to form with an increased brine concentration. The brine is retracted from an underlying zone, distinguishable in the differential images by a reduced CsCl concentration.

A prolonged drying experiment was conducted in one additional rock plug from the De Geerdalen Formation. This plug was subjected to a small scale three-point bending test in order to induce a fracture perpendicular to the longitudinal axis of the plug. The plug, with a length of 14 mm and diameter of 5 mm, was fully saturated with a 450 kppm CsCl-brine and subjected to a confining pressure of 2.1 MPa. CO_2 was injected in the plug at a constant pressure of 0.5 MPa. The drying sequence was followed for 5 sequential days starting from the initial injection of CO_2. During this time, a total of 68 micro-CT scans were taken with a temporal resolution of 12 minutes and a spatial resolution of 11.5 µm. The results are depicted in Figure 6.6.

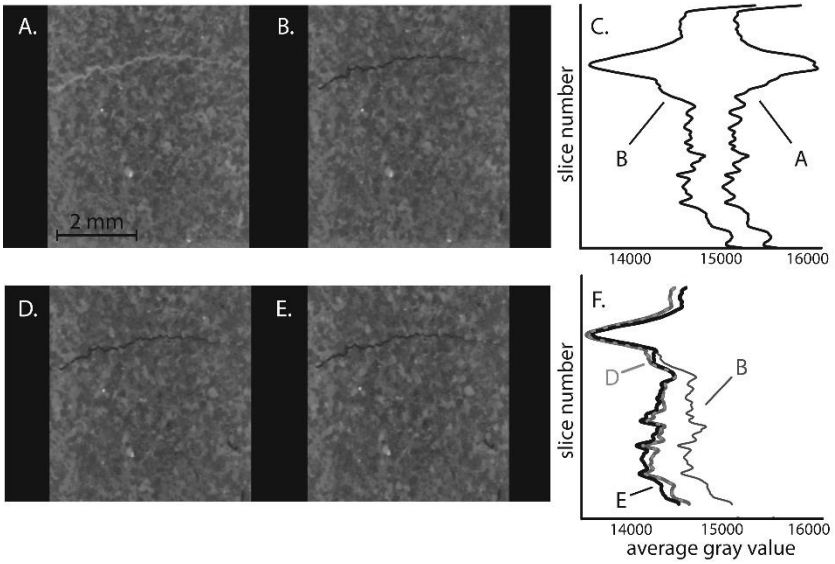

Figure 6.6. A. Rock plug, with a crack perpendicular to the flow direction, fully saturated with a CsCl-brine; B. The same rock plug, after continuous drying of 24 hours, the fracture is fully drained. C. Average grey value per slice for the micro-CT scans conducted during situation A & B. The average grey value drops, not only for the slices affected by the fracture, but also in the rock matrix; D. and E. Micro-CT images after 48 and 92 hours of drying respectively; F. Average grey value per slice for the micro-CT scans depicted in B, D and E.

When the injected CO_2 reached the horizontal crack, the brine was drained quite rapidly. The average grey value of the zone affected by the fracture drops significantly (Figure 6.6.C), as does the average grey value in the rock matrix. Continued CO_2 injection causes gradual drying in the rock matrix below the crack, and an accumulation of brine concentration above it (Figure 6.6.F). Although the crack itself does not form an advective pathway in the rock plug, the CO_2 accumulated within the crack. Non-wetting fluids, such as CO_2 in this experiment, tend to occupy the largest pore spaces. In this plug, this is the horizontal crack. Although the experiment did not last long enough to distinctively show the precipitation of salt, it is expected that the system will behave as in the model of Ott et al. (2014). If micro-pores are present, for example in clay minerals, the crack is expected to be lined with salt precipitates, eventually fully closing and leaving behind micro-

pores between the salts. In this case, this does not necessarily affect the permeability of the system significantly, but it lowers the effective porosity of the system, which is crucial for the potential storage capacity of the rock.

6.2. Chemical alteration due to flow of acidified brine

6.2.1. State-of-the-art

Further away from the injection well (zone 2 and 3 in Figure 0.5), the injected CO_2 will start to dissolve in the formation brine, lowering its pH from near neutral values to 4.0 - 5.0 (Gaus et al. 2008; Rosenbauer et al. 2005; André et al. 2007). This causes acidic reactions between the formation brine, the storage unit and caprock formation (Rohmer et al. 2016). For the assessment of the storage performance, it is important to understand the alteration of rock properties due to these reactions. Typically, the difference is made between short term effects, which occur in the injection phase over a time period of 25-50 years, and long term effects, which occur in the storage phase with time scales over 100 years and up to several 10,000 years (Gaus 2010; Rohmer et al. 2016). Because of its high solubility and kinetic rates, calcite is frequently expected to be the most reactive rock-forming mineral (Rohmer et al. 2016; Lamy-Chappuis et al. 2014). Reactions between calcite and the acidified brine will thus primarily influence the near-well environment in the injection phase. Also sulphates and evaporitic minerals will contribute to the alteration of the reservoir in this phase because of their fast reaction kinetics (Gaus 2010). Longer term geochemical reactions typically affect alumino-silicate minerals, which are characterized by very slow reaction rates (Gaus 2010).

To understand the effect of these geochemical reactions on the pore-scale structure of the actual reservoir materials, experimental studies at the laboratory scale are indispensable (Gaus 2010; Izgec et al. 2008; Rosenbauer et al. 2005; Garing et al. 2015). Reservoir samples can be subjected to controlled batch reactor tests, or to flow through tests. When possible, a brine is used in which CO_2 is

dissolved under high pressure to form an acidic equivalent to the formation water in which CO_2 is injected. Menke et al. (2017) gave an overview of the latest core-scale experiments in which dissolution of geomaterials due to an acidic CO_2-enriched brine was studied through micro-CT imaging. Most of this research, however, focuses on dissolution patterns in limestone rocks. It shows that the dissolution regime which develops is highly dependent on the initial structural heterogeneity and the flow regime used in the experiments. Small changes in this flow regime can already alter the outcome of the experiments.

Whereas dissolution patterns in unfractured rocks can be subdivided based on the dimensionless Péclet (Pe) and Damköhler numbers (Da) (section 1.3.4), which describe the flow regime in the rock, the situation becomes more difficult in already fractured rock samples. In such samples, the fracture provides the dominant pathway for flow and the geochemical reactions predominantly take place along the fracture surfaces. Flow of reactive fluids can cause preferential dissolution along these fracture walls, thereby altering the fractures' aperture distribution and changing the fracture's contribution to the overall permeability (Detwiler et al. 2003; Gouze et al. 2003; Noiriel et al. 2013). Dissolution patterns along the fracture are not only considered to be dependent on the Pe- and Da numbers, but rely also on the aperture distribution of the fracture. Local aperture variability can cause instabilities in the dissolution front which can cause the formation of preferential dissolution channels within the fracture (Hanna & Rajaram 1998; Szymczak & Ladd 2009). Similar to the experimental study of acidified brine flow through unfractured geomaterials, studies on reactive flow through fractured rocks are mostly focused on limestones (Gouze et al. 2003; Noiriel et al. 2013), or the cement used to encase the drillhole well (Cao et al. 2015) to study potential leakage of CO_2.

6.2.2. Chemical alteration in reservoir samples with ideal fractures.

6.2.2.1. Experimental setup

In order to understand these processes within the reservoir sections of the Longyearbyen CO_2 project, simple fluid flow setups were constructed (Figure 6.7). In a first series of experiments, three cylindrical rock plugs with a diameter of 10 mm and a length of approximately 30 mm were prepared: two sandstone plugs from the De Geerdalen Formation (both with an open porosity of 10 %) and one from the Wilhelmøya Subgroup (with an open porosity of 8.4 %). Within these plugs, a saw-cut fracture was made, parallel to the long axis of the plug. The two halves were glued into the sample holder with a spacer, ensuring the separation of both halves. As such, an artificial fracture was created with parallel fracture walls and a fixed aperture of approximately 100 µm.

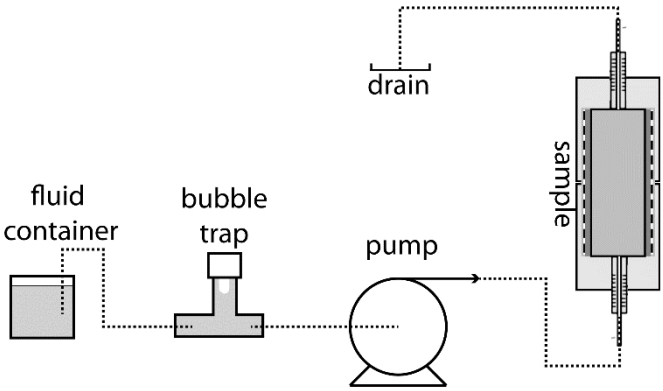

Figure 6.7. Simplified fluid flow setup to study the effect of acidic fluid flow through the Longyearbyen CO_2 project reservoir sections.

The rock plugs were fully water saturated, after which they were flushed with diluted sulfuric acid (pH 3.5). This pH represents a slightly more acidic solution than what is expected in reality. However, this was chosen in order to enhance the chemical processes in these small-scale experiments. At different time steps, the percolating fluids could be sampled at the outflow drain in order to determine the chemical composition of the outflowing liquids. The experiments took place on the sample stage of the

EMCT, under controlled room temperature conditions. During each experiment, a series of micro-CT scans was made in order to follow the dissolution patterns along the fractured plug. In the beginning of the experiment, micro-CT scans were taken once every hour, after which it was chosen to increase the time between consecutive scans to two hours. Table 6.1 provides information on the duration and fluid flow rate in each of the conducted experiments. In order to image the plug across its entire length, so-called stacked scans had to be made. In such a scan, several individual micro-CT scans were taken at different heights of the rock plug, which were merged together in the reconstruction phase, with the Acquila software suite. In the case of these experiments, three scans were made which overlapped approximately 10% with each other. Each complete stacked scan took approximately 36 minutes to complete (12 minutes per individual micro-CT scan).

Table 6.1. Summary of acidic fluid flow experiments on rock plugs from the Longyearbyen CO_2 reservoir.

Sample	**Open porosity (%)**	**Flow speed (µL/s)**	**Experimental time span (h)**
De Geerdalen Fm. sst I	10.0	0.5	54
De Geerdalen Fm. sst II	10.0	0.2	93
Wilhelmøya Subgroup sst	8.4	0.2	68

6.2.2.2. Fluid flow conditions

The acidic solution was flushed through the artificially fractured rock plug with flow speeds of 0.2 µL/s and 0.5 µL/s. This ensured laminar flow through the fractures (Re-numbers << 1). At these flow rates, Péclet numbers smaller than 1 are expected when considering the mean fracture aperture as characteristic length for the system and a typical free water molecular diffusion coefficient in the order of 10^{-9} m/s (Dijk & Berkowitz 1998). This implicates that the solute transport in these experiments would be dominated by

molecular diffusion. However, in a porous medium, the effective diffusion coefficient is linked to the pore structure of the material, more specifically to the connectivity and tortuosity of the pore space (Shen & Chen 2007). These are parameters which are difficult to determine in tight sandstones. Moreover, the fluid flow mechanism in the fracture is expected to be different from the fluid flow from the fracture to the matrix. It is thus difficult to specify fixed Pe- and Da numbers for the experiments.

Experimental work, described in literature, in which an artificial fracture with a mean hydraulic aperture of 126 µm was constructed with two textured glass surfaces, reported on Pe numbers between 54 and 216 when using a flow rate of 3.6 µL/s and 14.5 µL/s respectively (Detwiler et al. 2003). Gouze et al. (2003) even reported a Pe number of approximately 440 in their experiments in rock fractures with a mean aperture of 20 to 50 µm and a flow rate of 2.8 µL/s. It shows the difficulty of defining these dimensionless numbers to characterize the flow regime in fractured rocks. The flow rates used in the experiments described in this work (0.2 to 0.5 µL/s), however, are rather low. Within a reservoir they would represent natural flow regimes in sections which are unaffected by the injection pressure.

6.2.2.3. Micro-CT visualization of dissolution

Each individual experiment was performed with the flow cell on the sample stage of the EMCT. Micro-CT images were taken at different time steps in order to visualise the dissolution pattern along the fracture. Differential imaging between the different time steps allows the quantitative and qualitative inspection of the dissolution patterns. In both experiments with the De Geerdalen Fm. sandstone plugs a clear difference was observed between the unaltered rock plug and the end-state of the plug after the experiment based on differential imaging. In the sample from the Wilhelmøya Subgroup however, little to no difference was observed on the differential images. Figure 6.8 illustrates the

observed difference between the unaltered plugs and the end states after 54h and 93h of acidic flow through the De Geerdalen plugs I and II respectively.

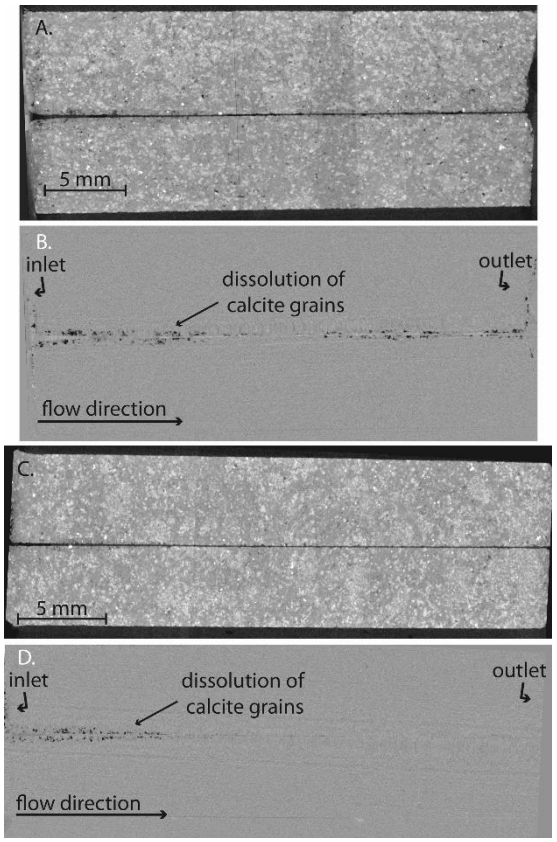

Figure 6.8. A. Micro-CT image across the De Geerdalen sandstone plug I which was subjected for 54h to an acidic flow with a flow rate of 0.5 µL/s; B. represents the differential image of this micro-CT scan with the micro-CT scan of the unaltered plug. Dark areas represent the removal of matter, due to dissolution of minerals. C. and D. represent the micro-CT image and the differential image of the experiment with the De Geerdalen sandstone plug II, which was subjected to 93h long acidic flow with a flow rate of 0.2 µL/s.

The plug, which was subjected to an acidic flow with a constant rate of 0.5 µL/s (Figure 6.8.A. and Figure 6.8.B.), shows dissolution of the rock matrix across the full length of the fracture. The rock, out of which both plugs from the De Geerdalen Formation were drilled, consists mainly of quartz grains, within a fine grained carbonate

cement. In lower quantities, also plagioclase is present, as well as pyrite and clay minerals such as biotite and illite. Based on the micro-CT images, the dissolution mainly affects the carbonate cement in the rock matrix.

During the course of the experiments, the outflowing fluids were regularly tested for their pH. This is illustrated in Figure 6.9. In the plug from the De Geerdalen Fm which was tested with a flow rate of 0.5 µL/s (De Geerdalen Fm. sst I), the outflowing liquids were continously characterized by low pH values, despite the visualization of carbonate minerals dissolving due to the acidic flow. Towards the end of the experiment, a slight increase in pH was observed from 3.5 to 4.5. This indicates that the advective transport through the fracture was higher than the reaction rate of the acidic fluid with the fastest reacting mineral(s). The dissolution of the matrix is thus controlled by the advective transport through the fracture, causing a dissolution pattern along the entire length of the fracture (Figure 6.8.A. and Figure 6.8.B). The dissolution seemed most pronounced at the inlet of the rock plug. Here, chemical reactions change the acidity of the injected solution, so that there is a gradual decrease in the reaction rate across the plug. However, as the pH measurements show, the increase in pH was rather limited. The pH of the injected acidic solution was 3.5. For the first 30 hours of the experiment, the pH of the outflowing solution was identical to this value.

At lower flow rates (0.2 µL/s in the De Geerdalen sandstone plug II), the dissolution only took place at the inlet of the acidic fluids (Figure 6.8.C. and Figure 6.8.D.). The pH of the outflowing fluids from this rock plug was stable at a pH of 7 during the entire experiment (Figure 6.9). This implies that the acidic solution completely reacted with the reactive minerals. At this flow rate, the reaction rate of the acidic fluid is thus higher than the advective transport through the fracture. In both experiments, gas bubbles formed within the fracture. This can be linked to the dissolution of calcite within an acidic environment, through which CO_2 can be exempted.

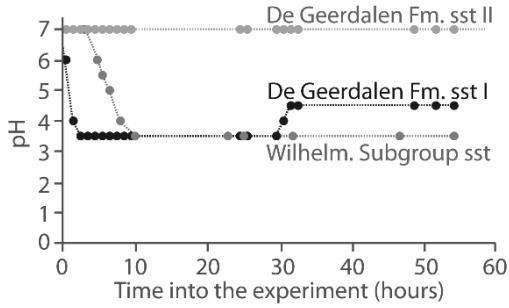

Figure 6.9. pH evolution during the dissolution experiments for the De Geerdalen Fm. sandstones I and II, and the Wilhelmøya Subgroup sandstone.

In the rock plug of the Wilhelmøya Subgroup, the pH of the outflowing solution remained identical to the pH of the injected acidic solution. Because of the low flow rate (0.2 µL/s), this implies that only a limited amount of reactive minerals were present which came in contact with the acidic solution.

The dissolution of the rock matrix locally increases the porosity and possibly the permeability of the system. However, it is known that exposure of calcite crystals to sulfuric acid can lead to the formation of a gypsum crust on the surface of the calcite grains, which passivates them from further reaction and dissolution (Booth et al. 1997). This takes place via following reactions (Booth et al. 1997; Bouchelaghem 2010):

$$CaCO_3 + 2HSO_4^- \rightarrow Ca^{2+} + 2SO_4^{2-} + H_2CO_3 \quad (6.1)$$

$$Ca^{2+} + SO_4^{2-} + H_2O \rightarrow CaSO_4.2H_2O \quad (6.2)$$

Gypsum overgrowth on calcite crystals can affect the diffusion of the diluted acid into the rock matrix, thereby lowering the interaction between the fluids inside the fracture system and the pore space of the rock. The resolution of the micro-CT images (approximately 10.5 µm), however, is too low to distinguish gypsum overgrowth layers in the obtained images. SEM imaging after the fluid flow experiments did not indicate the presence of gypsum. However, because the samples were glued into the fluid flow cell, sample preparation for SEM imaging might have altered fragile minerals which could have precipitated along the fracture. Besides

calcite, also other minerals are expected to dissolve at a low pH (Jun et al. 2013). Clay minerals, such as biotite, typically show an anisotropic dissolution in which the dissolution rate strongly depends on the crystallographic orientation (Kalinowski & Schweda 1996). Also plagioclase is expected to dissolve (Oxburgh et al. 1994). However, in the micro-CT images, it is difficult to distinguish plagioclase and clay minerals from the calcitic matrix based on the grey value of the minerals. Therefore, it is unclear to what extent each mineral contributes to the observed dissolution of the rock matrix.

The rock plug of the Wilhelmøya Subgroup showed very limited to no dissolution on the micro-CT images after it was flushed for 68h with a continuous flow rate of 0.2 µL/s. This is strongly linked to the absence of reactive minerals in this sandstone plug. SEM analysis showed a very low calcite content within this plug, but did show the presence of plagioclase and clay minerals which were expected to react to the acidic fluid.

6.2.2.4. Elemental analysis of outflow liquids

As micro-CT does not allow to fully understand the geochemical reactions which take place at the pore-scale, the waste fluids were sampled at regular intervals and analysed with Inductively Coupled Plasma Optical Emission Spectrometry (ICP-OES), with a Varian 720-ES ICP-OES device at Ghent University. This technique allows the elemental analysis of the fluids after they passed through the rock plugs. A virgin sample of the sulfuric acid, which did not flow through any rock plug, was used as a baseline measurement to ensure that only the ions which were released due to dissolution reactions were witheld. Figure 6.10 shows the main results for both De Geerdalen Formation rock plugs in which the diluted acid was pumped through the plug at flow rates of 0.5 µL/s (Figure 6.10.A and Figure 6.10.C) and 0.2 µL/s (Figure 6.10.B and Figure 6.10.D). Both experiments show a fast initial peak in Ca^{2+} concentrations, which then stabilises to a plateau in the experiment with a lower

flow rate. The reason why it fluctuates in the fast flow rate experiment and reaches a stable plateau in the slow flow rate experiment, is because the diluted acid is fully buffered by the dissolution of the calcitic matrix in the slow flow rate experiment. The amount of calcite which can be dissolved depends on the amount of diluted acid provided. In the fast flow rate experiment, the outflowing solution still has a low pH (Figure 6.9). The acid is thus not entirely buffered by the dissolution of calcite, so that the amount of Ca^{2+} ions is linked to the free reacting surface of calcite grains.

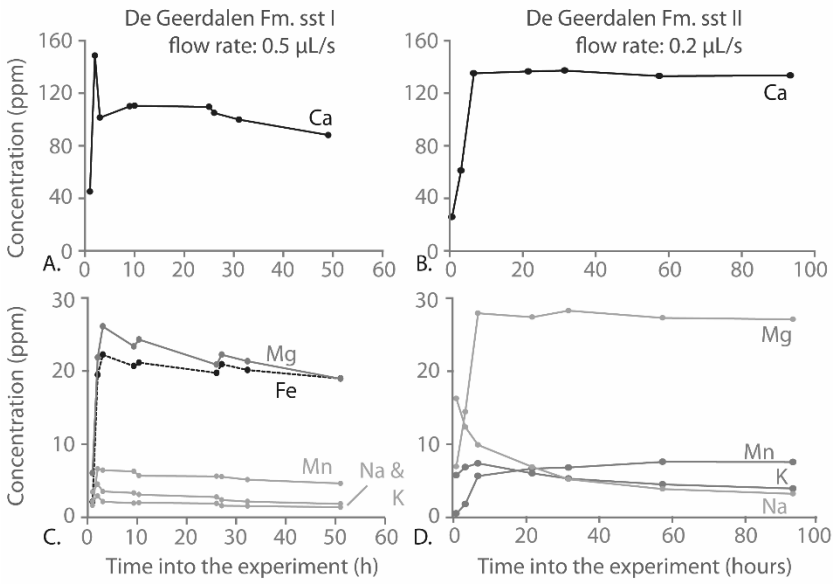

Figure 6.10. Elemental analysis of outflowing liquids in the De Geerdalen rock plugs, flushed with an acidic solution with a flow rate of 0.5 µL/s (A & C) and 0.2 µL/s (B & D).

Figure 6.10.C. and Figure 6.10.D show the evolution of the main elemental constituents in the outflowing liquids, excluding Ca^{2+}. In the experiment with a flow rate of 0.5 µL/s, the evolution of Mg^{2+} and Fe^{2+} shows a similar elemental dissolution behavior. These are two constituents of biotite minerals, just like K^{+}. Biotite typically releases K^{+}-ions preferentially, before leaching out Mg^{2+} or Fe^{2+} (Kalinowski & Schweda 1996; Malmström & Banwart 1997). In the experiment with a flow rate of 0.2 µL/s (Figure 6.10.D), the K^{+}-

concentration reaches a maximum after which the concentration gradually lowers. In both experiments, also Mn^{2+} can be found, an ion which can substitute Mg^{2+} and Fe^{2+} in biotite. In this experiment (with the De Geerdalen Fm. sst II), only very limited Fe^{2+}-concentrations were detected (< 0.1 ppm). Therefore, this is not included in Figure 6.10.D.

In both experiments, the concentrations of the Mg^{2+}-, Fe^{2+}- and Mn^{2+}-ions could also be explained if the carbonate cement were to be partly dolomitized. This is known to be the case in the sandstones of the De Geerdalen Formation. This would imply that the main dissolution which is observed is dissolution of (partly) dolomitized carbonate cement, providing Ca^{2+}, Mg^{2+}, Fe^{2+} and Mn^{2+}-ions, in combination with leaching of K^{+} and Al^{2+}-ions from clay minerals.

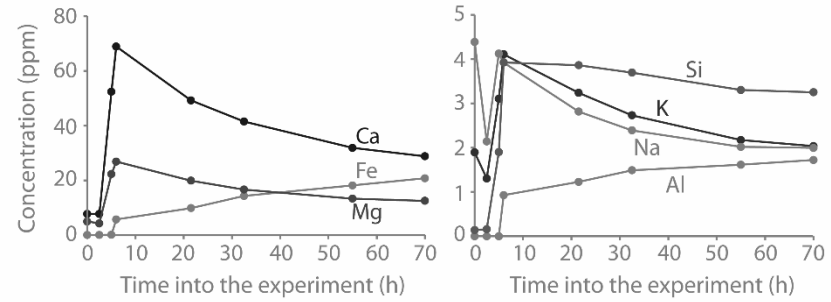

Figure 6.11. Elemental analysis of outflowing liquids in the Wilhelmøya Subgroup rock plug, flushed with an acidic solution with a flow rate of 0.2 µL/s.

In the Wilhelmøya Subgroup plug, micro-CT images did not reveal significant dissolution along the fracture. The carbonate content of this sample was very limited. However, elemental analysis revealed dissolution mechanisms similar to those observed in the De Geerdalen plugs (Figure 6.11). The Ca^{2+}-concentrations were approximately half as high as those observed in the De Geerdalen Fm sst II plug which was tested at the same flow rate. This once more shows that the geochemical reactions were limited by the absence of reactive minerals in the rock matrix.

A striking difference with the plugs from the De Geerdalen Formation, is that in the outflowing liquids of the Wilhelmøya Subgroup plug Si^{4+}-ions were detected. This indicates that silicate minerals have dissolved during the experiment.

6.2.3. Chemical alteration in reservoir samples with rough fractures.

6.2.3.1. Experimental setup

The experiments described above were retaken with slight alterations to the experimental setup, the fluid and rock (fracture) characteristics, and the duration of the experiment. The changes to the experiments are summarized in Table 6.2.

Table 6.2. Changes to the experiments, compared to the experiments described in section 6.2.2.

Component	Previously	New experiments	Reason
Fluid flow pump	MilliGAT® pump	Open source syringe pumps	More experiments can be performed simultaneously
Wilhelmøya sandstone plug	Quartz arenite	Conglomerate from the Brentskardhaugen Bed	The quartz arenite had little to no reactive minerals, as opposed to the conglomerate plug
Rock fracture	Ideal fracture with parallel walls	Rough fracture induced by a Brazilian test	To understand the influence of fracture roughness on dissolution patterns
Acidic solution	Sulfuric acid	Formic acid	Sulfuric acid is known to react with carbonates to form a gypsum crust. This is not the case with formic acid
Experimental duration	Almost 4 days	12 days	A longer time period was chosen to follow the dissolution
Micro-CT system	EMCT	HECTOR	Because of the duration of the experiment, it was not possible to occupy one system continuously as on EMCT

The fluid flow setup was adjusted so that open-source syringe pumps were used to control the fluid flow (Wijnen et al. 2014). This offers the possibility to simultaneously control fluid flow through several rock plugs. However, one has to compromise on both the accuracy of the flow rate, and the maximum pore pressure which can be applied by the pumps. A calibration of the in-house constructed syringe pumps made it possible to set the flow rate to approximately 0.2 µL/s. Three rock plugs, with a diameter of 10 mm and a length of approximately 30 mm, were subjected to a small-scale Brazilian test to induce a tensile, rough fracture in them. These plugs were then glued into a basic fluid flow cell. Two of these rock plugs were obtained from the Brentskardhaugen Bed, the conglomerate section of the Wilhelmøya Subgroup, and one plug was obtained from the same De Geerdalen Formation sandstone section which was previously used. For each of the plugs, a NaCl-brine was made which was set to chemically equilibrate with the different lithologies at a temperature of 40°C for 48h. Subsequently, the plugs were fully saturated with these brines, after which a formic acid solution with a pH of 3.5 was pumped into the plugs. The formic acid was chosen to counteract the possible formation of gypsum crusts on carbonate grains due to the interaction with sulfuric acid. For a total of 12 days, the diluted acid was pumped through the plugs. At regular intervals, the plugs were detached from the fluid flow lines and micro-CT scans were taken on HECTOR. A spatial resolution of approximately 25 µm was obtained.

6.2.3.2. Micro-CT visualization of dissolution

Figure 6.12 shows three cross sections through the obtained micro-CT images after the samples were subjected to an acidic flow for 12 consecutive days. The images show dissolution along the fracture at the lower side of the plug (the inlet side of the acidic solution). This dissolution pattern thins out towards the top of the plug, which is the side of the outflow. Similar to the experiments with an ideal

fracture, the acid is thus buffered by the chemical dissolution of carbonates within the matrix.

At the tested flow rate, the dissolution seems to be spread out into the rock matrix in a homogeneous way across the fracture. No clear observations were made about the precise effect of the roughness of the fracture on the advective flow through the fracture itself. It seemed that the dissolution patterns evolved very similar to the dissolution patterns in Section 6.2.2, with the ideal fractures. If the fluid flow, which constricts the dissolution along the fracture would be greatly affected by the roughness, the fluid flow in the fracture would be concentrated in individual channels. This then would lead to a heterogeneous dissolution pattern across the fracture. Due to pressure constraints of the in-house constructed syringe pumps, it was impossible to increase the flow rate, which is expected to lead to clear wormholing within the fracture.

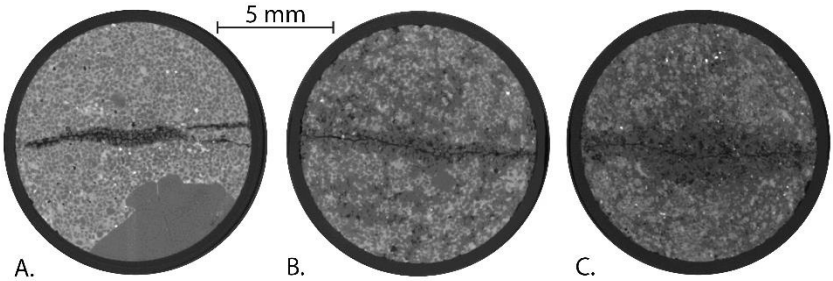

Figure 6.12. Horizontal micro-CT cross-sections through the lower section of the Brentskardhaugen plugs (A & B) and one sandstone plug from the De Geerdalen Formation (C), after being subjected to an acidic flow for 12 days at a flow rate of approximately 0.2 µL/s. This lower section is the side of the inlet of the acidic solution and thus represents the maximum alteration of the rock plugs.

Differential images allowed to quantify the increase in porosity due to the dissolution of the rock's matrix. In the plug of the Brentskardhaugen bed, characterized by a high amount of cementation, this amounted to an increase of only 0.5 % in the entire rock plug. However, it should be noted that this increase was obtained during the first two days of acid testing, at which point the fluid flow lines became obstructed, probably due to quartz grains

which were released from the rock's matrix after dissolution of the carbonate cement around it. In the second plug from the Brentskardhaugen Bed, which represents a porous section of the conglomerate matrix, an increase of 1.9 % in the porosity was observed over 12 days of testing. In the De Geerdalen Formation sandstone plug, the porosity of the sample increased with 3.3 %. It must be noted that these increases are very locally observed and that these values are obtained by applying a very conservative threshold. The quantification of the dissolution is a very user-dependent process. Depending on the applied threshold, the value of the porosity increase can change rapidly. In samples in which the pores are well connected, the dissolution of the matrix can occur further away from the fracture.

6.3. Conclusion

Physical and chemical processes, related to CO_2 injection in a reservoir can locally alter the microscopic structure of the storage unit. With simplified experiments, it was investigated how fractures influence the drying and dissolution behavior in rock plugs of the Longyearbyen CO_2 project. Micro-CT imaging allowed the visualization of the most pronounced processes. The drying behavior in fractured reservoir rocks could be explained by the governing models concerning drying processes in bimodal porous media. However, due to the low inherent permeability of the investigated rock plugs, the experiments could not be conducted up to the point that salt crystallization took place. In the experiments with an acidic flow through fractured rock plugs, micro-CT imaging was limited to the observation of dissolution patterns across the fractures. No precipitation from the brine was observed. It shows that this approach definitely has its drawbacks, linked to the rock volume, the spatial resolution which can be obtained and the limitations of the simple flow cells which were used. To increase chances of observing precipitation from the rock's brine, one would have to test decimeter-long cores, or even longer, in order to ensure that the brine becomes oversaturated

with dissolved matter. The sample preparation for such an experiment would become very difficult if this should be done on the actual reservoir materials. However, one could construct an artificial pore network, resembling that of the reservoir and test this. This would entail a much larger setup than those used in this work, but would allow to visualize the location of both dissolution within the rock material and the precipitation of newly formed minerals.

In Chapter 5, it was shown how natural and induced fractures close when rock plugs are brought to reservoir conditions. The experiments described in this chapter all investigate induced fractures, so that the fracture itself can be distinguished in the micro-CT images. These fractures are characterized by apertures which are several tens of times larger than those of the natural fractures discussed in Chapter 5. Indisputably, this influences the fluid flow properties greatly. Still, as the experiments in Chapter 5 have shown, the main fluid flow pathways in naturally fractured samples are governed by the fractures at depth. On top of this, it is known that the reservoir sections of the Kapp Toscana Group in Spitsbergen are characterized by different fracture sets (as discussed in Chapter 3). The reservoir is at least a triple-porosity system, potentially even a higher-order porosity system. This means that fractures of a larger scale as depicted in Chapter 5 can be expected in the reservoir sections. As such, the induced fractures can still be representative for natural fractures.

Still, it would be advisable to subject induced fractured rock plugs to a high confinement prior to the experiment. This would partly close the induced fracture by crushing weak asperities in it. As such, the fracture aperture distribution would decrease and the roughness of the fracture would be more comparable to naturally fractured samples. The dissolution experiments would further benefit from the use of a brine in which CO_2 is dissolved at high pressures instead of an analogues acidic solution. As such, the actual geochemical reactions would occur in the investigated plugs.

However, in order to ensure that the dissolved CO_2 would not be released as a gas during the course of the experiment, it would be necessary to keep the fluids under pressure during the course of the experiment. This necessitates the use of a more sophisticated fluid flow cell as used in the discussed experiments. From all fluid flow cells available at the UGCT, currently only the small-scale triaxial device provided by SINTEF, Norway would be suited for this. This fluid flow cell comes with more limitations towards the sample size and the amount of samples which can be tested in a given time frame. Although the simplified setups thus do not fully represent the true pore-scale fracture geometries, they do allow more flexibility in adjusting the experimental setup.

7.
Conclusion and future outlook

In this work, unconventional reservoir rocks of the Longyearbyen CO_2 project were used in order to get an insight in pore-scale processes related to CO_2 sequestration in fractured reservoirs. The storage units in the Longyearbyen CO_2 project are known to have a generally low to moderate matrix porosity and a very low related permeability. However, it is also known that these sections contain fractures, ranging from sub-millimetric sizes to several decimeter-long structures. The fluid flow behavior in this system is believed to be greatly affected by the presence of these fractures. In order to understand their influence, it is paramount to get a detailed characterization of their 3D morphology and, more specifically of their aperture distribution. Fracture models can be obtained from logging outcrop sections and slimhole drill cores. This provides insights in fracture occurrence, connectivity and orientation. However, this does not allow to measure the aperture distribution.

In combination with traditional characterization techniques, micro-CT imaging was applied to reservoir sections obtained from rock outcrops and slimhole drill cores (Chapter 3). Only through the combination of different techniques, a full understanding of the

complex pore structure can be obtained in geomaterials in which the pores range from the nanometer scale to several tens of micrometers. As obtaining drill cores is a time-consuming and very costly operation, drill core samples are very valuable. Micro-CT imaging, in combination with other non-destructive techniques to characterize such cores, is thus a very promising technique in order to obtain information on them.

However, some parameters, such as the UCS and the tensile strength of geomaterials, cannot be obtained through non-destructive testing. International standards require decimeter-long cores to be destructively tested in order to obtain data on the mechanical strength of the material. This is a reservoir property, necessary to estimate the wellbore integrity, as well as to approximate rock failure in the fluid injection phase. Obtaining this type of data from rock plugs, with a size much smaller than the prescribed size in the governing international standards, would allow to obtain more valuable data from a similar rock volume. In Chapter 4, a series of small-scale UCS measurements on well-known and fully characterized limestone samples with rather simple to complex pore structures were performed in order to determine if the results on the small samples remained in the range of values expected from tests on bigger samples. For these specific rock types, the UCS could be determined on small-scale plugs. Micro-CT imaging allowed the visualization of weak zones in these plugs along which fractures propagated during the tests. Unfortunately, for the rock plugs from the Longyearbyen CO_2 project reservoir, the UCS was too high for the compression cell available at UGCT. However, as there is a link between the UCS and tensile strength, tensile strength measurements on the rock plugs from the Longyearbyen CO_2 project reservoirs were performed.

In Chapters 5 and 6, fluid flow experiments were conducted to understand the behavior of fractures at depth, as well as the influence of fractures on fluid flow within the reservoir and pore-scale processes related to CO_2 sequestration. Micro-CT scans

allowed a direct measurement of local fracture apertures at different confining pressures in which aperture measurements up to 1/10th of the image resolution could be obtained. Fluid flow simulations based on the segmented fractures at different confining conditions showed the channelization of the fluid's pathway within the fracture with an increasing confinement. The investigated pore-scale processes related to CO_2 sequestration included the drying of the reservoir due to the injection of CO_2, accompanied by the precipitation of salt from the formation brine; as well as the dissolution of carbonates upon dissolution of CO_2 within the formation brine. Both processes are known to occur in the underground, at a given distance from the injection well and can locally alter the reservoir's flow characteristics.

The most important conclusions from these research chapters are summarized below, together with a future outlook towards the optimization of the discussed experiments.

7.1. Material characterization

The sandstone sections of the De Geerdalen Formation and the Wilhelmøya Subgroup are characterized by complex pore structures. Micro-CT scanning allowed to visualize this with a maximum resolution of approximately 3 µm. With the lab-based systems available at the UGCT, higher resolution imaging is possible, up to a resolution of approximately 700 nm. However, this would infer the use of small-scale rock plugs with a diameter just below 1 mm. This is not considered to be desirable due to the heterogeneity within the rock samples. Micro-CT imaging of rock plugs with a diameter of 5 mm at resolutions of 3 µm allowed the extraction of nearly the entire pore space in several high permeable sections within the described sandstone intervals. In this case, image-based fluid flow modelling can help in the understanding of non-wetting phase trapping in the pore network. Different commercially available software packages exist which allow a pore network extraction from segmented micro-CT images. These

models are constantly being improved to include more and more information in order to refine their ability to accurately predict fluid flow properties of the investigated geomaterials. Particularly in the case of the Longyearbyen CO_2 project, they allowed a prediction of local trapping of the injected non-wetting phase in approximately 50% of the pore space of a permeable sandstone section, as well as the determination of relative permeabilities during multi-phase flow. The results which were obtained are in agreement with experimental values obtained through laboratory measurements. However, these experiments are typically very time-consuming, which make the approach in which simulations are performed based on micro-CT images very valuable. Such modelling approaches can however only be applied in the sections in which both the pore bodies and pore throats are resolved by the resolution of the micro-CT scan. Since fluid flow mechanisms in fractures are not necessarily the same as in the remainder of the pore space of geomaterials, fluid flow modelling in fractured rocks is a difficult task. Typically, the pore-network models described in Chapter 3 cannot adequately simulate fluid flow in fractured geomaterials. Since the reservoir sections of the Longyearbyen CO_2 project heavily rely on fractures for their injectivity and, to a lesser amount, for their storage capacity, it is important to understand their influence on fluid flow properties.

7.1.1. Fracture characterization (at depth)

Fracture segmentation from micro-CT images is a difficult task, especially in heterogeneous rock samples. Although specialized scripts and software exist, which keep on getting refined, it remains challenging to digitally isolate the fracture from the overall pore space of the sample. In the reservoir sections from the Longyearbyen CO_2 project, micro-CT scans with a resolution between 30 µm and 50 µm allowed the segmentation of core-scaled fractures. At this resolution, the pore space typically is not resolved, so that the fractures form the least attenuating structures in the cores. Using specialized fracture filtering scripts, it was

possible to segment these fractures in the micro-CT images. Classical micro-CT analysis allowed the further subdivision of the fracture in different fracture segments. Each of these segments can then be treated as an individual object on which different fracture parameters can be determined, such as the aperture and orientation. In this work, the aperture was approximated as the maximum opening of each of these individual fracture segments. By subdividing the fracture in several segments, an estimate of the aperture distribution could be obtained. This was the first time in the Longyearbyen CO_2 project that hard data on the fracture apertures from the drill core samples was obtained. Fracture apertures were similar to those observed in outcrop material from the reservoir, ranging between 40 and 500 µm. Most of the observed fractures were characterized by apertures between 100 and 300 µm.

This type of fracture analysis requires the isolation of the fracture from the micro-CT images, which is strongly user-dependent. As such, measurement errors can be induced which are difficult to avoid. On top of this, the fracture segmentation is done semi-automatically by the software. This implies that the user has little to no choice of the location within the fracture in which a maximum opening is calculated.

To avoid these limitations in the classical micro-CT analysis approach, a Matlab script was written which allows to determine the fracture aperture in micro-CT images as a full-width-half-maximum, or missing attenuation approximation of the attenuation dip caused by a fracture. In this script, the input is a grey value profile across the fracture. To overcome problems related to the heterogeneity of the rock sample, differential imaging can be applied in which micro-CT scans are registered to one another: one micro-CT scan represents the fracture filled with an attenuating fluid (e.g. CsCl-brine), while in the second micro-CT scan, the fracture is drained by the injection of a gas. As such, differential images can be constructed in which the fracture stands

out from the rest of the rock plug. Experiments were conducted with an in-situ triaxial device, in which fractured rock plugs from the Longyearbyen CO_2 project were brought to reservoir pressures. This triaxial device thus simulates the actual conditions at a depth of approximately 700 meters. The experiments were imaged using the EMCT at UGCT. Previously, decompacted cores were scanned in order to get an estimate on the maximum fracture apertures. In this study, however, micro-CT imaging with a spatial resolution of approximately 11 µm allowed the characterization of local fracture apertures as small as 1 µm. Experiments with a natural fracture in a rock plug from the De Geerdalen Formation showed that fractures remained the most important fluid flow pathways, even at a confining pressure of 10 MPa. This is approximately the pressure which is expected at a depth of 700 meters. Although the fracture was barely visible in the micro-CT scans, grey value profiles across it showed that the fracture remained open in at least some locations. These local areas, in which the fracture aperture was measured to be somewhere between 1 µm and 10 µm were responsible for an increase in permeability more than 4 times higher than the permeability of an analogues plug without fracture.

Unfortunately, fracture aperture measurements with this latter technique are also prone to errors. The grey value profiles are supposed to be made perpendicular to the fracture, so small angular discrepancies can affect the aperture measurements. Also, the Matlab script, on which the aperture measurements are based, still requires a strong user-input. A further optimization of this script towards automation would allow a more elaborate and complete characterization of individual fractures. However, this script does allow a more precise aperture characterization than the classical micro-CT approach. On top of this, the aperture of fractures below the resolution of the images can also be quantified based on the partial volume effect. Still, the measurements need to be critically reviewed in order to eliminate occasional measurement errors.

7.1.2. Critical remark on micro-CT imaging of fractures

Fractures tend to complicate micro-CT imaging and quantification in all sorts of materials. Not only in the tight sandstones of the Longyearbyen CO_2 project, but also in geotechnical applications (e.g. desiccation of polymer treated clays used as hydraulic barriers), engineering applications (e.g. self-healing studies in cementitious or polymer materials) and weathering of natural stones (e.g. freeze-thaw disintegration of building stones). Often, the initiation and growth, or closure of micro-cracks is the subject of interest in these applications. Micro-CT imaging allows a way to follow up dynamic interactions in fractured materials. However, in order to identify the smallest fractures, small samples are required. It is the known trade-off between sample size and image resolution which often prohibits the detailed investigation of micro-fractures which are commonly important features with regards to material strength, fluid flow properties, self-healing efficiency of (engineered) materials, onset of weathering, and many other applications. Often, even region of interest scans, in which is focused on only a part of the sample to achieve a higher resolution, is not enough to qualitatively visualize the onset or closure of (micro-) fractures. Experimental setups are therefore often adjusted in order to meet the required sample sizes. However, it is important to keep in mind the scale of the observations and the samples.

In the core samples of the Longyearbyen CO_2 lab, natural fractures were observed in centimeter-wide cores which were scanned at a resolution of 30 – 50 µm. Subsamples from these cores were scanned at a higher resolution (3 – 5 µm), which revealed smaller fractures. Because of the roughness and self-similar structure of natural fractures, not one particular spatial resolution is fully adequate to characterize them. At each resolution, part of the natural fracture will remain unresolved. At a certain moment, it is undesirable to try and increase the resolution further because this would mean that the sample size becomes so small that further

measurements become irrelevant. In this work, the smallest rock plugs were characterized by a diameter of 5 mm and a length of 14 mm. Within this rock plug, a natural fracture was detected with a mean aperture smaller than 10 µm. One could argue about the significance of such fractures within a reservoir in which fractures are present from several micrometer long to more than 1-10 meter long. However, it was shown that even this small fracture locally increases the permeability within the reservoir to a factor of 4-5 times the permeability of an unfractured plug. This information is just as valuable as knowing the influence of decimeter-long fractures, which can be obtained from different testing methods, such as injection tests. In combination with a detailed mapping of the fracture occurrence and connectivity across the different reservoir sections, this information allows a more detailed reservoir model to be constructed, helping in the understanding of the potential storage capabilities of the reservoir. The large fractures are important as potential leakage pathways. The microscopic fractures, however, will influence the storage potential of the system.

7.2. Mechanical behavior

Using a small-scale uniaxial compressive- and tensile device, UCS and tensile strength measurements were performed on small-scale plugs, while having the possibility to monitor the experiment using micro-CT. The UCS measurements were performed on 4 limestone types, which mainly differed from each other in their pore structure. The small-scale UCS measurements were shown to produce reliable UCS values, compared to standard-sized measurements on identical rock types. This is highly valuable in studies in which sample material is sparse, expensive and/or difficult to obtain. Drill core samples from reservoirs at depth comply with this description. However, the well-characterized limestone types, which were tested as reference materials, are commonly used as building material and in cultural heritage. Also in these kind of studies, drilling decimeter-long cores, as required

by the governing international standards, can be problematic. It is not favorable to drill such large samples from buildings or monuments. Small-scale plug measurements can then offer a solution. The combination of the actual strength measurements with micro-CT imaging prior to and after rock mechanical testing further allows a qualitative check through the identification of failure patterns. In the tested materials, this was linked to weak zones of (dissolved) fossils. However, in building materials, weaker zones might be present due to physical, chemical and/or biological weathering. Micro-CT imaging would then allow the identification of patterns which can lower the original mechanical strength of the material.

In the specific case of the Longyearbyen CO_2 lab, the maximum load of the CT5000-TEC device was too limited in order to perform UCS tests on the reservoir samples. However, it was possible to determine the tensile strength of parts of the reservoir section through small-scale Brazilian tests. The results of these tensile strength tests are found within the range of expected strengths reported in literature. However, a larger study would be necessary in order to determine the validity of small-scale plug measurements for tensile strength determination. In such an investigation, high-strength standard sized sandstone samples should be tested alongside a series of small-scaled plugs.

7.3. Pore-scale processes

CO_2 injection into reservoirs locally alters the microscopic structure of the storage unit via several physical and chemical processes. In the direct vicinity of the injection well, the reservoir will dehydrate due to the injection of CO_2. Locally, the reservoir will be fully gas saturated. Behind this zone, a highly saline zone will form in which salts will precipitate from the formation brine. With simplified experiments, drying and precipitation of salt were investigated in a reservoir analogue. This reservoir analogue is known to have a complex pore structure, with micro- and macro-pores which are accessible for fluids through advection through the rock plug, or

through diffusion. These experiments showed initial drying within the advective fluid flow path. The formation brine retracted in the micro-porous zones, accessible through diffusion. Here, the brine concentration increased due to the evaporation of water from the brine. Eventually, salt crystals formed along the crystal surfaces where gas advection took place. This was in agreement with proposed models on drying within multi-modal porous media.

After this, it was investigated how fractures influence the drying behavior in rock plugs of the Longyearbyen CO_2 project. The fracture, which formed the main pathway for both the brine and injected gas within the investigated rock plugs, acted as an advective pathway. The fracture was drained, after which the concentration of the CsCl-brine in the rock matrix along the fracture started to increase. Fluids started to evaporate along the fracture surfaces, which led to the increase of salt-concentration close to the fracture. Because of the low permeability of the rock plugs and the limited time on the micro-CT systems, the experiments could not be conducted long enough to visualize salt precipitation. However, the observed behavior is similar to the model describing drying in the reservoir analogue. This would mean that upon increasing drying, salts would precipitate along the fracture surfaces, locally reducing both fracture porosity and permeability.

Within samples from the De Geerdalen Formation and the Wilhelmøya Subgroup, experiments were also conducted to visualize the effect of acidic flows through fractured reservoir samples. In literature, (reactive) fluid flow in fractured rock sections is most often studied in (chemically pure) limestones or fracture replicas. However, these processes are more complex within sandstones, which are often characterized by a more heterogeneous chemical and mineralogical composition, in which (swelling) clays and minerals such as feldspars contribute to the reactivity within the rocks. The experiments in this PhD thesis showed an increase in the local porosity along the fractures. However, the penetration depth of the alteration was linked to the

pore connectivity within the rock matrix. Samples from the Brentskardhaugen Bed conglomerate section, which were characterized by a high degree of cementation showed pronounced dissolution along the fracture. With increasing permeability, the dissolution was shown to affect the rock plug to a greater depth. In these experiments it is believed that only the fast reacting minerals were seen to dissolve. The applied fluid flow rates were low enough to form homogeneous dissolution patterns across the fracture, in which the roughness of the fracture does not seem to affect the advective flow through the fracture itself. Within the reservoir, the experiments would reflect natural flow regimes. Due to experimental limitations, experiments with a faster flow rate were not conducted. However, considering the injection of CO_2 within the reservoir, such flow rates are to be expected. This would potentially lead to wormholing within the fracture, causing an even more localized dissolution along the widest flow paths of the fracture.

7.4. Impact of research on the Longyearbyen CO_2 project

The Longyearbyen CO_2 project is currently paused. Despite successful water injection tests, no further injection tests are planned and the slimhole wells are closed off. This is mostly related to the reduction of funding for the project. The obtained geophysical data of the reservoir, as well as the drill cores, are, however, still studied an can be obtained for further testing. This is because this data allows a more thorough understanding of unconventional reservoirs in general. This is especially the case when considering the effect of the heterogeneous nature of the reservoir on the subsurface fluid flow.

In this PhD thesis, the first ever hard data on the fractures' aperture distribution of both drill core and outcrop samples was obtained for the Longyearbyen CO_2 project. Also the impact of the burial depth on these fractures was quantified. This can be used to modify the pre-existing models of fluid flow on the field scale. However, as noted, the reservoir of the Kapp Toscana Group is very complex. It

is likely a triple- or even higher-order porosity system. Field scale fluid flow modelling of such networks is highly complicated. The reservoir therefore can be subdivided in different sections. To understand the distribution of fractures and their effect on the fluid conductivity, a fracture mapping per section would be recommended to increase the amount of data on which the fracture aperture input is based.

The investigated pore-scale processes related to CO_2 sequestration have shown the in-situ complex interactions between the pore fluids and the rock's matrix. Although the experiments represented simplified situations, it was possible to visualize the redistribution of brine inside the rock matrix and dissolution of the reactive minerals in centimeter-scaled plugs. In the future, these experiments should be improved in order to represent the in-situ conditions better, so that exact locations of dissolution and especially precipitation of minerals can be determined inside the fractures. Dissolution of material along the fracture walls will also affect the reservoir integrity and strength. This is a crucial parameter for successful injection and storage of CO_2. A separate study on the effect of dissolution on the strength of the reservoir would thus be recommended.

7.5. Experimental recommendations and future outlook

The experiments which were carried out show the broad possibilities in the application of micro-CT scanning to understand subsurface behavior related to the injection of CO_2 for CCS purposes. They will, however, not make or break a CCS project. These experiments can only focus on very limited subsections of the reservoir and provide very detailed information on centimeter-scaled plugs. In the case of the Longyearbyen CO_2 project, reservoir material is relatively readily available. Not only is the Wilhelmøya Subgroup fully cored in two separate drill holes, but both the Wilhelmøya Subgroup and the De Geerdalen Formation are found in outcrop close to the injection site. In other, more conventional reservoirs, rock material is often much less available. In many cases,

the only material which is available from the subsurface reservoir sections are drill cuttings. These small pieces of rock are chipped off and carried to the surface with the drilling fluids. In such cases, the small-scale experiments discussed in this PhD thesis can provide much more valuable information on the reservoir sections at depth. To obtain information on the field scale, several tens to hundreds of these experiments should be carried out, depending on the heterogeneity of the reservoir sections.

In order to understand the influence of fractures on the pore-scale processes within the reservoir sections of the Longyearbyen CO_2 lab, a series of experiments were conducted on fractured plugs. In many of these experiments, the fracture was induced with a Brazilian test. In order to improve the experimental approach, it would be advisable to subject induced fractured rock plugs to a high confinement prior to the experiment. This would partly close the induced fracture by crushing weak asperities in it. As such, the fracture aperture would be more comparable to naturally fractured samples.

The dissolution experiments would further benefit from the use of a brine in which CO_2 is dissolved at high pressures instead of an analogues acid solution. As such, the actual geochemical reactions would occur in the investigated plugs. However, in order to ensure that the dissolved CO_2 would not be released as a gas during the course of the experiment, it would be necessary to keep the fluids under pressure during the course of the experiment. The fluid flow setups should therefore be extended with a backpressure regulator. In the case of the experiments with the in-situ triaxial device of SINTEF, Norway, this would further allow to also control the pore pressure within the investigated rock plugs. As an increase in pore pressure would reduce the effective pressure on a rock plug, different injection pressure settings and their effect on the fracture aperture could be investigated.

It is believed that the in-situ triaxial device, provided by SINTEF, Norway, is not yet used to its full capacity. Temperature control

should be added, as well as a third high pressure pump to control the pore fluids. This triaxial device provides unique opportunities for reservoir testing at lab-based CT facilities. In combination with the fast imaging capability of the EMCT, this allows the visualization of reservoir processes at the pore scale with a temporal resolution of maximum 12 seconds per scan.

References

Abas, N., Kalair, A., and Khan, N., 2015, Review of fossil fuels and future energy technologies: Futures, v. 69, p. 31–49.

Adler, P.M., Thovert, J.-F., and Mourzenko, V. V., 2013, Fractured Porous Media: 175 p.

Al-rkaby, A.H.J., and Alafandi, Z.M.S., 2015, Size Effect on the Unconfined Compressive Strength and Modulus of Elasticity of Limestone Rock: Electronic journal of geotechnical engineering, v. 20, p. 5143–5149.

Ameli, P., Elkhoury, J.E., and Detwiler, R.L., 2013, High-resolution fracture aperture mapping using optical profilometry: Water Resources Research, v. 49, p. 7126–7132.

Andrä, H., Combaret, N., Dvorkin, J., Glatt, E., Han, J., Kabel, M., Keehm, Y., Krzikalla, F., Lee, M., Madonna, C., Marsh, M., Mukerji, T., Saenger, E.H., Sain, R., Saxena, N., Ricker, S., Wiegmann, A., Zhan, X., 2013, Digital rock physics benchmarks—part II: Computing effective properties: Computers & Geosciences, v. 50, p. 33–43.

André, L., Audigane, P., Azaroual, M., and Menjoz, A., 2007, Numerical modeling of fluid–rock chemical interactions at the supercritical CO2–liquid interface during CO2 injection into a carbonate reservoir, the Dogger aquifer (Paris Basin, France): Energy Conversion and Management, v. 48, p. 1782–1797.

Andrew, M., Bijeljic, B., and Blunt, M.J., 2014, New frontiers in

experimental geoscience: X-ray microcomputed tomography and fluid flow: Microscopy and analysis, v. 130, p. s4–s7.

Arts, R., Chadwick, A., Eiken, O., Thibeau, S., and Nooner, S., 2008, Ten years' experience of monitoring CO2 injection in the Utsira Sand at Sleipner, offshore Norway: First Break, v. 26, p. 65–72.

Asadi, M.S., Khaksar, A., Ring, M.J., and Yin Yin, K., 2016, Comprehensive Geomechanical Modeling and Wellbore Stability Analysis for Infill Drilling of High-Angled Wells in a Mature Oil Field, *in* SPE Asia Pacific Oil & Gas Conference and Exhibition, p. SPE-182220-MS.

ASTM C170/C170M-16, 2016, Standard test method for compressive strength of dimension stone, *in* Book of ASTM standards, volume 04.07, West Conshohocken, PA, 2016.

Bachu, S., 2008, CO2 storage in geological media: Role, means, status and barriers to deployment: Progress in Energy and Combustion Science, v. 34, p. 254–273.

Bachu, S., and Dusseault, M.B., 2005, Underground Injection of Carbon Dioxide in Salt Beds: Developments in Water Science, v. 52, p. 637–648.

Barton, N., Bandis, S., and Bakhtar, K., 1985, Strength, deformation and conductivity coupling of rock joints: International Journal of Rock Mechanics and Mining Sciences & Geomechanics Abstracts, v. 22, p. 121–140.

Barton, C.C., and La Pointe, P.R., 2012, Fractals in petroleum geology and earth processes: Springer Science & Business Media, 317 p.

Baruchel, J., Buffiere, J.-Y., Cloetens, P., Di Michiel, M., Ferrie, E., Ludwig, W., Maire, E., and Salvo, L., 2006, Advances in synchrotron radiation microtomography: Scripta Materialia, v. 55, p. 41–46.

Békri, S., Thovert, J.F., and Adler, P.M., 1995, Dissolution of porous media: Chemical Engineering Science, v. 50, p. 2765–2791.

Benson, S., Cook, P., Anderson, J., Bachu, S., Nimir, H.B., Basu, B., Bradshaw, J., Deguchi, G., Gale, J., von Goerne, G., Heidug, W., Holloway, S., Kamal, R., Keith, D., Lloyd, P., Rocha, P., Senior, B., Thomson, J., Torp, T., Wildenbor, T., Wilson, M., Zarlenga, F., and

Zhou, D., 2005, Underground geological storage, *in* Ipcc special report on carbon dioxide capture and storage, p. 195–276.

Bergh, S.G., Braathen, A., and Andresen, A., 1997, Interaction of basement-involved and thin-skinned tectonism in the Tertiary fold-thrust belt of central Spitsbergen, Svalbard: AAPG Bulletin, v. 81, p. 637 - 661.

Bhat, S.K., Kovscek, A.R., and others, 1999, Statistical network theory of silica deposition and dissolution in diatomite: In Situ, v. 23, p. 21–53.

Bieniawski, Z.T., and Bernede, M.J., 1979, Suggested methods for determining the uniaxial compressive strength and deformability of rock materials: International Journal of Rock Mechanics and Mining Sciences & Geomechanics Abstracts, v. 16, p. 137.

Blunt, M.J., Bijeljic, B., Dong, H., Gharbi, O., Iglauer, S., Mostaghimi, P., Paluszny, A., and Pentland, C., 2013, Pore-scale imaging and modelling: Advances in Water Resources, v. 51, p. 197–216.

Blunt, M., Fayers, F.J., and Orr, F.M., 1993, Carbon dioxide in enhanced oil recovery: Energy Conversion and Management, v. 34, p. 1197–1204.

Blythe, A.E., and Kleinspehn, K.L., 1998, Tectonically versus climatically driven Cenozoic exhumation of the Eurasian plate margin, Svalbard: Fission track analyses: Tectonics, v. 17, p. 621–639.

Bohloli, B., Skurtveit, E., Grande, L., Titlestad, G.O., Børresen, M.H., Johnsen, Ø., and Braathen, A., 2014, Evaluation of reservoir and cap-rock integrity for the Longyearbyen CO2 storage pilot based on laboratory experiments and injection tests: Norwegian Journal of Geology, v. 94, p. 171–187.

Boone, M.A., De Kock, T., Bultreys, T., De Schutter, G., Vontobel, P., Van Hoorebeke, L., and Cnudde, V., 2014, 3D mapping of water in oolithic limestone at atmospheric and vacuum saturation using X-ray micro-CT differential imaging: Materials Characterization, v. 97, p. 150–160.

Booth, J., Hong, Q., Compton, R.G., Prout, K., and Payne, R.M., 1997, Gypsum overgrowths passivate calcite to acid attack: Journal of

colloid and interface science, v. 192, p. 207–214.

Bouchelaghem, F., 2010, A numerical and analytical study on calcite dissolution and gypsum precipitation: Applied Mathematical Modelling, v. 34, p. 467–480.

Braathen, A., Bælum, K., Christiansen, H.H., Dahl, T., Elvebakk, H., Hansen, F., Hanssen, T.H., Jochmann, M., Johansen, T.A., Johnsen, H., Larsen, L., Lie, T., Mertes, J., Mørk, A., et al., 2012, The Longyearbyen CO2 Lab of Svalbard, Norway - initial assessment of the geological conditions for CO2 sequestration: Norwegian Journal of Geology, v. 92, p. 353–376.

Brabant, L., Vlassenbroeck, J., De Witte, Y., Cnudde, V., Boone, M.N., Dewanckele, J., and Van Hoorebeke, L., 2011, Three-dimensional analysis of high-resolution X-ray computed tomography data with Morpho+.: Microscopy and microanalysis, v. 17, p. 252–263.

Brown, S.R., 1995, Simple mathematical model of a rough fracture: Journal of Geophysical Research: Solid Earth, v. 100, p. 5941–5952.

Bultreys, T., Boone, M.A., Boone, M.N., De Schryver, T., Masschaele, B., Van Loo, D., Van Hoorebeke, L., and Cnudde, V., 2015a, Real-time visualization of Haines jumps in sandstone with laboratory-based microcomputed tomography: Water Resources Research, v. 51, p. 8668–8676.

Bultreys, T., Van Hoorebeke, L., and Cnudde, V., 2015b, Multi-scale, micro-computed tomography-based pore network models to simulate drainage in heterogeneous rocks: Advances in Water Resources, v. 78, p. 36–49.

Bultreys, T., De Boever, W., and Cnudde, V., 2016a, Imaging and image-based fluid transport modeling at the pore scale in geological materials: A practical introduction to the current state-of-the-art: Earth-Science Reviews, v. 155, p. 93–128.

Bultreys, T., Boone, M.A., Boone, M.N., De Schryver, T., Masschaele, B., Van Hoorebeke, L., and Cnudde, V., 2016b, Fast laboratory-based micro-computed tomography for pore-scale research: Illustrative experiments and perspectives on the future: Advances in Water Resources, v. 95, p. 341–351.

Bultreys, T., Van Stappen, J., De Kock, T., De Boever, W., Boone, M.A., Van Hoorebeke, L., and Cnudde, V., 2016c, Investigating the relative permeability behavior of microporosity-rich carbonates and tight sandstones with multiscale pore network models: Journal of Geophysical Research: Solid Earth, v. 121, p. 7929–7945.

Cao, P., Karpyn, Z.T., and Li, L., 2015, Self-healing of cement fractures under dynamic flow of CO_2-rich brine: Water Resources Research, v. 51, p. 4684–4701.

Chadwick, R.A., Arts, R., and Eiken, O., 2005, 4D seismic quantification of a growing CO2 plume at Sleipner, North Sea, *in* Geological Society, London, Petroleum Geology Conference series, v. 6, p. 1385–1399.

Chang, C., Zoback, M.D., and Khaksar, A., 2006, Empirical relations between rock strength and physical properties in sedimentary rocks: Journal of Petroleum Science and Engineering, v. 51, p. 223–237.

Cnudde, V., and Boone, M.N., 2013, High-resolution X-ray computed tomography in geosciences: A review of the current technology and applications: Earth-Science Reviews, v. 123, p. 1–17.

Coal industry advisory board, 2010, Power Generation from Coal Measuring and Reporting Efficiency Performance and CO 2 Emissions, 112 p.

Costanza-Robinson, M.S., Estabrook, B.D., and Fouhey, D.F., 2011, Representative elementary volume estimation for porosity, moisture saturation, and air-water interfacial areas in unsaturated porous media: Data quality implications: Water Resources Research, v. 47 (7), p. W07513 1-12.

Dallmann, W.K., 1999, Lithostratigraphic lexicon of Svalbard. Upper Paleozoic to Quaternary bedrock. Review and recommendations for nomenclature use: Norwegian Polar Institute, Tromsø, 318 p.

Darcy, H., 1856, The public fountains of the city of Dijon: Dalmont, Paris, 647 p.

Deng, H., Fitts, J.P., and Peters, C.A., 2016, Quantifying fracture geometry with X-ray tomography: Technique of Iterative Local Thresholding (TILT) for 3D image segmentation: Computational Geosciences, v. 20, p. 231–244.

Derluyn, H., Dewanckele, J., Boone, M.N., Cnudde, V., Derome, D., and Carmeliet, J., 2014, Crystallization of hydrated and anhydrous salts in porous limestone resolved by synchrotron X-ray microtomography: Nuclear Instruments and Methods in Physics Research B, v. 324, p. 102–112.

Detwiler, R.L., Glass, R.J., and Bourcier, W.L., 2003, Experimental observations of fracture dissolution: The role of Peclet number on evolving aperture variability: Geophysical Research Letters, v. 30, p. 50 1-4.

Dierick, M., Van Loo, D., Masschaele, B., Van den Bulcke, J., Van Acker, J., Cnudde, V., and Van Hoorebeke, L., 2014, Recent micro-CT scanner developments at UGCT: Nuclear Instruments and Methods in Physics Research Section B: Beam Interactions with Materials and Atoms, v. 324, p. 35–40.

Dijk, P., and Berkowitz, B., 1998, Precipitation and dissolution of reactive solutes in fractures: Water Resources Research, v. 34, p. 457–470.

Dong, H., and Blunt, M., 2009, Pore-network extraction from micro-computerized-tomography images: Physical Review E, v. 80, p. 36307 1–11.

Doughty, C., Freifeld, B.M., and Trautz, R.C., 2008, Site characterization for CO2 geologic storage and vice versa: The Frio brine pilot, Texas, USA as a case study: Environmental Geology, v. 54, p. 1635–1656.

Dunham, R.J., 1962, Classification of carbonate rocks according to depositional texture: American Association of Petroleum Geologists Memoir, v. 1, p. 108–121.

Dvorkin, J., and Nur, A., 2009, Scale of experiment and rock physics trends: The Leading Edge, v. 28, p. 110–115.

Eberhardt, E., Stead, D., and Stimpson, B., 1999, Quantifying progressive pre-peak brittle fracture damage in rock during uniaxial compression: International Journal of Rock Mechanics and Mining Sciences, v. 36, p. 361–380.

Egermann, P., Bekri, S., and Vizika, O., 2005, An integrated approach to assess the petrophysical properties of rocks altered by rock/fluid

interactions (CO2 injection), *in* International symposium of the Society of Core Analysts, Toronto, Canada, p. SCA2005-03: 1-14.

Eysa, E.A., Ramadan, F.S., El Nady, M.M., and Said, N.M., 2016, Reservoir characterization using porosity--permeability relations and statistical analysis: a case study from North Western Desert, Egypt: Arabian Journal of Geosciences, v. 9, p. 403.

Farokhpoor, R., Torsaeter, O., Baghbanbashi, T., Mørk, A., and Lindeberg, E., 2010, Experimental and Numerical Simulation of CO 2 Injection Into Upper-Triassic Sandstones in Svalbard, Norway, *in* Society of Petroleum Engineers, New Orleans, USA, p. SPE 139524 1-11.

Farokhpoor, R., Baghbanbashi, T., Torsæter, O., Lindeberg, E., and Mørk, A., 2011, Experimental and simulation analysis of CO2 storage in tight and fractured sandstone under different stress conditions, *in* 73rd European Association of Geoscientists and Engineers Conference and Exhibition 2011: Unconventional Resources and the Role of Technology. Incorporating SPE EUROPEC, v. 1, p. SPE 143589 1-10.

Farokhpoor, R., Lindeberg, E., Mørk, M.B.E., and Torsæter, O., 2012, CO2-brine relative permeability characteristics of low permeable sandstones in Svalbard, *in* Proceedings of the International Symposium of the Society of Core analysts, Aberdeen, Scotland, UK, p. SCA2012-42: 1-6.

Farokhpoor, R., Lindeberg, E.G.B., Torsaeter, O., Mørk, M.B., and Mørk, A., 2014, Permeability and relative permeability measurements for CO_2 -brine system at reservoir conditions in low permeable sandstones in Svalbard: Greenhouse Gases: Science and Technology, v. 4, p. 36–52.

Fronteau, G., Moreau, C., Thomachot-Schneider, C., and Barbin, V., 2010, Variability of some Lutetian building stones from the Paris Basin, from characterisation to conservation: Engineering Geology, v. 115, p. 158–166.

Fuss, S., Canadell, J.G., Peters, G.P., Tavoni, M., Andrew, R.M., Ciais, P., Jackson, R.B., Jones, C.D., Kraxner, F., Nakicenovic, N., Le Quere, C., Raupach, M.R., Sharifi, A., Smith, P., et al., 2014, Betting on negative

emissions: Nature Climate Change, v. 4, p. 850–853.

Garing, C., Gouze, P., Kassab, M., Riva, · M, Guadagnini, A., Kassab, · M, and Riva, M., 2015, Anti-correlated Porosity–Permeability Changes During the Dissolution of Carbonate Rocks: Experimental Evidences and Modeling: Transport phenomena in Porous Media, v. 107, p. 595–621.

Gasser, T., Guivarch, C., Tachiiri, K., Jones, C.D., and Ciais, P., 2015, Negative emissions physically needed to keep global warming below 2 °C: Nature communications, v. 6, p. 7958 1-7.

Gaus, I., 2010, Role and impact of CO2-rock interactions during CO2 storage in sedimentary rocks: International Journal of Greenhouse Gas Control, v. 4, p. 78–89.

Gaus, I., Audigane, P., André, L., Lions, J., Jacquemet, N., Durst, P., Czernichowski-Lauriol, I., and Azaroual, M., 2008, Geochemical and solute transport modelling for CO2 storage, what to expect from it? International Journal of Greenhouse Gas Control, v. 2, p. 605–625.

Gouze, P., Noiriel, C., Bruderer, C., Loggia, D., and Leprovost, R., 2003, X-ray tomography characterization of fracture surfaces during dissolution: Geophysical Research Letters, v. 30, p. 71: 1-4.

Gustafsson, M.G., 2000, Surpassing the lateral resolution limit by a factor of two using structured illumination microscopy.: Journal of microscopy, v. 198, p. 82–87.

Hakami, E., and Larsson, E., 1996, Aperture measurements and flow experiments on a single natural fracture: International Journal of Rock Mechanics and Mining Sciences & Geomechanics Abstracts, v. 33, p. 395–404.

Hangx, S.J.T., Spiers, C.J., and Peach, C.J., 2010, Mechanical behavior of anhydrite caprock and implications for CO2 sealing capacity: Journal of Geophysical Research B: Solid Earth, v. 115, p. 1–22.

Hanna, R.B., and Rajaram, H., 1998, Influence of aperture variability on dissolutional growth of fissures in Karst Formations: Water Resources Research, v. 34, p. 2843–2853.

Harland, W.B., Anderson, L.M., Manasrah, D., Butterfield, N.J., Challinor, A., Doubleday, P.A., Dowdeswell, E.K., Dowdeswell, J.A.,

Geddes, I., and Kelly, S.R.A., 1997, The geology of Svalbard: Memoirs of the Geological Society of Londen, Geological Society, London, 521 p.

Hawkins, A.B., 1998, Aspects of rock strength: Bulletin of Engineering geology and the environment, v. 57, p. 17–30.

Helland-Hansen, W., 2010, Facies and stacking patterns of shelf-deltas within the Palaeogene Battfjellet Formation, Nordenskiöld Land, Svalbard: implications for subsurface reservoir prediction: Sedimentology, v. 57, p. 190–208.

Henriksen, E., Ryseth, A.E., Larssen, G.B., Heide, T., Rønning, K., Sollid, K., and Stoupakova, A. V, 2011, Tectonostratigraphy of the greater Barents Sea: implications for petroleum systems: Memoirs of the Geological Society of Londen, Geological Society, London, v. 35, p. 163–195.

Hisdal, V., 1998, Svalbard nature and history (A. Brekke, Ed.): Oslo, Norsk Polarinstitutt, 123 p.

Hoek, E., and Brown, E.T., 1980, Underground excavations in rock: Institution of Mining & Metallurgy, 527 p.

Hounsfield, G.N., 1973, Computerized transverse axial scanning (tomography): Part 1. Description of system.: British journal of radiology, v. 46, p. 1016–1022.

Hudson, J.A., and Harrison, J.P., 2000, Engineering rock mechanics - an introduction to the principles.: Elsevier, 441 p.

Huo, D., and Benson, S.M., 2015, An experimental investigation of stress-dependent permeability and permeability hysteresis behavior in rock fractures, *in* Faybishenko, B., Benson, S.M., and Gale, J.E. eds., Fluid dynamics in complex fractured-porous systems, p. 99–114.

Huo, D., Pini, R., and Benson, S.M., 2016, A calibration-free approach for measuring fracture aperture distributions using X-ray computed tomography: Geosphere, v. 12, p. 558–571.

International Energy Agency, 2016, Energy Technology Perspectives 2016: Towards Sustainable Urban energy systems, 16 p.

IPCC, 2013, Summary for Policymakers, *in* Stocker, T.F., D. Qin, G.-K.

Plattner, M. Tignor, S.K. Allen, J. Boschung, A. Nauels, Y. Xia, V.B. and P.M.M. ed., Climate Change 2013: The physical science basis. Contribution of working group I to the fifth assesment report of the Intergovernmental Panel on Climate change, Cambridge, United Kingdom and New York, NY, USA, Cambridge University Press.

IPCC, 2014, Climate Change 2014: Mitigation of Climate Change. Contribution of Working Group III to the Fifth Assessment report of the Intergovernmental Panel on Climate Change (O. Edenhofer, R. Pichs-Madruga, Y. Sokona, E. Farahani, S. Kadner, K. Seyboth, A. Adler, I. Baum, S. Brunner, P. Eickemeier, B. Kriemann, J. Savolainen, S. Schlömer, C. von Stechow, et al., Eds.): Cambridge, United Kingdom and New York, NY, USA., Cambridge University Press.

ISRM, 2007, Suggested method for determining tensile strength of rock materials, *in* Ulusay, R. and Hudson, J.A. eds., The complete ISRM suggested methods for rock characterization, testing and monitoring: 1974-2006, International Society for Rock Mechanics, p. 181–183.

Izgec, O., Demiral, B., Bertin, H., and Akin, S., 2008, CO2 injection into saline carbonate aquifer formations I: Laboratory investigation: Transport in Porous Media, v. 72, p. 1–24.

Jaege, J.C., Cook, N.G.W., and Zimmerman, R.W., 2007, Fundamentals of Rock Mechanics: Blackwell Publishing Ltd, v. 1, 475 p.

Jakubek, J., Holy, T., Jakubek, M., Vavrik, D., and Vykydal, Z., 2006, Experimental system for high resolution X-ray transmission radiography: Nuclear Instruments and Methods in Physics Research Section A: Accelerators, Spectrometers, Detectors and Associated Equipment, v. 563, p. 278–281.

Josh, M., Esteban, L., Delle Piane, C., Sarout, J., Dewhurst, D.N., and Clennell, M.B., 2012, Laboratory characterisation of shale properties: Journal of Petroleum Science and Engineering, v. 88–89, p. 107–124.

Jun, Y.-S., Giammar, D.E., and Werth, C.J., 2013, Impacts of Geochemical Reactions on Geologic Carbon Sequestration: Envirionmental Science and Technology, v. 47, p. 3–8.

Kalinowski, B.E., and Schweda, P., 1996, Kinetics of muscovite, phlogopite, and biotite dissolution and alteration at pH 1-4, room

temperature: Geochimica et Cosmochimica Acta, v. 60, p. 367–385.

Keenan, T.F., Prentice, I.C., Canadell, J.G., Williams, C.A., Wang, H., Raupach, M., and Collatz, G.J., 2016, Recent pause in the growth rate of atmospheric CO2 due to enhanced terrestrial carbon uptake: Nature communications, v. 7, p. 13428 1-9.

Ketcham, R.A., and Carlson, W.D., 2001, Acquisition, optimization and interpretation of X-ray computed tomographic imagery: applications to the geosciences: Computers & Geosciences, v. 27, p. 381–400.

Ketcham, R.A., and Iturrino, G.J., 2005, Nondestructive high-resolution visualization and measurement of anisotropic effective porosity in complex lithologies using high-resolution X-ray computed tomography: Journal of Hydrology, v. 302, p. 92–106.

Ketcham, R.A., Slottke, D.T., and Sharp, J.M., 2010, Three-dimensional measurement of fractures in heterogeneous materials using high-resolution X-ray computed tomography: Geosphere, v. 6, p. 499–514.

Kling, T., Huo, D., Schwarz, J.-O., Enzmann, F., Benson, S., and Blum, P., 2016, Simulating stress-dependent fluid flow in a fractured core sample using real-time X-ray CT data: Solid Earth, v. 7, p. 1109–1124.

Klinkenberg, L.J., 1941, The permeability of porous media to liquids and gases, *in* API Drilling and Production Practice, p. 200-213.

Kranzz, R.L., Frankel, A.D., Engelder, T., and Scholz, C.H., 1979, The permeability of whole and jointed Barre Granite: International Journal of Rock Mechanics and Mining Sciences & Geomechanics Abstracts, v. 16, p. 225–234.

Kwak, H.T., Zhang, G., and Songhua, C., 2005, The effects of salt type and salinity on formation water viscosity and NMR responses, *in* Proceedings of the Society of Core Analysts, Toronto, Canada, p. SCA2005-51 1-13.

Lamy-Chappuis, B., Angus, D., Fisher, Q., Grattoni, C., and Yardley, B.W.D., 2014, Enriched brine injection: Geophysical Research Letters, v. 41, p. 399–406.

Landis, E.N., and Keane, D.T., 2010, X-ray microtomography: Materials Characterization, v. 61, p. 1305–1316.

Lehmann, P., and Or, D., 2009, Evaporation and capillary coupling across vertical textural contrasts in porous media: Physical Review E, v. 80, p.046318 1-13.

Leung, D.Y.C., Carmanna, G., and Maroto-Valer, M.M., 2014, An overview of current status of carbon dioxide capture and storage technologies: Renewable and sustainable energy reviews, v. 39, p. 426–443.

Li, D., and Wong, L.N.Y., 2013, The brazilian disc test for rock mechanics applications: Review and new insights: Rock Mechanics and Rock Engineering, v. 46, p. 269–287.

Lockner, D., 1993, The role of acoustic emission in the study of rock fracture: International Journal of Rock Mechanics and Mining Sciences & Geomechanics Abstracts, v. 30, p. 883–899.

Long, J.C.., Aydin, A., Brown, S.R., Einstein, H.H., Hestir, K., Hsieh, P.A., Myer, L.R., Nolte, Kenneth, G., Norton, D.L., Olsson, O.L., Paillet, F.L., Smith, J.L., and Thomsen, L., 1996, Rock Fractures and Fluid Flow: contemporary understanding and applications: National Academy of Sciences, USA, 568 p.

Lüthje, C.J., Milàn, J., Hurum, J.H., Milan, J., and Hurum, J.H., 2010, Paleocene tracks of the mamal pantodont genus Titanoides in coal-bearing strata, Svalbard, Arctic Norway: Journal of Vertebrate Paleontology, v. 30, p. 521–527.

Magnabosco, C., Braathen, A., and Ogata, K., 2014, Permeability model of tight reservoir sandstones combining core-plug and miniperm analysis of drillcore; Longyearbyen CO2 lab, Svalbard: Norwegian Journal of Geology, v. 94, p. 189–200.

Maire, E., and Withers, P.J., 2014, Quantitative X-ray tomography: International Materials Reviews, v. 59, p. 1–43.

Makhloufi, Y., Collin, P.Y., Bergerat, F., Casteleyn, L., Claes, S., David, C., Menendez, B., Monna, F., Robion, P., Sizun, J.P., Swennen, R., and Rigollet, C., 2013, Impact of sedimentology and diagenesis on the petrophysical properties of a tight oolitic carbonate reservoir. The case of the Oolithe Blanche Formation (Bathonian, Paris Basin, France): Marine and Petroleum Geology, v. 48, p. 323–340.

Maldal, T., and Tappel, I.., 2004, CO2 underground storage for Snøhvit gas field development: Energy, v. 29, p. 1403–1411.

Malmström, M., and Banwart, S., 1997, Biotite dissolution at 25°C: The pH dependence of dissolution rate and stoichiometry: Geochimica et Cosmochimica Acta, v. 61, p. 2779–2799.

Marrett, R., Ortega, O.J., and Kelsey, C.M., 1999, Extent of power-law scaling for natural fractures in rock: Geology, v. 27, p. 799–802.

Marshall, C., Large, D.J., Meredith, W., Snape, C.E., Uguna, C., Spiro, B.F., Orheim, A., Jochmann, M., Mokogwu, I., Wang, Y., and Friis, B., 2015, Geochemistry and petrology of Palaeocene coals from Spitsbergen — Part 1: Oil potential and depositional environment: International journal of coal geology, v. 143, p. 22–33.

Masschaele, B.C., Cnudde, V., Dierick, M., Jacobs, P., Van Hoorebeke, L., and Vlassenbroeck, J., 2007, UGCT: New X-ray radiography and tomography facility: Nuclear Instruments and Methods in Physics Research Section A: Accelerators, Spectrometers, Detectors and Associated Equipment, v. 580, p. 266–269.

Masschaele, B., Dierick, M., Loo, D. Van, Boone, M.N., Brabant, L., Pauwels, E., Cnudde, V., and Van Hoorebeke, L., 2013, HECTOR: A 240kV micro-CT setup optimized for research: Journal of Physics: Conference Series, v. 463, p. 12012 1-4.

Matter, J.M., Broecker, W.S., Stute, M., Gislason, S.R., Oelkers, E.H., Stefánsson, A., Wolff-Boenisch, D., Gunnlaugsson, E., Axelsson, G., and Björnsson, G., 2009, Permanent Carbon Dioxide Storage into Basalt: The CarbFix Pilot Project, Iceland: Energy Procedia, v. 1, p. 3641–3646.

Matter, J.M., Stute, M., Hall, J., Mesfin, K., Snæbjörnsdóttir, S.Ó., Gislason, S.R., Oelkers, E.H., Sigfusson, B., Gunnarsson, I., Aradottir, E.S., Alfredsson, H.A., Gunnlaugsson, E., and Broecker, W.S., 2014, Monitoring permanent CO2 storage by in situ mineral carbonation using a reactive tracer technique: Energy Procedia, v. 63, p. 4180–4185.

Mazumder, S., Wolf, K.-H.A.A., Elewaut, K., and Ephraim, R., 2006, Application of X-ray computed tomography for analyzing cleat spacing and cleat aperture in coal samples: International Journal of

Coal Geology, v. 68, p. 205–222.

van der Meer, L.G.H., 1993, The conditions limiting CO2 storage in aquifers: Energy Conversion and Management, v. 34, p. 959–966.

Mehrabi Mazidi, S., Haftani, M., Bohloli, B., and Cheshomi, A., 2012, Measurement of uniaxial compressive strength of rocks using reconstructed cores from rock cuttings: Journal of Petroleum Science and Engineering, v. 86–87, p. 39–43.

Menke, H.P., Bijeljic, B., and Blunt, M.J., 2017, Dynamic reservoir-condition microtomography of reactive transport in complex carbonates: Effect of initial pore structure and initial brine pH: Geochimica et Cosmochimica Acta, v. 204, p. 267–285.

Metz, B., Davidson, O., De Coninck, H., Loos, M., and Meyer, L., 2005, IPCC special report on carbon dioxide capture and storage, Cambridge University Press, New York, 431 p.

Miao, T., Yu, B., Duan, Y., and Fang, Q., 2015, A fractal analysis of permeability for fractured rocks: International Journal of Heat and Mass Transfer, v. 81, p. 75–80.

Michael, G., 2001, X-ray computed tomography: Physics Education, v. 36, p. 442–451.

Michael, K., Golab, A., Shulakova, V., Ennis-King, J., Allinson, G., Sharma, S., and Aiken, T., 2010, Geological storage of CO2 in saline aquifers - A review of the experience from existing storage operations: International Journal of Greenhouse Gas Control, v. 4, p. 659–667.

Miri, R., Hellevang, H., Braathen, A., and Aagaard, P., 2014, Phase relations in the Longyearbyen CO2 lab reservoir - forecasts for CO2 injection and migration: Norwegian Journal of Geology, v. 94, p. 217–232.

Mørk, A., Embry, A.F., and Weitschat, W., 1989, Triassic transgressive-regressive cycles in the Sverdrup Basin, Svalbard and the Barents Shelf, *in* Correlation in hydrocarbon exploration, Springer, p. 113–130.

Mørk, M.B.E., 2013, Diagenesis and quartz cement distribution of low-permeability Upper Triassic - Middle Jurassic reservoir sandstones,

Longyearbyen CO2 lab well site in Svalbard, Norway: American Association of Petroleum Geology Bulletin, v. 97, p. 577–596.

Mourzenko, V.V., Thovert, J.-F., and Adler, P.M., 1995, Permeability of a Single Fracture; Validity of the Reynolds Equation: Journal of Physics, v. 5, p. 465–482.

Mulrooney, M.J., Larsen, L., Rismyhr, B., Van Stappen, J., Senger, K., Braathen, A., Mork, M.B., Olaussen, S., Cnudde, V., and Ogata, K., in prep.: Fluid flow properties of a potential unconventional CO2 storage unit in central Spitsbergen: the Upper Triassic to Middle Jurassic Wilhelmoya Subgroup: Norwegian Journal of Geology.

Nachshon, U., Weisbrod, N., Dragila, M.I., and Grader, A., 2011, Combined evaporation and salt precipitation in homogeneous and heterogeneous porous media: Water Resources Research, v. 47, p. W03513 1-16.

Nachtrab, F., Hofmann, T., Speier, C., Lučić, J., Firsching, M., Uhlmann, N., Takman, P., Heinzl, C., Holmberg, A., Krumm, M., and Sauerwein, C., 2015, Development of a Timepix based detector for the NanoXCT project: Journal of Instrumentation, v. 10, p. C11009 1-8.

Noiriel, C., Gouze, P., and Madé, B., 2013, 3D analysis of geometry and flow changes in a limestone fracture during dissolution: Journal of Hydrology, v. 486, p. 211–223.

Oelkers, E.H., Gislason, S.R., and Matter, J., 2008, Mineral Carbonation of CO2: Elements, v. 4, p. 333–337.

Ogata, K., Senger, K., Braathen, A., Tveranger, J., and Olaussen, S., 2012, The importance of natural fractures in a tight reservoir for potential CO2 storage: a case study of the upper Triassic–middle Jurassic Kapp Toscana Group (Spitsbergen, Arctic Norway), *in* Advances in the study of fractured reservoirs, Geological Society of London, Special publications, v. 374, p. 395–415.

Ogata, K., Senger, K., Braathen, A., Olaussen, S., and Tveranger, J., 2013, High-resolution Fracture Characterization of a Siliciclastic Aquifer Targeted for CO2 Sequestration, Svalbard, Norway, *in* Sustainable Earth Sciences, Pau, France, p. P006 1-5.

Ogata, K., Senger, K., Braathen, A., Tveranger, J., and Olaussen, S.,

2014, Fracture systems and mesoscale structural patterns in the siliciclastic Mesozoic reservoir-caprock succession of the Longyearbyen CO2 Lab project : Implications for geological CO2 sequestration in Central Spitsbergen , Svalbard: Norwegian Journal of Geology, v. 4, p. 121–154.

Olajire, A.A., 2013, A review of mineral carbonation technology in sequestration of CO2: Journal of Petroleum Science and Engineering, v. 109, p. 364–392.

Olson, R.K., and Grigg, M.W., 2008, Mercury injection capillary pressure MICP a useful tool for improved understanding of porosity and matrix permeability distributions in shale reservoirs: Annual Meeting - American Association of Petroleum Geologists, San Antonio, Texas, USA, p. 90078.

Orr, F.M.J., 2009, CO2 capture and storage: are we ready?: Energy and Environmental Science, v. 2, p. 449–458.

Ott, H., Andrew, M., Snippe, J., and Blunt, M.J., 2014, Microscale solute transport and precipitation in complex rock during drying: Geophysical Research Letters, v. 41, p. 8369–8376.

Oxburgh, R., Drever, J.I., and Sun, Y.-T., 1994, Mechanism of plagioclase dissolution in acid solution at 25°C: Geochimica et Cosmochimica Acta, v. 58, p. 661–669

Page, B., 2016, The Global Status of CCS: 2016 Summary report, 28 p.

Paterson, M.S., and Wong, T., 2005, Experimental rock deformation-the brittle field: Springer Science & Business Media, 255 p.

Piessens, K., and Dusar, M., 2004, Feasibility of CO2 sequestration in abandoned coal mines in Belgium: Geologica Belgica, v. 7, p. 165–180.

du Plessis, A., le Roux, S.G., and Guelpa, A., 2016, Comparison of medical and industrial X-ray computed tomography for non-destructive testing: Case Studies in Nondestructive Testing and Evaluation, v. 6, p. 17–25.

Poon, C.Y., Sayles, R.S., and Jones, T.A., 1992, Surface measurement and fractal characterization of naturally fractured rocks: Journal of Physics D: Applied Physics, v. 25, p. 1269–1275.

Rabbani, E., Sharif, F., Koolivand Salooki, M., and Moradzadeh, A., 2012, Application of neural network technique for prediction of uniaxial compressive strength using reservoir formation properties: International Journal of Rock Mechanics and Mining Sciences, v. 56, p. 100–111.

Rahmouni, A., Boulanouar, A., Boukalouch, M., Géraud, Y., Samaouali, A., Harnafi, M., and Sebbani, J., 2014, Relationships between porosity and permeability of calcarenite rocks based on laboratory measurements: Journal of materials and environmental sciences, v. 5, p. 931–936.

Rismyhr, B., Bjaerke, T., Olaussen, S., Mulrooney, M.J., Mork, A., and Senger, K., in prep.: Sedimentological, palynological and sequence stratigraphic analysis of a highly condensed Upper Triassic to Middle Jurassic succession; the Wilhelmoya Subgroup in central western Spitsbergen: Norwegian Journal of Geology.

Rocco, C., Guinea2, G. V, Planas, J., and Elices, M., 1999, Size effect and boundary conditions in the Brazilian test: Experimental verification: Materials and Structures, v. 32, p. 210–217.

Rød, R.S., Hynne, I.B., and Mørk, A., 2014, Depositional environment of the Upper Triassic De Geerdalen Formation - an E-W transect from Edgeoya to Central Spitsbergen, Svalbard: Norwegian Petroleum Directorate Bulletin, v. 11, p. 21–40.

Roels, S., Elsen, J., Carmeliet, J., and Hens, H., 2001, Characterisation of pore structure by combining mercury porosimetry and micrography: Materials and Structures, v. 34, p. 76–82.

Rohmer, J., Pluymakers, A., and Renard, F., 2016, Mechano-chemical interactions in sedimentary rocks in the context of CO2 storage: Weak acid, weak effects?: Earth-Science Reviews, v. 157, p. 86–110.

Rosenbauer, R.J., Koksalan, T., and Palandri, J.L., 2005, Experimental investigation of CO2-brine–rock interactions at elevated temperature and pressure: Implications for CO2 sequestration in deep-saline aquifers: Fuel Processing Technology, v. 86, p. 1581–1597.

Roy, S., Senger, K., Braathen, A., Noormets, R., Hovland, M., and Olaussen, S., 2014, Fluid migration pathways to seafloor seepage in

inner Isfjorden and Adventfjorden, Svalbard: Norwegian Journal of Geology, v. 94, p. 99–119.

Sahimi, M., 2011, Characterization of fractures, fracture networks and fractured porous media, *in* Flow and transport in Porous media and fractured rock: from classical methods to modern approaches, p. 143–177.

Sand, G., Braathen, A., and Olaussen, S., 2014, Longyearbyen CO2 Lab - tales of research and education: Norwegian Journal of Geology, v. 94, p. 77–82.

Sanderson, B.M., O'Neill, B.C., and Tebaldi, C., 2016, What would it take to achieve the Paris temperature targets? Geophysical Research Letters, v. 43, p. 7133–7142.

Schindelin, J., Arganda-Carreras, I., Frise, E., Kaynig, V., Longair, M., Pietzsch, T., Preibisch, S., Rueden, C., Saalfeld, S., Schmid, B., Tinevez, J.-Y., White, D.J., Hartenstein, V., Eliceiri, K., et al., 2012, Fiji: an open-source platform for biological-image analysis: Nature Methods, v. 9, p. 676–682.

Schmittbuhl, J., Steyer, A., Jouniaux, L., and Toussaint, R., 2008, Fracture morphology and viscous transport: International Journal of Rock Mechanics and Mining Sciences, v. 45, p. 422–430.

Seibert, J.A., and Boone, J.M., 2005, X-ray imaging physics for Nuclear Medicine Technologists. Part 2: X-ray interactions and image formation: Journal of Nuclear Medicine Technology, v. 33, p. 3–18.

Senger, K., Tveranger, J., Braathen, A., Olaussen, S., Ogata, K., and Larsen, L., 2015, CO2 storage resource estimates in unconventional reservoirs: insights from a pilot-sized storage site in Svalbard, Arctic Norway: Environmental Earth Sciences, v. 73, p. 3987–4009.

Senger, K., Betlem, P., Liira, M., Roy, S., Midttomme, K., Beka, T.I., Olaussen, S., and Ohm, S., 2017, Integrated thermo-baric modelling of the gas hydrate stability zone onshore Svalbard, Arctic Norway, *in* 9th International Conference on Gas Hydrates, poster.

Shen, L., and Chen, Z., 2007, Critical review of the impact of tortuosity on diffusion: Chemical Engineering Science, v. 62, p. 3748–3755.

Siegesmund, S., and Dürrast, H., 2011, Physical and Mechanical

Properties of Rocks, *in* Stone in Architecture - Properties, Durability, p. 97-224.

Snow, D.T., 1968, Rock fracture spacings, openings, and porosities.: Journal of Soil Mechanics & Foundations Div., v. 94, p. 73–91.

Solomon, S., Carpenter, M., and Flach, T.A., 2008, Intermediate storage of carbon dioxide in geological formations: A technical perspective: International Journal of Greenhouse Gas Control, v. 2, p. 502–510.

Van Geet, M., and Swennen, R., 2001, Quantitative 3D-fracture analysis by means of microfocus X-ray Computed tomography (µCT): An example from coal.: Geophysical Research Letters, v. 28, p. 3333–3336.

Van Stappen, J., De Kock, T., Boone, M.A., Olaussen, S., and Cnudde, V., 2014, Pore-scale characterisation and modelling of CO2 flow in tight sandstones using X-ray micro-CT; Knorringfjellet Formation of the Longyearbyen CO2 Lab, Svalbard: Norwegian Journal of Geology, v. 94, p. 201–215.

Steel, R.J., and Worsley, D., 1984, Svalbard's post-Caledonian strata: an atlas of sedimentational patterns and palaeogeographic evolution, *in* Petroleum geology of the North European margin, Springer, p. 109–135.

Stern, N., 2006, The economics of climate change: the stern review: 643 p.

Szwedzicki, T., and Shamu, W., 1999, The effect of discontinuities on strength of rock samples: The AusIMM Proceedings., Australasian institute of mining an metallurgy, v. 304, p. 23–28.

Szymczak, P., and Ladd, A.J.C., 2009, Wormhole formation in dissolving fractures: Journal of Geophysical Research: Solid Earth, v. 114, p. B06203 1-22.

Tanikawa, W., and Shimamoto, T., 2006, Klinkenberg effect for gas permeability and its comparison to water permeability for porous sedimentary rocks: Hydrology and Earth System Sciences Discussions, European Geosciences Union, v. 3, p. 1315–1338.

Tharp, T.M., 1987, Conditions for crack propagation by frost wedging:

Geological Society of America Bulletin, v. 99, p. 94–102.

Throndsen, J., 1982, Oil pollution and plankton dynamics: III. Effects on flagellate communities in controlled ecosystem experiments in Lindåspollene, Norway, June 1980 and 1981: Sarsia, v. 67, p. 163–169.

Thuro, K., Plinninger, R.J., Zäh, S., and Schütz, S., 2001, Scale effects in rock strength properites. Part 1: Unconfined compressive test and Brazilian test, *in* Särkkä and Eloranta eds., ISRM Regional Symposium Eurorock, Espoo, Finland, p. 169–174.

UNE-EN 1926, 2007, Natural stone test methods - Determination of uniaxial compressive strength: European Committee for Standardization, 17 p.

UNE-EN 1936, 2006, Natural stone test methods - Determination of Real Density and Apparent Density, and of Total and Open Porosity: European Committee for Standardization, 11 p.

UNFCCC, 2015, United Nations framework convention on climate change; Adoption of the Paris agreement, 32 p.

US Energy Information Administration, 2016, International energy outlook 2016 with projections to 2040, 276 p.

Vandersteen, K., Busselen, B., Van Den Abeele, K., and Carmeliet, J., 2003, Applications of X-ray computed tomography in the geosciences: Geological Society, London, Special Publications, v. 215, 61-68 p.

Vincent, L., and Soille, P., 1991, Watersheds in digital spaces: an efficient algorithm based on immersion simulations: IEEE Transactions on Pattern Analysis and Machine Intelligence, v. 13, p. 583–598.

Vlassenbroeck, J., Dierick, M., Masschaele, B., Cnudde, V., Van Hoorebeke, L., and Jacobs, P., 2007, Software tools for quantification of X-ray microtomography at the UGCT: Nuclear Instruments and Methods in Physics Research Section A: Accelerators, Spectrometers, Detectors and Associated Equipment, v. 580, p. 442–445.

Vlassenbroeck, J., 2009, Advances in laboratory-based X-ray microtomography: PhD thesis, Ghent University.

Voorn, M., Exner, U., and Rath, A., 2013, Multiscale Hessian fracture filtering for the enhancement and segmentation of narrow fractures in 3D image data: Computers & Geosciences, v. 57, p. 44–53.

Washburn, E.W., 1921, Note on method of determining the distribution of pores sizes in a porous material: Proceedings of the National Academy of Sciences, v. 7, p. 115–116.

Whittaker, S., Rostron, B., Hawkes, C., Gardner, C., White, D., Johnson, J., Chalaturnyk, R., and Seeburger, D., 2011, A decade of CO2 injection into depleting oil fields: Monitoring and research activities of the IEA GHG Weyburn-Midale CO2 Monitoring and Storage Project: Energy Procedia, v. 4, p. 6069–6076.

Wijnen, B., Hunt, E.J., Anzalone, G.C., and Pearce, J.M., 2014, Open-Source Syringe Pump Library: PLOS ONE, v. 9, p. 1–8.

Wildenschild, D., and Sheppard, A.P., 2013, X-ray imaging and analysis techniques for quantifying pore-scale structure and processes in subsurface porous medium systems: Advances in Water Resources, v. 51, p. 217–24.

Witherspoon, P.A., Wang, J.S.Y., Iwai, K., and Gale, J.E., 1980, Validity of Cubic Law for Fluid Flow in a Deformable Rock Fracture: Water Resources Research, v. 16, p. 1016–1024.

Würdemann, H., Möller, F., Kühn, M., Heidug, W., Christensen, N.P., Borm, G., Schilling, F.R., and Group, the C., 2010, CO2SINK-From site characterisation and risk assessment to monitoring and verification: One year of operational experience with the field laboratory for CO2 storage at Ketzin, Germany: International Journal of Greenhouse Gas Control, v. 4, p. 938–951.

Zimmerman, R.W., Al-Yaarubi, A., Pain, C.C., and Grattoni, C.A., 2004, Non-linear regimes of fluid flow in rock fractures: International Journal of Rock Mechanics and Mining Sciences, v. 41, p. 163–169.

Appendix A

In this appendix, the Matlab codes used for fracture aperture and orientation characterization are shortly described. To clarify the script itself, short comment sections are added, preceded by the percentage sign (%). It must be noted that the variables in this script are defined by a mix between English and Dutch words. Undoubtedly, the script can be shorter and more efficient. However, these are the codes that were used to analyze fractures in this work. The Matlab version that was used in this dissertation is Matlab R2015b. No guarantee is given that these codes work on earlier versions of the software.

A.1. Aperture characterization

This script uses grey value profiles perpendicular to fractures. A number of such profiles can be made in Fiji (Schindelin et al., 2012) and saved in a folder as individual .txt-files. As a first step, the Matlab script imports the data in these individual files into one matrix in which each column contains the grey values of each voxel along one grey value profile.

```
% Determination of the number of profiles taken (q) and the
% number of voxels per grey value profile (g).
d = dir('*.txt');
nfiles = length(d);
q = nfiles;
g = importdata(d(1).name);
g = g.data;
g = size(g);
g = g (1,1);

% Import of the grey values per voxel for each of the grey value
% profiles.
x = [];
GreyValues = zeros(g, q);
for k = 1:q
    x = [x; importdata(d(k).name)];
    GreyValues(1:g, k) = x(k).data(1:g, 2);
end

% Clear working variables
 clear  d k x
```

When the data has been imported, a point-spread function has to be fitted to each of the profiles. Normally, the grey value peak, which represents the fracture in the micro-CT data is found at approximately the same position in the consecutive profiles. The user is therefore asked to define some initial parameters in order to fit the point-spread function to the profiles. The previously defined parameters ‘g’ and ‘q’, which represent the number of voxels per profile and the amount of grey value profiles respectively, are taken along to the following section.

```
warning('off','curvefit:cfit:subsasgn:coef
fsClearingConfBounds');
```

% Definition of input parameters.

```
prompt = {'Guess the peak height a:','Guess the
peak position b:','Guess the peak width
c:','Guess the amplitude d of the variation in
material greyscale:','Guess the frequency e of
the variation in material greyscale:','Guess the
phase f of the variation in material
greyscale:','Give the average material greyscale
value g:'};
name = 'Input for Peaks function';
guess = {'20000', '(number of rows)/2', '10',
'2000','5', '500', '34000'};
answer = inputdlg(prompt,name, 1, guess);
```

% Change the user answers from a string to a number.

```
A = answer(1);  A=cell2mat(A); A= str2num(A);
B = answer(2);  B=cell2mat(B); B= str2num(B);
C = answer(3);  C=cell2mat(C); C= str2num(C);
D = answer(4);  D=cell2mat(D); D= str2num(D);
E = answer(5);  E=cell2mat(E); E= str2num(E);
F = answer(6);  F=cell2mat(F); F= str2num(F);
G = answer(7);  G=cell2mat(G); G= str2num(G);
Startingpoint = [A B C D E F G];
clear prompt name guess answer A B C D E F G;
```

% Definition of working variables.

```
X_values = zeros(g,1);
for n = 1:g
    X_values(n, 1) = n;
end
valuesfromfit = zeros(1,q);
```

% Fit the model to the data per grey value profile.
% Plot each fit separately and ask the user to evaluate the fit.

```
for n = 1:q
    test = GreyValues(1:g, n);
    [xData, yData] = prepareCurveData(X_values,
     test);
    % Set up fittype and options.
    ft    =    fittype(    'g    -    a*exp(-((x-
     b)/c)^2)+d*sin(2*pi*x/e+f)',
     'independent', 'x', 'dependent', 'y' );
```

```
        opts = fitoptions( ft );
        opts.Display = 'Off';
        opts.Lower = [-Inf -Inf -Inf -Inf -Inf -Inf
       -Inf];
        opts.StartPoint = Startingpoint;
        opts.Upper = [Inf Inf Inf Inf Inf Inf Inf];

        % Fit model to data.
        [CT_results{n}, gof] = fit(xData, yData, ft,
       opts);
        % Plot fit to data.
        j = figure('Name', num2str(n));
        h = plot(CT_results{n}, xData, yData);
        legend(h, 'test vs. xtest', 'untitled fit
       1', 'Location', 'SouthEast');
        % Label axes
        xlabel('position (voxels)');
        ylabel('CT value');
        grid on;
        button = MFquestdlg([0.2,0.2],'Do we need to
       retain this graph?');
            switch button
            case 'No'
                CT_results{1,n}.a = 0;
                CT_results{1,n}.g = 0;
            end
        close(j);
        % Save the result from an individual fit
        valuesfromfit(1,n) = CT_results{1,n}.a;
        valuesfromfit(2,n) = CT_results{1,n}.b;
        valuesfromfit(3,n) = CT_results{1,n}.c;
        valuesfromfit(4,n) = CT_results{1,n}.d;
        valuesfromfit(5,n) = CT_results{1,n}.e;
        valuesfromfit(6,n) = CT_results{1,n}.f;
        valuesfromfit(7,n) = CT_results{1,n}.g;
    end

% Save the results of the fits and clean up the workspace.
    assignin('base', 'FittedFunction', CT_results);
    clear button c CT_results ft gof grootte h j n
    opts r Startingpoint test valuesfromfit X_values
    xData yData
```

At this moment, the user has fitted a PSF to each of the grey value profiles initially determined. This is a computationally intensive task. Therefore, it was chosen to separate the PSF fitting process

and the determination of a FWHM, or MA from each of the PSF fits. The user has to save the workspace at this moment and use another function to determine the FWHM, or MA. All data can be deleted in the workspace, except for the “FittedFunction” variable, and the initial “GreyValues” variable. In the following function, the user has to put in the name of the workspace that was just saved (XXX.mat).

```
% The user is asked for the workspace variable to work with.
% This is the “FittedFunction” variable. The user is also asked
% for the resolution of the micro-CT scan. This is defined in
% micrometer.
prompt = 'Define the workspace variable to work
with:';
FittedValues = input(prompt,'s');
prompt = {'What is the resolution of the micro-
CT scan (in micrometer)?'};
name = 'Resolution';
answer = inputdlg(prompt,name, 1);
resolution = answer(1);
resolution=cell2mat(resolution); resolution=
str2num(resolution);
warning('off','symbolic:solve:FallbackToNumeric
al');

% In the following section, the user has to put in the name of
% the workspace that was just saved.
werking = load('XXX.mat', FittedValues);

% This workspace is opened and the parameters of the PSF fit
% are loaded and saved as FittedValues.
FittedValues = getfield(werking, FittedValues);
clear werking;

% Definition of working variables.
grootte=size(FittedValues);
k = grootte(1,2);
FWHM = zeros(4,k);
values_function = zeros(7,k);
syms a b c d e f g x real;
```

At this moment, the user has prepared the workspace in order to define the FWHM and/or MA of the dip in attenuation based on

the PSF fitting process. First, the method to determine the FWHM is given:

```
for n= 1:k;
    h = waitbar(n/k, [num2str(n/k*100) '%']);
    a = FittedValues{1,n}.a;
    b = FittedValues{1,n}.b;
    c = FittedValues{1,n}.c;
    d = FittedValues{1,n}.d;
    e = FittedValues{1,n}.e;
    f = FittedValues{1,n}.f;
    g = FittedValues{1,n}.g;
    values_function(1,n) = a;
    values_function(2,n) = b;
    values_function(3,n) = c;
    values_function(4,n) = d;
    values_function(5,n) = e;
    values_function(6,n) = f;
    values_function(7,n) = g;
    % If the PSF fit was discarded by the user,
    no FWHM is determined
    if a == 0 && g == 0;
      FWHM(1,n) = 0;
      FWHM(2,n) = 0;
      FWHM(3,n) = 0;
      FWHM(4,n) = 0;
    else
    % Else, the FWHM is defined:
      Y_1 = g - a + d*sin(2*pi*b/e + f);
      delta_Y = g - Y_1 ;
      Y_2 = delta_Y/2 + Y_1 ;
      Y_3 = g-a*exp(-((x-b)/c)^2) +
      d*sin(2*pi*x/e + f);
      assume (x > 0);
      s1 = solve (Y_3 == Y_2, x) ;
      if s1 < b;
        assume(x > b);
        s2 = solve(Y_3 == Y_2, x);
      elseif s1 > b;
        assume(x < b);
        s2 = solve(Y_3 == Y_2, x);
      end
    FWHM(1,n) = s1;
    FWHM(2,n) = s2;
    FWHM(3,n) = s2 - s1;
    if FWHM(3,n) < 0;
      FWHM(3,n) = -FWHM(3,n);
    end
```

```
   FWHM(4,n) = FWHM(3,n)*resolution;
  end
close(h);
end
clear s1 s2 s3 s4 s5 s6 Y_1 Y_2 Y_3 x name
prompt g k n f e d a b c answer delta_Y h
```

The FWHM of each of the fits is now saved in the variable FWHM, in the 4th row. Each fit is saved in a different column. To determine the MA, a similar code is written in which first the appropriate data from the PSF fits is taken, and then the MA is determined. In this example, the value for the calibration of air in the sample is taken as 5000:

```
for n= 1:k;
    h = waitbar(n/k, [num2str(n/k*100) '%']);
    a = FittedValues{1,n}.a;
    b = FittedValues{1,n}.b;
    c = FittedValues{1,n}.c;
    d = FittedValues{1,n}.d;
    e = FittedValues{1,n}.e;
    f = FittedValues{1,n}.f;
    g = FittedValues{1,n}.g;
    values_function(1,n) = a;
    values_function(2,n) = b;
    values_function(3,n) = c;
    values_function(4,n) = d;
    values_function(5,n) = e;
    values_function(6,n) = f;
    values_function(7,n) = g;
    % If the PSF fit was discarded by the
   user, no MA is determined
    if a == 0 && g == 0;
      MA1(1,n) = 0;
      MA1(2,n) = 0;
      MA1(3,n) = 0;
      MA1(4,n) = 0;
    else
      % Else, the MA is determined:
      FirstInt = b - c/2; FirstInt =
      ceil(FirstInt) - 1;
      LastInt = b + c/2; LastInt =
      floor(LastInt) + 1 ;
      MA1(1,n) = FirstInt; MA1(2,n) = LastInt;
      for i = FirstInt:LastInt;
        CTi(1,i) = ActualCTvalues(i,n);
```

```
            MA1(3,n) = MA1(3,n) + (g -
            CTi(1,i))/(g - 5000);
          end
          MA1(4,n) = resolutie * MA1(3,n);
        end
       close(h);
end
clear s1 s2 s3 s4 s5 s6 Y_1 Y_2 Y_3 x name
prompt g k n f e d a b c answer delta_Y h
```

A.2. Fracture orientation

In order to determine the fracture orientation from micro-CT images, the fracture needs to be thresholded and divided in separate fracture segments. These different fracture segments are then to be saved as individual objects. A former version of the Octopus Analysis software (Morpho+) saves the different fracture objects and information on its orientation and size in individual .mp0-files. It is with these .mp0-files that the following script works. Within the .mp0-files, information on the orientation of the object is saved as vector information. The different vectors are *Axis_small, Axis_middle* and *Axis_large*. These vectors are evaluated and converted to meaningful data in order to determine a strike and dip based on them:

```
% Determine the number of different objects in the dataset, as
% well as the length of an individual .mp0-file.
    d = dir ('*.mp0');
    nfiles = length(d);
    grootte = importdata(d(1).name);
    grootte = size(grootte);
    g = grootte(1,1);
    x = cell(g, nfiles);
    y = cell(6, nfiles);
    c = zeros(2, nfiles);

% Define the vectors of the x-axis and the z-axis in the images.
    a = [0 1 0];
    t = [0 0 1];

% Open one .mp0-file in order to save the data of it. This is done
% in order to define the structure of the data within the .mp0-
% file.
    for n = 1:nfiles;
        x(1:g, n) = importdata(d(n).name);
    end

% Based on the info from one of the .mp0 files, we define the
% exact location of the information on the orientation of the
% object.
```

```
for f =1:g;
       if strcmp(x(f,1),'[Axis_small]') == 1
       && strncmpi(x{f+3,1},'x=', 2) == 1;
           x_middle = f + 3;
       end
       if strcmp(x(f,1),'[Axis_middle]') == 1
       && strncmpi(x{f+3,1},'x=', 2) == 1;
           x_large = f + 3;
       end
end
```

```
% Since the object is represented as an ellipsoid, the
% information on the orientation of the object is contained in
% the length of the ellipsoid axes. This information is taken
% from the .mp0-files. Based on that information, the strike
% and dip can then be determined.
for n = 1:nfiles;
    y(1, n)= x(x_middle,n); y(2, n)=
     x(x_middle + 1,n);
    y(3, n)= x(x_middle + 2,n); y(4, n)=
     x(x_large,n);
    y(5, n)= x(x_large + 1,n); y(6, n)=
     x(x_large + 2,n);
    for i = 1:6;
        s = y{i,n};
        y{i,n} = {s(3:end)};
    end

    x1 = cell2mat(y{1,n}); x1 = str2num(x1);
    y1 = cell2mat(y{2,n}); y1 = str2num(y1);
    z1 = cell2mat(y{3,n}); z1 = str2num(z1);
    x2 = cell2mat(y{4,n}); x2 = str2num(x2);
    y2 = cell2mat(y{5,n}); y2 = str2num(y2);
    z2 = cell2mat(y{6,n}); z2 = str2num(z2);

    % Two vectors are determined that form the
    plane of the fracture, when combined.
    P1 = [x1 y1 z1];
    P2 = [x2 y2 z2];
    % The vector perpendicular to the plane of
    the fracture is determined.
    normal = cross(-P1, -P2);
    u = sign (normal);
    if u(1,3) == -1;
        normal = -normal;
```

```
    u = -u;
end

% The dip is determined.
DipInDegrees = atan2(norm(cross(normal,
t)),dot(normal,t));
DipInDegrees = DipInDegrees*180/pi;

% If the dip would be larger than 90°,
something has gone wrong
if DipInDegrees > 90;
    h = msgbox ('Dip bigger than 90° ->
    invalid value!',n,'error')
end

% The strike is determined by taking the
vector perpendicular to the plane
consisting of the vector perpendicular to
the fracture plane and the z-axis.
strike = cross(normal, t);
u = sign(normal); v = sign(strike);
% In order to fulfill the right-hand rule
used for the geological orientation of
fracture planes, the strike might have to
be mirrored.
if u == [1 1 1];
    if v == [1 -1 0];
        strike = -strike;
    end
elseif u == [-1 -1 -1];
    if v == [1 -1 0];
        strike = -strike;
    end
elseif u == [1 -1 1];
    if v == [-1 -1 0];
        strike = -strike;
    end
elseif u == [-1 1 -1];
    if v == [-1 -1 0];
        strike = -strike;
    end
elseif u == [-1 -1 1];
    if v == [-1 1 0];
        strike = -strike;
    end
elseif u == [1 1 -1];
```

```
            if v == [-1 1 0];
                strike = -strike;
            end
        elseif u == [-1 1 1];
            if v == [1 1 0];
                strike = -strike;
            end
        elseif u == [1 -1 -1];
            if v == [1 1 0];
                strike = -strike;
            end
        end

        % The strike is determined with respect to
        the x-, y- and z-axis determined in the
        micro-CT scan.
        StrikeInDegrees = atan2(norm(cross(strike,
        a)),dot(strike,a));
        StrikeInDegrees = StrikeInDegrees*180/pi;
        v = sign(strike);
        if v == [-1 -1 0] & StrikeInDegrees < 180;
            StrikeInDegrees = 360 -
        StrikeInDegrees;
        elseif v == [-1 1 0] & StrikeInDegrees <
        180;
            StrikeInDegrees = 360 -
        StrikeInDegrees;
        elseif v == [1 -1 0] & StrikeInDegrees >
        180;
            StrikeInDegrees = 360 -
        StrikeInDegrees;
        elseif v == [1 1 0] & StrikeInDegrees >
        180;
            StrikeInDegrees = 360 -
        StrikeInDegrees;
        End

        % Information on the strike and dip is
        saved in a separate variable.
        c(1,n) = StrikeInDegrees;
        c(2,n) = DipInDegrees;
    end
```

```
% The strike and dip of each of the fracture segments is now
% determined. The data is saved in a .dat-file, accessible in the
% folder of the original .mp0-files.
    c = c';
    uiwait(msgbox('Congratulations, calculations
    are over. No error encountered!','Well
    done!'));
    csvwrite('Strike&Dip.dat', c);
    clear a t b i n nfiles grootte v DipInDegrees
    P1 P2 StrikeInDegrees
    clear f strike normal x1 x2 y1 y2 z1 z2
```

Appendix B

In this appendix, a detailed sedimentological profile is given of the Wilhelmøya Subgroup, as found in outcrop and in the slimhole wells DH2 and DH4. The different facies sections in these profiles are correlated across the different locations. This figure was published in the Norwegian Journal of Geology as part of Van Stappen et al. (2014): Pore-scale characterization and modelling of CO_2 flow in tight sandstones using X-ray micro-CT; Knorringfjellet Formation of the Longyearbyen CO_2 Lab, Svalbard. Also, the samples used for fracture characterization, discussed in Chapter 3 are indicated in the figure.

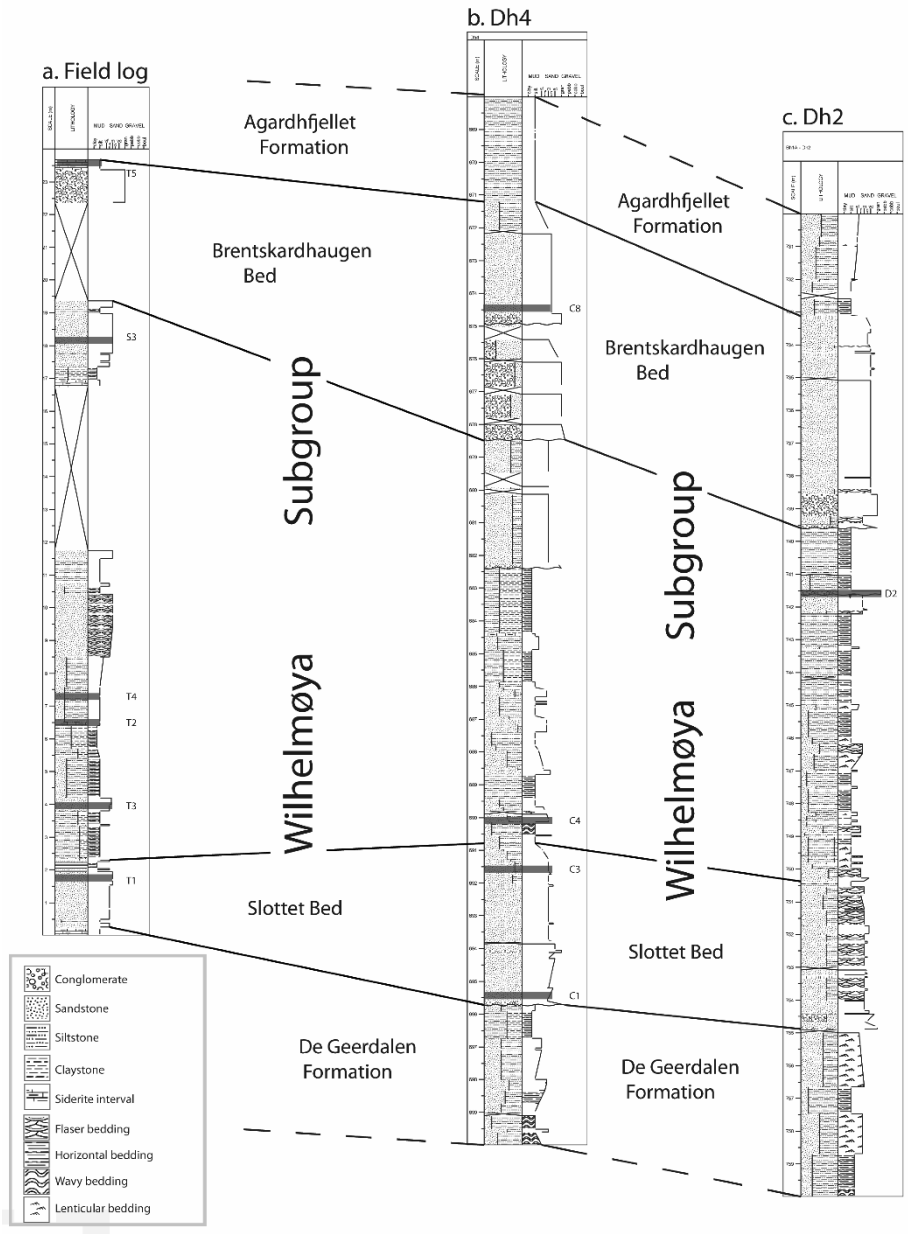

Figure B.1. Sedimentological logs of the Wilhelmøya Subgroup in outcrop at Konusdalen, and within the slimhole cores DH2 and DH4. In DH2, the section from 730 m to 760 m depth is represented, while in DH4 the section from 688 m to 700 m is represented.

Bibliography

A1 Publications

Gilabert, F.A., Van Tittelboom, K., **Van Stappen, J.**, Cnudde, V., De Belie, N., Van Paepegem, W. (2017): Integral procedure to assess crack filling and mechanical contribution of polymer-based healing agent in encapsulation-based self-healing concrete. *Cement and concrete composites*, vol. 77, pp. 68-80. (peer reviewed journal, impact factor 2017: 4,265).

De Kock, T., **Van Stappen, J.**, Fronteau, G., Boone, M.A., De Boever, W., Dagrain, F., Silversmit, G., Vincze, L., Cnudde, V. (2017): Laminar gypsum crust on Lede stone: Microspatial characterization and laboratory acid weathering. *Talanta*, vol. 162, pp. 193-202. (peer reviewed journal, impact factor 2016: 4,162).

De Camillis, M., Di Emidio, G., Bezuijen, A., Flores, D.V., **Van Stappen, J.**, Cnudde, V. (2017): Effect of wet-dry cycles on polymer treated bentonite in seawater: swelling ability, hydraulic conductivity and crack analysis. *Applied Clay Science*, vol. 142, pp. 52-59. (peer reviewed journal, impact factor 2016: 3,101).

Van Stappen, J., Bultreys, T., Gilabert, F.A., Hillewaere, X.D., Gómez, D.G., Van Tittelboom, K., Dhaene, J., De Belie, N., Van Paepegem, W., Du Prez, F.E., Cnudde, V. (2016): The microstructure of capsule containing self-healing

materials: a micro-computed tomography study. *Materials Characterization*, vol. 119, pp. 99-109. (peer reviewed journal, impact factor 2016: 2,714).

De Boever, W., Diaz, A., Derluyn, H., De Kock, T., **Van Stappen, J.**, Dewanckele, J., Bultreys, T., Boone, M., De Schryver, T., Skjønsfjell, E.T.B., Holler, M., Breiby, D.W., Cnudde, V. (2015): Characterization of composition and structure of clay minerals in sandstone with ptychographic X-ray nanotomography. *Applied Clay Science*, vol 118, pp. 258-264. (peer reviewed journal, impact factor 2015: 2,586).

Cnudde, V., De Kock, T., Boone, M., De Boever, W., Bultreys, T., **Van Stappen, J.**, Vandevoorde, D., Dewanckele, J., Derluyn, H., Càrdenes, V., Van Hoorebeke, L. (2015): Conservation studies of cultural heritage: X-ray imaging of dynamic processes in building materials. *European Journal of Mineralogy*, vol 27 (3), pp. 269-278 . (peer reviewed journal, impact factor 2015: 1,464).

De Kock, T., Boone, M.A., De Schryver, T., **Van Stappen, J.**, Derluyn, H., Masschaele, B., De Schutter, G., Cnudde, V. (2015): A pore-scale study of fracture dynamics in rock using X-ray micro-CT under ambient freeze-thaw cycling. *Environmental Science & Technology,* vol.49 (5), pp. 2867-2874. (peer reviewed journal, impact factor 2015: 5,393).

Van Stappen, J., De Kock, T., Boone, M.A., Olaussen, S., Cnudde, V. (2014): Pore-scale characterization and modelling of CO2 flow in tight sandstones using X-ray micro-CT; Knorringfjellet Formation of the Longyearbyen CO2 Lab, Svalbard. *Norwegian Journal of Geology*, vol 94, pp. 201-215. (peer reviewed journal, impact factor 2014: 2,225).

Submitted

Mahmoodlu, G., Raoof, A., Bultreys, T., **Van Stappen, J.**, Cnudde, V.: Large-scale pore network simulations of the solute dispersivity of a saturated sand column. *Advances in Water Resources.* (peer reviewed journal, impact factor 2016: 3,221).

In preparation

Van Stappen, J., Meftah, R., Boone, M.A., Bultreys, T., De Kock, T., Blykers, B.K., Olaussen, S., Cnudde, V.: In-situ triaxial testing to determine fracture permeability and aperture distribution for CO_2 sequestration in Svalbard,

Norway. *Environmental Science and Technology*. (peer reviewed journal, impact factor 2016: 6,198).

Mulrooney, M. J., Larsen, L., Rismyhr, B, **Van Stappen, J.**, Senger, K. Braathen, A. Mørk, M.B, Olaussen, S., Cnudde, V. and Ogata K.: Fluid flow properties of a potential unconventional CO2 storage unit in central Spitsbergen: the Upper Triassic to Middle Jurassic Wilhelmøya Subgroup. *Norwegian Journal of Geology* (peer reviewed journal, impact factor 2016: 0,485).

Conference proceedings

Van Stappen, J., Meftah, R., De Kock, T., Bultreys, T., Boone, M.A., Hangx, S.J.T., Spiers, C.J., Cnudde, V. (2017): Visualization of rock alteration processes in fractured reservoir rocks. *3rd International conference om Tomography of Materials and Structures, Proceedings*, Lund, Sweden, p. ICTMS2017-155 1-2.

De Kock, T., Gyffroy, J., **Van Stappen, J.**, Boone, M.N., Lanzon, M., Cnudde, V. (2017): Micro-CT in the study of gypsum crusts and patina formation on Lede stone. *3rd International conference om Tomography of Materials and Structures, Proceedings*, Lund, Sweden, p. ICTMS2017-154 1-2.

De Schryver, T., **Van Stappen, J.**, Boone, M.A., Boone, M.N., Dierick, M., Cnudde, V., Van Hoorebeke, L. (2017): 4D visualization of in-situ aluminum foam compression with lab-based motion compensated X-ray micro-CT. *7th Conference on Industrial Computed Tomography (iCT),* Leuven, Belgium, 6 p.

De Kock, T., Boone, M.A., De Schryver, T., Derluyn, H. **Van Stappen, J.**, Van Loo, D., Masschaele, B., Cnudde, V. (2015): Freeze-thaw decay in sedimentary rocks: a laboratory study with CT under controlled ambient conditions. *2nd International conference om Tomography of Materials and Structures, Proceedings*, Quebec, Canada, p. 578-582.

Van Stappen, J., Bultreys, T., Boone, M.A., De Kock, T., Cnudde, V. (2015): Dynamic micro-CT analysis of fracture formation in rock specimens subjected to multi-phase fluid flow. *2nd International conference om Tomography of Materials and Structures, Proceedings*, Quebec, Canada, p. 466-470.

De Boever, W., Derluyn, H., **Van Stappen, J.**, Dewanckele, J., Bultreys, T., Boone, M.N., De Schryver, T., De Kock, T., Skjonsfjell, E.T.B., Diaz, A., Holler, M., Cnudde, V. (2015): 3D imaging of clay minerals inside sandstone – pushing the spatial resolution limits using ptychographic tomography. *2nd*

International conference om Tomography of Materials and Structures, Proceedings, Quebec, Canada, p. 661-664.

Conference contributions

Van Steenberge, S. Verheyden, S., Quinif, Y., Genty, D., Blamart, D., Deprez, M., **Van Stappen, J.**, Cnudde, V., Cheng, H., Edwards, R.L. (2017): The last glacial inception in continental northwestern Europe: characterization and timing of the Late Eemian Aridity Pulse (LEAP) recorded in multiple Belgian speleothems. *Geophysical research abstracts, EGU2017*, Vienna, Austria, v. 19, p. EGU2017-980.

Boone, M.A., **Van Stappen, J.**, Bultreys, T., Boone, M.N., De Schryver, T., Masschaele, B., Van Loo, D., Van Hoorebeke, L., Cnudde, V. (2015): A laboratory micro-CT setup for fast continuous scanning: applications for pore scale fluid flow research. *2nd International conference om Tomography of Materials and Structures,* Quebec, Canada, p. 74.

De Kock, T., Boone, M.A., De Schryver, T., De Boever, W., Delepierre, J., **Van Stappen, J.**, Derluyn, H., Cnudde, V. (2015): Freezing rocks: a pore scale study. *5th International Geologica Belgica Meeting: Mother Earth*, Mons, Belgium, p. 200.

Van Daele, M., Cnudde, V., Vermassen, F., **Van Stappen, J.**, De Batist, M. (2015): X-ray (µ)CT in turbidite research: state-of-the-art and future challenges. *2nd UGCT seminar: book of abstracts*, Ghent, Belgium.

Hillewaere, X., Bultreys, T., **Van Stappen, J.**, Cnudde, V., Du Prez, F. (2015): Using micro-CT in the context of self-healing polymers. *2nd UGCT seminar: book of abstracts*, Ghent, Belgium.

Cnudde, V., Bultreys, T. Derluyn, H., Boone, M.A., De Kock, T., De Boever, W., **Van Stappen, J.**, De Schryver, T., Boone, M.N., Masschaele, B., Van Hoorebeke, L. (2015): Looking at pore scale processes in geomaterials using time-resolved 3D imaging and multi-scale imaging. *2nd UGCT seminar: book of abstracts*, Ghent, Belgium.

Bultreys, T., Dewanckele, J., Derluyn, H., Boone, M.A., De Kock, T., De Boever, W., **Van Stappen, J.**, De Schryver, T., Boone, M.N., Masschaele, B., Van Hoorebeke, L., Cnudde, V. (2015): Analysis of pore scale processes in geo-materials: perspectives on multi-scale and time-resolved 3D imaging. *Engineering Mechanics Institute conference, abstracts*, Stanford, USA, p.6851293 – 1.

Cnudde, V., Bultreys, t., Boone, M.N., Dewanckele, J., Derluyn, H., De Kock, T., De Boever, W., **Van Stappen, J.**, De Schryver, T., Boone, M.A., Masschaele, B., Van Hoorebeke, L. (2015): Analysing pore scale processes in geomaterials with multi-scale time-resolved 3D imaging. *7th International conference of the International Society for Porous Media, abstracts*, Padova, Italy.

Derluyn, H., De Kock, T., Boone, M.A., De Schryver, T. **Van Stappen, J.**, Masschaele, B., Boone, M.N., Cnudde, V. (2015): Chemo-mechanics of salt and ice crystallization in rocks: a 4D study using X-ray micro computed tomography. *7th International conference of the International Society for Porous Media, abstracts*, Padova, Italy.

Van Stappen, J., Bultreys, T., Boone, M.A., Cnudde, V. (2015): Micro-CT analysis of fracture formation in rock specimens subjected to multi-phase fluid flow: an experimental study at the pore-scale. *7th International conference of the International Society for Porous Media, abstracts*, Padova, Italy.

Van Stappen, J., De Kock, T., Boone, M.A., Olaussen, S., Cnudde, V. (2014): CO_2 uptake in the Wilhelmøya Subgroup reservoir section using X-ray micro-CT, Svalbard, Norway. *6th International conference of the International Society for Porous Media, abstracts*, Milwaukee, USA.

Miscellaneous

Van Stappen, J., De Kock, T., Boone, M., Senger, K., (2013): Digital dissection of reservoir samples – CT scanning reveals cracks in rocks. *News Letter 48a of the* UNIS CO_2 Lab (http://co2-ccs.unis.no).

Boone, M., **Van Stappen, J.**, De Kock, T., Cnudde, V. (2012): Applications of µCT scanning in CO_2 flooding experiments. *Longyearbyen CO_2 Lab International Workshop*, Longyearbyen, Norway, 17 Sep. 2012 – 20 Sep. 2012.